Title
Stability of Reinforced Concrete Wall Boundaries

Author
Parra Torres, Pablo Fernando

Publication Date
2015

Peer reviewed|Thesis/dissertation

Stability of Reinforced Concrete Wall Boundaries

By

Pablo Fernando Parra Torres

A dissertation submitted in partial satisfaction of the

requirements for the degree of

Doctor of Philosophy

in

Engineering - Civil and Environmental Engineering

in the

Graduate Division

of the

University of California, Berkeley

Committee in charge:

Professor Jack P. Moehle, Chair
Professor Khalid M. Mosalam
Professor Ming Gu

Fall 2015

Abstract

Stability of Reinforced Concrete Wall Boundaries

by

Pablo Fernando Parra Torres

Doctor of Philosophy in Engineering - Civil and Environmental Engineering

University of California, Berkeley

Jack P. Moehle, Chair

Structural (shear) walls are used worldwide to resist gravity and earthquake loads. In many countries, structural walls commonly are constructed with a rectangular cross section, or a cross section made up of interconnected rectangles, without an enlarged boundary element. In some countries, design practice has resulted in walls that are more slender than those used in the past. For example, in Chile and elsewhere it is not unusual to find rectangular wall edges having thickness of 6 to 8 in. (150 to 200 mm), resulting in floor-to-floor slenderness ratios reaching $h_u/b = 16$ or greater. Such walls can be susceptible to overall wall buckling in which a portion of the wall buckles out of the plane. The main objective of this research is to develop a methodology for evaluation of the onset of lateral instability in reinforced concrete slender walls. First, a simplified buckling mechanics solution for prismatic columns under inelastic tension/compression cycles is presented and later evaluated using the results of column tests. Later, three numerical models for buckling in columns are evaluated: nonlinear beam-column elements with fibers, and two-dimensional and three-dimensional nonlinear finite element models. Wall boundaries have strain gradient along the wall length, which would tend to brace the edge of the wall with the result that the simplified mechanics solution may give an over-conservative estimation of the onset of buckling. The theory may also be conservative for walls where the axial force in the boundary elements is not constant along the unsupported height, as may occur where moment gradients occur. To study these effects, analytical models of columns and walls are implemented. A simple approach is proposed to reduce the over conservatism of the simplified mechanics in cases where strain gradients cannot be neglected. Later, two-dimensional nonlinear finite element models are used to analytically reproduce the experimental response of wall tests. These models are used to estimate strain profiles for evaluation of the onset of lateral buckling in slender boundaries. Strain profiles are also estimated from a plastic hinge model. Finally, three damaged buildings in Chile are analyzed using linear models for the buildings and nonlinear models for isolated walls. Both buildings had some buckled walls after the 2010 Maule earthquake. Based on these studies, it is concluded that buckling in Chilean buildings most likely was a secondary failure that occurred after initial crushing of the wall boundaries.

ACKNOWLEDGMENTS

I would like to thank Comisión Nacional de Investigación Científica y Tecnológica (CONICYT, Chile) and the Fulbright Student Program, for providing necessary financial assistance to pursue my doctoral studies at the University of California Berkeley.

This research was also partially supported by the National Institute of Standards and Technology through the ATC 94 project. Their support is gratefully acknowledged.

I would like to express my deepest gratitude to my research advisor, Professor Jack P. Moehle. Learning from you during all these years was always a great privilege.

I thank Professors Khalid M. Mosalam, Ming Gu, Filip C. Filippou and Raymond B. Seed, for serving as members in my qualifying exam and dissertation committees.

I am also grateful to Computers & Structures, Inc. (CSI) and Professor Khalid M. Mosalam, for providing the computer software used for this study.

Likewise, I would like to thank the support of all my friends and colleagues in the Structural Engineering, Mechanics and Materials Program at University of California Berkeley.

Finally, I would like to dedicate this work to my wife Jeannette, without your love and support this achievement would not have been possible, to my two beautiful kids, Tomás and Mariano, and my parents, Sara and Miguel Angel, for always being there for me.

CONTENTS

LIST OF FIGURES

LIST OF TABLES

1 Introduction

1.1 THE PROBLEM OF WALL BOUNDARY ELEMENT INSTABILITY

Design practices prior to the 1990s favored rectangular walls with enlarged boundary elements, contributing to stability of the flexural compression zone. More recently, prevailing practices in many countries favor rectangular sections without enlarged boundaries. The more slender flexural compression zones can be susceptible to inelastic lateral buckling as shown in Figure 1.1.

Figure 1.1 Buckled wall in first story of Building #1 (DICTUC, 2010).

Figure 1.2 depicts a wall in a multistory building. A typical wall boundary will be subjected to alternating tension and compression as a building responds to an earthquake. Compressive loading acting over a wall boundary (Figure 1.2a, right edge in first story wall) may cause directly failure due to out-of-plane instability, especially if very slender. Additionally, in walls subjected to cyclic loading, buckling can also be strongly influenced by the magnitude of the tensile strain experienced by the wall for prior loading in the opposite direction (Paulay and Priestley 1993, Chai and Elayer 1999, Parra and Moehle 2014). This is because residual tensile strains in the previously yielded longitudinal reinforcement leave the wall boundary with open cracks, resulting in reduced lateral stiffness (Figure 1.2b, left edge of first story wall). Two failure modes are hypothesized. One hypothesis is that tensile yielding for loading in one direction softens the boundary for subsequent loading in the opposite direction, leading to lateral instability of an otherwise intact wall. A second hypothesis is that the wall crushes first, leaving an even smaller, irregular and probably unsymmetrical cross section, increasing the tendency for instability. This crushed section may become immediately unstable or, alternatively, subsequent tension and compression cycles

may lead to instability of the reduced cross section according to the first hypothesis, leading to a secondary buckling failure. In such cases, the compression zone of a well confined slender wall behaves basically as a plastic material with very low lateral stability (Moehle, 2014). Either type of buckling can lead to critical loss of axial force capacity in the flexural compression zone of the wall. The many questions surrounding the occurrence of wall instability led to the research that is summarized in this dissertation.

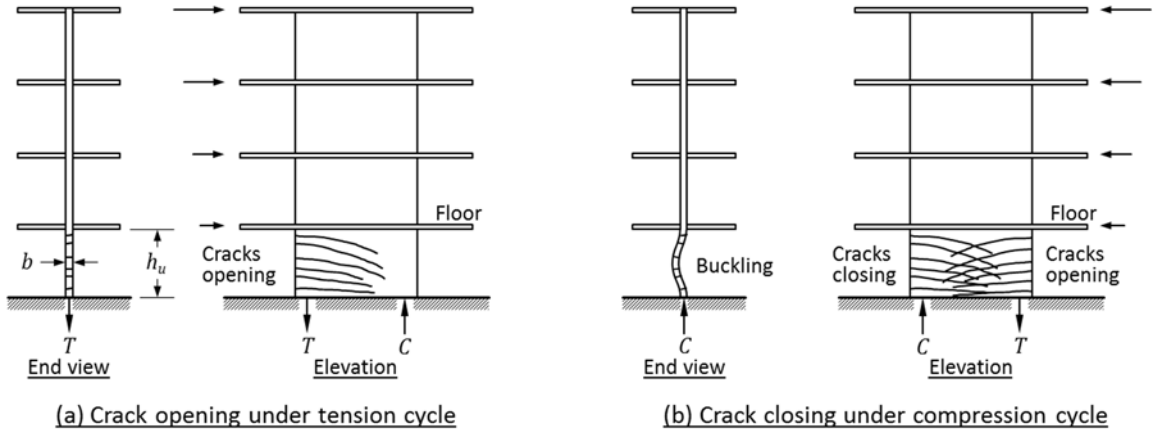

Figure 1.2 Lateral instability of wall boundary previously yielded in tension (After Chai and Elayer, 1999).

1.2 REVIEW OF PRIOR STUDIES

Prior 2010, out-of-plane buckling of columns and structural walls during cyclic loading had been reported only in a few laboratory tests but not in an actual earthquake. In 2010, following the Mw 8.8 Maule Earthquake, out-of-plane buckling of slender walls was reported in two buildings in Chile (Parra and Moehle, 2014). Damage associated with out-of-plane deformation of structural wall boundaries was also observed following the Mw 7.1 New Zealand Earthquake in 2011 (Sritharan et al., 2014). These observations created a renewed interest in the practical aspects of inelastic buckling of slender structural walls. As part of the research that ensued, several past studies related to out-of-plane instability were identified as being particularly relevant.

In the 1970s, the Portland Cement Association (PCA) conducted a combined experimental and analytical investigation to develop design criteria for seismically loaded structural walls (Oesterle et. al, 1976). The testing program included two rectangular walls, six barbell walls and one flanged wall, all of them under reversing lateral loading. Large out-of-plane displacement of the boundary region was reported in one of the rectangular walls (specimen R2), followed by failure induced by lateral instability. This was the first documented case of failure in a slender wall due to out-of-plane buckling.

Goodsir (1985) conducted a testing program with the purpose of assessing the effects of slenderness ratio and confinement of the flexural compression region on the hysteretic response of structural walls. Approximately quarter-scale models were built and loaded with reversed cyclic lateral forces. Failure due to out-of-plane-instability of the wall boundary was reported.

Paulay and Priestley (1993) postulated that the main cause of instability in wall boundaries was the inelastic tensile steel strains imposed by preceding earthquake-induced displacements, rather than excessive compressive strains. They developed a theoretical model for the prediction of the onset of out-of-plane buckling, based on considerations of fundamental structural behavior. Paulay and Priestley compared their model with the experimental response in walls obtained by Goodsir (1985). Their work forms part of the basis of the simplified mechanics of wall instability presented in the present research.

Chai and Elayer (1999) conducted a set of tests of reinforced concrete columns under reversed cyclic axial tension and compression. Fourteen specimens were tested, with incremental tension/compression cycles until buckling failure was reached. They also developed a model for the prediction of the maximum tensile strain required to buckle a column during load reversal.

Thomsen and Wallace (2004) conducted an experimental and analytical study of reinforced concrete structural walls with symmetrical and unsymmetrical cross sections, designed under a displacement-based methodology. Four, approximately quarter-scale walls (two rectangular and two T-shaped walls) where tested under constant axial load and reversed cyclic lateral displacements. For one of the T-shaped walls (TW2) with closely spaced hoops at the wall boundaries, failure due to global instability of the wall stem was reported.

Dashti, Dhakal, and Pampanin (2014) investigated the ability of finite element models in predicting nonlinear behavior and failure patterns of reinforced concrete walls. The software TNO DIANA with curved shell elements and embedded reinforcement was used for this purpose. They reported that finite element models can simulate the response of structural walls at global and local levels with reasonable accuracy, with failure patterns that include shear, flexure, flexure-shear, and flexure-out-of-plane modes, depending on different parameters, particularly the shear-span ratio of the specimens.

Rosso, Almeida, and Beyer (2015) report tests of two thin reinforced concrete walls with single layers of vertical and horizontal reinforcement. The two walls were subjected to unidirectional (in-plane) and bidirectional (in-plane and out-of-plane) loading, respectively. Failure in both walls was triggered by out-of-plane instability of the boundary elements.

1.3 RELEVANT CODE REQUIREMENTS AND DESIGN PRACTICE

Provisions governing the slenderness of structural walls designed as compression members are contained in Chapter 11 of ACI 318-14, Building Code Requirements for Structural Concrete and Commentary (ACI, 2014). According to section 11.3.1 of ACI 318-14, for a given unsupported wall height, h_u, an empirical method limits wall slenderness ratios to $h_u/b \leq 25$, and corresponding wall thicknesses to $b \geq 4$ inches, in which b is the thickness of the extreme flexural compression fiber. Alternatively, walls can be designed by section 11.5.2 or analyzed by 11.8 of ACI 318-14, in which case there are no minimum thickness requirements.

Previously, the Uniform Building Code (ICBO, 1997) required $h_u/b \leq 16$ for structural walls providing lateral resistance in regions of highest seismicity. This provision was intended to ensure lateral stability for wall boundaries. This provision was not carried forward into the International Building Code (ICC, 2000) and subsequent editions.

Up through its 2011 edition, ACI 318 did not limit the slenderness of special structural walls, that is walls intended to provide lateral force resistance in buildings assigned to the highest seismic design categories. However, the 2014 edition of ACI 318 introduced slenderness provisions for such walls. According to section 18.10.6.4(b), when special boundary elements are required, the width of the flexural compression zone, b, along the special boundary element region, including flange if present, shall be at least $h_u/16$. This is a new requirement of ACI 318-14 introduced to prevent lateral instability failures of slender wall boundaries observed in recent earthquakes (Wallace et al., 2012; Parra and Moehle, 2014; ATC-94, 2014). For walls with large cover, where spalling of cover concrete would lead to a significantly reduced section, ACI 318-14 recommends considering a larger thickness for the boundary element.

ACI 318-14, section 11.7.2.3 requires two curtains of reinforcement for walls thicker than 10 inches. Additionally, section 18.10.2.2 requires at least two curtains of reinforcement in walls having a factored design shear force $V_u > 2A_{cv}\lambda\sqrt{f_c'}$ or $h_w/l_w \geq 2$ where h_w and l_w refer to height and length of the entire wall, A_{cv} is the web area (equal to wall length, l_w, times wall web thickness, b_w), λ is a modification factor for lightweight aggregate concrete, and f_c' is the specified compressive strength of the concrete (psi). Otherwise one curtain of reinforcement is permitted. These provisions are intended to improve stability of wall boundaries.

Prior to the 1990s, common design and construction practice used enlarged boundary elements that provided inherent stability against overall wall buckling. Current practice embeds the boundary element within the rectangular cross-section. According to NIST GCR 11-917-11, Seismic Design of Cast-in-Place Concrete Special Structural Walls and Coupling Beams: A Guide for Practicing Engineers (NIST, 2011), 8 inches is a practical lower limit on thickness for special structural walls; however, construction quality and wall performance are generally improved if the thickness is at least 12 inches where special boundary elements are used, and at least 10 inches elsewhere. Thinner wall sections are permitted by ACI 318, and are not uncommon in the United States or other countries that use ACI 318 as a basis.

Eurocode 8 (2004) specifies minimum wall thickness of 8 inches (200mm) for confined parts of walls. Moreover, if the length of the confined part does not exceed the larger of $2b$ and $0.2l_w$, b should be at least $h_u/15$. Otherwise, b should be at least $h_u/10$. According to NZ 3101 (2006), the thickness of the wall boundary over the height of the plastic hinge but not less than the full height of the first story shall be at least:

$$b_m = \frac{\alpha_r k_m \beta (h_u/l_w + 2) l_w}{1700\sqrt{\xi_r}} \tag{1.1}$$

in which $\alpha_r = 1$ for walls with two curtains of longitudinal reinforcement and 1.25 for walls with one curtain, $\beta = 7$ for ductile plastic regions, $k_m = 1$ except for long walls it can be defined as:

$$k_m = \frac{l_u}{(0.25 + 0.055\, h_u/l_w) l_w} \leq 1.0 \tag{1.2}$$

$$\xi_r = 0.3 - \frac{\rho_l f_y}{2.5\, f_c'} \geq 0.1 \tag{1.3}$$

The term ρ_l refers to the local longitudinal reinforcement ratio in the wall boundary. These equations result in wall slenderness ratio h_u/b ranging from around 8 for slender, heavily reinforced walls to around 30 for more squat, lightly reinforced walls.

1.4 RESEARCH PROGRAM OBJECTIVES

This research addresses the key aspects involved in out-of-plane stability of reinforced concrete wall boundaries during cyclic (earthquake) loading. The research program had the following specific objectives:

- To develop a simplified buckling mechanics solution for evaluation of the onset of out-of-plane instability in slender columns subjected to inelastic tension/compression cycles, and to evaluate its accuracy using the results of previous column tests.
- To analytically study the onset of out-of-plane instability in column specimens using three numerical models: force-based elements in OpenSees, and two-dimensional and three-dimensional nonlinear finite elements in TNO DIANA.
- To study the effects of strain gradients along the length and height of a wall using OpenSees and TNO DIANA models.
- To develop a simple method for the estimation of the onset of out-of-plane instability in slender walls for constant and variable strain gradients along their length and height.
- To analytically study the onset of out-of-plane instability in wall specimens using two-dimensional nonlinear finite element models in TNO DIANA and a plastic hinge model.
- To study two damaged buildings in Chile where wall buckling was observed following the 2010 Maule earthquake, to explore the failure mechanism in buckled walls, and to provide recommendations for the improvement of current design practices of slender walls. To study one collapsed building in Chile, following the 2010 earthquake, to determine if buckling was one of the causes that triggered the observed failure.

1.5 ORGANIZATION OF REPORT AND SCOPE

Chapter 1 introduces the study of out-of-plane instability in columns and slender walls. Chapter 2 presents the main theoretical background of four models for out-of-plane instability: simplified buckling mechanics, OpenSees force-based elements with fibers, and TNO DIANA finite element models using shell and solid elements. Chapter 3 presents an evaluation of each analytical model by comparison with the results of column tests. These studies include sensitivity analysis of the response for the variation of some key parameters. Chapter 4 studies the influence of a variable strain profile along the wall length and unsupported height in the onset of out-of-plane instability of slender walls. Chapter 5 evaluates the onset of out-of-plane instability in wall tests using different models (nonlinear finite elements, nonlinear beam-column elements, and simplified approaches). Chapters 6 presents analysis results for two buildings where walls showed apparent damage due to buckling following the 2010 Maule earthquake and one building that collapsed following the same earthquake. For Building #1, analyses include an ETABS linear model of the full structure and two approaches for the analysis of isolated walls: a PERFORM 3D model and a simplified nonlinear models. Building #2 is also analyzed using ETABS. Nonlinear analysis of

isolated walls considers only simplified methods for this case. For Building #3, results of linear analysis of the full building (Tanyeri, 2014) are considered for this research. Simplified nonlinear models are used here to analyze isolated walls. For buckling evaluation, the simplified mechanics is used for the three buildings. These analyses provide data from which to assess the likelihood of failure being triggered by concrete crushing or by wall lateral instability. Chapter 7 presents a summary of the findings of the study and Appendix A presents analysis results of OpenSees models used to determine buckling in columns for different axial force profiles.

2 Analytical Models for Global Instability

2.1 INTRODUCTION

Figure 1.2 presented a typical multistory wall, where the foundation, floor diaphragms, and roof diaphragm provide lateral support at every story level. Thus, the unsupported height of the wall boundary can be taken equal to the story clear height, h_u. An effective length kh_u can be defined based on the rotational restraints at the different floor levels. In the present analysis, which is concerned with very slender walls, it may be reasonable to consider the wall to be fixed at top and bottom of the clear height. Accordingly, k is taken equal to 0.5. If the boundary yields in tension, a cracked section is produced, with crack width dependent on the amplitude of the reinforcement tensile strain ϵ_{sm} during the tension excursion. In a previously yielded wall, crack closure under deformation reversal may require yielding of the longitudinal reinforcement in compression. In a wall with two curtains of reinforcement, any slight asymmetry in the reinforcement is likely to result in one curtain yielding before the other, leading to out-of-plane curvature and a tendency to buckle out of plane. In a wall with one curtain of reinforcement, out-of-plane curvature occurs even more readily. Whether the wall remains stable depends on the amplitude of the prior tensile strain ϵ_{sm} and the slenderness ratio h_u/b of the wall. As a design approximation, the critical slenderness ratio can be related to the maximum prior tensile strain ϵ_{sm}, as will be shown later. In this research different procedures are used to estimate ϵ_{sm} in laboratory tested walls (Oesterle et al., 1976; Thomsen and Wallace, 2004) and walls in two Chilean buildings (Buildings #1 and #2). The estimated tensile strain values are compared with the limit given by the buckling theory developed in section 2.2. This enables an assessment of whether the walls are likely to have buckled prior to concrete crushing.

2.2 SIMPLIFIED MECHANICS OF GLOBAL INSTABILITY[1]

Consider the wall shown in Figure 2.1. Wall lateral buckling is constrained by the story clear height (Figure 2.1a). We assume the wall has been flexed previously such that the boundary yields in tension (Figure 2.1b), with a unit length (measured in the horizontal direction) of the boundary element developing tension force T, maximum tensile stress f_{sm}, and tensile strain ϵ_{sm}. Upon deformation reversal, just before the boundary element yields in compression, the longitudinal reinforcement will have unloaded by strain $\epsilon_s = f_{sm}/E_s$ and reloaded in compression to $-\epsilon_y$,

[1] In the following theoretical development, some concepts introduced by Paulay and Priestley (1993) and Chai and Elayer (1999) are followed.

ignoring the Bauschinger effect, such that the residual tensile strain is approximately $\epsilon_{res} = \epsilon_{sm-} f_{sm}/E_s - \epsilon_y$. To simplify the model, the residual tensile strain is approximated as $\epsilon_{res} \approx \epsilon_{sm} - 0.005$. Invariably, one curtain of reinforcement will yield before the other, producing the curvature shown in Figure 2.1d, and out-of-plane displacement as illustrated in Figure 2.1a and Figure 2.1c. Whether the boundary remains stable depends on magnitude of the lateral displacement δ_{max} relative to the wall thickness b, which relates to the maximum previous tensile strain ϵ_{sm} and the resulting curvature as illustrated in Figure 2.1c.

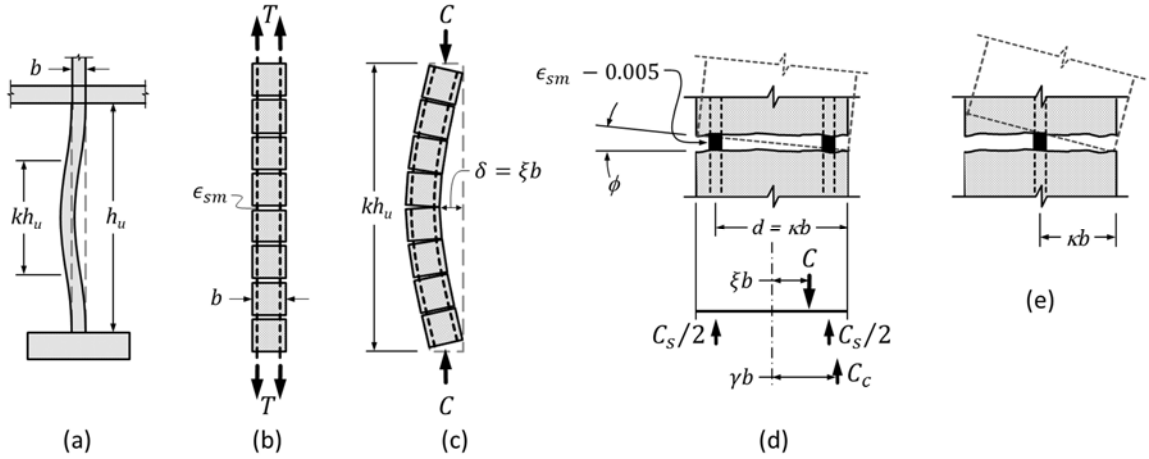

Figure 2.1 Lateral instability of wall boundary previously yielded in tension, partly after Paulay and Priestley (1993).

To estimate conditions for stability, we first approximate the effective length (height). For a multi-story wall with length l_w not less than the first-story clear height h_u, it is reasonable to assume that the flexural plastic hinge extends over the height of the first story. Assuming fixity at top and bottom, the effective length in Figure 2.1a is $kh_u = 0.5h_u$. Examining the effective length more closely (Figure 2.1c) and assuming a simple harmonic buckled shape, we can express the lateral displacement as:

$$\delta(x) = \delta_{max} \cdot sin\left(\frac{x}{kh_u}\pi\right) \tag{2.1}$$

Computing the second derivative of Equation (2.1).

$$\delta''(x) = -\delta_{max} \left(\frac{\pi}{kh_u}\right)^2 sin\left(\frac{x}{kh_u}\pi\right) \tag{2.2}$$

Now Equation (2.2) is evaluated at the element midheight to obtain the maximum curvature.

$$\delta''\left(\frac{kh_u}{2}\right) = \phi_{max} = -\delta_{max} \left(\frac{\pi}{kl_u}\right)^2 \tag{2.3}$$

The maximum lateral displacement is defined as $\delta_{max} = \xi b$ in Figure 2.1c. Therefore, the relation between δ_{max} and the maximum curvature ϕ_{max} is:

$$\delta_{max} = \xi b = \phi_{max} \left(\frac{k h_u}{\pi}\right)^2 \tag{2.4}$$

As indicated before, the residual tensile strain is approximated as $\epsilon_{res} \approx \epsilon_{sm} - 0.005$. Therefore, from Figure 2.1d the maximum curvature is:

$$\phi_{max} = \frac{\epsilon_{sm} - 0.005}{d} \tag{2.5}$$

Combining Equation (2.4) and (2.5):

$$\xi b = \frac{\epsilon_{sm} - 0.005}{d} \left(\frac{k h_u}{\pi}\right)^2 \tag{2.6}$$

Equilibrium of forces and moments in the free-body diagram of Figure 2.1d result in the following two expressions:

$$\sum F = 0 \rightarrow C = C_c + C_s \tag{2.7}$$

$$\sum M = 0 \rightarrow C\xi b = C_c \gamma b \tag{2.8}$$

From Equation (2.8) we obtain:

$$C = \frac{\gamma}{\xi} C_c \tag{2.9}$$

In Equation (2.8), moments are taken about the centerline, such that moments of longitudinal reinforcement compressive force resultants (assumed equal) cancel. Assuming longitudinal reinforcement is stressed to f_y and assuming the concrete compressive force C_c is represented by the usual rectangular stress block with depth $\beta_1 c$ and average stress $0.85 f_c'$, we can write:

$$C_s = \rho b f_y \tag{2.10}$$

$$C_c = 0.85 f_c' \beta_1 c \tag{2.11}$$

From Figure 2.1d:

$$\gamma b = \frac{b}{2} - \frac{1}{2}\beta_1 c \tag{2.12}$$

Then Equation (2.11) can be expressed as:

$$C_c = 0.85\, f_c'(1-2\gamma)b \tag{2.13}$$

Substituting Equation (2.9), Equation (2.10) and (2.13) in Equation (2.7):

$$\frac{\gamma}{\xi} 0.85\, f_c'(1-2\gamma)b = 0.85\, f_c'(1-2\gamma)b + \rho b f_y \tag{2.14}$$

Manipulating Equation (2.14) we obtain:

$$\gamma^2 - \gamma\left(\frac{1}{2}+\xi\right) + \frac{\xi}{2}\left(1+\frac{m}{0.85}\right) = 0 \tag{2.15}$$

in which $m = \rho f_y / f_c'$ is the mechanical reinforcement ratio.

Equation (2.16) shows the solutions of the quadratic equation:

$$\gamma = \frac{\left(\frac{1}{2}+\xi\right) \pm \sqrt{\left(\frac{1}{2}+\xi\right)^2 - 2\xi\left(1+\frac{m}{0.85}\right)}}{2} \tag{2.16}$$

To have a real solution and stability, the term in the radical must be positive. Then:

$$\left(\frac{1}{2}+\xi\right)^2 \geq 2\xi\left(1+\frac{m}{0.85}\right) \tag{2.17}$$

Rearranging terms of Equation (2.17):

$$\xi^2 - \xi\left(1+\frac{2m}{0.85}\right) + \frac{1}{4} \geq 0 \tag{2.18}$$

In order to meet Equation (2.18), the upper bound of ξ is given by the smallest solution of the quadratic equation. Therefore:

$$\xi \leq 0.5\left(1+\frac{2m}{0.85} - \sqrt{\left(\frac{2m}{0.85}\right)^2 + \frac{4m}{0.85}}\right) \tag{2.19}$$

Equation (2.19) was originally introduced by Paulay and Priestley (1993). From Figure 2.1d, $d = \kappa b$. From Equation (2.6), defining the width b as the critical width b_{cr} and solving for b/kh_u results in:

$$\frac{b_{cr}}{kh_u} = \frac{1}{\pi}\sqrt{\frac{\epsilon_{sm} - 0.005}{\kappa\xi}} \tag{2.20}$$

The main variables appearing in Equation (2.20) are slenderness ratio kh_u/b, maximum tensile strain ϵ_{sm} in longitudinal reinforcement, effective depth parameter κ for longitudinal reinforcement, and ξ. Parameter κ can be found from $d = \kappa b$, where it is noted that $\kappa \approx 0.8$ for thin walls with two curtains of reinforcement and 0.5 for walls with single layer of reinforcement. From this, it is clear that walls with two curtains of longitudinal reinforcement are inherently more stable than walls with a single curtain.

Parameter ξ relates to the mechanical reinforcement ratio as shown in Equation (2.19). The somewhat complex expression for this parameter makes it inconvenient for preliminary design. For practical construction, $0.4 \leq \sqrt{\xi} \leq 0.6$. By selecting typical values, a more practical preliminary design tool might be developed.

Equation (2.20) is plotted in Figure 2.2 for the two practical limit values of $\sqrt{\xi}$, $\kappa = 0.8$, and considering fixed-fixed boundary conditions (k =0.5). The strain corresponding to fracture of the boundary element longitudinal reinforcement represents a practical upper bound for strain in the reinforcement. Considering the effects of low-cycle fatigue, the fracture strain of reinforcement bars depends on the number of cycles and the strain range ϵ_a of each cycle (Coffin, 1954; Manson, 1953; Brown and Kunnath, 2004). For earthquake loading, a commonly accepted maximum tensile strain is 0.05 (Moehle, 2014). Therefore, the practical range of strain indicated in Figure 2.2 is limited by 0.05. Also shown in the figure is the limiting slenderness ratio of $h_u/b = 16$, as specified in the 1997 Uniform Building Code. If this slenderness limit is considered, the maximum useable tensile strain before buckling in compression ranges from 0.025 to 0.05.

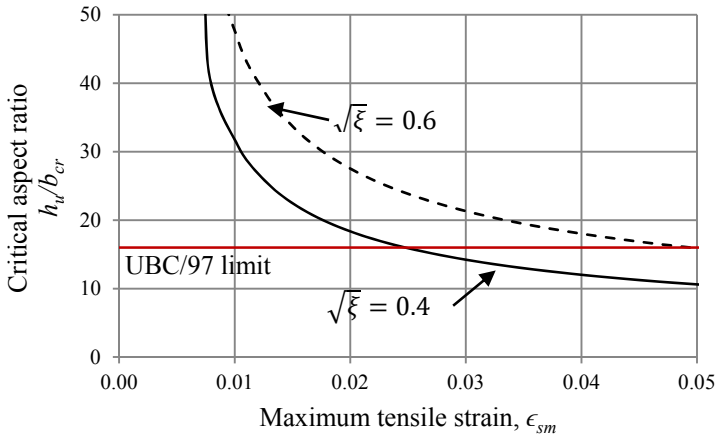

Figure 2.2 Critical slenderness ratio as a function of maximum tensile strain.

The preceding derivation is based on an idealized wall boundary subjected to uniform compressive strain. Actual wall boundaries have strain gradient along the wall length, which would tend to brace the edge of the wall. This suggests that the preceding results should be conservative for actual wall boundaries.

2.3 NONLINEAR BEAM-COLUMN ELEMENTS WITH FORCE-BASED FORMULATION

2.3.1 Introduction

Two approaches are usually followed to perform nonlinear analysis of frame structures: concentrated plasticity and distributed inelasticity elements. For the case of concentrated plasticity elements, inelastic deformations take place at predetermined locations at the element ends. For the case of distributed inelasticity elements, nonlinearity is defined at the sectional level. The element is modeled with a number of controlling sections and then the inelastic behavior is integrated to obtain the global inelasticity of the structure. Therefore, there is no need to predefine the regions where nonlinear excursions can occur.

One way of computing the section response is by discretizing it using fibers, with each fiber following a uniaxial nonlinear material behavior. By this approach, the model does not require calibration of the moment-curvature relation. However, reproducing flexure-shear interaction can be challenging.

Two formulations are normally used in distributed inelasticity elements: displacement-based and the force-based formulations. For this study, force-based beam-column elements with fibers and nonlinear geometry are considered to model buckling of prismatic sections under tension/compression loading. Open Systems for Earthquake Engineering Simulation (OpenSees) is used as the analysis platform. The use of OpenSees force-based elements here is limited to the buckling analysis of columns. For walls, where buckling does not involve the entire cross section and is limited to the boundary elements region, a different approach using nonlinear finite element methods is considered, as described in section 2.4. Frame analyses are performed in the buckling plane only.

2.3.2 Two-dimensional element formulation

The basic principles of distributed inelasticity elements with force-based formulation in 2D problems are presented next (Filippou and Fenves, 2004). Section level analysis is a crucial step, since the material nonlinear behavior is introduced at this level using uniaxial constitutive relationships of the form $\sigma_x = \sigma_x(\epsilon_x)$ for each fiber. The strain and stress are functions of the position x along the element axis and the position within the cross sections specified in local coordinates y and z. The axial strain at point M in Figure 2.3 can be written as the product of two functions:

$$\epsilon_X(x, y, z) = \{1 \quad -y\} \begin{Bmatrix} \epsilon_a(x) \\ \phi_z(x) \end{Bmatrix} = \{a_s(y)\}\{e(x)\} \tag{2.21}$$

where $\{e(x)\}$ is the section deformations vector (ϵ_a = axial strain at coordinate origin; $\phi_z(x)$ = curvature about z-axis) and $\{a_s(y)\}$ represents the strain distribution at section x according to Bernoulli's assumption of plane sections remaining plane.

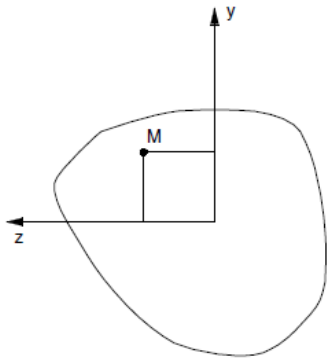

Figure 2.3 Cross section with coordinates axes.

Section forces vector is defined as:

$$\{s(x)\} = \begin{Bmatrix} N(x) \\ M_Z(x) \end{Bmatrix} = \int_A \begin{Bmatrix} 1 \\ -y \end{Bmatrix} \sigma_x(\epsilon_X) dA \tag{2.22}$$

where N is the axial force and M_Z is the moment about the z-axis. The area integral of Equation (2.22) is evaluated numerically using fiber discretization in the y-direction. The same approach is used to evaluate Equation (2.23). The section stiffness matrix $[k_s(x)]$ is defined as the partial derivative of the section forces $\{s(x)\}$ with respect to section deformations $\{e(x)\}$, as shown next:

$$[k_s(x)] = \frac{\partial\{s(x)\}}{\partial\{e(x)\}} = \int_A \begin{Bmatrix} 1 \\ -y \end{Bmatrix} \frac{\partial \sigma_x}{\partial \epsilon_X} \{a_s(y)\} dA \tag{2.23}$$

The differential equations of equilibrium for a frame element in the undeformed configuration are:

$$\frac{\partial N}{\partial \mathrm{x}} + w_x(x) \quad ; \quad \frac{\partial^2 M_z}{\partial \mathrm{x}^2} - w_y(x) \tag{2.24}$$

in which w_x and w_y are the axial and transverse components of the distributed element load.

Figure 2.4 shows the basic force system of a 2D beam-column element $\{q\} = [q_1 \quad q_2 \quad q_3]^{\mathrm{T}}$, which comprises an axial load and two end moments. In the basic system the shear forces depend on the end moments and provide equilibrium. The basic deformations $\{v\} = [v_1 \quad v_2 \quad v_3]^{\mathrm{T}}$ comprise one axial deformation and two rotations of the end nodes. These flexural deformations are measured relative to the element chord in the deformed configuration.

Using the basic forces $\{q\}$ (Figure 2.4) as boundary values of the problem to obtain the statement of equilibrium:

$$\{s(x)\} = \begin{Bmatrix} N(x) \\ M(x) \end{Bmatrix} = \begin{bmatrix} 1 & 0 & 0 \\ 0 & \left(\frac{x}{L} - 1\right) & \frac{x}{L} \end{bmatrix} \begin{Bmatrix} q_1 \\ q_2 \\ q_3 \end{Bmatrix} = [b(x)]\{q\} \tag{2.25}$$

The matrix $[b(x)]$ represents the force-interpolation functions and can be regarded also as an equilibrium transformation matrix between section forces $\{s(x)\}$ and basic forces $\{q\}$. In the presence of element loads, the internal forces represent the particular solution of the differential equations in Equation (2.24), which only need to satisfy homogeneous boundary conditions. Denoting the particular solution $\{s_w(x)\}$, the equilibrium equation is:

$$\{s(x)\} = [b(x)]\{q\} + \{s_w(x)\} \tag{2.26}$$

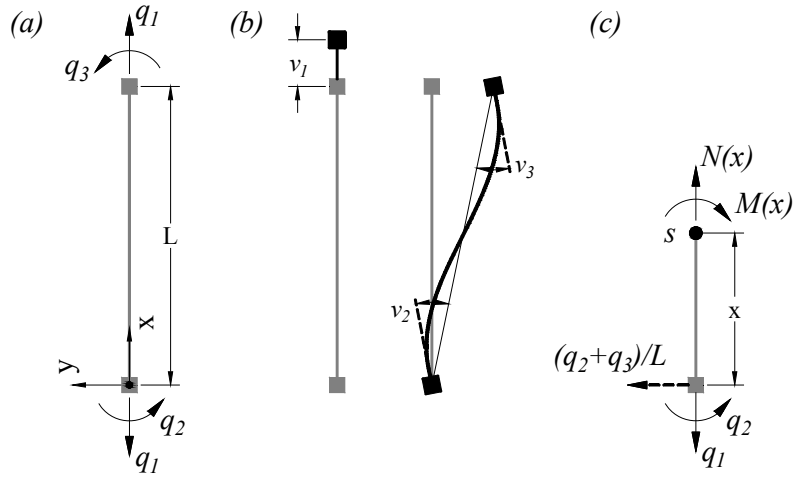

Figure 2.4 (a) Element basic force system; (b) basic deformation system; (c) forces at the section level.

The geometric compatibility of the frame element can be established with the principle of virtual forces as shown.

$$\delta\{q\}^T\{v\} = \int_L \delta\{e\}^T\{s(x)\}dx \tag{2.27}$$

where $\{v\}$ is the intra-element deformation vector shown in Figure 2.4. Using Equation (2.26) for the equilibrium relation of the virtual force system, $\delta\{s(x)\} = [b(x)]\delta\{q\}$, and after substitution into Equation (2.27) gives the compatibility statement as:

$$\{v\} = \int_L [b(x)]^T\{e(x)\}dx \tag{2.28}$$

In the force-based formulation (Spacone et al., 1996) we make use of the fact that the internal forces $\{s(x)\}$ at a distance x for the end i of a two-node frame element are given as the product of the force-interpolation functions $[b(x)]$ and the basic forces $\{q\}$ according to Equation (2.25). Note that these relations hold for any material response, as long as the equilibrium can be satisfied in the undeformed configuration (small displacements). The element deformations can then be established by the principle of virtual forces from Equation (2.28). This implies that the section deformations $\{e(x)\}$ can be obtained from the section forces $\{s(x)\}$. However, the inverse

of this relation is available. Therefore, finding $\{e(x)\}$ requires solving the following nonlinear system of equations:

$$[b(x)]\{q\} + \{s_w(x)\} - \{s(e(x))\} = 0 \tag{2.29}$$

This is a main difference with respect to the displacement-based element formulation, which is based in standard finite element approach where section deformations are estimated as the derivatives of an imposed displacement field.

The force-based formulation uses the available exact static equilibrium equations between the end nodal forces, $\{q\}$ and the internal forces, $\{s\}$. This results in constant axial load and linear bending moment distribution along the element length. On the other hand, the displacement-based formulation uses the principle of virtual displacements to formulate "weak" equilibrium between these two sets of forces, resulting in an error where the internal forces at each section are not in equilibrium with the element basic forces, if fine meshes are not implemented. Due to the enforced displacement field along the element length, the displacement-based element has constant axial deformation and linear curvature distribution. To properly represent nonlinear behavior of non-prismatic elements, the displacement-based approach requires mesh refinement to overcome the restrictions in the axial deformation and curvature distribution, while the force-based approach requires the addition of more integration points but still using fewer elements.

The solution of this nonlinear system requires establishing the change of the element deformations with $\{q\}$. This change is reflected in the following expression:

$$\frac{\partial\{v\}}{\partial\{q\}} = \frac{\partial}{\partial\{q\}}\int_0^L [b(x)]^T\{e(x)\}dx = \int_0^L [b(x)]^T[f_s(x)][b(x)]dx \tag{2.30}$$

where $[f_s(x)]$ is the section flexibility (inverse of section stiffness $[k_s(x)]$ defined in Equation (2.23). Equation (2.30) depicts the tangent flexibility matrix $[f_t]$ of the element.

Equations (2.28) and (2.30) for the state determination of the distributed inelasticity elements involve integrals over the element length. These integrals are evaluated numerically as follows:

$$\int_{\mathrm{L}} \mathrm{g(x)}dx \approx \sum_{i=1}^{nIP} w_i g(x_i) \tag{2.31}$$

Several quadrature rules are available to evaluate Equation (2.31). Section 2.3.7 describes the Gauss-Lobatto quadrature, which is used here. This rule is particularly suitable when it is important to include the ends of the element in the evaluation. This is indeed the case in earthquake engineering applications, where the largest inelastic deformations quite often take place at the element ends. Four points suffice for the integrals in Equations (2.28) and (2.30) as long as we are not interested in the effect of the midspan section. In the latter case, five integration points are recommended.

2.3.3 State determination of elements with force-based formulation

Solving structural analysis problems requires determining the element basic forces, $\{q\}$, given the element deformations, $\{v\}$ (element state determination). In force-based formulation elements this task is not as straightforward task as it is for displacement-based formulation elements.

A complication of the force-based formulation is that there is not a direct relation between the element deformations and the basic forces, as shown in Equation (2.29). State determination of force-based elements requires nested iterative procedures to find equilibrium between the end deformations and the section deformations. Figure 2.5 shows the first iteration of this process.

The force-based formulation is computationally more expensive in comparison with the displacement-based formulation. However, it guarantees exact equilibrium between the end forces of the element and those at the section level, allows representing a non-uniform curvature field along the element length, and allows a fewer number of elements to be used to converge to the exact solution. These three reasons justify the selection of the force-based formulation to model buckling of prismatic under tension/compression cycles.

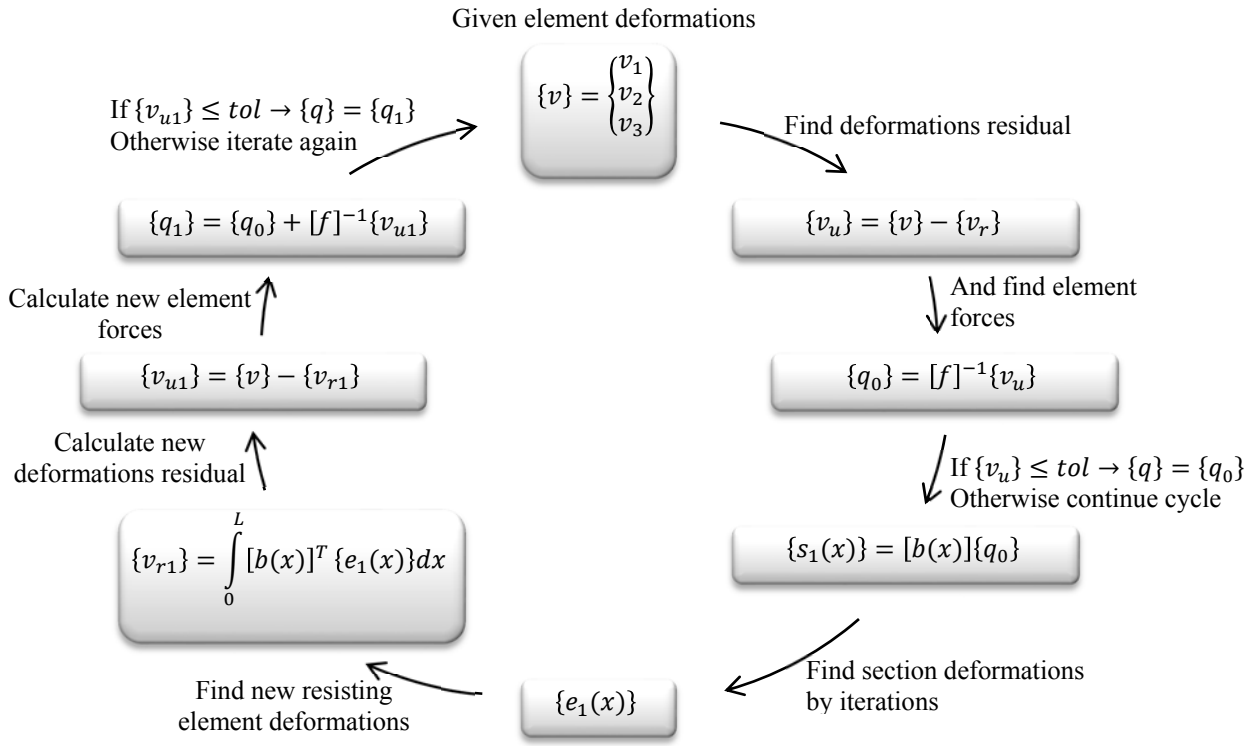

Figure 2.5 First iteration of force-based element state determination.

2.3.4 Uniaxial stress-strain relationship of concrete

For OpenSees modeling of column specimens, the material object used for confined and unconfined concrete is Concrete01. This is a uniaxial concrete model (Kent and Park, 1971; Scott

et al., 1980; Hognestard, 1951; Roy and Sozen, 1964) with degraded linear unloading/reloading stiffness according to the work of Karsan and Jirsa (1969) and no tensile strength.

Equation (2.32) shows the concrete stress f_c as a function of the given strain ϵ_c for Concrete01 model.

$$f_c = \begin{cases} f_c' \left[\frac{2\epsilon_c}{\epsilon_0} - \left(\frac{\epsilon_c}{\epsilon_0} \right)^2 \right] & for\ \epsilon_c \leq \epsilon_0 \\ f_c'[1 - Z(\epsilon_c - \epsilon_0)] \geq 0.2 f_c' & for\ \epsilon_c > \epsilon_0 \end{cases} \tag{2.32}$$

In Equation (2.32), the peak stress value $f_c = f_c'$ occurs at a strain ϵ_0. For this study ϵ_0 is taken as 0.002 (unconfined concrete). Equation (2.33) defines the parameter Z.

$$Z = \frac{0.5}{\frac{3 + 0.002 f_c'}{f_c' - 1000} - \epsilon_0} \tag{2.33}$$

where f_c' is in psi.

2.3.5 Localization in force-based elements

Modeling structures with a strain softening constitutive model is numerically challenging because the response is mesh dependent. Localization in displacement-based solid finite elements has been extensively studied in the past by, among several others, Bazant and Oh (1983), Bazant and Planas (1998) and De Borst (1994). The concept of constant fracture energy has been used to deal with localization and mesh sensitive response in continuum finite element analysis (Bazant and Oh, 1983; Bazant and Planas, 1998).

Force-based elements lose objectivity at local and global levels depending on the section constitutive behavior (Scott and Hamutcuoglu; 2008). Moreover, in force-based elements, strains localize at one integration point, which is a disadvantage in comparison to the displacement-based elements, where the displacement interpolation functions force localization within a single element. The number and placement of the integration points of the numerical integration scheme used for element integrals define not only the accuracy of the result but also the structural response during material softening (Coleman and Spacone, 2001).

The concept of constant fracture energy can be applied to force-based elements that soften in compression, according to the work of Coleman and Spacone (2001). This is the approach followed in this study to regularize the force-based elements avoiding ill-posed solutions and mesh-dependent response. Equation (2.34) defines the fracture energy in compression G_c for the post-peak part of the compressive stress-strain relation of concrete.

$$G_c = \int f_c du_i \tag{2.34}$$

where f_c is the concrete stress and u_i is the inelastic displacement. Equation (2.34) represents the area under the post-peak portion of the compressive stress-displacement curve. Equation (2.34) can be also expressed in terms of stress and strain as shown next.

$$G_c = h \int f_c d\epsilon_i \tag{2.35}$$

where h is a length scale. For smeared cracking models in nonlinear finite element analysis, h represent the crack bandwidth (section 2.4.5). Here, for force-based elements h becomes the length (weight) of the softening integration point.

The constant fracture energy regularization is now applied to the material model defined in section 2.3.4. The pre-peak behavior is still given by Equation (2.32), with a post-peak behavior given by a linear softening branch until a stress of $0.2f_c'$ is reached at a strain ϵ_{20}, according to Figure 2.6.

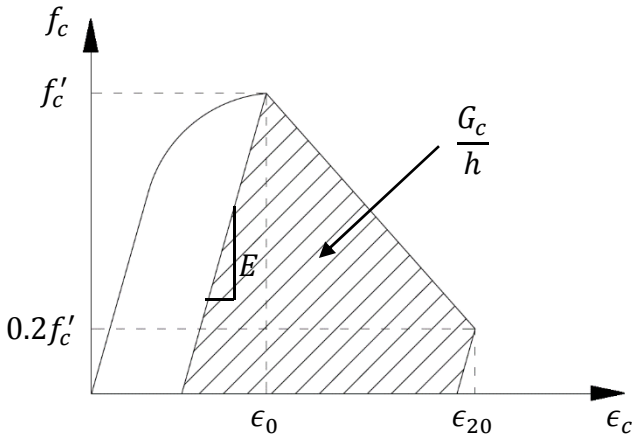

Figure 2.6 Fracture energy in Kent and Park (1971) relation.

The value of ϵ_{20} must be calibrated according to Equation (2.36) to get a constant energy release.

$$\epsilon_{20} = \frac{G_c}{0.6f_c'h} - \frac{0.8f_c'}{E} + \epsilon_0 \tag{2.36}$$

Experimental tests (Feenstra, 1993) have shown that the total compressive fracture energy of concrete ranges from 10 to 25 $\mathrm{Nmm/mm^2}$ (0.06 and 0.14 kip in./in.^{2}). According to Equation (2.36), the constitutive model must be calibrated for each integration point given that each point has a different weight. However, for analysis of out-of-plane instability in slender columns, only the weight of one integration point, located at the position where the plastic hinge is expected to form, is used to calculate ϵ_{20}.

2.3.6 Uniaxial stress-strain relationship of steel reinforcement

The uniaxial Giuffré-Menegotto-Pinto (Menegotto et al. 1973, Filippou et al. 1983) steel material object with isotropic strain hardening is used to model reinforcement bars (Steel02 in OpenSees). This model is capable of representing the hysteretic behavior of steel reinforcement exhibiting the Bauschinger effect together with isotropic strain hardening. The constitutive response consists of one-dimensional stress-strain relations for branches between two subsequent load reversal points. The material state parameters are updated after each load reversal. The model is expressed in terms of a dimensionless stress σ^* and a scaled strain ϵ^*.

$$\epsilon^* = \frac{\epsilon - \epsilon_r^n}{\epsilon_y^{n+1} - \epsilon_r^n} \tag{2.37}$$

$$\sigma^* = \frac{\sigma - \sigma_r^n}{\sigma_y^{n+1} - \sigma_r^n} \tag{2.38}$$

where ϵ^* and σ^* are expressed in the strain-stress coordinates of the last reversal point (ϵ_r^n, σ_r^n) and in the strain-stress coordinates of the updated yield point (ϵ_y^{n+1}, σ_y^{n+1}). Equation (2.39) shows the basic expression of the model.

$$\sigma^* = b\epsilon^* + \frac{(1-b)\epsilon^*}{\left(1+\epsilon^{*R}\right)^{\frac{1}{R}}} \tag{2.39}$$

where b is the ratio of the strain hardening to the initial modulus and R is the curvature parameter controlling the shape of the unloading/reloading cycles defined in Equation (2.40).

$$R = R^0 - \frac{A_1 \xi_p^{max}}{A_2 + \xi_p^{max}} \tag{2.40}$$

In Equation (2.40) R^0 is the initial curvature parameter and ξ_p^{max} is the maximum plastic excursion during a previous half-cycle. Equation (2.41) depicts the isotropic strain hardening.

$$\frac{\sigma_{sh}}{\sigma_{y0}} = A_3 \left(\frac{\epsilon_{max}^t}{\epsilon_{y0}} - A_4 \right) \tag{2.41}$$

where σ_{y0} and ϵ_{y0} are the initial yield stress and corresponding strain, ϵ_{max}^t is the maximum absolute total strain at the instant of strain reversal, and σ_{sh} is the stress shift in the linear yield asymptote for isotropic hardening. A_1 to A_4 are material constants that require experimental determination.

2.3.7 Quadrature rule for beam-column elements

A wide range of numerical integration options are available in OpenSees to be used in force-based beam-column elements (Scott, 2011). Only the Gauss-Lobatto quadrature is used for this study, as described in the following.

The discrete forms for numerical evaluation of Equations (2.28) and (2.30) are:

$$\{v\} \approx \sum_{i=1}^{nIP} [b(x_i)]^T \{e(x_i)\} w_i \tag{2.42}$$

$$[f_t] \approx \sum_{i=1}^{nIP} [b(x_i)]^T [f_s(x_i)][b(x_i)] w_i \tag{2.43}$$

where nIP is the number of integration points along the element length, x_i is the location of each integration point within the element length and w_i is its associated weight. Distributed plasticity methods permit yielding at any integration point along the element length.

Gauss-Lobatto integration is the default rule in OpenSees and the most used approach in force-based elements because it places an integration point at each end of the element, where bending moments are largest in the absence of interior element loads. The order of accuracy of this rule is $2nIP - 3$.

Table 2.1 shows the locations of integration points and weights for the Gauss-Lobatto integration rule.

Table 2.1 Gauss-Lobatto rule: integration points and weights for -1≤x_i≤1.

Number of integration points, nIP	x_i	w_i
3	0	$\frac{4}{3}$
	±1	$\frac{1}{3}$
4	$\pm\sqrt{\frac{1}{5}}$	$\frac{5}{6}$
	±1	$\frac{1}{6}$
5	0	$\frac{32}{45}$
	$\pm\sqrt{\frac{3}{7}}$	$\frac{49}{90}$
	±1	$\frac{1}{10}$

2.4 NONLINEAR FINITE ELEMENTS

2.4.1 Introduction

The use of force-based nonlinear beam-column elements in OpenSees for buckling analysis is limited to axially loaded columns (section 2.3). In walls, buckling is a more complicated phenomena because it occurs locally at the boundary elements and does not necessarily propagate through the entire cross section. Therefore, the use of a single beam-column element located at the centroid of the cross section cannot accurately represent the complex behavior expected in a wall boundary.

Two-dimensional or three-dimensional nonlinear finite element models can be used to perform buckling analysis in columns and walls. These models allow representing the local buckling expected in wall edges more accurately. For this case, the software TNO DIANA is used to perform nonlinear finite element analysis in buckled specimens. Geometric nonlinearity is considered using a Total Lagrange description. Different elements are considered for column and wall analyses.

For columns, a four-node, three-side isoparametric solid pyramid element (TE12L) are used to model concrete. These elements have 12 degrees of freedom and use a linear interpolation polynomial for the translations. Therefore, the stress and strain distribution is constant over the element. Buckling modeling requires using several elements within the member thickness. This is computationally very expensive for the case of walls, where two dimensions (length and height) are much larger than the third one (thickness). For this reason, solid elements are not used to model buckling in walls. Instead, four-node, quadrilateral isoparametric curved shell elements (Q20SH) are selected instead. These elements are based on an isoparametric degenerated-solid approach by introducing two shell hypotheses: straight normal and zero normal stress. The first hypothesis assumes plane sections remain plane but not necessarily orthogonal to the reference surface (it includes shear deformation according to Reissner-Mindlin theory). The second hypothesis assumes that the normal stress component in the normal direction of a lamina basis is forced to zero. This formulation allows using several integration points within the element thickness, which is fundamental for buckling modeling. For comparison purposes, columns are also analyzed using Q20SH curved-shell elements.

In DIANA, longitudinal reinforcing bars can be modeled as embedded reinforcement, which means that the bars do not have degrees of freedom of their own and their strains are computed from the displacement field of the mother elements (TE12L for columns, Q20SH for walls). Therefore, there is perfect bond between the reinforcement and the surrounding concrete. In this formulation the finite element mesh can be defined independently of the bar locations.

2.4.2 Four-node isoparametric solid pyramid element (TE12L)

The TE12L (Figure 2.7) is a four-node, three-side isoparametric solid pyramid element with three degrees of freedom per node (displacements in three orthogonal directions). This element is used here to study buckling of prismatic columns under tension-compression cycles. It is based on linear interpolation and numerical integration.

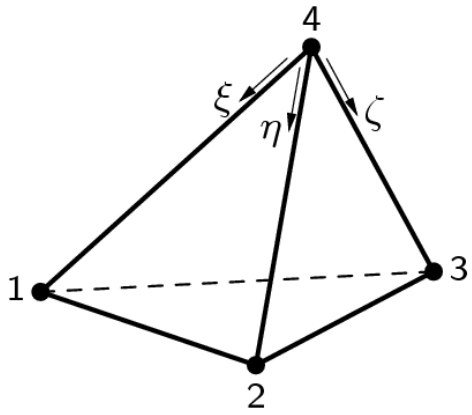

Figure 2.7 TE12L solid element (DIANA, 2014).

The polynomials for the translations u_{xyz} can be expressed as:

$$\mathrm{u}_i(\xi,\eta,\zeta) = a_0 + a_1\xi + a_2\eta + a_3\zeta \tag{2.44}$$

These polynomials yield a constant strain and stress distribution over the element volume. This study uses the default integration scheme which is one point over the element volume.

2.4.3 Four-node quadrilateral isoparametric curved shell elements (Q20SH)

The Q20SH element (Figure 2.8) is a four-node quadrilateral isoparametric curved shell element with five degrees of freedom per node (displacements in three orthogonal directions and rotation around two orthogonal axes in the element plane).

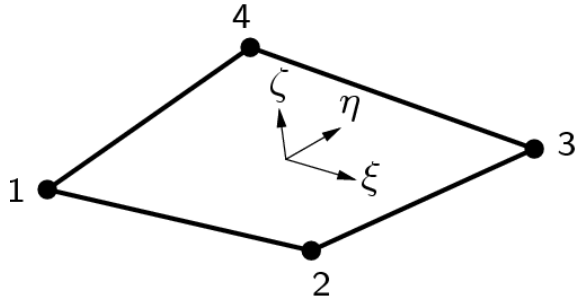

Figure 2.8 Q20SH curved shell element (DIANA, 2014).

It is based on linear interpolation. The polynomials for the translations u and the rotations ϕ can be expressed as:

$$u_i(\xi,\eta) = a_0 + a_1\xi + a_2\eta + a_3\xi\eta \tag{2.45}$$

$$\theta_i(\xi,\eta) = b_0 + b_1\xi + b_2\eta + b_3\xi\eta \tag{2.46}$$

Typically, for a rectangular element, these polynomials yield approximately the following strain and stress distribution in the element plane xy (z axis perpendicular to the element plane). The strain ϵ_{xx}, the curvature ϕ_{xx}, the moment m_{xx}, the membrane force n_{xx} and the shear force q_{xz} are constant in x direction and vary linearly in y direction. The strain ϵ_{yy}, the curvature ϕ_{yy}, the moment m_{yy}, the membrane force n_{yy} and the shear force q_{yz} are constant in y direction and vary linearly in x direction.

The in-plane lamina strains ϵ_{xx}, ϵ_{yy} and γ_{xy} vary linearly in the thickness direction. The transverse shear strains γ_{xz} and γ_{yz} are forced to be constant in the thickness direction. A shear reduction factor is used to obtain an equivalent uniform shear stress, since the actual transverse shear stress varies parabolically over the thickness. For the case of thin shells (walls in this case), this factor is considered as 1.2, which is the default value used in TNO DIANA. This modification gives a constant shear stress that yields approximately at the same shear strain energy that the actual parabolic shear stress.

The curved shell elements are based on isoparametric degenerated-solid approach by introducing two shell hypotheses:

- Plane sections — It assumes that plane sections remain plane, but not necessarily orthogonal to the reference surface.
- Zero-normal-stress — It assumes that the normal stress component in the normal direction of a lamina basis is forced to zero.

For this study, the Q20SH quadrilateral element is numerically integrated using a 2x2 Gauss scheme for in-plane integration (Figure 2.9).

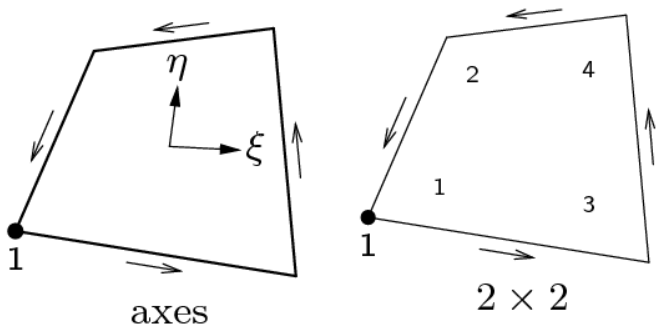

Figure 2.9 Gauss integration scheme 2x2 for Q20SH element.

Figure 2.10 shows the enumeration of the integration points in the thickness direction for various schemes. Note that two-point integration is according to a Gauss rule. In any other case, a Simpson rule is applied. This study considers the Simpson rule with eleven integration points.

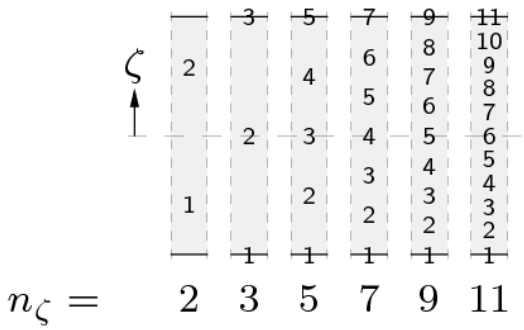

Figure 2.10 Thickness integration schemes for Q20SH element.

2.4.4 Total strain crack model

There are several approaches to model concrete fracture. In this study, the smeared crack model (Rashid 1968, Feenstra et al., 1991) is used. By this approach, the cracked solid is considered as a continuum. Therefore, the behavior of cracked concrete is described in terms of stress-strain relations and, upon cracking, the initial stress-strain relation is replaced by an orthotropic stress-strain relation. The finite element mesh is then preserved, which makes this model computationally efficient. The concrete constitutive model can be based on different concepts like decomposed or total strain. The decomposed strain concept (De Borst et al. 1985, Rots 1988) is based on the decomposition of the strain into an elastic part and an inelastic part, $\epsilon = \epsilon^{el} + \epsilon^{cr}$. In the total strain concept the stress is a function of the total strain and this is the approach followed here.

The constitutive model based on total strain was developed along the lines of the modified compression field theory proposed by Vecchio and Collins (1986) and extended to 3D by Selvy and Vecchio (1993). The concrete constitutive behavior depends on the model adopted for the shear stress-strain relation. This results in different crack models, the fixed and the rotating smeared crack model. For this study, the rotating crack model embedded in a total strain concept is used. This model uses the coaxial stress-strain approach, in which the stress-strain relationships are evaluated in the principal directions of the strain vector, corresponding to the crack directions.

The strain vector $\{\epsilon_{xyz}\}$ in the global coordinate system xyz is updated according to:

$$\{\epsilon_{xyz}\}^{i+1} = \{\epsilon_{xyz}\}^{i} + \Delta\{\epsilon_{xyz}\}^{i+1} \tag{2.47}$$

which is transformed to the strain vector in the crack directions *nst* with the strain transformation matrix $[T]$.

$$\{\epsilon_{nst}\}^{i+1} = [T] \cdot \{\epsilon_{xyz}\}^{i+1} \tag{2.48}$$

In the rotating crack model the strain transformation matrix depends on the current strain vector $\left[T\left(\{\epsilon_{xyz}\}^{i+1}\right)\right]$. This transformation matrix is determined by calculating the eigenvectors of the strain tensor given by Equation (2.49).

$$[E] = \begin{bmatrix} \epsilon_{xx} & \epsilon_{xy} & \epsilon_{xz} \\ \epsilon_{yx} & \epsilon_{yy} & \epsilon_{yz} \\ \epsilon_{zx} & \epsilon_{zy} & \epsilon_{zz} \end{bmatrix} \tag{2.49}$$

The eigenvalues are stored in the rotation matrix $[R]$.

$$[R] = [\{n\} \quad \{s\} \quad \{t\}] = \begin{bmatrix} c_{xn} & c_{xs} & c_{xt} \\ c_{yn} & c_{ys} & c_{yt} \\ c_{zn} & c_{zs} & c_{zt} \end{bmatrix} \tag{2.50}$$

where $c_{xn} = cos(\emptyset_{xn})$, that is, the cosine between the *x* axis and the *n* axis.

In the general 3D stress situation, the strain transformation matrix $[T]$ is calculated by substituting the appropriate values.

$$[T] = \begin{bmatrix} c_{xn}^2 & c_{yn}^2 & c_{zn}^2 & c_{xn}c_{yn} & c_{yn}c_{zn} & c_{zn}c_{xn} \\ c_{xs}^2 & c_{ys}^2 & c_{zs}^2 & c_{xs}c_{ys} & c_{ys}c_{zs} & c_{zs}c_{xs} \\ c_{xt}^2 & c_{yt}^2 & c_{zt}^2 & c_{xt}c_{yt} & c_{yt}c_{zt} & c_{zt}c_{xt} \\ 2c_{xn}c_{xs} & 2c_{yn}c_{ys} & 2c_{zn}c_{zs} & c_{xn}c_{ys} + c_{yn}c_{xs} & c_{yn}c_{zs} + c_{zn}c_{ys} & c_{zn}c_{xs} + c_{xn}c_{zs} \\ 2c_{xs}c_{xt} & 2c_{ys}c_{yt} & 2c_{zs}c_{zt} & c_{xs}c_{yt} + c_{ys}c_{xt} & c_{ys}c_{zt} + c_{zs}c_{yt} & c_{zs}c_{xt} + c_{xs}c_{zt} \\ 2c_{xt}c_{xn} & 2c_{yt}c_{yn} & 2c_{zt}c_{zn} & c_{xt}c_{yn} + c_{yt}c_{xn} & c_{yt}c_{zn} + c_{zt}c_{yn} & c_{zt}c_{xn} + c_{xt}c_{zn} \end{bmatrix} \tag{2.51}$$

The constitutive model is formulated in the crack coordinate system as shown.

$$\{\sigma_{nst}\}^{i+1} = \left\{\sigma\left(\{\epsilon_{nst}\}^{i+1}\right)\right\} \tag{2.52}$$

The updated vector in the *xyz* coordinate system is given by:

$$\left\{\sigma_{xyz}\right\}^{i+1} = [T]^T \cdot \{\sigma_{nst}\}^{i+1} \tag{2.53}$$

The strain transformation matrix $[T]$ is given by the current strain transformation matrix $\left[T\left(\left\{\epsilon_{xyz}\right\}^{i+1}\right)\right]$ in the coaxial rotating concept. In a fixed concept the matrix is given by its value at incipient cracking.

During loading the concrete is subjected to both tensile and compressive stress, which can result in cracking and crushing of the material. In the 3D concrete material, the deterioration due to cracking and crushing is monitored with six internal damage variables α_k, collected in the vector $\{\alpha\}$. Internal variables *k*=1, 2 and 3 are monitoring the maximum strain, hence, are greater or equal zero, and variables *k*=4, 5 and 6 are monitoring the minimum strain and, hence, are smaller or equal zero (Figure 2.11). It is assumed that damage recovery is not possible and therefore the values of internal damage variables α_k are always increasing.

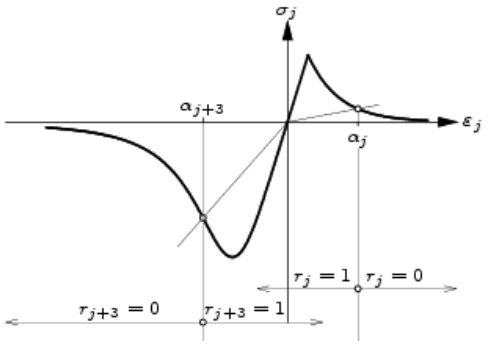

Figure 2.11 Loading-unloading parameters.

The loading-unloading-reloading condition is monitored with the additional unloading constraints r_k (Figure 2.11), which model separately the stiffness degradation in tension and compression. The tension unloading constraints are:

$$r_k = \begin{cases} 0 & if\ \epsilon_k^{i+1} > \alpha_k \\ 1 & if\ \epsilon_k^{i+1} \leq \alpha_k \end{cases}, \quad k = 1,2,3 \tag{2.54}$$

The compression unloading constraints are:

$$r_k = \begin{cases} 0 & if\ \epsilon_{k-3}^{i+1} < \alpha_k \\ 1 & if\ \epsilon_{k-3}^{i+1} \geq \alpha_k \end{cases}, \quad k = 4,5,6 \tag{2.55}$$

The internal variables vector is updated as shown:

$$\{\alpha\}^{i+1} = \{\alpha\}^{i+1} + [W] \cdot \Delta\{\epsilon\} \tag{2.56}$$

The matrix $[W]$ is given by:

$$[W] = \begin{cases} W_{k,k} = 1 - r_k & k = 1,2,3 \\ W_{k,k-3} = 1 - r_k & k = 4,5,6 \end{cases} \tag{2.57}$$

With the assumption of no damage recovery, the stress in direction *j* is given by:

$$\sigma_j = f_j(\{\alpha\}, \{\epsilon_{nst}\}) \cdot g_j(\{\alpha\}, \{\epsilon_{nst}\}) \tag{2.58}$$

where f_j is the uniaxial stress-strain relationship and g_j is the loading-unloading function with $0 \leq g_j \leq 1$. If unloading and reloading are modeled with a secant approach, determined by the maximum and minimum strain in each crack direction, the loading-unloading function is given by:

$$g_j = \begin{cases} 1 - \dfrac{\propto_j - \epsilon_j}{\alpha_j} & if\ \epsilon_j > 0 \\ 1 - \dfrac{\propto_{j+3} - \epsilon_j}{\alpha_{j+3}} & if\ \epsilon_j < 0 \end{cases} \tag{2.59}$$

A secant stiffness matrix is considered to impose equilibrium between applied and resisting forces in an incremental-iterative solution scheme. This approach has proved to be robust and stable in reinforced concrete structures with extensive cracking. For tension, the secant stiffness terms in the *j-th* cracking direction are given by:

$$\bar{\bar{E}}_j = \frac{f_j(\{\alpha\}, \{\epsilon_{nst}\})}{\propto_j} \tag{2.60}$$

For compression, the terms are:

$$\bar{\bar{E}}_j = \frac{f_j(\{\alpha\}, \{\epsilon_{nst}\})}{\propto_{j+3}} \tag{2.61}$$

The secant stiffness matrix indicated in Equation (2.62) is obtained in the principal coordinate system for and orthotropic material with zero Poisson's ratio in all directions.

$$[D]_{secant} = \begin{bmatrix} \bar{E}_1 & 0 & 0 & 0 & 0 & 0 \\ 0 & \bar{E}_2 & 0 & 0 & 0 & 0 \\ 0 & 0 & \bar{E}_3 & 0 & 0 & 0 \\ 0 & 0 & 0 & \bar{G}_{12} & 0 & 0 \\ 0 & 0 & 0 & 0 & \bar{G}_{23} & 0 \\ 0 & 0 & 0 & 0 & 0 & \bar{G}_{31} \end{bmatrix} \tag{2.62}$$

For the rotating crack model, the shear modulus $\bar{G}_{12} = \bar{G}_{23} = \bar{G}_{31} = 0$.

The Poisson effect of a material determines the lateral displacement of a specimen subjected to a uniaxial tensile or compressive loading. If these displacements are constrained a passive lateral confinement will act on the specimen. This effect is considered important in a 3D model of reinforced concrete structures. In the work of Selby and Vecchio (1993) this effect is modeled through a pre-strain concept in which the lateral expansion effects are accounted for with an additional external loading on the structure. This implies that the computational flow of the finite element engine is adapted to this method. The Poisson effect is taken into account via the equivalent uniaxial strain concept. In case of linear-elastic behavior the constitutive relationship in a 3D stress-strain situation is given by:

$$\{\sigma_{nst}\} = \frac{E}{(1+\nu)(1-2\nu)} \begin{bmatrix} 1-\nu & \nu & \nu \\ \nu & 1-\nu & \nu \\ \nu & \nu & 1-\nu \end{bmatrix} \{\epsilon_{nst}\} \tag{2.63}$$

This relationship is now expressed in terms of equivalent uniaxial strains as:

$$\{\sigma_{nst}\} = \begin{bmatrix} E & 0 & 0 \\ 0 & E & 0 \\ 0 & 0 & E \end{bmatrix} \{\tilde{\epsilon}_{nst}\} \tag{2.64}$$

with the equivalent uniaxial strain vector $\{\tilde{\epsilon}_{nst}\}$ defined by:

$$\begin{Bmatrix} \tilde{\epsilon}_1 \\ \tilde{\epsilon}_2 \\ \tilde{\epsilon}_3 \end{Bmatrix} = \begin{bmatrix} \frac{1-\nu}{(1+\nu)(1-2\nu)} & \frac{\nu}{(1+\nu)(1-2\nu)} & \frac{\nu}{(1+\nu)(1-2\nu)} \\ \frac{\nu}{(1+\nu)(1-2\nu)} & \frac{1-\nu}{(1+\nu)(1-2\nu)} & \frac{\nu}{(1+\nu)(1-2\nu)} \\ \frac{\nu}{(1+\nu)(1-2\nu)} & \frac{\nu}{(1+\nu)(1-2\nu)} & \frac{1-\nu}{(1+\nu)(1-2\nu)} \end{bmatrix} \begin{Bmatrix} \epsilon_1 \\ \epsilon_2 \\ \epsilon_3 \end{Bmatrix} \tag{2.65}$$

Rewriting Equation (2.65).

$$\{\tilde{\epsilon}_{nst}\} = [P]\{\epsilon_{nst}\} \tag{2.66}$$

This concept is also applied to the nonlinear material model implemented in TNO DIANA. The stress vector in the principal coordinate system, Equation (2.52), is evaluated in terms of the equivalent uniaxial strain vector, $\{\tilde{\epsilon}_{nst}\}$, and not in terms of the principal strain vector, $\{\epsilon_{nst}\}$. The

equivalent uniaxial strain vector is simply determined when the principal strain vector and the (constant) Poisson's ratio are known.

In a cracked state, the Poisson effect of a material ceases to exist. Stretching of a cracked direction no longer leads to contraction of the perpendicular directions. To model this phenomenon, an orthotropic formulation is adapted for Poisson's ratios. Similar to a damage formulation where the secant modulus reduces after cracking, the Poisson's ratios reduce at the same pace. Assuming that

$$\begin{aligned} \nu_{yz} &= \nu_{zy} \\ \nu_{zx} &= \nu_{xz} \\ \nu_{xy} &= \nu_{yx} \end{aligned} \tag{2.67}$$

the matrix $[P]$ of Equation (2.66) is written as:

$$[P] = \begin{bmatrix} \frac{1-\nu_{yz}^2}{\Delta'} & \frac{\nu_{yx}+\nu_{zx}\nu_{yz}}{\Delta'} & \frac{\nu_{zx}+\nu_{yx}\nu_{zy}}{\Delta'} \\ \frac{\nu_{xy}+\nu_{xz}\nu_{zy}}{\Delta'} & \frac{1-\nu_{zx}^2}{\Delta'} & \frac{\nu_{zy}+\nu_{zx}\nu_{xy}}{\Delta'} \\ \frac{\nu_{xz}+\nu_{xy}\nu_{yz}}{\Delta'} & \frac{\nu_{yz}+\nu_{xz}\nu_{yx}}{\Delta'} & \frac{1-\nu_{xy}^2}{\Delta'} \end{bmatrix} \tag{2.68}$$

where

$$\Delta' = 1 - \nu_{xy}^2 - \nu_{yz}^2 - \nu_{zx}^2 - 2\nu_{xy}\nu_{yz}\nu_{zx} \tag{2.69}$$

For recomputation of the shear moduli both stiffnesses and Poisson's ratios are reduced.

$$G = \frac{E}{2(1+\nu)} \tag{2.70}$$

2.4.5 Uniaxial stress-strain relationship of concrete

The tensile behavior of reinforced concrete can be modeled using different approaches. For the total strain crack model, several softening functions based on fracture energy are implemented in DIANA. Tensile behavior which is not directly related to the fracture energy can also be modeled in DIANA within the total strain concept. For this study, a brittle behavior according to Figure 2.12 is considered for concrete in tension.

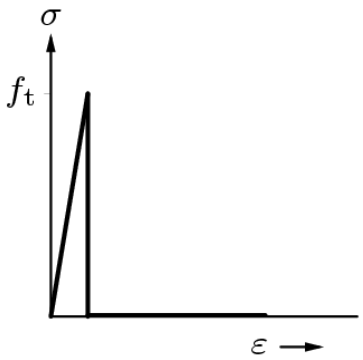

Figure 2.12 Concrete stress-strain relationship in tension (DIANA, 2014).

ACI 363R-92 (1992) recommends the following expression for the tensile strength of concrete having a compressive strength in the range of 3,000 to 12,000 psi (21 to 83 MPa).

$$f_t = 7.4\sqrt{f_c'} \tag{2.71}$$

where f_c' is the concrete compressive strength (psi).

In order to avoid the mesh dependence of the response when the concrete experiences softening in compression, a parabolic curve based on fracture energy formulation according to Feenstra (1993) is used to model its compressive behavior, according to Equation (2.72) and Figure 2.13.

$$f_c = \begin{cases} f_c' \dfrac{1}{3}\dfrac{\epsilon_c}{\epsilon_{0/3}} & if \quad 0 \le \epsilon_c < \epsilon_{0/3} \\ f_c' \dfrac{1}{3}\left(1 + 4\left(\dfrac{\epsilon_c - \epsilon_{0/3}}{\epsilon_0 - \epsilon_{0/3}}\right) - 2\left(\dfrac{\epsilon_c - \epsilon_{0/3}}{\epsilon_0 - \epsilon_{0/3}}\right)^2\right) & if \quad \epsilon_{0/3} \le \epsilon_c < \epsilon_0 \\ f_c' \dfrac{1}{3}\left(1 - \left(\dfrac{\epsilon_c - \epsilon_0}{\epsilon_{cu} - \epsilon_0}\right)^2\right) & if \quad \epsilon_0 \le \epsilon_c < \epsilon_{cu} \\ 0 & if \quad \epsilon_{cu} \le \epsilon_c \end{cases} \tag{2.72}$$

where $\epsilon_{0/3}$ is the strain at which one-third of the maximum compressive strength f_c' is reached, ϵ_0 is the strain at stress f_c', and ϵ_{cu} is the strain at which the concrete is completely softened in compression. These three parameters are defined in Equations (2.73) to (2.75).

$$\epsilon_{0/3} = \frac{1}{3}\frac{f_c'}{E_c} \tag{2.73}$$

$$\epsilon_0 = \frac{5}{3}\frac{f_c'}{E_c} = 5\epsilon_{0/3} \tag{2.74}$$

$$\epsilon_{cu} = \frac{3}{2}\frac{G_c}{h f_c'} - \epsilon_0 \tag{2.75}$$

where G_c is the post-peak concrete compressive fracture energy and h the crack bandwidth to be defined later. Both parameters govern the softening part of the curve defined in Equation (2.72). Experimental tests done by Feenstra (1993) showed that the compressive fracture energy of concrete ranges from 10 to 25 $\mathrm{Nmm/mm^2}$ (0.06 to 0.14 kip in./in.^{2}).

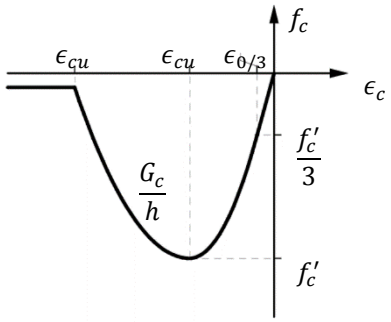

Figure 2.13 Concrete stress-strain relationship in compression (DIANA, 2014).

This study considers default values for crack bandwidth given by Equation (2.76) for shell elements and Equation (2.77) for solid elements.

$$h = \sqrt{2A} \tag{2.76}$$

$$h = \sqrt[3]{V} \tag{2.77}$$

where A is the total area of the element and V its volume.

The strength and ductility of concrete under compressive stresses increase with increasing isotropic stress. Enhanced mechanical properties due to lateral confinement are considered directly in the determination of the uniaxial stress-strain relationship of confined concrete and it is an input for the TNO DIANA model. Lateral cracking effects in the uniaxial stress-strain relationship are not considered for this study. The modeling of shear behavior is only necessary in the fixed crack approach. Therefore, it is not considered here.

2.4.6 Uniaxial stress-strain relationship of steel reinforcement

The uniaxial Giuffré-Menegotto-Pinto model (Menegotto et al. 1973, Filippou et al. 1983) is used. Details of this model were presented in section 2.3.6.

3 Evaluation of Analytical Models for Global Instability in Column Tests

3.1 INTRODUCTION

Several tests have been done (Chai and Elayer, 1999; Creagh et al., 2010; Acevedo et al., 2010) with prismatic sections loaded under tension/compression cycles. The data from Chai and Elayer (1999) are especially relevant, as those tests gradually increased tensile and compressive strains until overall prism buckling occurred. These data were based on test of axial columns under large strain amplitudes expected in the plastic hinge region of a ductile reinforced concrete wall. This experimental program is presented in section 3.2. Subsequent sections apply analytical models to simulate the observed responses.

3.2 EXPERIMENTAL PROGRAM

Fourteen reinforced concrete column specimens were tested under an axial reversed cyclic tension and compression. The column specimens were mounted vertically in a steel reaction frame where a quasi-static axial force was applied to the specimen using a double acting actuator. Figure 3.1 shows a photograph of the test setup for the specimen. With the exception of two specimens, the loading cycle consisted of an initial half-cycle of axial tensile strain followed by compression half cycle with a nominal target compressive strain 1/7 of the axial tensile strain unless the compression cycle was limited by the capacity of the actuator [approximately 185 kips (823 kN)]. In the other two specimens, the target compressive strain was increased to 1/5 of the axial tensile strain. A load cycle is considered to be stable if the target compressive strain or the compression capacity of the actuator can be reached in three successive cycles without developing an excessive out-of-plane displacement in the specimen.

Figure 3.2 shows the reinforcement details for the test specimens. The test specimens were 4 x 8 in. rectangular in cross section (102 x 203 mm), with height-to-thickness ratios L_0/b= 11.75, 14.75, and 17.75. The length of the specimen L_0 included the 5.5-in. (140-mm) steel brackets used for connection to the actuator. Two longitudinal reinforcement area ratios, namely, 2.1 and 3.8 percent, were investigated and provided by six No. 3 or six No. 4 deformed bars. A cover of 0.5 in. (12.7 mm) was used for the longitudinal reinforcement. Transverse ties fabricated from ¼ in. (6.4 mm) diameter cold drawn smoothed bars were provided at a spacing of six times the longitudinal bar diameter, i.e., 2.25 in. (57 mm) for No. 3 bars, and 3 in. (76 mm) for No. 4 bars. The close spacing of the transverse ties was intended to simulate the well-confined condition in

the end regions of ductile walls and to prevent the local buckling of the longitudinal bars. To ensure a proper transfer of the actuator force to the specimen, six 3/8 in. (9.5 mm) diameter all thread rods with a 10 in. (254 mm) anchorage length were added to the two ends of the specimen to increase the tensile capacity at the connection. In addition to the all-thread rods, two sets of steel plates, 2.5 in. (64 mm) wide by 1 in. (25 mm) thick, were used to externally confine the concrete in the end regions so that the transfer of the longitudinal bar forces to the concrete would not result in a local bond failure for the longitudinal reinforcement.

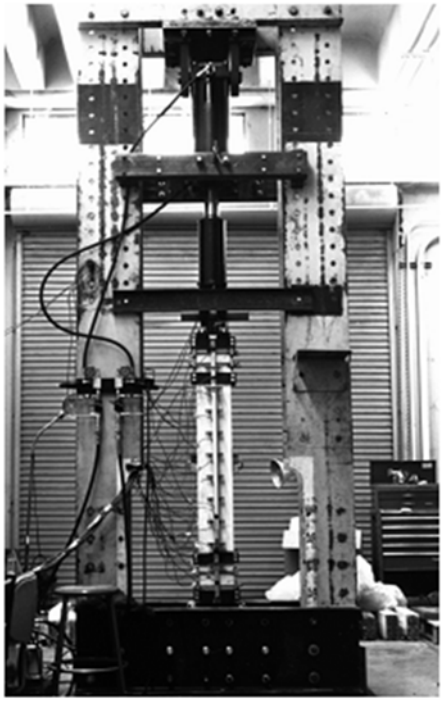

Figure 3.1 Experimental test setup.

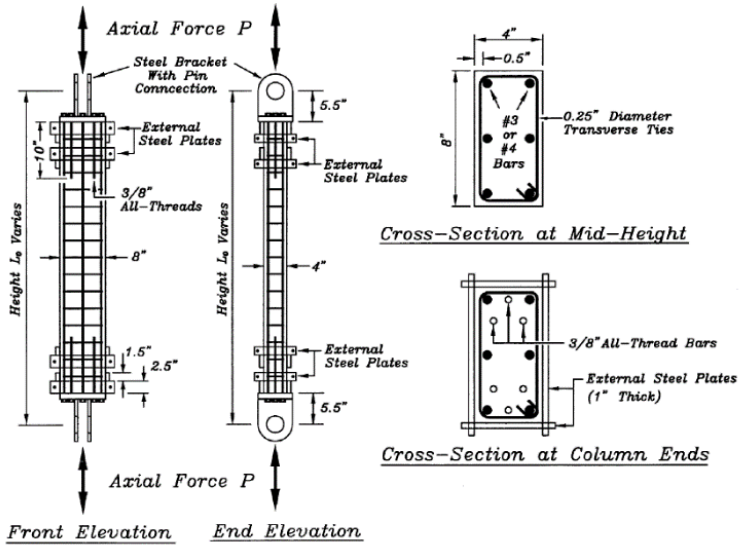

Figure 3.2 Reinforcement details for test specimens (1 in. = 25.4 mm).

Table 3.1 summaries the matrix for the test program.

Table 3.1 Test matrix.

Height-to-thickness ratio L_0/b	Longitudinal reinforcement ratio, percent	Transverse steel spacing, in. (mm)	No. of specimens tested
11.75	2.1	2.25 (57)	1
11.75	3.8	3.0 (76)	1
14.75	2.1	2.25 (57)	3
14.75	3.8	3.0 (76)	3
17.75	2.1	2.25 (57)	3
17.75	3.8	3.0 (76)	3

3.3 MATERIAL PROPERTIES

A normal weight concrete with an unconfined compressive strength of f'_c = 4,950 psi (34.1 MPa) was used for all specimens. The yield strengths of the longitudinal reinforcement were f_y = 51.8 and 66.0 ksi (357 and 455 MPa) for No. 3 and No. 4 bars, respectively, and the yield strength of the transverse ties was f_y = 99.0 ksi (683 MPa).

3.4 EVALUATION OF FORCE-BASED ELEMENTS AND NONLINEAR FINITE ELEMENT MODELS

Chai and Elayer (1999) provides detailed information regarding the experimental response of four column specimens (height to thickness ratios L_0/b =14.75 and 17.75 with longitudinal reinforcement ratios ρ = 2.1% and 3.8%). This information is used to evaluate the numerical models of global instability developed in OpenSees and TNO DIANA.

3.4.1 Sensitivity analysis to key parameters

3.4.1.1 Sensitivity in OpenSees forced-based elements model

Strain localization in force-based elements causes the response to be mesh-dependent. A procedure for material regularization according to the work of Coleman and Spacone (2001) was presented in section 2.3.5. Material regularization allows maintaining objectivity of the structural response independent of the number of integration points selected for analysis. To evaluate this procedure, one of the columns tested by Chai and Elayer (1999) is selected and analyzed using four force-based elements with four, five and six integration points per element according to the Gauss-Lobatto quadrature presented in section 2.3.7. The two limits values for compressive fracture energy presented by Feenstra (1993) are considered for analysis: 10 and 25 $\mathrm{Nmm/mm^2}$ (0.06 and 0.14 kip in./in.^{2}). The column ID is 4WC3_1 with height-to-thickness ratio L_0/b = 14.75 and longitudinal reinforcement ratio ρ = 2.1%. Figure 3.3 depicts the typical OpenSees model.

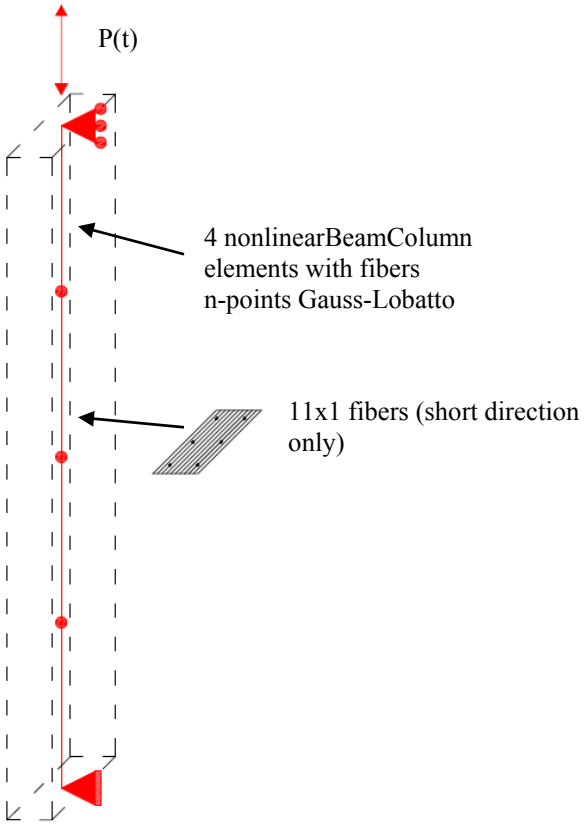

Figure 3.3 OpenSees model for column instability.

Table 3.2 presents the concrete strain ϵ_{20} at a stress $0.2f_c'$ for all analyzed cases obtained using Equation (2.36).

Table 3.2 Strain for Kent and Park model (1971) according to Equation (2.36).

L_0 (in.)	f_c' (psi)	E_c (psi)	Number of elements	Number of integration points, nIP	Integration point weight, w_i	h (in.)	$G_c\left(\frac{kip\ in.}{in.^2}\right)$	ϵ_{20}
59	4,950	4,000,000	4	4	1/6	1.23	0.06	0.017
59	4,950	4,000,000	4	5	1/10	0.74	0.06	0.027
59	4,950	4,000,000	4	6	1/15	0.49	0.06	0.040
59	4,950	4,000,000	4	4	1/6	1.23	0.14	0.040
59	4,950	4,000,000	4	5	1/10	0.74	0.14	0.066
59	4,950	4,000,000	4	6	1/15	0.49	0.14	0.099

From Table 2.1, the weight of each integration point w_i is calculated for a normalized domain of length 2. Therefore, the summation of all w_i for a given element must be 2.

In Table 3.2, w_i is the weight of the integration point where the plastic hinge is expected to form. For this case, the plastic hinge is located at the column midheight. Therefore, w_i is calculated for the integration point located at the element edge. The corresponding weight of the

integration point in the real domain of length $L_0/4$ is called h, which is an equivalent concept to the crack bandwidth defined for finite element analysis using smeared cracking models.

Figure 3.4 shows the concrete constitutive model for all analyzed cases. It is observed how the softening branch of the curve flattens when the number of integration points is increased to prevent failure localization.

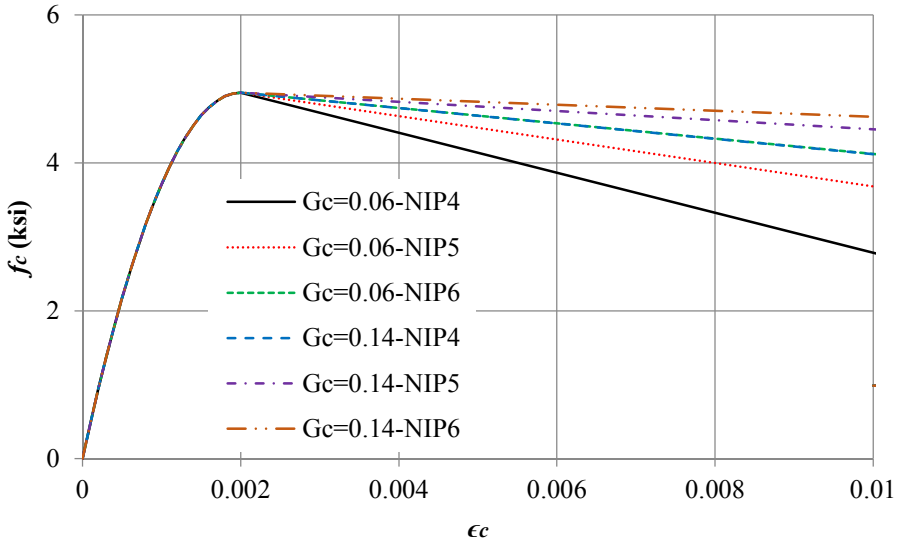

Figure 3.4 Kent and Park model (1971) for analyzed cases with material regularization according to Equation (2.36).

Figure 3.5a shows crushing in one of the column edges at the midheight. This indicates that buckling was a failure mode that followed edge crushing under flexural-compressive force during out of plane displacement. Figure 3.5b shows a buckled specimen with height-to-thickness ratio $L_0/b = 14.75$. The horizontal cracks were uniform in the center portion of the specimen outside the end-regions. The horizontal crack spacing corresponds to the transverse reinforcement spacing. This suggests that the presence of the transverse reinforcement created localized stresses leading to crack initiation.

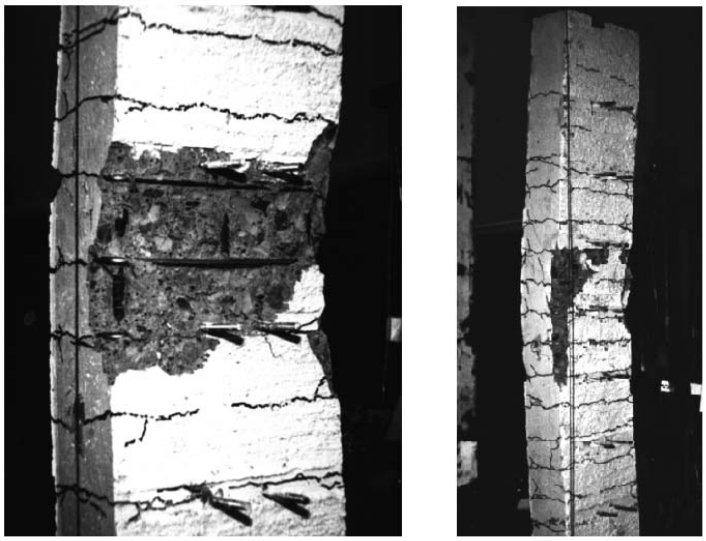

Figure 3.5 (a) Crushing of concrete at midheight of one of the column specimens; (b) buckled shape for column with L_o/b=14.75, after Chai and Elayer (1999).

Figure 3.6 shows the experimental response of the column specimen 4WC3_1 (height to thickness ratio L_0/b =14.75 with longitudinal reinforcement ratio $\rho = 2.1\%$). Figure 3.6a shows a plot of the nominal axial strain versus axial force and Figure 3.6b shows a plot the nominal axial strain versus maximum out-of-plane displacement normalized by the column width b. To keep the plot format used by Chai and Elayer (1999), compression variables have positive sign and tension variables have negative sign. During the test, the nominal axial strain was determined by averaging the displacements over a 15 in. (381 mm) length in the center portion of the specimen, and the out-of-plane displacement was determined by the average of two displacements measured at the midheight of the specimen.

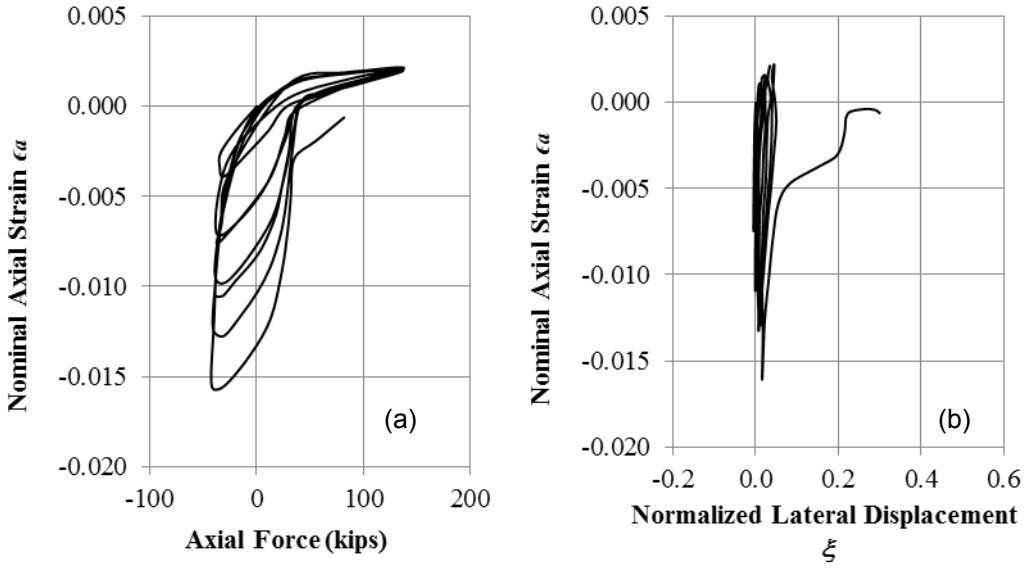

Figure 3.6 Column 4WC3_1 experimental response L_o/b=14.75, ρ=2.1%.

In Figure 3.6, a stable response was obtained for the specimen at low levels of axial tensile strain. For peak tensile strains up to -0.0133, the normalized out-of-plane displacements were less than 0.05. For the final cycle to the peak tensile strain close to -0.015, a rapid increase in the out-of-plane displacement occurred especially after reloading to tensile strain of -0.005. The rapid increase in the out-of-plane displacement was due to yielding in both layers of reinforcement at that strain level. The large increase in the out-of-plane displacement led to eventual closure of the cracks followed by crushing of the concrete edge in compression.

As indicated in section 2.2, lateral instability during crack closure initiates because the application point of the external force may not coincide with the centroid of the resistant force in the reinforcement, due to unavoidable irregularities in the placement of the reinforcement (Paulay and Priestley, 1993). To obtain this behavior in a numerical model, it is required to introduce some eccentricity to trigger the out-of-plane displacement. There are several ways to model this eccentricity, and for this study what was done is to reduce by 1 ksi the yielding stress of one layer of reinforcement. This is an arbitrary reduction of the yielding stress and later analyses will show that selecting a different value does not affect the structural response

Figure 3.7 compares the analytical results of all cases presented in Table 3.2 with the experimental response. First of all, it is observed that the structural response obtained from analysis does not change when the number of integration points increases. Therefore, regularizing the concrete material using the constant fracture energy concept allows getting a mesh-independent structural response at least for the considered cases.

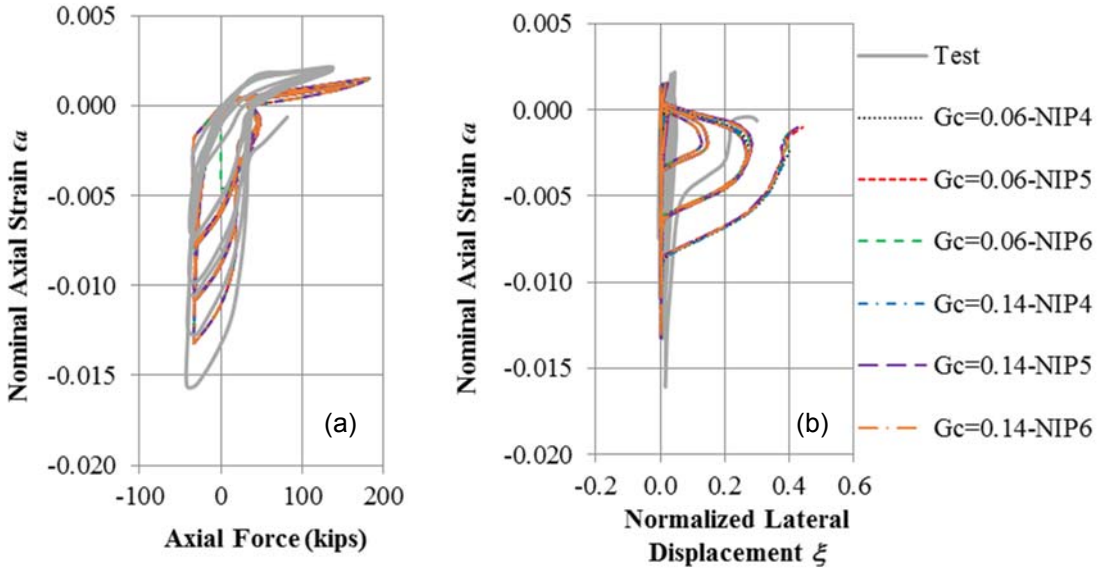

Figure 3.7 Column 4WC3_1, experimental versus analytical response for different number of integration points and compressive fracture energy.

Figure 3.7a shows a good agreement between the analytical and experimental curves of nominal axial strain versus axial force. Figure 3.7b shows that the OpenSees model tends to overestimate the normalized lateral displacement in the cycles before failure. Even for normalized lateral displacements of more than 0.2, during crack closure the column is able to recover its original undeformed shape without crushing the edge where the first contact between cracked surfaces occurs. Moreover, global instability occurs at a lower peak tensile strain of -0.0133. The

peak tensile strain during the last test cycle was -0.0161. Therefore, OpenSees models underestimate the peak tensile strain.

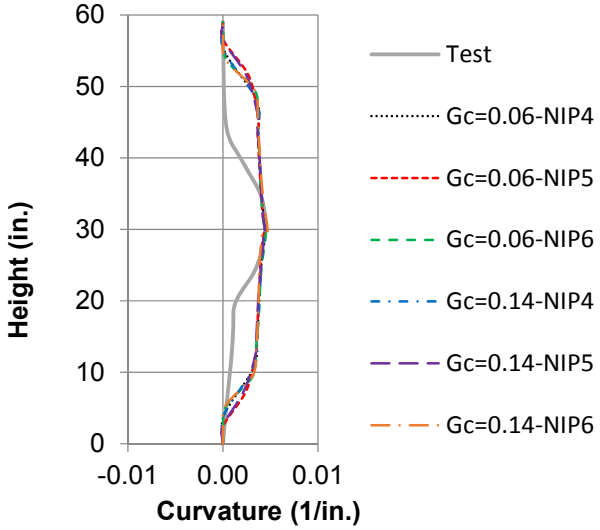

Figure 3.8 Column 4WC3_1, experimental versus analytical curvature distribution for different number of integration points and compressive fracture energy.

Figure 3.8 depicts a comparison between the experimental and analytical out-of-plane curvature distribution over the element height for column 4WC3_1, considering the cases presented in Table 3.2. The experimental curve was plotted for the center portion of the specimen of 40 in. (1016 mm). All curves are determined right before buckling failure. The experimental curve shows that the maximum curvature at the column midheight was $0.0044\ 1/\text{in.}$ ($1.75 \cdot 10^{-4}\ 1/\text{mm}$). The curvature in the end regions is likely affected by the steel plates used to confine concrete and avoid local bond failure in transfer bars. As will be shown later, this stiffening effect occurs only in the case of columns with $L_0/b = 14.75$ and it is negligible in longer columns. The analytical curves show that a mesh-independent structural response is successfully achieved by regularizing the concrete material considering constant fracture energy (Coleman and Spacone, 2001). Therefore, for the following analyses only one case will be considered: four elements with four integrations points on each one according to Gauss Lobatto quadrature and a constant fracture energy of 18 N mm$/mm^2$ (0.1 kip in.$/\text{in.}^2$), value at the middle of the plausible range introduced by Feenstra (1993). The stiffening effect in the end regions can be achieved by modifying the material properties of the first and last element of the mesh. However, introducing even minor modifications causes numerical problems in the OpenSees model affecting the response presented in Figure 3.7. Therefore, this is not considered in this study.

To trigger the out-of-plane displacement during axial loading it was necessary to introduce an eccentricity in the column cross section. This was achieved by reducing in 1 ksi the yielding stress of one later of reinforcement. This is an arbitrary value considered small enough to not affect the axial response presented in Figure 3.7. A study was conducted to evaluation how the analytical response is affected if a different yielding stress reduction is used. Figure 3.9a compares the experimental and analytical nominal axial strain versus axial force and Figure 3.9b compares the nominal axial strain versus normalized out-of-plane displacement. The model used to obtain the analytical curves considers four elements with four Gauss Lobatto integration points on each one and fracture energy of 0.1 kip in.$/\text{in.}^2$. Several yielding stress reductions were considered in order

to study the influence of this parameter in the structural response: 0.1, 0.3, 0.5, 0.7 and 1ksi. Figure 3.10 compares the out-of-plane curvature distribution over the column height for the test and these five analysis cases. For this range of yielding stress reduction, it can be observed that the structural response remains unchanged.

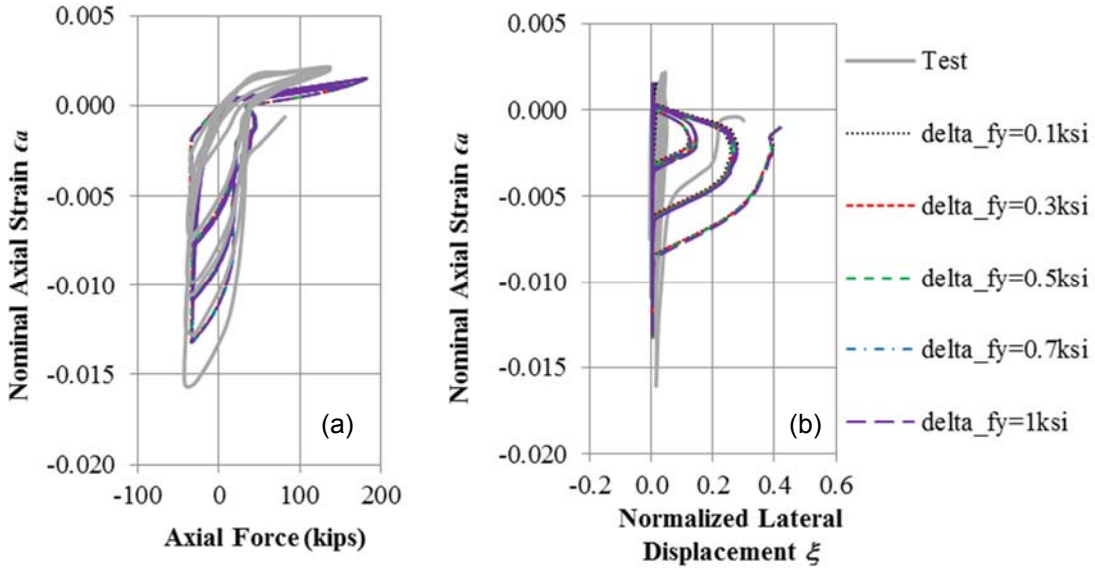

Figure 3.9 Column 4WC3_1, experimental versus analytical response for different reduction in yielding stress of one reinforcement layer.

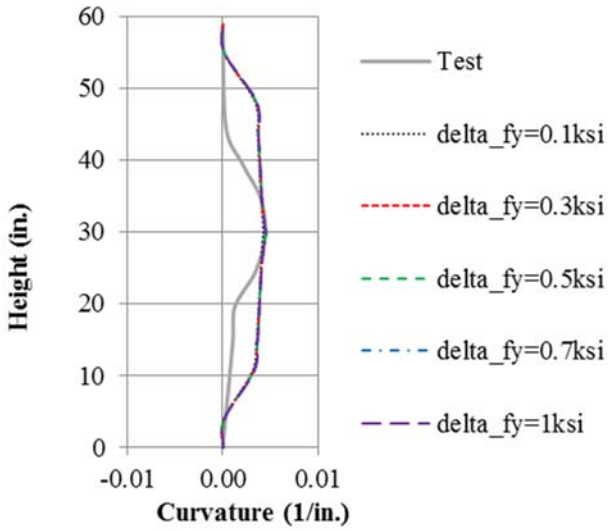

Figure 3.10 Column 4WC3_1, experimental versus analytical curvature distribution for different reduction in yielding stress of one reinforcement layer.

3.4.1.2 Sensitivity in DIANA 2D finite element model

Two-dimensional finite element models are now implemented in the software DIANA to analyze Chai and Elayer (1999) columns. The models consider Q20SH curved shell elements as described

in section 2.4.3. Support conditions include restrained translations in three orthogonal directions at the base and two horizontal directions at the top. A prescribed cyclic vertical displacement is imposed at the top, according to test conditions. Eleven integration points are considered in the thickness direction. The number of integration points is selected to match the number of fibers used in the OpenSees force-based elements. Detailed theoretical background of these models has been provided in section 2.4.

In order to achieve a mesh-independent structural response, concrete is modeled using a regularized material described in section 2.4.5, which is based on constant compressive fracture energy. Two cases are analyzed: G_c =0.06 and 0.14 kip in./in.^{2}, which are the limit values reported by Feenstra (1993). The eccentricity required to trigger out of plane displacement is obtained by reducing the yielding stress of one layer of reinforcement in 1 ksi as the case of force-based elements. A mesh sensitivity study is conducted for 4WC3_1 considering different element sizes as described in Figure 3.11.

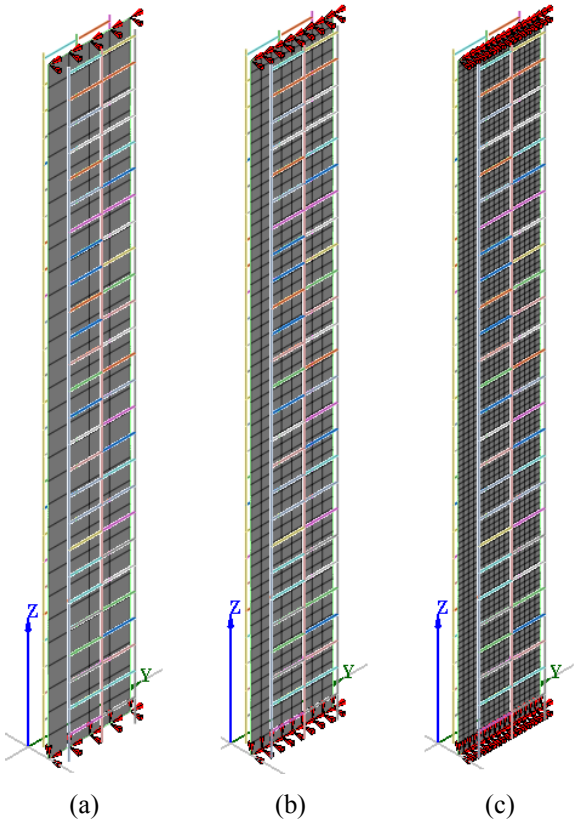

Figure 3.11 DIANA 2D models using Q20SH curved shell elements: a) mesh with h_{max}= 2in., a) mesh with h_{max}= 1 in. and c) mesh with h_{max}=0.5 in.

Figure 3.12 compares the experimental results with the analytical results obtained from six cases: maximum element size of 2, 1, and 0.5 in. with fracture energy of 0.06 and 0.14 kip in./in.^{2}. It can be observed that the analytical structural response does not change when element size decreases, which seems to indicate that using a constant fracture energy material for concrete is an appropriate approach to avoid strain localization and mesh dependency of the response. Figure 3.12a shows that the analytical responses accurately represent the test results. Figure 3.12b shows that the models overestimate the normalized lateral displacement in the cycles before failure and

underestimate the tensile strain before failure. This trend was also observed in the OpenSees models used for sensitivity analysis in section 3.4.1.1. Moreover, careful comparison between OpenSees and DIANA results (Figure 3.7 and Figure 3.12) shows that both analytical results are almost identical.

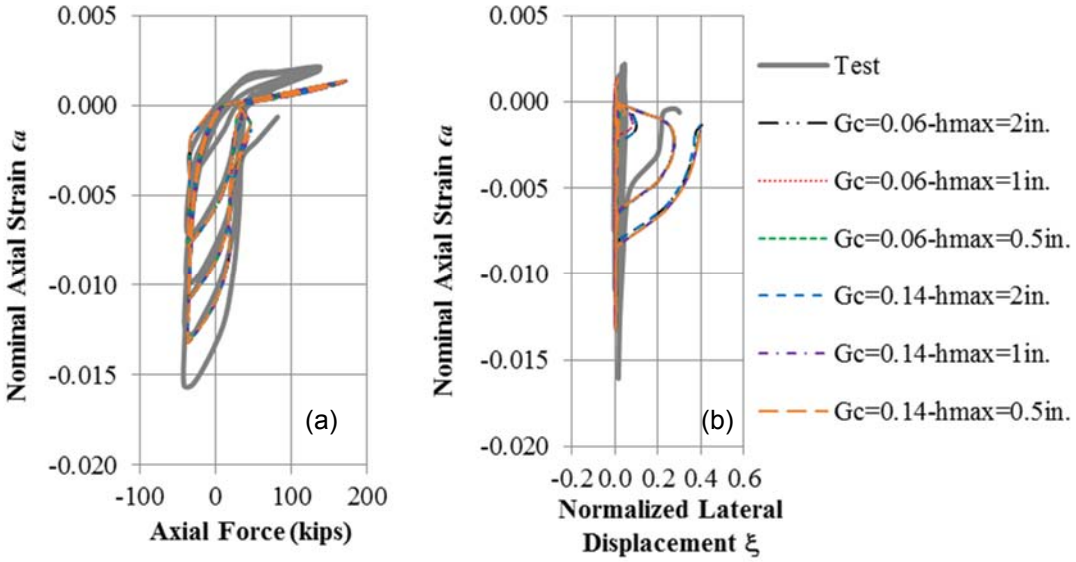

Figure 3.12 Column 4WC3_1, experimental versus analytical response for different mesh size and compressive fracture energy.

The analytical curvature distribution over the column height is mesh and fracture energy independent, as shown in Figure 3.13. Again, results are identical to those obtained from OpenSees force-based elements shown in Figure 3.8.

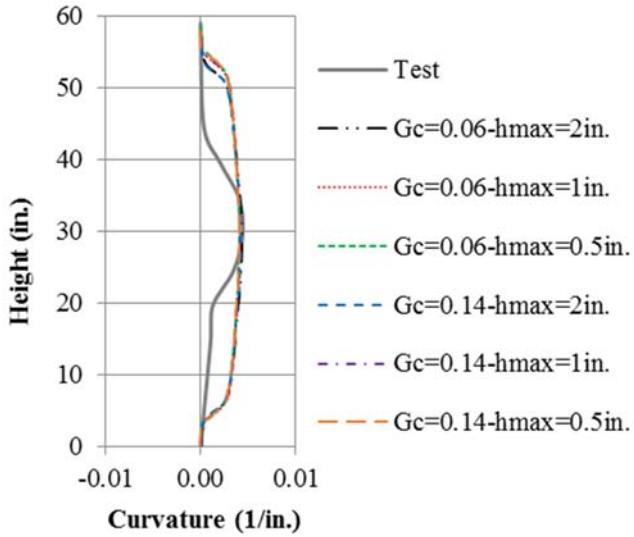

Figure 3.13 Column 4WC3_1 experimental versus analytical curvature distribution for different mesh size and compressive fracture energy.

Figure 3.14 shows the out-of-plane displacement before failure for compressive strain energy of 0.14 kip in./in.^{2} (upper bound of the plausible range) and for the three meshes analyzed. It is observed the mesh-independency of the displacement field.

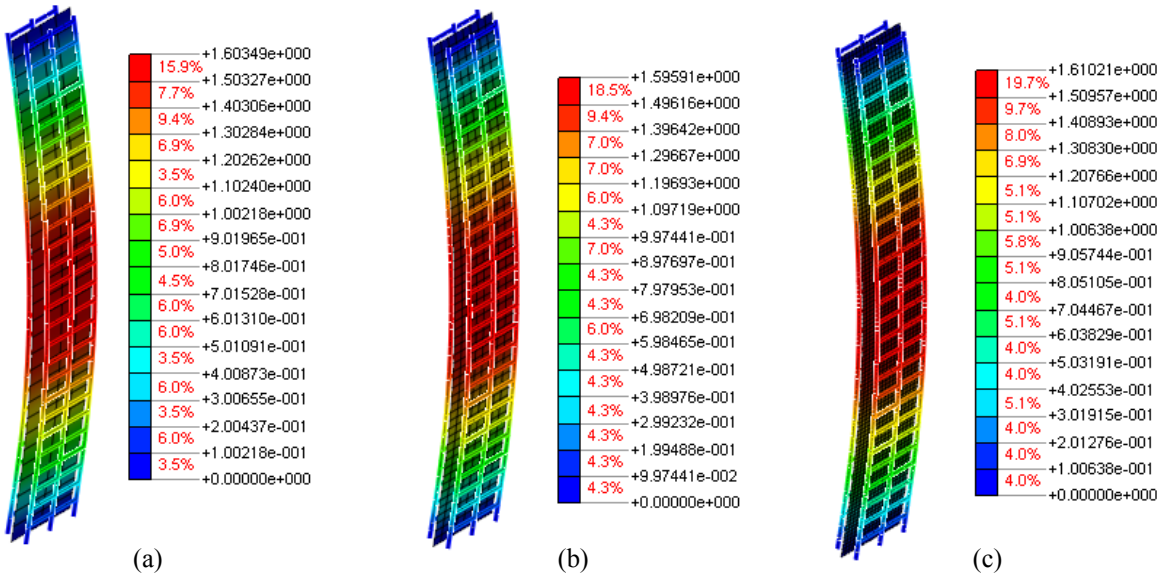

Figure 3.14 Column 4WC3_1 out-of-plane displacement (in.) before failure for G_c = 0.14 kip in./in.^{2} with a) h_{max}= 2in., b) h_{max}= 1 in. and c) h_{max}=0.5 in.

3.4.2 Experimental versus analytical response

In this section the four specimens tested by Chai and Elayer (1999), for which detail information was provided, are analyzed. These specimens are: 4WC3_1 (L_0/b =14.75 with ρ = 2.1%), 4WC4_2 (L_0/b =14.75 with ρ = 3.8%), 5WC3_2 (L_0/b =17.75 with ρ = 2.1%) and 5WC4_3 (L_0/b =17.75 with ρ = 3.8%). The parameters considered for analysis are: constant fracture energy G_c = 0.1 kip in./in.^{2}, yielding stress reduction Δf_y =1 ksi in one layer of reinforcement, four elements with Gauss Lobatto integration points per element in OpenSees models, mesh with maximum element size h_{max} = 1 in. in DIANA 2D and 3D models. The first specimen 4WC3_1 was used for sensitivity analysis in the previous sections. However, for completeness, this specimen is also analyzed for this specific set of parameters. Table 3.3 shows the regularized strain at a stress of $0.2f_c'$ needed to regularize the OpenSees concrete material.

Table 3.3 Strain for Kent and Park model (1971) according to Equation (2.36).

Specimen	L_0 (in.)	f_c' (psi)	E_c (psi)	Number of elements	Number of integration points, nIP	Integration point weight, w_i	h (in.)	G_c $\left(\frac{kip\ in.}{in.^2}\right)$	ϵ_{20}
4WC3_1	59	4,950	4,000,000	4	4	1/6	1.23	0.10	0.029
4WC4_2	59	4,950	4,000,000	4	4	1/6	1.23	0.10	0.029
5WC3_2	71	4,950	4,000,000	4	4	1/6	1.48	0.10	0.024
5WC4_3	71	4,950	4,000,000	4	4	1/6	1.48	0.10	0.024

Figure 3.15 shows the experimental and analytical nominal axial strain versus axial force and nominal axial strain versus normalized lateral displacement for 4WC3_1 specimen. Analytical

curves are obtained from three models: OpenSees force-based elements, DIANA 2D and 3D models. Figure 3.16 shows the experimental and analytical curvature distribution over the specimen height. Analytical values are plotted for OpenSees and DIANA 2D models. For the last case, curved shell elements do not allow getting the curvatures as a direct output, and there were obtained from vertical strains measured at the first and last integration points in the thickness direction, considering linear strain profile in that direction.

The sensitivity analysis showed that the structural response is mesh-independent when a constant fracture energy material is used, and it is also insensitive to any change in the fracture energy within the considered range. The analytical responses obtained for all models are identical to the corresponding ones obtained during the sensitivity studies, which is an expected result. The response obtained from OpenSees and DIANA 2D models are identical. Both of them underestimate by 17% the maximum tensile strain that triggers buckling during load reversal (-0.00133 from models versus -0.0016 from test), both overestimate the maximum out-of-plane displacement during each cycle and reproduce the maximum curvature at the column midheight right before failure with some stiffening in the end regions. DIANA 3D model gives a better approximation of the experimental response. For this case, the maximum tensile strain is obtained exactly, and even though there is still some overestimation of the out-of-plane displacement during cycles, its magnitude is lower than the obtained from the other models.

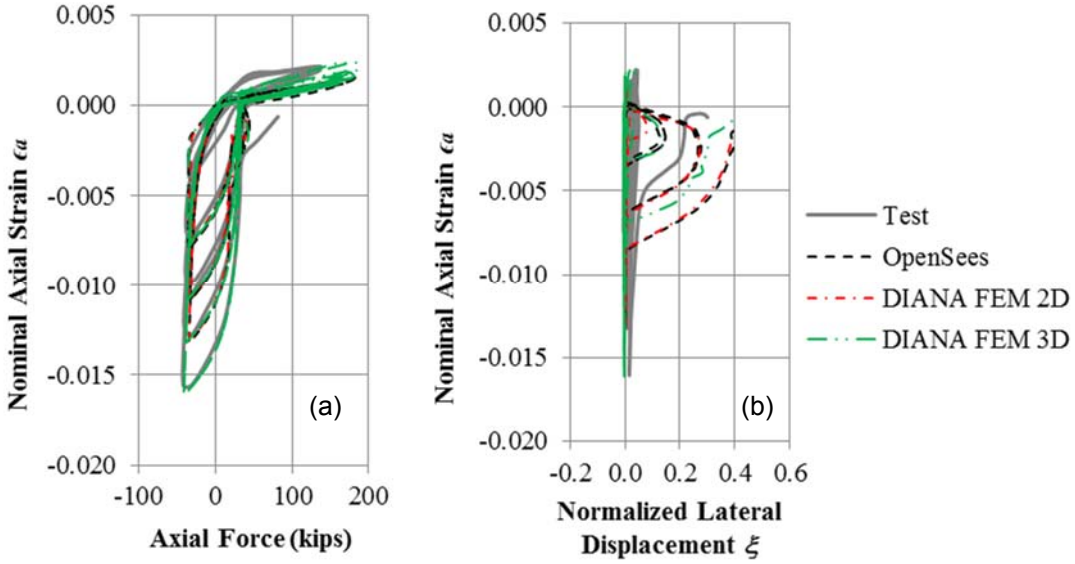

Figure 3.15 Column 4WC3_1, experimental versus analytical response (L_0/b = 14.75, ρ = 2.1%).

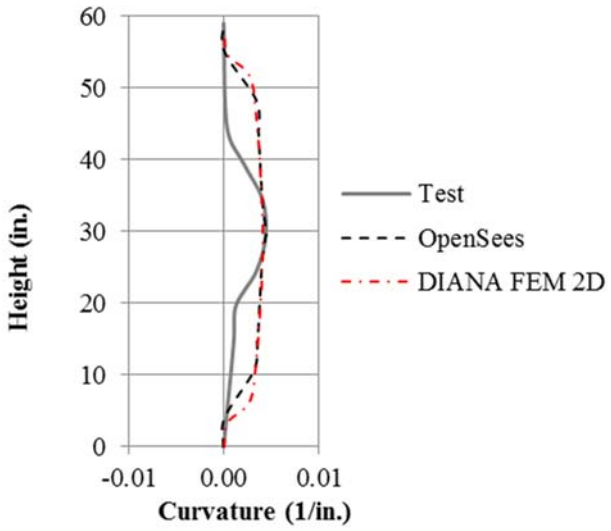

Figure 3.16 Column 4WC3_1, experimental versus analytical curvature distribution (L_0/b = 14.75, ρ = 2.1%).

Figure 3.17 and Figure 3.18 show the response of 4WC4_2 specimen (height-to-thickness ratio $L_0/b = 14.75$ and longitudinal reinforcement ratio $\rho = 3.8\%$). With an increased longitudinal reinforcement ratio, a smaller peak tensile strain was required to cause a large out-of-plane displacement and failure of the specimen. This is an expected result from Equation (2.20). The failure mode is similar to the observed in the previous specimen, yielding in compression of the reinforcement layers and crushing of the concrete edge where the first contact during crack closure occurs. As in the previous case, the analytical response obtained from OpenSees and DIANA 2D models are almost identical. Both models closely reproduce the nominal axial strain versus axial force curve. However, they underestimate the maximum tensile strain prior instability during load reversal by 20% and overestimate the normalized lateral displacement during each cycle and the column capacity to recover its original shape during crack closure without crushing the edge. Regarding the curvature distribution of Figure 3.18, OpenSees and DIANA 2D models reproduce well the peak at the column midheight. DIANA 3D model does not underestimate the maximum tensile strain before buckling, and the approximation of the out-of-plane displacement during all cycles is better in comparison to the one obtained from OpenSees and DIANA 2D models.

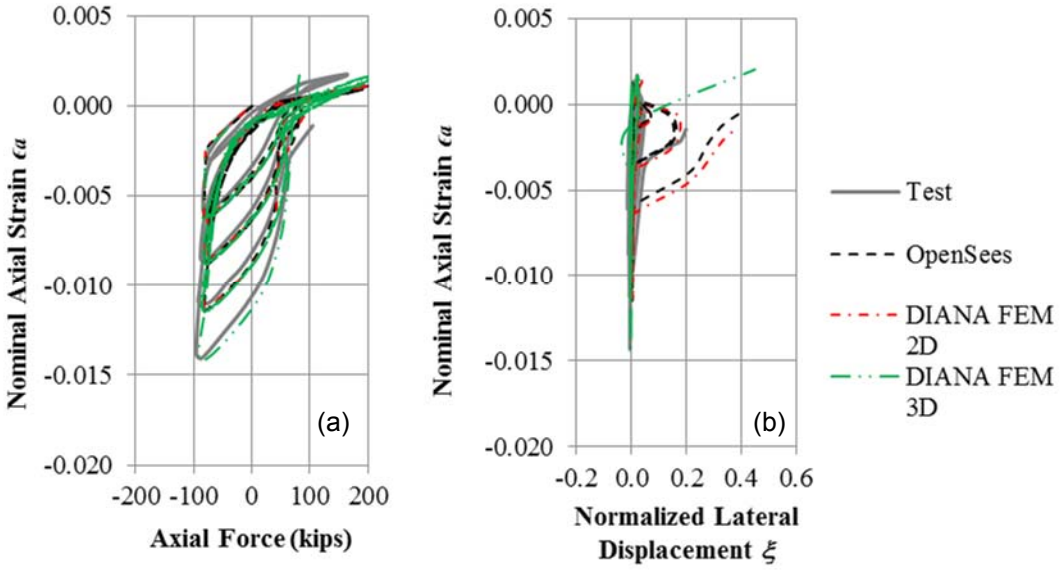

Figure 3.17 Column 4WC4_2, experimental versus analytical response (L_0/b = 14.75, ρ = 3.8%).

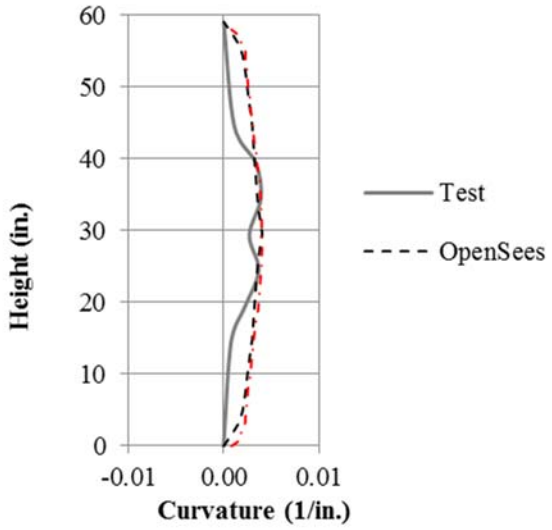

Figure 3.18 Column 4WC4_2, experimental versus analytical curvature distribution (L_0/b = 14.75, ρ = 3.8%).

Figure 3.19 shows the response of 5WC3_2 specimen which has an increased height-to-thickness ratio of $L_0/b = 17.75$ and a longitudinal reinforcement ratio of $\rho = 2.1\%$. According to the experimental data of Figure 3.19b, the maximum tensile strain required to buckle the column in compression during load reversal is -0.014. As expected, this value is smaller than -0.016, which is the required value to buckle a column with the same reinforcement ratio but a smaller slenderness (Figure 3.15). For this case, the analytical response of the three models is very similar. All of them underestimate the peak tensile strain prior buckling by 13% and overestimate the maximum out-of-plane displacement at each cycle. However, this overestimation is lower for the

case of DIANA 3D model. Figure 3.20 shows no difference between the analytical estimations of curvature distribution obtained from OpenSees and DIANA 2D models. It is observed that the stiffening effect in the specimen ends tends to disappear for the case of longer columns, which improves the analytical estimations in comparison to the obtained for the previous cases.

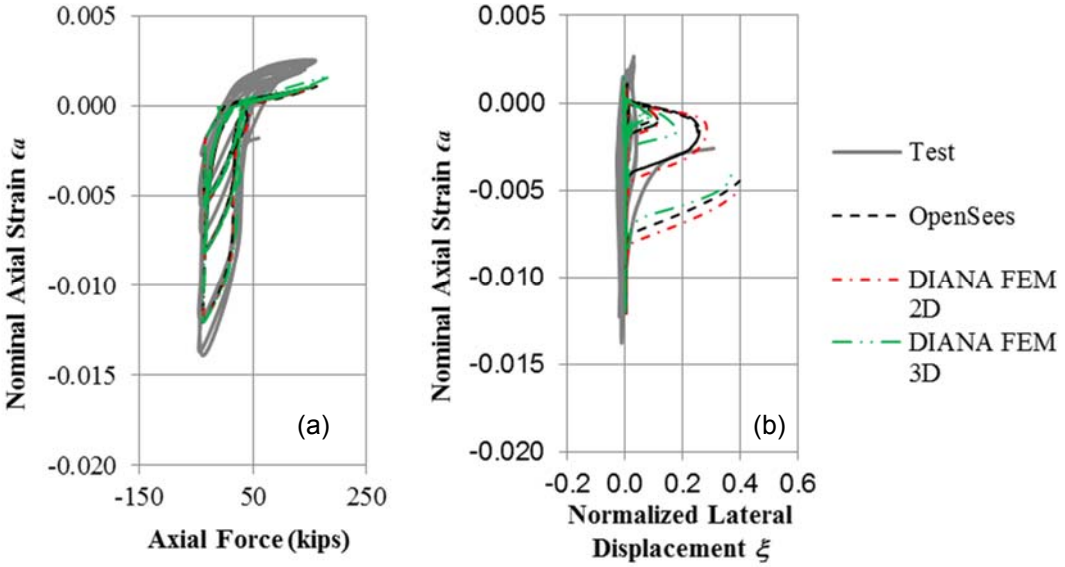

Figure 3.19 Column 5WC3_2, experimental versus analytical response (L_0/b = 17.75, ρ = 2.1%).

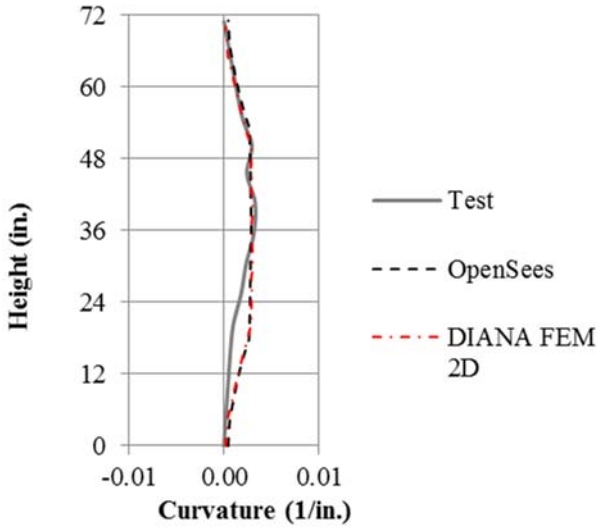

Figure 3.20 Column 5WC3_2, experimental versus analytical curvature distribution (L_0/b = 17.75, ρ = 2.1%).

Figure 3.21 shows the response of 5WC4_3 specimen ($L_0/b = 17.75$ and $\rho = 3.8\%$). With an increase in the longitudinal reinforcement, the peak tensile strain to cause failure of the specimen decreased to -0.012. As before, the best analytical approximation is obtained from DIANA 3D model for which the maximum tensile strain prior buckling is exactly obtained. The

three models show some overestimation in the maximum out-of-plane displacement during each cycle. However, DIANA 3D model is the one that reproduces the experimental maximum out-of-plane displacement more closely. For this case, OpenSees and DIANA 2D models behave almost identically. Similarly to the previous specimens, both underestimate the maximum tensile strain before buckling. For this case this underestimation is 26%. Figure 3.22 shows very good analytical approximations of the experimental curvature distribution right before failure, from both OpenSees and DIANA 2D models.

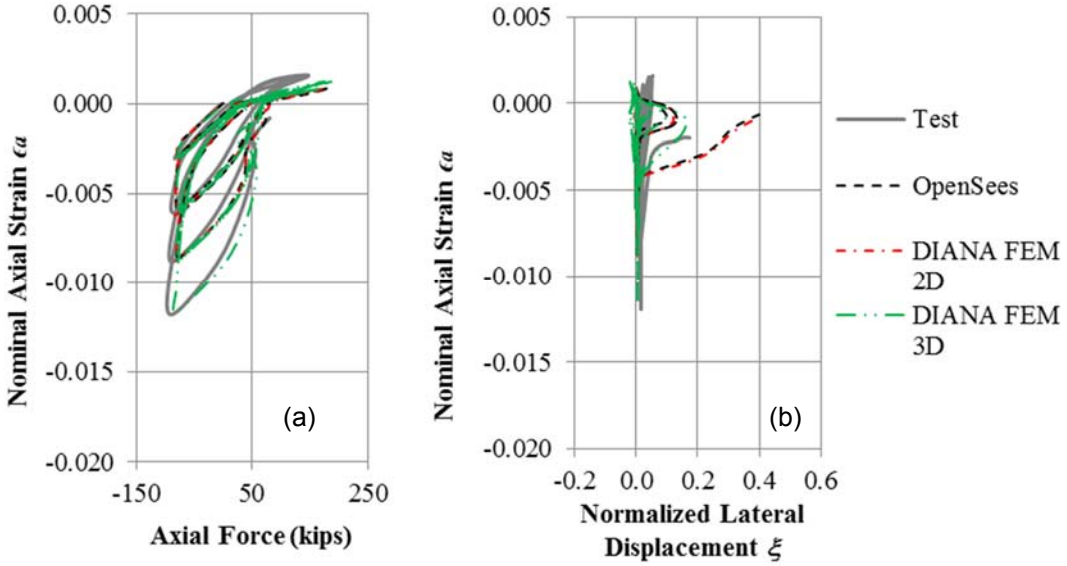

Figure 3.21 Column 5WC4_3, experimental versus analytical response (L_0/b = 17.75, ρ = 3.8%).

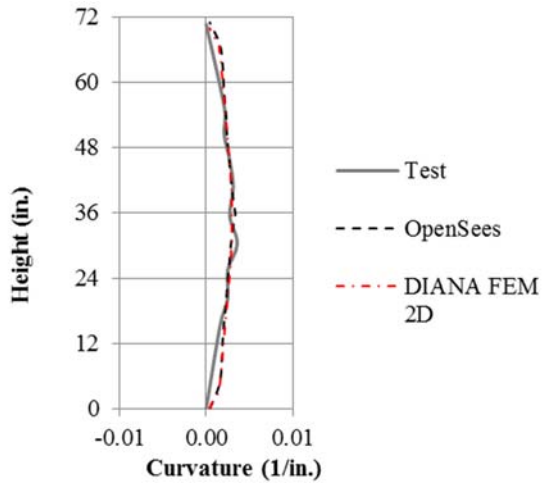

Figure 3.22 Column 5WC4_3, experimental versus analytical curvature distribution (L_0/b = 17.75, ρ = 3.8%).

3.5 EVALUATION OF SIMPLIFIED MECHANICS OF GLOBAL INSTABILITY

The simplified mechanics of global instability introduced in section 2.2 is now evaluated using the experimental data and the analytical data obtained from OpenSees and DIANA models. First, values of the maximum tensile strain prior buckling ϵ_{sm} are estimated for each specimen according to Table 3.4.

Table 3.4 Parameters for buckling simplified mechanics.

Specimen	L_0/b	Material Properties, psi		Column Slenderness b/kh_u	ρ	m	ξ	κ	ϵ_{sm}
		f'_c (psi)	f_y (psi)						
4WC3_1	14.75	4,950	51,800	0.07	2%	0.22	0.189	0.83	**0.012**
4WC4_2	14.75	4,950	66,000	0.07	4%	0.49	0.123	0.81	**0.010**
5WC3_2	17.75	4,950	51,800	0.06	2%	0.22	0.189	0.83	**0.010**
5WC4_3	17.75	4,950	66,000	0.06	4%	0.49	0.123	0.81	**0.008**

In Table 3.4 all specimens had pin-ended boundary conditions (k =1). The values of ϵ_{sm} obtained from tests are now compared with the corresponding values obtained from the simplified mechanics and the numerical models presented in sections 2.3 and 2.4.

Table 3.5 Comparison between experimental and analytical values of ϵ_{sm}.

Specimen	ϵ_{sm} test	ϵ_{sm} OpenSees	$\Delta\epsilon_{sm}$ %	ϵ_{sm} DIANA 2D	$\Delta\epsilon_{sm}$ %	ϵ_{sm} DIANA 3D	$\Delta\epsilon_{sm}$ %	ϵ_{sm} simplified mechanics	$\Delta\epsilon_{sm}$ %
4WC3_1	0.016	0.013	-17%	0.013	-17%	0.016	0%	0.012	-25%
4WC4_2	0.014	0.012	-20%	0.012	-20%	0.014	0%	0.010	-30%
5WC3_2	0.014	0.012	-13%	0.012	-13%	0.012	-13%	0.010	-28%
5WC4_3	0.012	0.009	-26%	0.009	-26%	0.012	0%	0.008	-32%

The DIANA 3D finite element model produces strain estimates that are closest to those measured during the tests. The other models (DIANA 2D finite elements, OpenSees and simplified mechanics of section 2.2 consistently underestimate the strain needed to buckle the column under load reversal. The highest relative difference is observed for the case of the simplified mechanics theory. OpenSees models using force-based elements with fibers and DIANA 2D finite element models give identical accuracy.

Chai and Elayer (1999) reported values of ϵ_{sm} from additional tests. The results of Equation (2.20) and the test results are are plotted simultaneously in Figure 3.23.

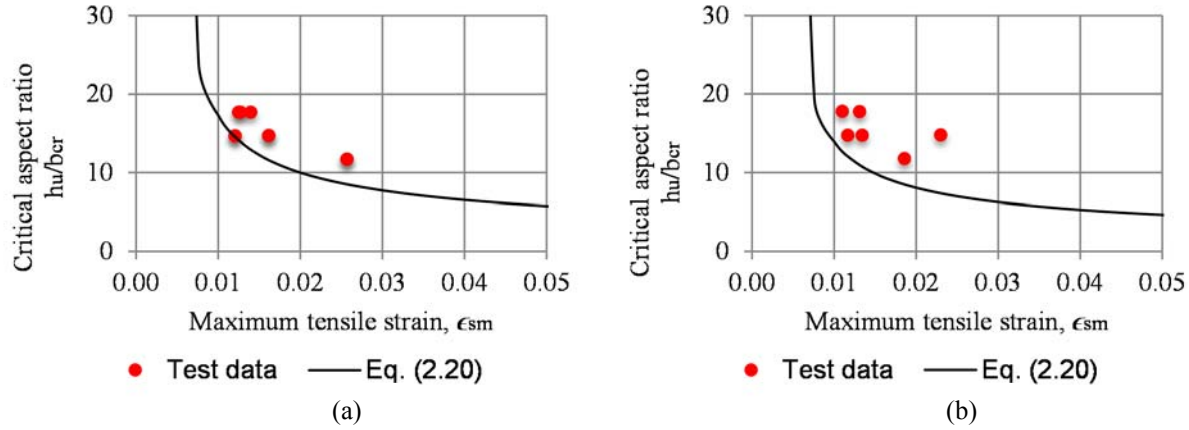

Figure 3.23 Calculated and measured maximum tensile strains according to Equation (2.20), a) ρ = 2.1% and b) ρ = 3.8%.

The parameter ξ defined in Equation (2.20) is inconvenient for preliminary design, and $\sqrt{\xi} = 0.5$ (mid-value in the practical range) may be considered in order to further simplify Equation (2.20). Therefore Equation (2.20) becomes:

$$\frac{b_{cr}}{kh_u} = 0.7\sqrt{\epsilon_{sm} - 0.005} \tag{3.1}$$

This simple expression can be easily incorporated in design regulations and used for preliminary design purposes. Equation (3.1) is now plotted with the results of all the column tests reported by Chai and Elayer (1999).

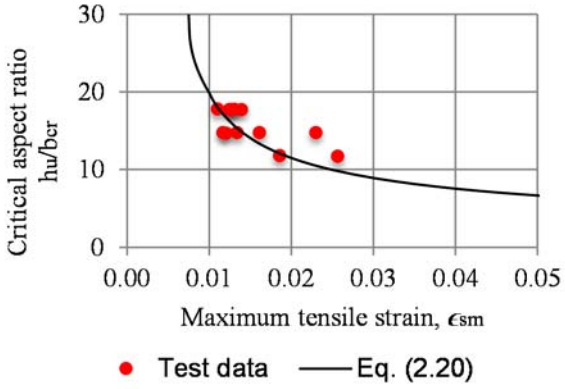

Figure 3.24 Comparison between calculated and measured maximum tensile strains according to Equation (3.1).

The results suggest that Equation (3.1) is a reasonable approximation to describe behavior of uniformly loaded prisms.

4 Global Instability of Boundary Elements in Slender Walls

4.1 INTRODUCTION

The derivation of the simplified model of global instability shown in section 2.2 is based on a prismatic column subjected to tension/compression cycles, where the axial force and the axial strain are uniform along the column height. Studies presented in section 3.5 showed that this model is a reasonable approximation of uniformly loaded slender columns.

Instability analysis of boundary elements in slender walls requires considering other aspects that influence the response. Figure 4.1a depicts a typical slender wall in a multistory building. The moment diagram shown next to each elevation illustrates the demand over a wall that interacts with a frame. Buckling is expected to occur where the maximum demand is. For this case, given the wall geometry and an assumed nearly constant moment demand over the first story height, it is reasonable to assume that buckling will occur at the first story, and the plastic hinge length will be no less than the first story height. This is even more reasonable for the case of residential buildings in Chile (section 6), where walls have typically a setback at the first story due to architectural requirements (known as "flag walls"), and hinging is expected to extend over the entire first story. For out-of-plane analysis, it is also a reasonable assumption to consider fixed support conditions at the top and bottom of the first story, given that the wall is continuous beyond that story. For this case, the axial demand over boundary elements is expected to be constant or close to constant, and the simplified theory is a good representation of the mechanics that governs the problem. However, the wall also has a strain gradient along its length, which might tend to brace the boundary element preventing buckling. This effect is not being considered by the simplified mechanics model of section 2.2 and will be evaluated in section 4.3.

In Figure 4.1b depicts a wall with a taller first story, which is not uncommon in buildings and industrial facilities. Here, we can still assume fixed support conditions at the top and bottom of the first story for out-of-plane displacement. However, the moment cannot be assumed constant anymore, and the plastic hinge is not expected to extend over the entire first story. The shape of the moment diagram was chosen to clearly illustrate that in some cases the moment gradient over the first story height is relevant and the assumption of constant axial demand over boundary elements can lead to an underestimation of the maximum tensile strain required to buckle the boundary element during load reversal, and therefore an over-conservative design for buckling prevention. The effect of strain gradients along the length and height of the wall are analyzed in sections 4.2.

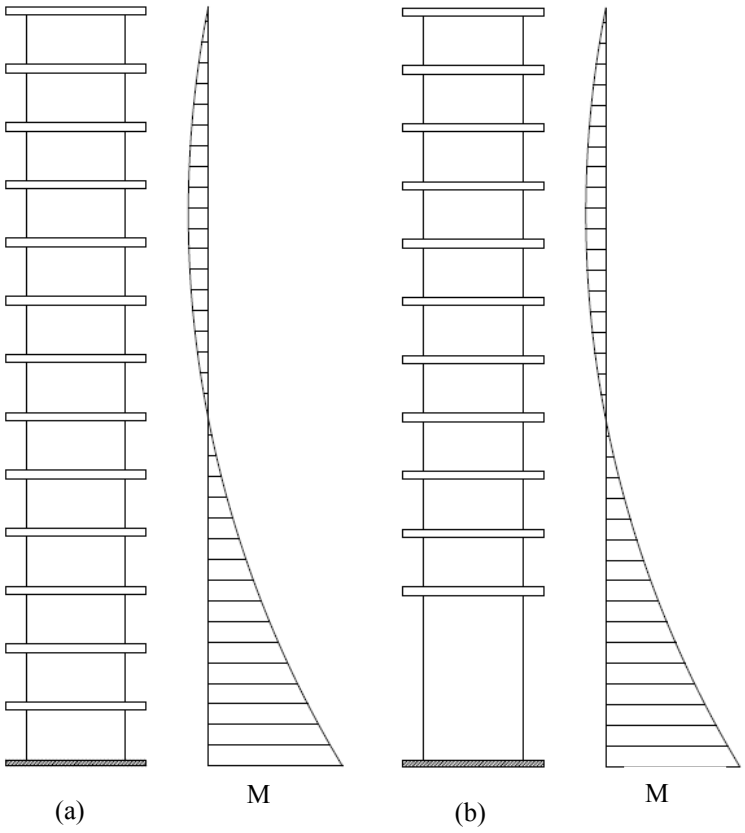

Figure 4.1 Slender multistory wall and moment diagram over the height: a) *M* ≈ constant at first story, b) *M* varies linearly at first story.

4.2 EFFECT OF STRAIN GRADIENT ALONG THE BOUNDARY ELEMENT HEIGHT

Prismatic sections under uniform tension/compression cycles are the cases that have been studied analytically and experimentally in the past (Paulay and Priestley, 1993; Chai and Elayer, 1999; Parra and Moehle, 2014). In some specific cases, this assumption leads to a reasonable estimation of the onset of out-of-plane instability, as described in section 4.1. However, in the more general case, strain gradients along the wall length and height are expected to influence the onset of out-of-plane instability in slender walls.

The influence of strain or force gradients along the wall length and height are now studied separately. In this section, the effect of the force variation along the wall height is evaluated using one-dimensional OpenSees models of isolated boundary elements, as shown in Figure 4.2. The force variation is intended to represent the variation of the flexural compression force over wall height due to the presence of a moment gradient. Each boundary element is modeled using ten nonlinear beam-column elements with fibers, force-based formulation and corotational transformation for nonlinear geometry. Nonlinear material models are those described in sections 2.3.4, 2.3.5 and 2.3.6. Currently the corotational transformation in OpenSees does not deal with element loads and these are ignored during the analysis. Therefore, the axial load is applied through point forces at the nodes. This vertical load pattern is selected to obtain a specific axial force

diagram, as shown in Figure 4.2b to f. Several axial force diagrams are considered to evaluate how the variation of the axial force over the height affects the onset of out-of-plane instability in isolated boundary elements under cyclic loading. The column is subjected to tension/compression cycles by multiplying the vertical load pattern by a unique variable factor (positive for compressive loading and negative for tensile loading). The boundary element is fixed at the base, and the rotation and horizontal displacements are restrained at the top.

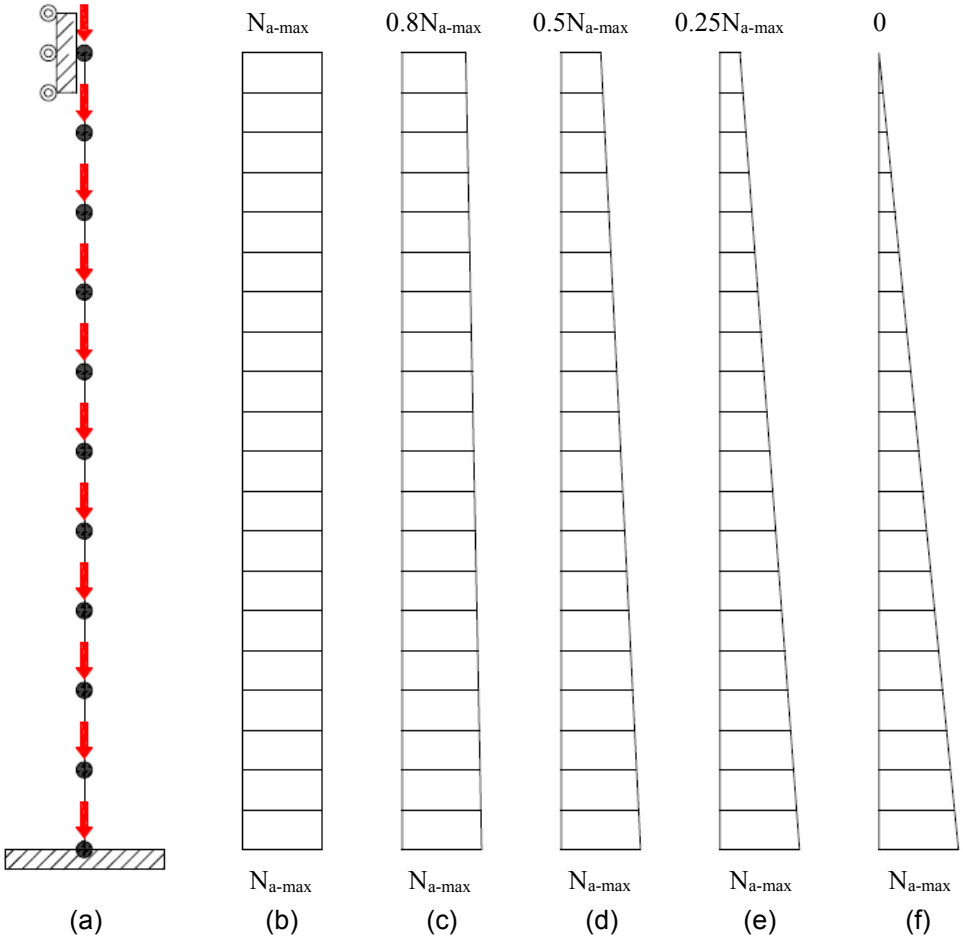

Figure 4.2 Slender wall boundary element: a) OpenSees model with ten force-based elements; b) axial force gradient with α= 1, c) α= 0.8, d) α= 0.5, e) α= 0.25 and f) α= 0, where $\alpha = N_{a\text{-}top} / N_{a\text{-}bottom}$.

Five boundary elements are analyzed: Chai and Elayer's specimens 4WC3_1 (slenderness $L_0/b = 14.75$ and longitudinal steel ratio $\rho = 2.1\%$), 4WC4_2 ($L_0/b = 14.75$ and $\rho = 3.8\%$), 5WC3_2 ($L_0/b = 17.75$ and $\rho = 2.1\%$) and 5WC4_3 ($L_0/b = 17.75$ and $\rho = 3.8\%$), where L_0 is the specimen unsupported height. All these specimens were tested under pinned boundary conditions (top and bottom). According to Figure 4.2a, this analysis considers restrained rotations at the top and bottom. Therefore, the unsupported height h_u for OpenSees models is $2L_0$, in order to get the same effective slenderness (kh_u/b, with $k = 0.5$ for fixed-fixed boundary conditions). The last boundary element considered for this study has slenderness $h_u/b = 50$ with longitudinal steel ratio $\rho = 2.1\%$. This case may be found in industrial facilities, where longer unsupported heights are not unusual.

The boundary elements are analyzed considering incremental tension cycles according to Figure 4.3, where the top vertical displacement is plotted. The peak vertical displacement is increased in 0.1 in. increments until reaching buckling failure during load reversal.

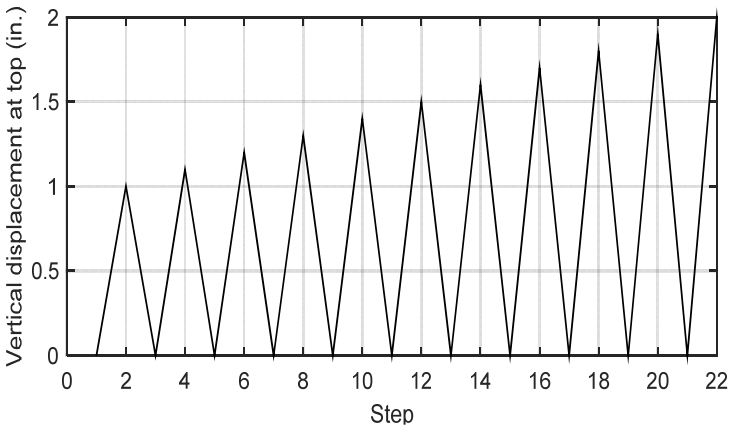

Figure 4.3 Incremental tension cycles for OpenSees analysis of boundary elements.

According to Figure 4.2, five cases of axial force profile are considered for each boundary element. For each case, four plots are provided: average axial strain (top vertical displacement divided by the element height) versus axial force at the base, the axial strain over the height normalized by the yielding strain at the point of maximum vertical displacement prior buckling during load reversal, the normalized axial force over the element height and a comparison between the out-of-plane displacement normalized by its maximum value for two cases: theoretical sine shape obtained from simplified mechanics for the case of uniform strain profile and the OpenSees buckled shape. Figure 4.4 shows the analysis results for the specimen 4WC3_1 with constant axial load over the height (Figure 4.4c). For this case, the buckled shape obtained from OpenSees matches exactly the theoretical shape presented in Equation (2.1) (Figure 4.4d). The maximum tensile strain prior buckling during load reversal is 0.013, close to seven times the yielding strain ϵ_y. This value is constant along the element height.

When the axial load is changed to a non-uniform profile like the one shown in Figure 4.5c, where the ratio between the axial load at the top and bottom of the element is $\alpha = 0.8$, the buckled shape obtained from analysis does not correspond to the theoretical buckled shape assumed in the derivation of the simplified mechanics. The maximum lateral displacement is not at the column mid-height anymore, it is now at a lower position close to $0.4h_u$ (Figure 4.5d). A second observation is related to the strain demand for the tensile peak prior buckling during load reversal (Figure 4.5b). This demand is not constant over the height anymore. Moreover, the maximum tensile strain at the element base increases with respect to the corresponding value obtained for the case of constant axial force. As shown in Figure 4.6 to Figure 4.8, the maximum lateral displacement shifts towards the base when the value of α is reduced from one (Figure 4.2b) to zero (Figure 4.2f), while the maximum tensile strain increases. This behavior was also observed in the other four boundary elements analyzed. These results are presented in Appendix A.

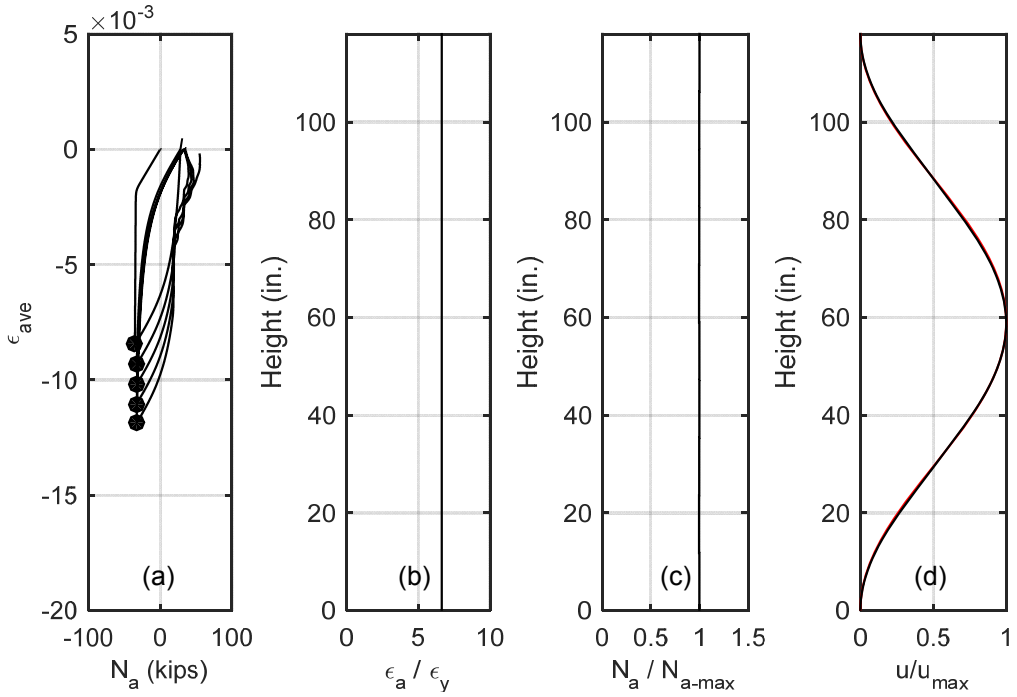

Figure 4.4 **Specimen 4WC3_1, α= 1: a) average axial strain versus axial force at the base, b) normalized axial strain, c) normalized axial force, d) normalized buckled shape.**

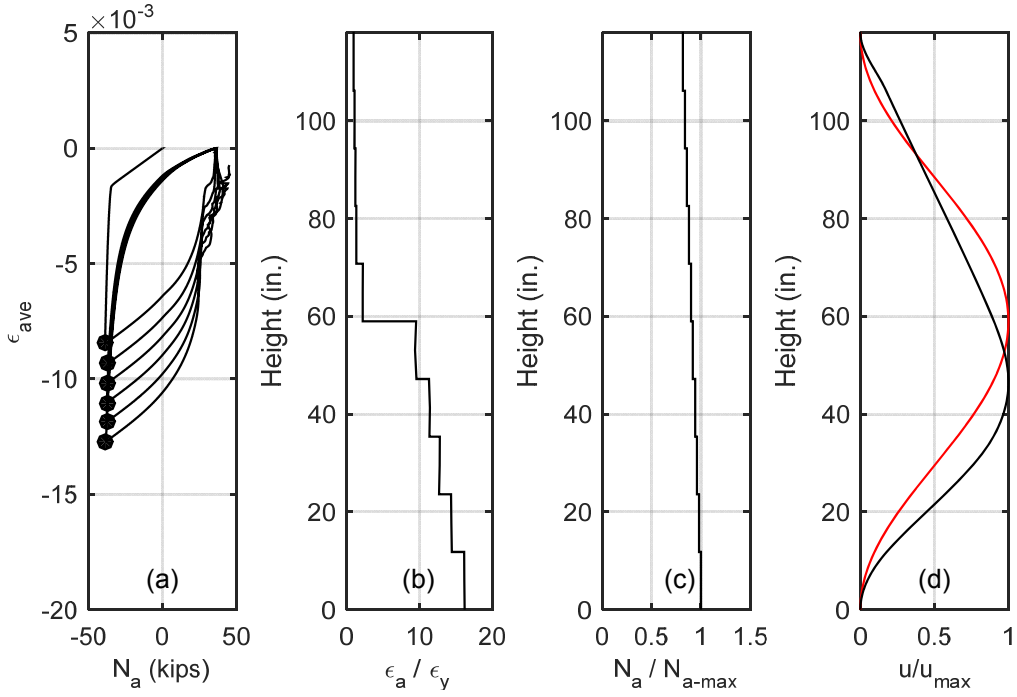

Figure 4.5 **Specimen 4WC3_1 (h_u/b = 29.5 and ρ = 2.1%) for α= 0.8: a) average axial strain versus axial force at the base, b) normalized axial strain, c) normalized axial force, d) normalized buckled shape.**

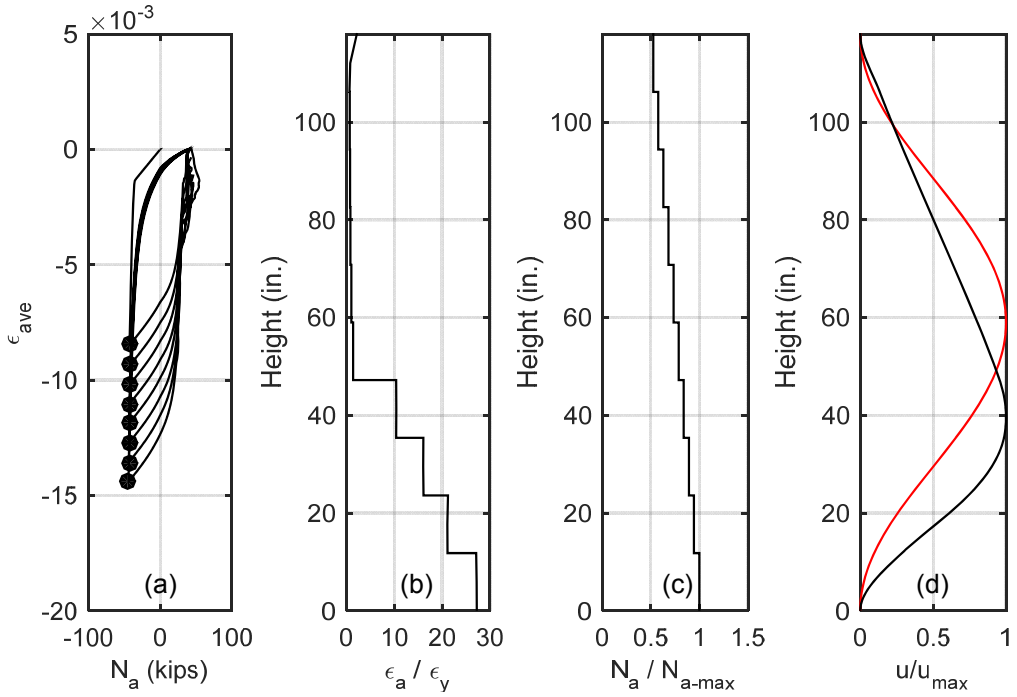

Figure 4.6 **Specimen 4WC3_1 (h_w/b = 29.5 and ρ = 2.1%) for α= 0.5: a) average axial strain versus axial force at the base, b) normalized axial strain, c) normalized axial force, d) normalized buckled shape.**

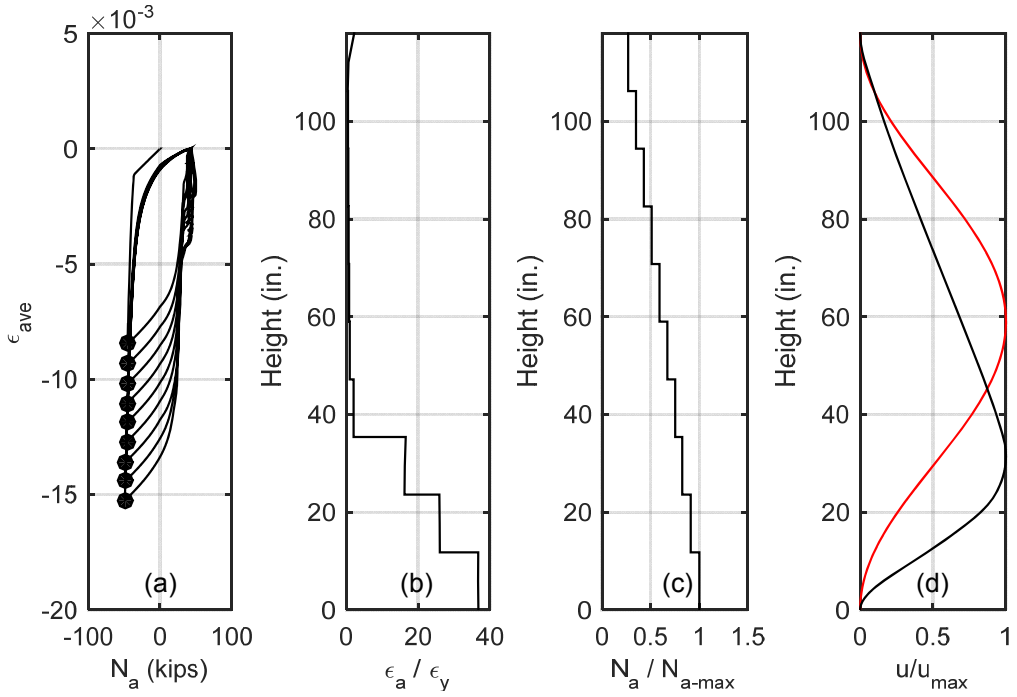

Figure 4.7 **Specimen 4WC3_1 (h_w/b = 29.5 and ρ = 2.1%) for α= 0.25: a) average axial strain versus axial force at the base, b) normalized axial strain, c) normalized axial force, d) normalized buckled shape.**

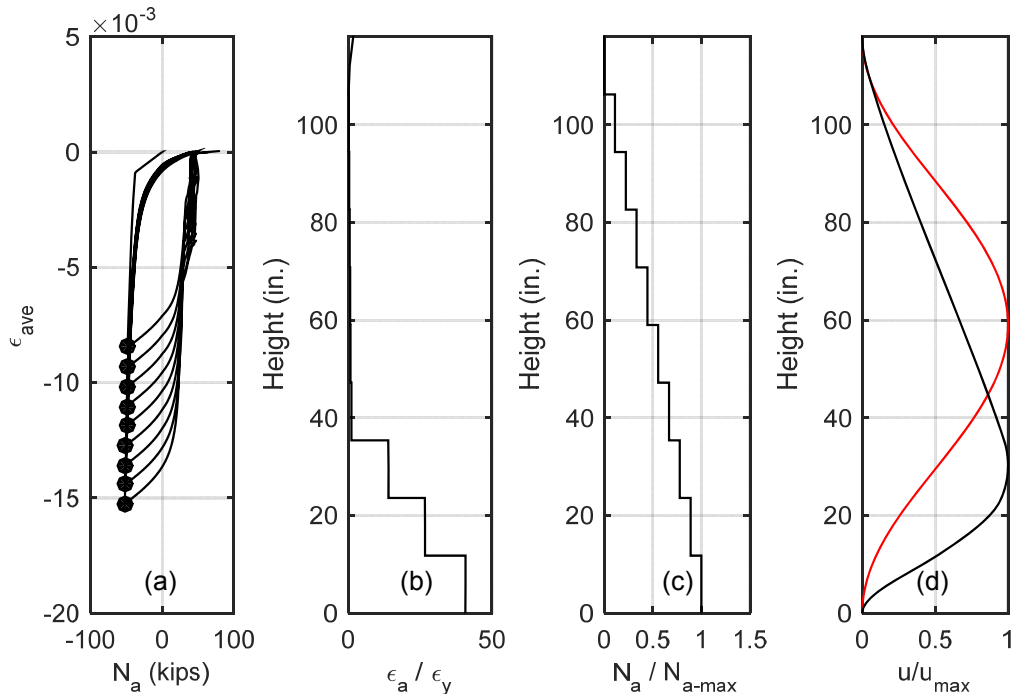

Figure 4.8 **Specimen 4WC3_1 (h_w/b = 29.5 and ρ = 2.1%) for α = 0: a) average axial strain versus axial force at the base, b) normalized axial strain, c) normalized axial force, d) normalized buckled shape.**

According to section 2.2, the most important parameter for the evaluation of the onset of out of plane instability is the maximum tensile strain prior buckling during load reversal. This value has been theoretically and experimentally obtained for uniformly loaded prisms and now has been analytically obtained for several axial load profiles, demonstrating that the results of the simplified theory are over-conservative for cases where the assumption of constant axial force/strain over the height is not valid. Figure 4.9 shows the maximum tensile strain prior buckling normalized by the corresponding value for constant axial force over the height ($\alpha = 1$) versus α, parameter that represents the axial force profile.

For the analyzed cases, which correspond to very slender walls with typical steel ratios at boundary elements between 2% and 4%, it is proposed to use a linear relation between the ratio $\epsilon_{sm}/\epsilon_{sm(\alpha=1)}$ and α (Figure 4.9). This ratio can be used to improve the estimation of the maximum tensile strain prior buckling obtained from the simplified mechanics (section 2.2), now considering a non-uniform stress profile along the boundary element height.

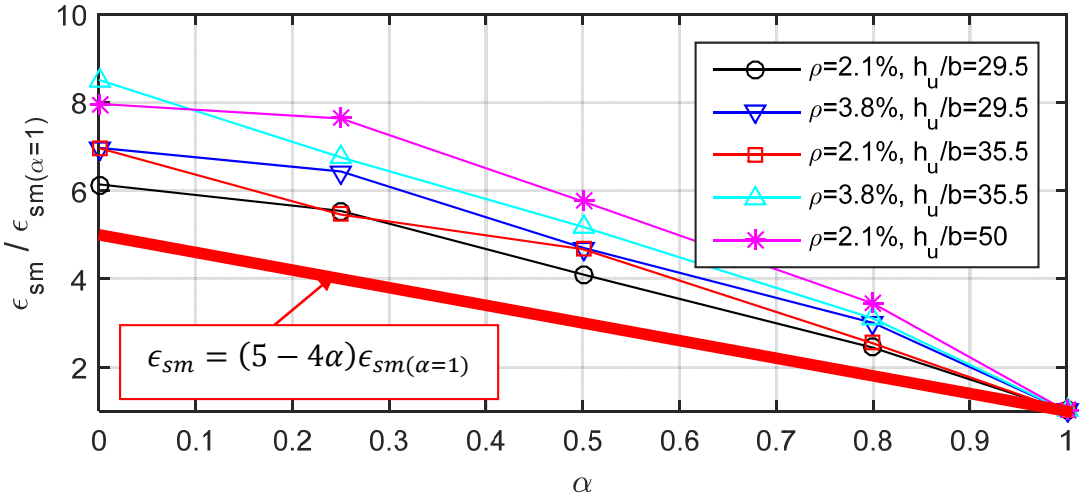

Figure 4.9 Normalized maximum tensile strain prior buckling during load reversal versus α (defined as $\alpha = N_{a\text{-}top} / N_{a\text{-}bottom}$).

Manipulating Equation (3.1) (obtained from the simplified mechanics for constant axial load), the tensile strain required to buckle the boundary element during load reversal is:

$$\epsilon_{sm} = \left(\frac{b_{cr}}{0.7kh_u}\right)^2 + 0.005 \tag{4.1}$$

For example, to estimate ϵ_{sm} for a wall of slenderness $h_u/b = 30$, $k = 0.5$ and $\propto = 0.2$, from Equation (4.1), $\epsilon_{sm} = 0.014$. This estimation can be improved considering the non-uniform load profile. From Figure 4.9, $\epsilon_{sm} = \big(5 - 4(0.2)\big)\, 0.014 = 0.06$, which is a more reasonable estimation of the maximum tensile strain expected at the base of the boundary element prior buckling during load reversal.

4.3 EFFECT OF STRAIN GRADIENT ALONG THE WALL LENGTH

In this section, the response of an isolated boundary element is compared with the response of corresponding walls (identical boundary elements details) of different lengths, in order to study the influence on instability of the strain gradient of the vertical strains along the wall length. Two-dimensional finite elements models of several fictitious walls are built and analyzed using the software TNO DIANA, based on the details of Chai and Elayer's column 4WC4_2 (slenderness $L_0/b = 14.75$ and longitudinal steel ratio $\rho = 3.8\%$). Figure 4.10 presents a typical wall elevation, where the left boundary element is labeled B.E. #1 and the right boundary element is B.E. #2. Translations in the direction orthogonal to the wall plane and rotations around the x-axis are restrained at the top and bottom to represent the wall continuity expected in a typical multistory wall. Considering these fixed-fixed support conditions, the wall height is $h_u = 2L_0$, where L_0 is 59 in., unsupported height of the specimen 4WC4_2 (tested under pinned-pinned support conditions). Bending moments and shear forces are applied and controlled to obtain a target axial force profile over the height of B.E. #1. The objective of this study is to determine the maximum tensile strain in B.E. #1 required to buckle it during load reversal, for several cases. Analyses of

walls of several lengths provide valuable information regarding the influence of the location of the neutral axis on the onset of lateral instability.

Regarding the variation of the axial force in B.E. #1 along the height, two cases are analyzed: constant axial force and linear variation with $\propto = 0.8$. Regarding the loading protocol, boundary loads that compress B.E. #2 are incrementally applied (Figure 4.9) until reaching a target upwards displacement at the top of B.E. #1. After this point, the boundary loads are gradually removed. This analysis is repeated by increasing the target upwards displacement at the top of B.E. #1 until reaching the minimum value needed to buckle it during unloading.

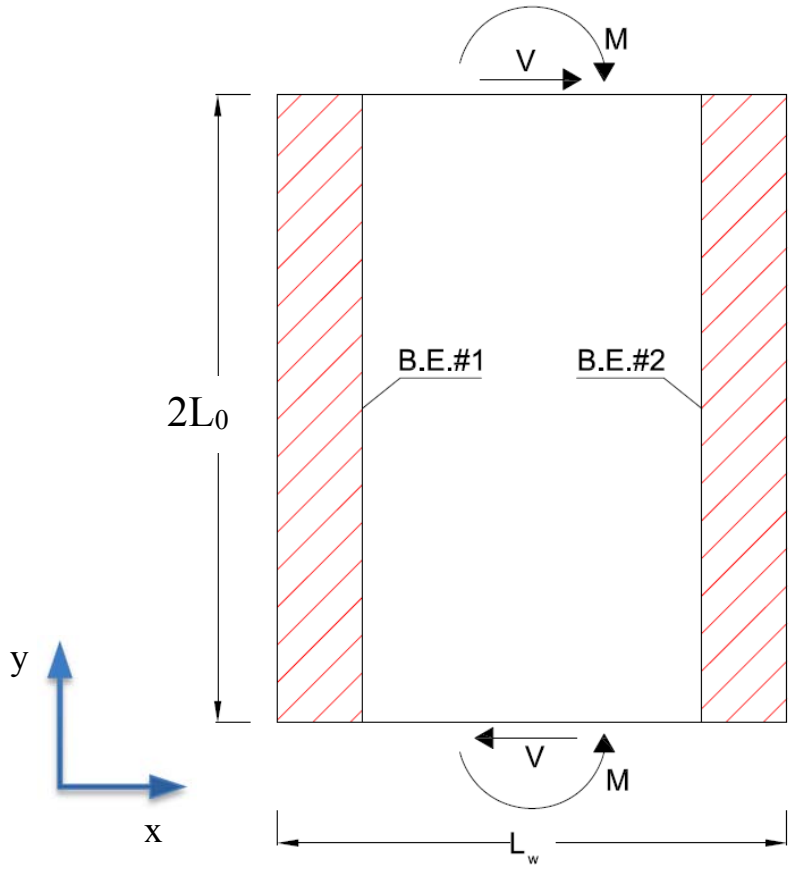

Figure 4.10 Typical wall elevation and loading detail.

Figure 4.11 shows the typical reinforcement, where the details of specimens 4WC4_2 are used in boundary elements. Two layers of vertical and horizontal reinforcement are provided for shear, considering a steel ratio of 0.0025, minimum required by Chapter 18 of ACI 318-14. The wall length varies according to the parameter n. For the case shown in Figure 4.11, $n = 3$. The finite element models consider a larger thickness for B.E. #2 to prevent its failure prior reaching the required tensile strain to buckle B.E. #1 during load reversal.

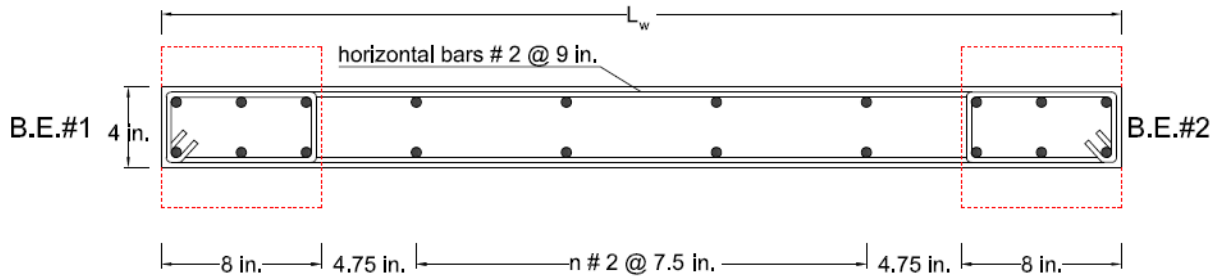

Figure 4.11 Reinforcement details in typical cross section.

The walls are analyzed using curved shell elements with embedded reinforcement and the following parameters: constant fracture energy $G_c = 0.1$ kip in./in.^{2}, yielding stress reduction Δf_y =1 ksi in one layer of reinforcement and Q20SH meshes with maximum element size h_{max} = 2 in. Figure 4.12 shows a typical model.

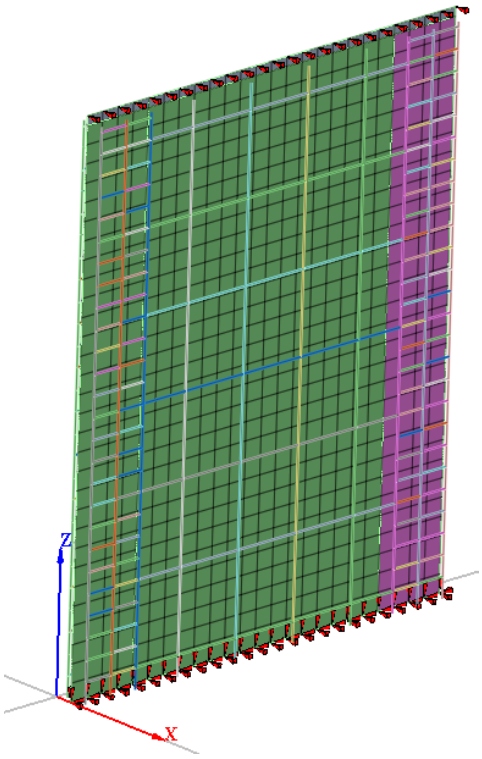

Figure 4.12 Typical FEM DIANA model (h_w/b = 29.5, L_w = 48 in.).

4.3.1 Constant Axial Force in Boundary Elements along the Height

This section presents the analysis results of six walls with lengths varying from 40.5 to. 123 in., all of them with identical details at boundary elements, corresponding to the details of specimen 4WC4_2 (Chai and Elayer, 1999). For this case the axial force profile at B.E. #1 is constant over the height.

The isolated specimen 4WC4_2 was analyzed in OpenSees using nonlinear beam-column elements with fibers, for several axial force profiles. Figure A.1 shows the results for constant axial force over the height. The maximum tensile strain prior buckling during load reversal is $\epsilon_{sm} = 5\epsilon_y$, uniform over the specimen height. The theoretical sine shape assumed in the derivation of the simplified mechanics (section 2.2) and the OpenSees buckled shape match perfectly.

Figure 4.13 presents five plots with the analysis results for the wall with length $L_w = 40.5$ in. Figure 4.13a and b show the undeformed wall and the buckled shape. Figure 4.13c and d present the strain demand over the boundary element height and wall length, at the point of maximum vertical strain prior buckling during load reversal. The strain profile over the height is normalized by the yielding strain. Figure 4.13e shows the normalized out-of-plane displacement along the wall length at the height where its maximum value was calculated. Figure 4.14 to Figure 4.18 present the same information for the other five walls.

For all cases the neutral axis depth is small when the maximum tensile strain prior buckling is reached in B.E. #1, and almost the entire cross section is in tension. Therefore, the extension of the tension zone for the analyzed cases ranges from $10t_w$ to $30t_w$. Results of this analysis show that in walls where the axial force is constant over the boundary element height with tension zones extending over $10t_w$ or more at the point of maximum tensile strain, the value of ϵ_{sm} is almost insensitive to the location of the neutral axis. For the six analyzed cases, this value is close to $5\epsilon_y$, which is the value calculated for the isolated boundary element in OpenSees. The distribution of the out-of-plane displacements along the wall length obtained for each wall (Figure 4.13e to Figure 4.18e) shows that there is not a specific portion of the wall were the lateral displacement concentrates. Lateral instability involves a significant length of the wall in all cases. Only the longest wall of Figure 4.18e (L_w =123 in.) shows a small portion next to B.E. #2 that does not seem to be affected by the lateral instability. Analysis results for the cases presented here and those presented in section 4.2 and Appendix A for isolated columns suggest that the maximum tensile strain prior buckling ϵ_{sm} is more influenced by the axial force distribution along the boundary element height rather than the variation of vertical strain along the wall length, for tension zones longer than $10t_w$, which is a very typical case in real buildings. Similar studies are presented in section 4.3.2 for walls with variable axial force over the height of B.E. #1.

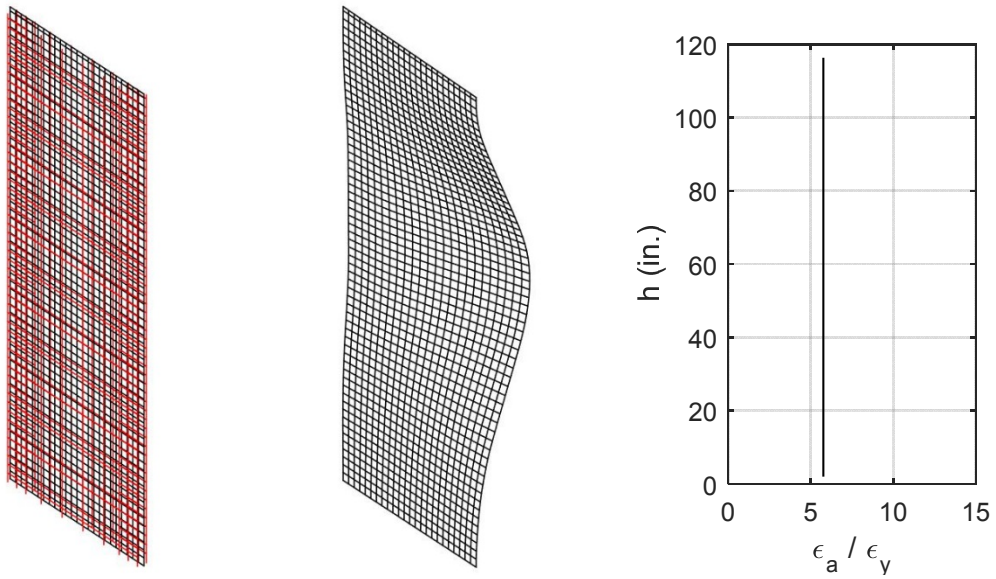

(a) (b) (c)

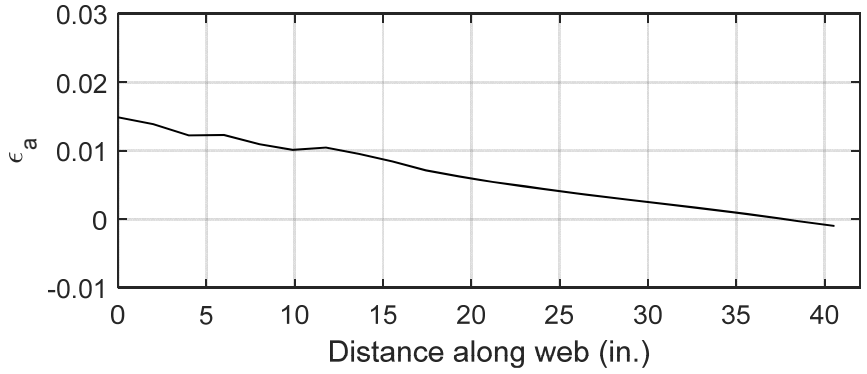

(d)

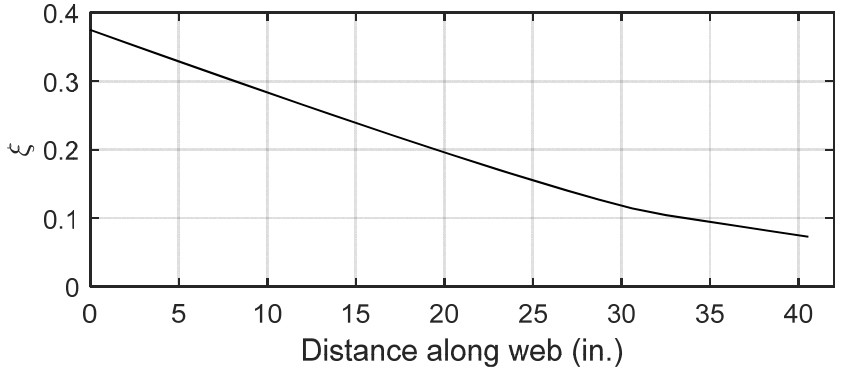

(e)

Figure 4.13 Wall with boundary element 4WC4_2 and L_w = 40.5 in.: a) undeformed shape, b) buckled shape, c) normalized tensile strain along the boundary element height at the tensile peak prior buckling, d) vertical strain gradient along the length at the tensile peak prior buckling, e) normalized lateral displacement along the wall length at buckling.

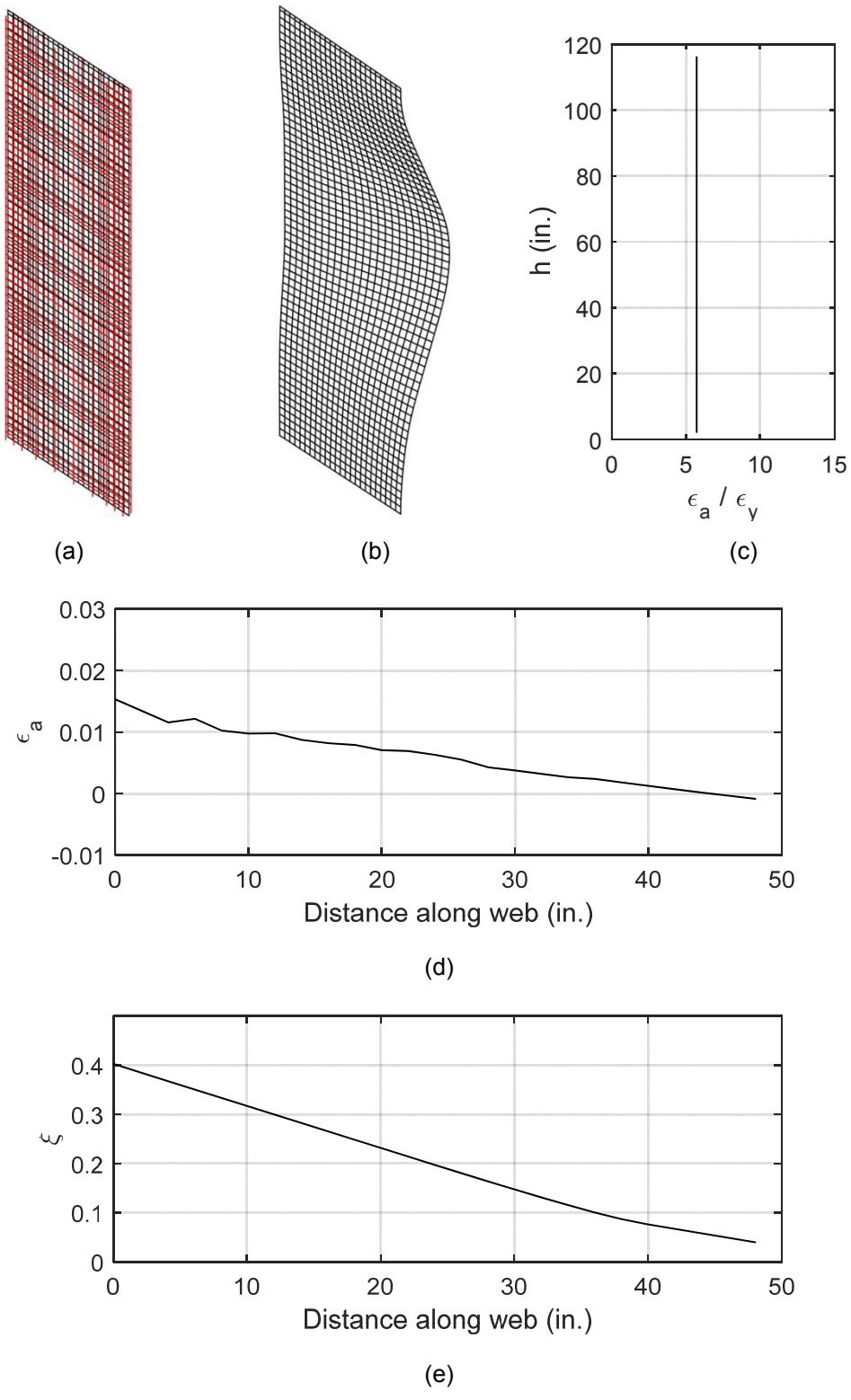

Figure 4.14 Wall with boundary element 4WC4_2 and L_w = 48 in.: a) undeformed shape, b) buckled shape, c) normalized tensile strain along the boundary element height at the tensile peak prior buckling, d) vertical strain gradient along the length at the tensile peak prior buckling, e) normalized lateral displacement along the wall length at buckling.

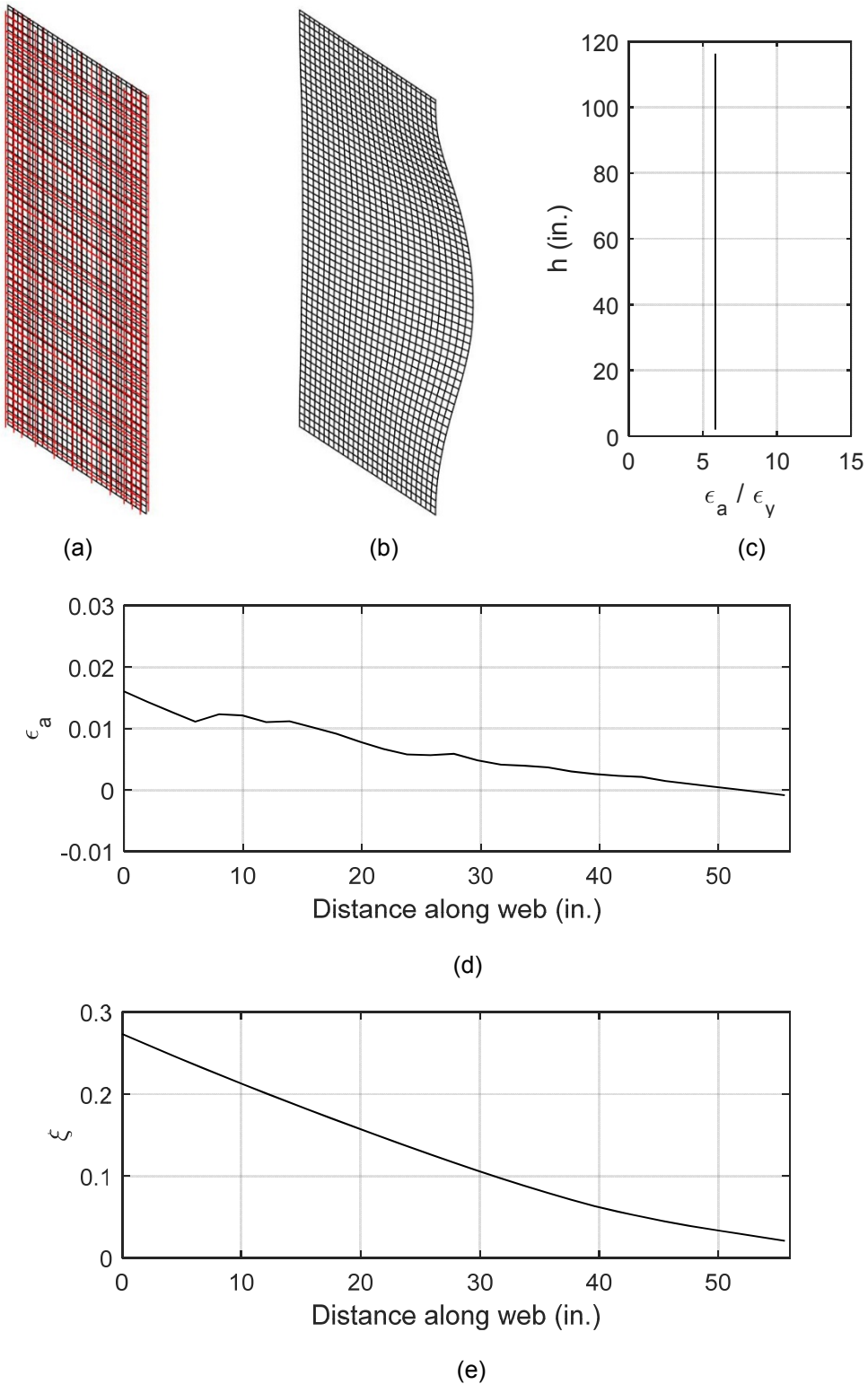

Figure 4.15 Wall with boundary element 4WC4_2 and L_w = 55.5 in.: a) undeformed shape, b) buckled shape, c) normalized tensile strain along the boundary element height at the tensile peak prior buckling, d) vertical strain gradient along the length at the tensile peak prior buckling, e) normalized lateral displacement along the wall length at buckling.

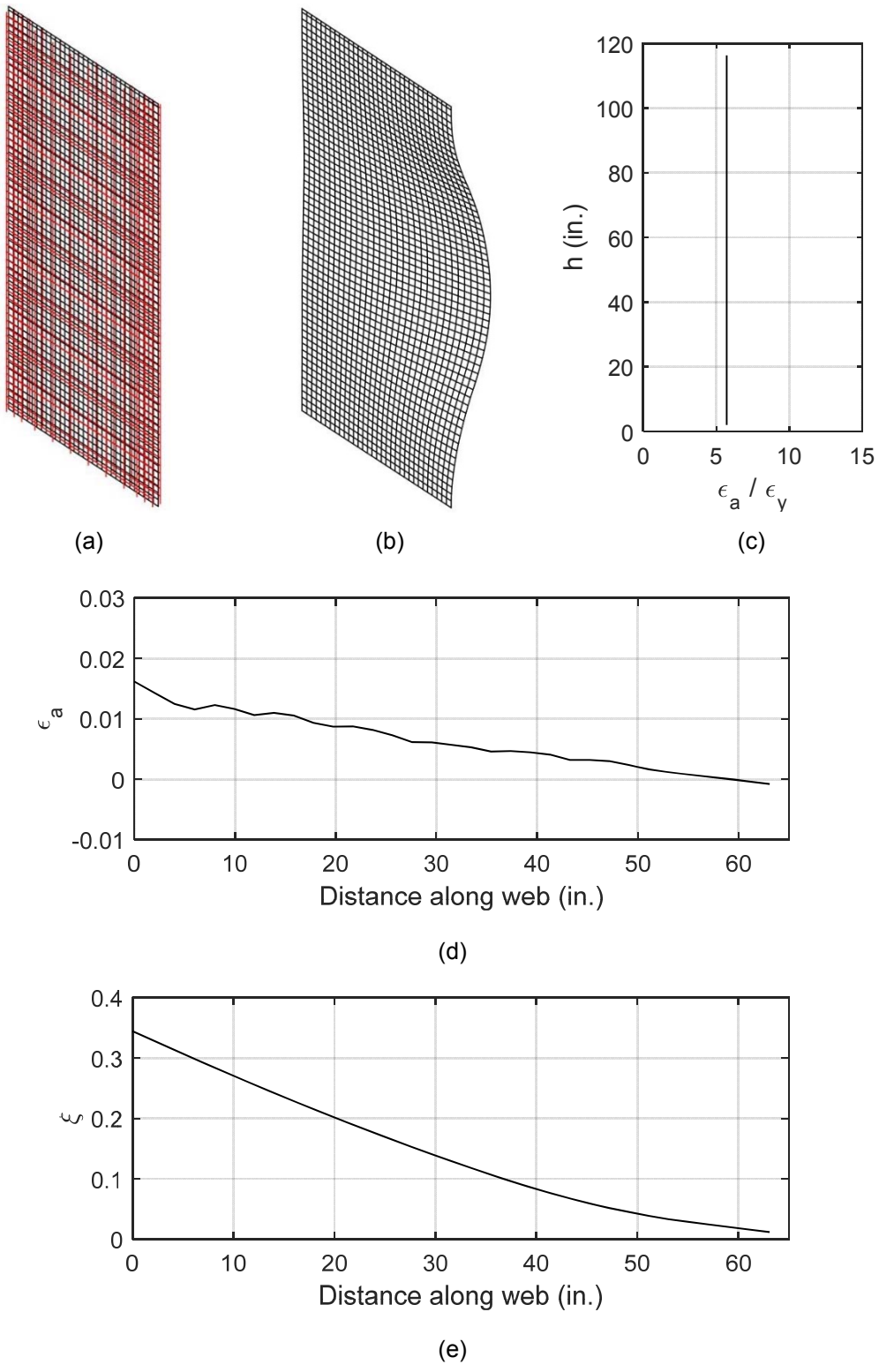

Figure 4.16 Wall with boundary element 4WC4_2 and L_w = 63 in.: a) undeformed shape, b) buckled shape, c) normalized tensile strain along the boundary element height at the tensile peak prior buckling, d) vertical strain gradient along the length at the tensile peak prior buckling, e) normalized lateral displacement along the wall length at buckling.

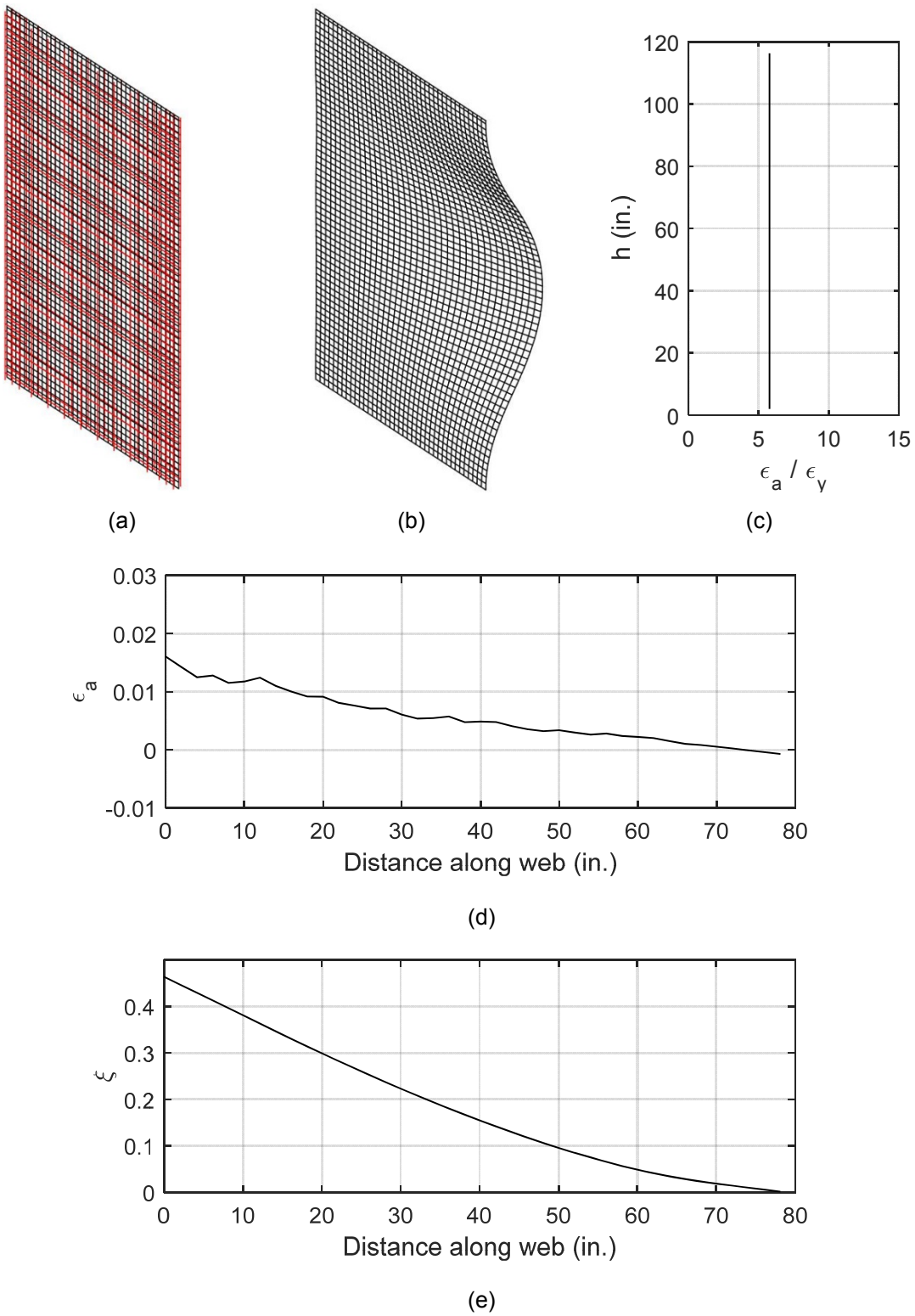

Figure 4.17 Wall with boundary element 4WC4_2 and L_w = 78 in.: a) undeformed shape, b) buckled shape, c) normalized tensile strain along the boundary element height at the tensile peak prior buckling, d) vertical strain gradient along the length at the tensile peak prior buckling, e) normalized lateral displacement along the wall length at buckling.

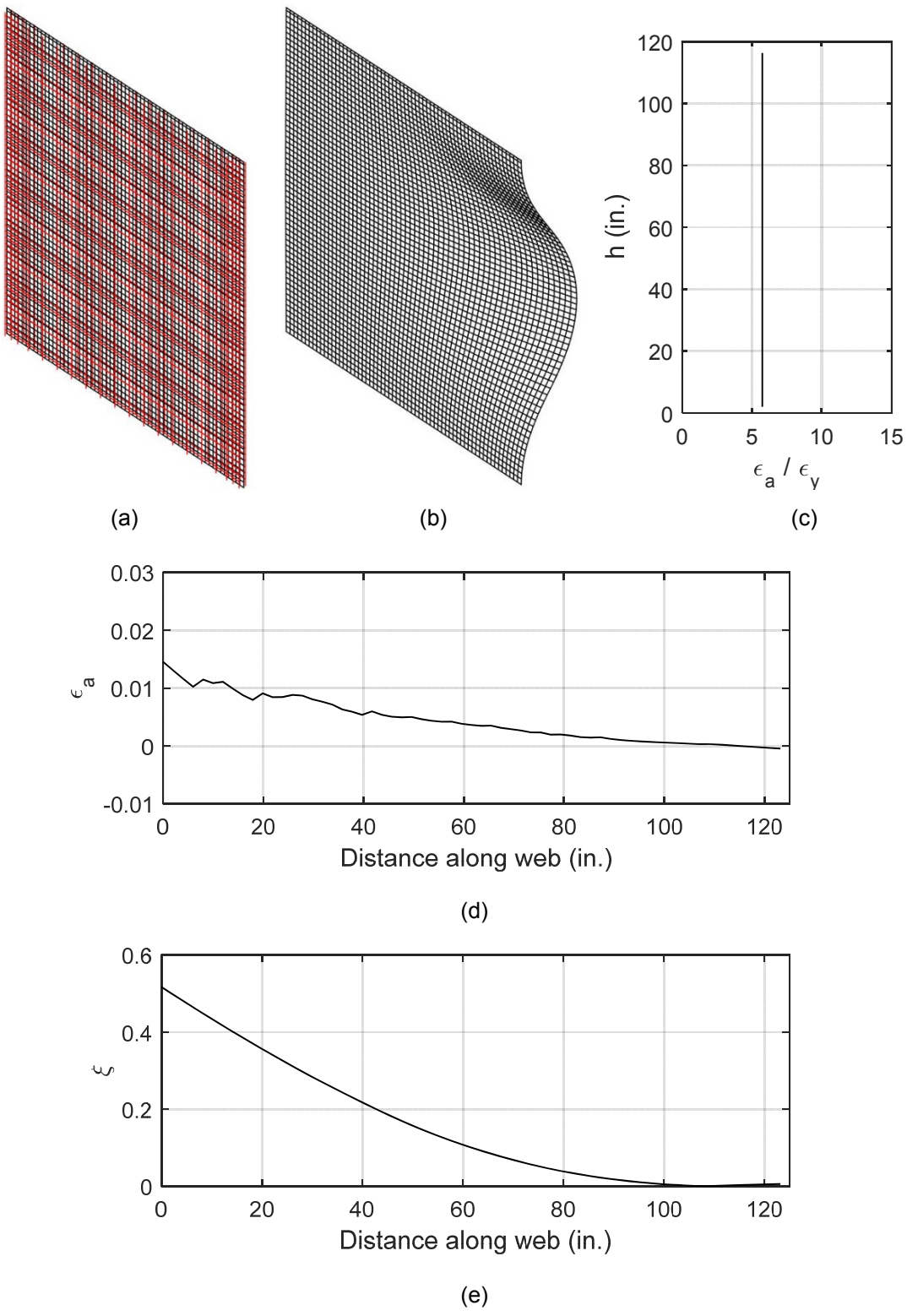

Figure 4.18 Wall with boundary element 4WC4_2 and L_w = 123 in.: a) undeformed shape, b) buckled shape, c) normalized tensile strain along the boundary element height at the tensile peak prior buckling, d) vertical strain gradient along the length at the tensile peak prior buckling, e) normalized lateral displacement along the wall length at buckling.

4.3.2 Linear Variation of Axial Force in Boundary Elements along the Height

This section presents the analysis results of walls where there is a linear variation in the axial force along B.E. #1 height. The value of α, which is the ratio between the top and bottom axial force at B.E. #1, is 0.8. The analysis includes five walls with length ranging from 40.5 to 78 in, all of them with details at boundary elements identical to those in specimen 4WC4_2 (Chai and Elayer, 1999).

Figure A.2 shows the results of OpenSees analysis for the isolated specimen 4WC4_2 under variable axial force along the height with $\alpha = 0.8$. For this case, the distribution of normalized axial vertical strain at the point of maximum vertical displacement prior buckling is not uniform anymore. Its maximum value, close to $\epsilon_{sm} = 13\epsilon_y$, is located at the specimen base. The buckled shape does not match the theoretical sine shape used in the simplified mechanics of section 2.2. The peak horizontal displacement is located in a lower position, close to $0.3h_u$. Figure 4.19 to Figure 4.23 present the analysis results for these five walls following the same format of section 4.3.1. Here, the vertical strain gradient along the wall length is shown for a cross section located at 40 in. over the wall base. For the analyzed cases, the extension of the tension zone at the point of maximum vertical strain in B.E. #1 prior buckling during load reversal, ranges from $8t_w$ to $18t_w$. Analysis results show that the value of ϵ_{sm} at the base of B.E. #1 changes with the position of the neutral axis. From Figure 4.19c to Figure 4.23c, ϵ_{sm} decreases from $20\epsilon_y$ to $13\epsilon_y$, which is the value obtained from OpenSees analysis of the isolated boundary element, as the tension zone at the peak tensile strain prior buckling increases from $8t_w$ to $14t_w$. For the first analyzed case (Figure 4.19), there is a 54% increment in ϵ_{sm} with respect to the value obtained from OpenSees. This increment decreases quickly to 7% when the tension zone reaches $12t_w$. Similar to the observations made in section 4.3.1, for these cases there is also a significant portion of the wall length involved in the out-of-plane instability.

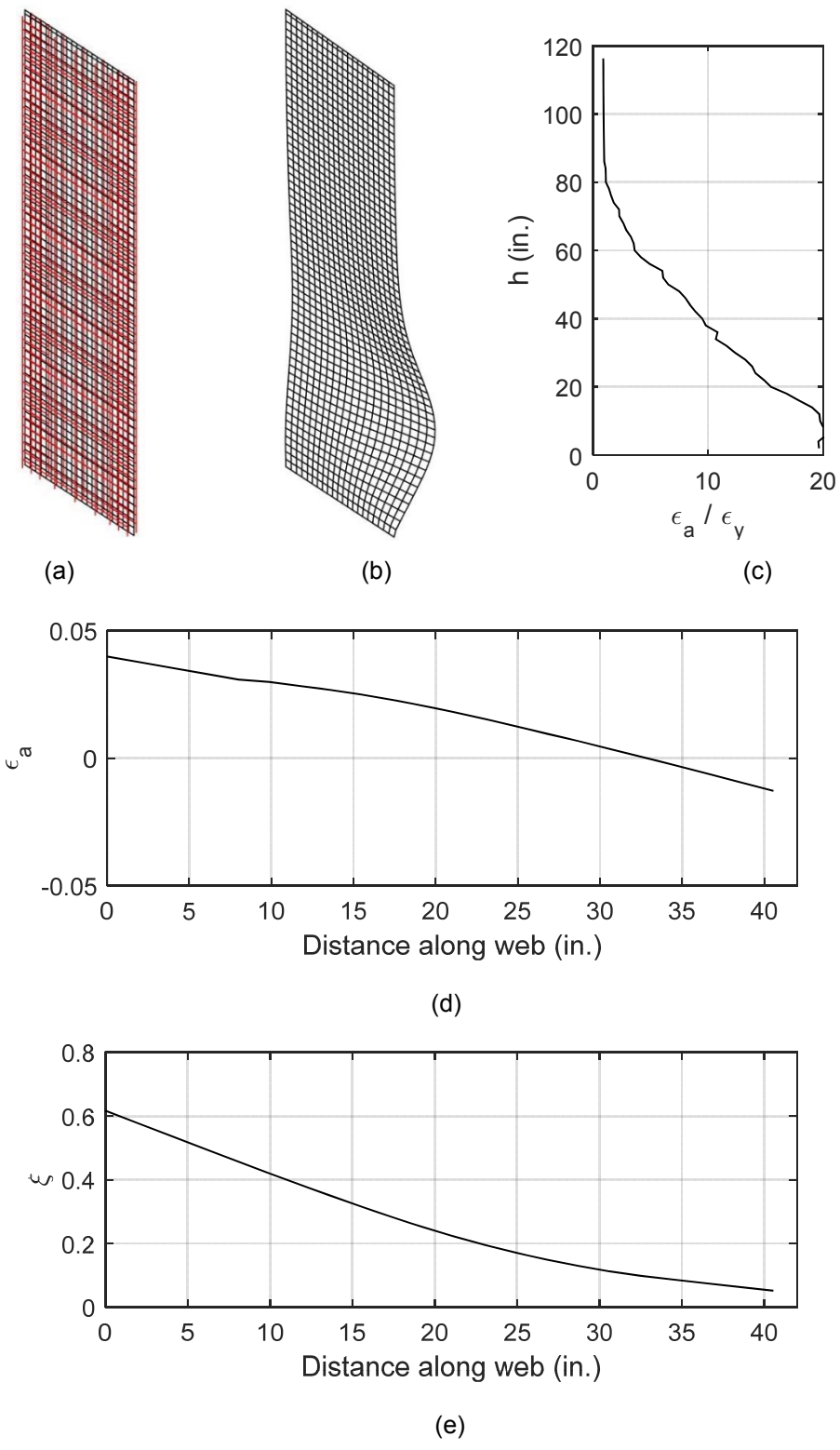

Figure 4.19 Wall with boundary element 4WC4_2 and L_w = 40.5 in.: a) undeformed shape, b) buckled shape, c) normalized tensile strain along the boundary element height at the tensile peak prior buckling, d) vertical strain gradient along the length at the tensile peak prior buckling, e) normalized lateral displacement along the wall length at buckling.

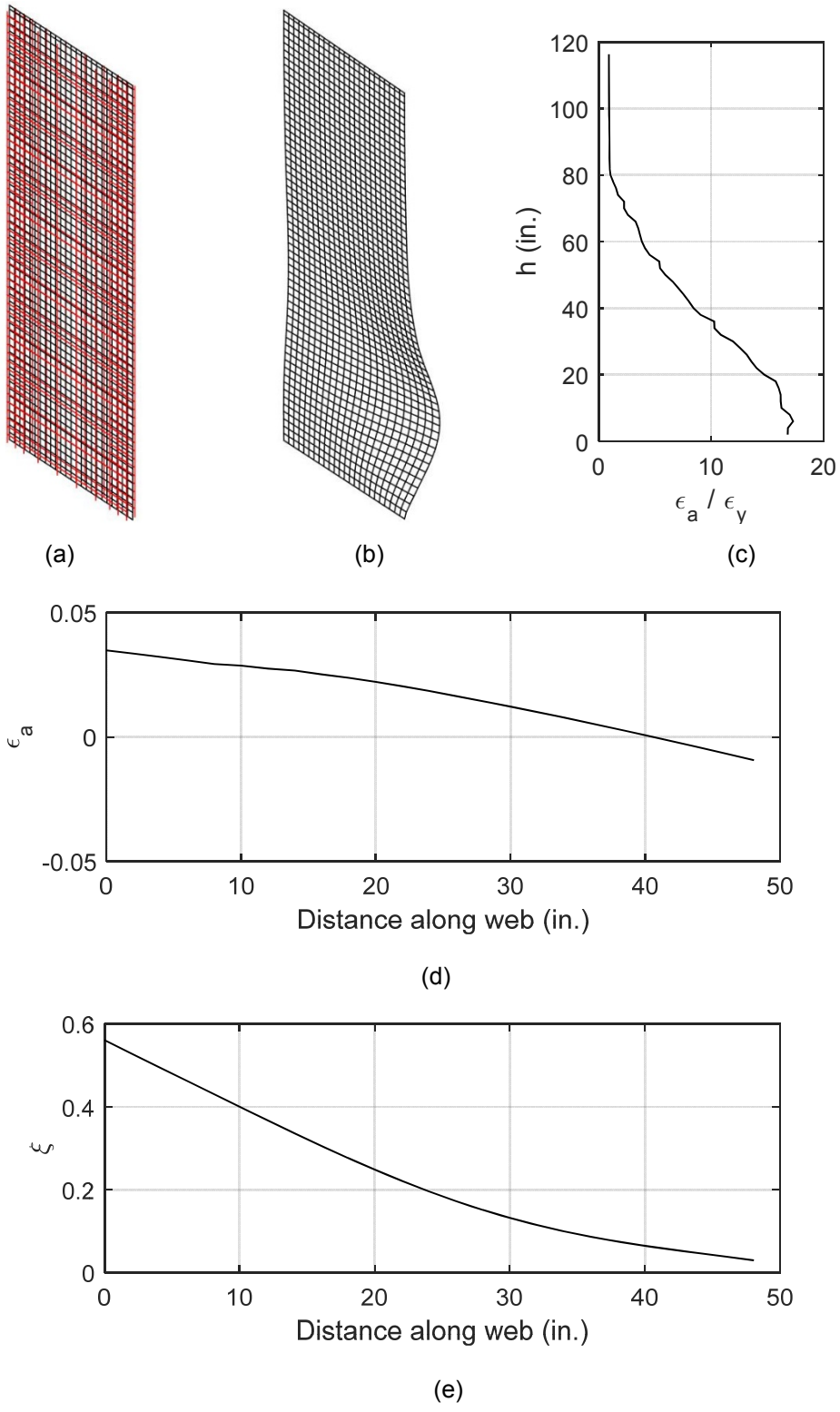

Figure 4.20 Wall with boundary element 4WC4_2 and L_w = 48 in.: a) undeformed shape, b) buckled shape, c) normalized tensile strain along the boundary element height at the tensile peak prior buckling, d) vertical strain gradient along the length at the tensile peak prior buckling, e) normalized lateral displacement along the wall length at buckling.

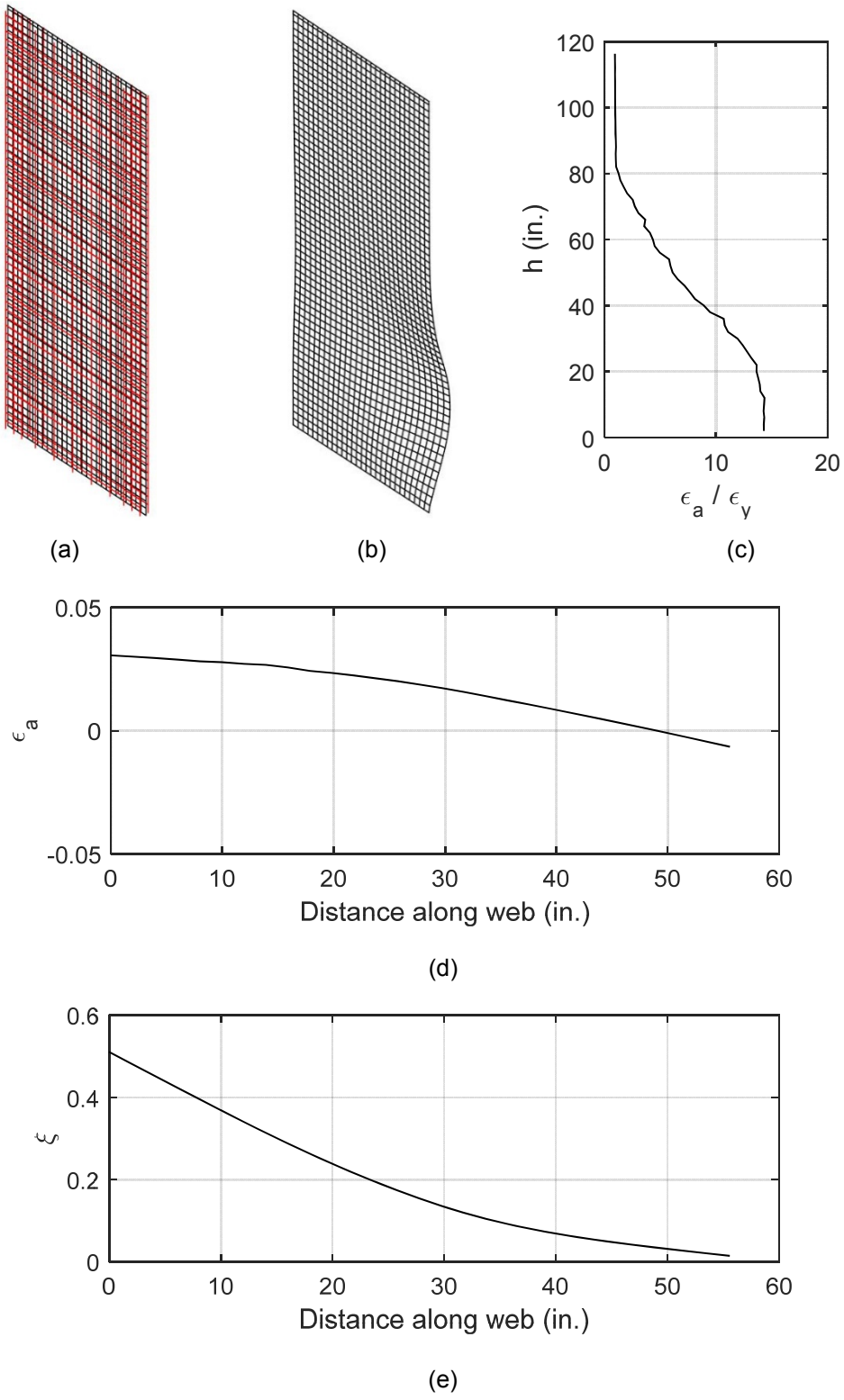

Figure 4.21 Wall with boundary element 4WC4_2 and L_w = 55.5 in.: a) undeformed shape, b) buckled shape, c) normalized tensile strain along the boundary element height at the tensile peak prior buckling, d) vertical strain gradient along the length at the tensile peak prior buckling, e) normalized lateral displacement along the wall length at buckling.

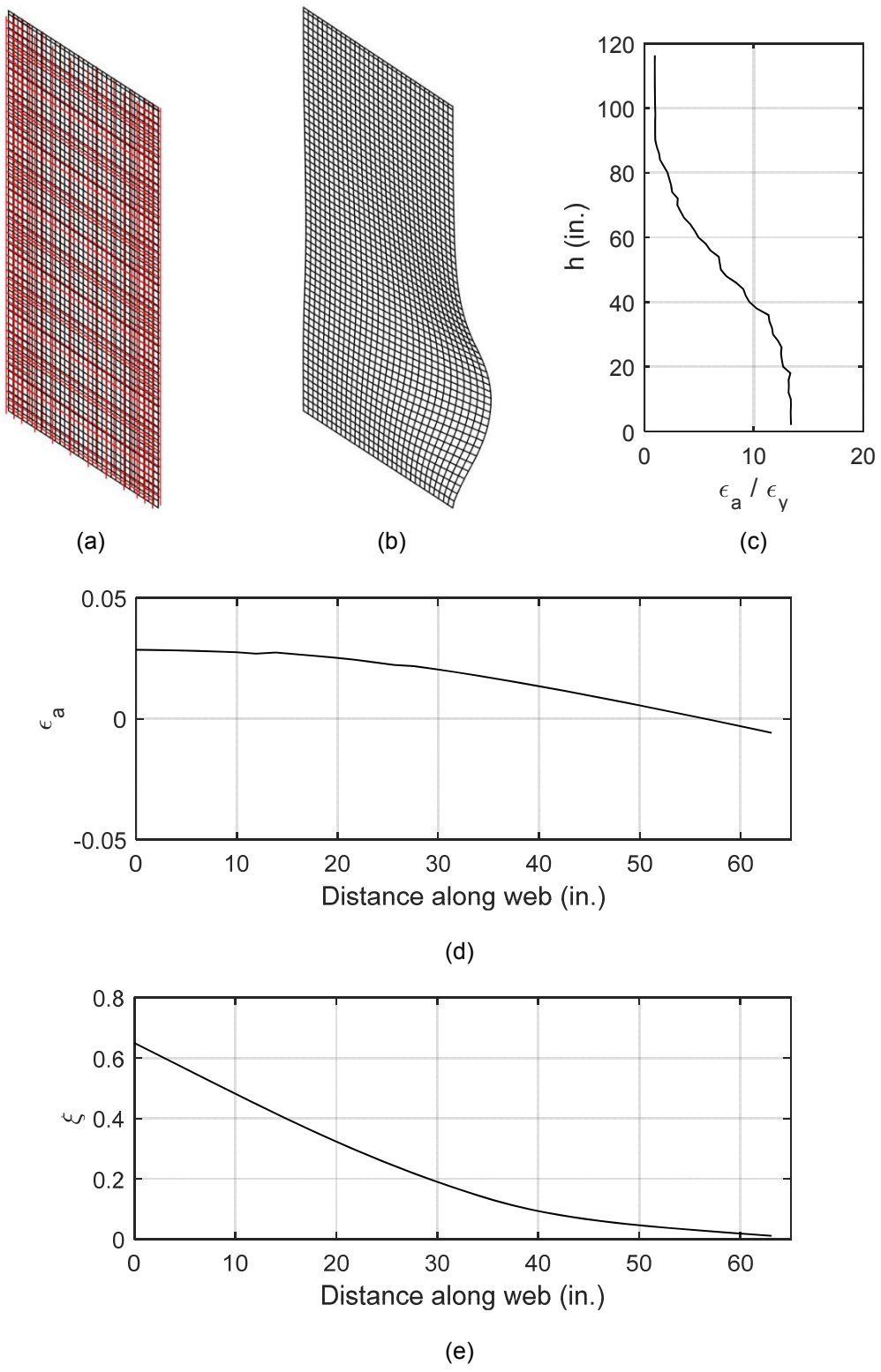

Figure 4.22 Wall with boundary element 4WC4_2 and L_w = 63 in.: a) undeformed shape, b) buckled shape, c) normalized tensile strain along the boundary element height at the tensile peak prior buckling, d) vertical strain gradient along the length at the tensile peak prior buckling, e) normalized lateral displacement along the wall length at buckling.

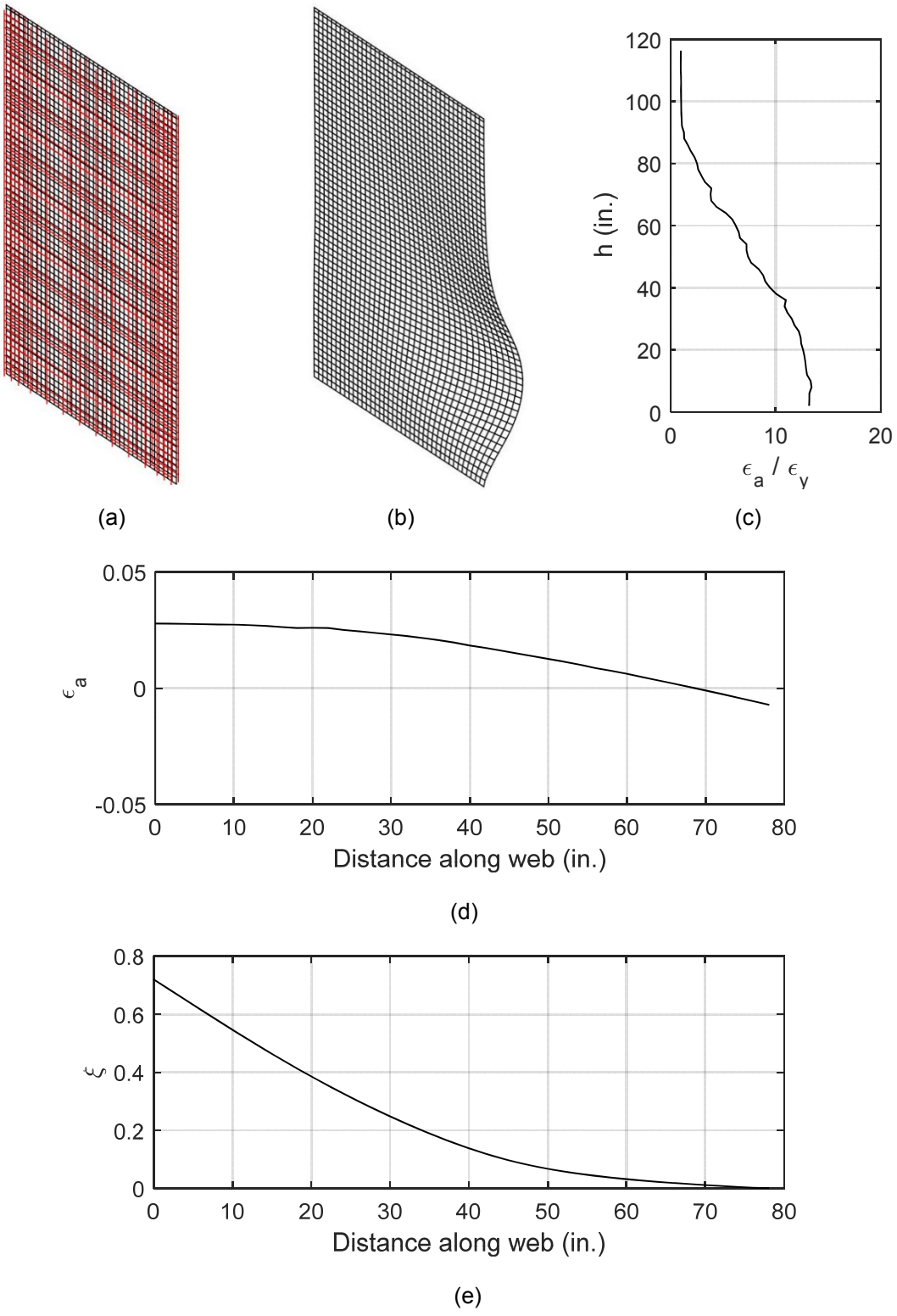

Figure 4.23 Wall with boundary element 4WC4_2 and L_w = 78 in.: a) undeformed shape, b) buckled shape, c) normalized tensile strain along the boundary element height at the tensile peak prior buckling, d) vertical strain gradient along the length at the tensile peak prior buckling, e) normalized lateral displacement along the wall length at buckling.

4.4 SUMMARY OF STRAIN GRADIENT EFFECTS

The key parameter for the evaluation of the onset of out of plane instability in slender walls is the maximum tensile strain at the boundary element prior buckling during load reversal (ϵ_{sm}), and this value can be safely estimated from the simplified mechanics presented in section 2.2. The mechanics was formulated for columns under uniform tension/compression cycles. For walls where the assumption of uniform strain along the boundary element height is reasonable, like the case of the "flag walls" in Chilean buildings, the analysis presented in section 4.3.1 suggests that the effect of the strain gradient along the wall length can be safely neglected for a typical case of a wall longer than $10t_w$.

A second case occurs when there is a strain gradient along the wall length and the boundary element height. For this case, the assumptions behind the simplified mechanics lead to a considerable underestimation of ϵ_{sm}, and then an over-conservative estimation of the minimum wall thickness required to prevent this from happening. There are several cases in practice where we can face this situation, and it is prudent to reduce the over conservatism in the design. The actual value of ϵ_{sm} is higher than the one obtained from the simplified mechanics due to effects of those two strain gradients, and these effects have been studied in sections 4.2 and 4.3. Results of the analyzed cases suggest that the gradient of axial force along the boundary element height is far more important than the strain gradient along the wall length. Section 4.2 showed that there is a quick increase in the value of ϵ_{sm} as the axial force profile changes from uniform to triangular. For this last case ϵ_{sm} is more than five times the value obtained for a uniform axial load profile. It is proposed to increase the value of ϵ_{sm} obtained from the simplified mechanics by a factor that depends linearly on the axial force profile in the flexural compression zone, which relates to the moment profile, in order to reduce the over conservatism of the simplified mechanics for these cases.

Section 4.3 showed that there is also an effect in the value of ϵ_{sm} caused by the strain gradient along the wall length. For short walls, ϵ_{sm} increases, especially when the gradient along the height is non-uniform. When the force profile over height is uniform, the gradient along the length does not seem to change the response obtained from analysis of an isolated boundary element.

The magnitude of the increment caused by the gradient over the height is much higher than the effect of the gradient along the length, which quickly decreases as the wall becomes longer. In these analyzed cases, for tension zones of more than $12t_w$ the increment in ϵ_{sm} is only 7%. It is proposed for pre-design purposes to neglect the effect of the strain gradient along the wall length, which seems reasonable for typical wall geometries observed in practice, and to consider only the effect of axial force gradients along the boundary element height, increasing the value of ϵ_{sm} accordingly.

5 Global Instability in Wall Tests

5.1 INTRODUCTION

Prior the Chile earthquake in 2010, out-of-plane instability in slender walls was observed in a few laboratory tests. In this chapter, the experimental programs of the Portland Cement Association (Oesterle et. al, 1976) and Thomsen and Wallace (2004), both with wall specimens that showed apparent buckling, are used to evaluate the analytical models for global instability introduced in section 2. Studies include estimations of strain demands for all the specimens tested by Thomsen and Wallace (two rectangular walls and two T-shaped walls, one of them buckled during the test), and the buckled rectangular specimen R2 of the Portland Cement Association program. The strain demands at ultimate drift are estimated following three approaches: direct extrapolation from data obtained at lower drift ratios (when data at ultimate drift are not available), a plastic hinge method, and two-dimensional nonlinear finite element models. Finally, OpenSees fibers models and the simplified buckling mechanics are used for evaluation of global instability.

5.2 SIMPLIFIED METHODS FOR THE ESTIMATION OF STRAIN DEMANDS

There are several approaches to analytically estimate the strain profile at the base of a wall and therefore the maximum tensile strain prior load reversal at boundary elements, starting from nonlinear analysis for an isolated wall of even a complete building to simplified methods of analysis. Simplified methods were preferred for analysis of buildings in Chile. Two approaches are presented here based on analysis of isolated walls: numerical integration of curvatures and a plastic hinge model.

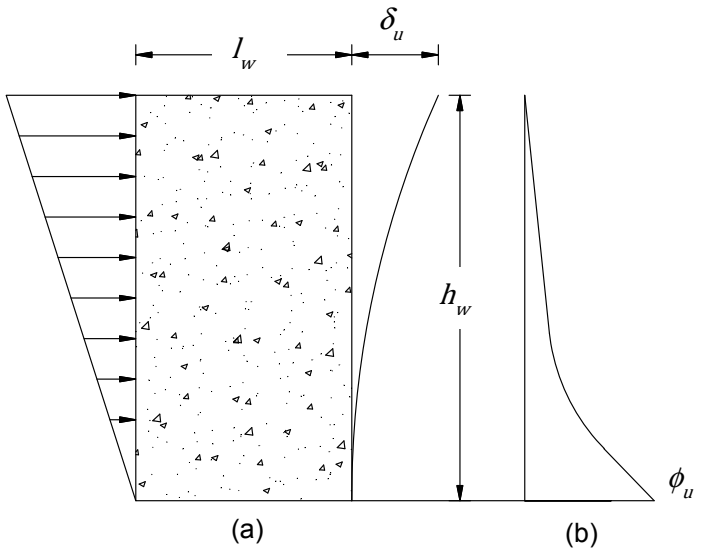

Figure 5.1 Wall flexural deformations: (a) elevation, loading and drift; (b) curvatures.

Figure 5.1a depicts a wall with an inverse triangular load pattern applied laterally. The curvature distribution over the height is shown in Figure 5.1b. The lateral displacement at wall top δ_u can be obtained from integration of the curvature diagram according to Equation (5.1). Note that this expression includes only wall flexure, and ignores displacement due to shear deformations and slip of reinforcement from the base anchorage.

$$\delta_u = \int_0^{h_w} \phi(h)(h_w - h)dh \tag{5.1}$$

where h_w is the wall height and $\phi(h)$ is the curvature distribution. Equation (5.1) can be numerically integrated using a suitable quadrature. For this research, the Gauss-Lobatto quadrature is used (section 2.3.7). Then, Equation (5.1) becomes:

$$\delta_u = \sum_{i=1}^{NiP} \phi(h_i)(h_w - h_i)w_i \tag{5.2}$$

where NiP is the number of integration points, h_i is the location of the integration point i and w_i is the weight of this integration point. The curvature at the first integration point $\phi(h_1)$ at the wall base for a given target displacement δ_u can be obtained from Equation (5.2). Starting from $\phi(h_1)$ it is straightforward to obtain ϵ_{sm} from section analysis, assuming that plane sections remain plane.

A second simplified method to obtain the relation between the top displacement and the curvature at the wall base is the plastic hinge approach, according to Figure 5.2.

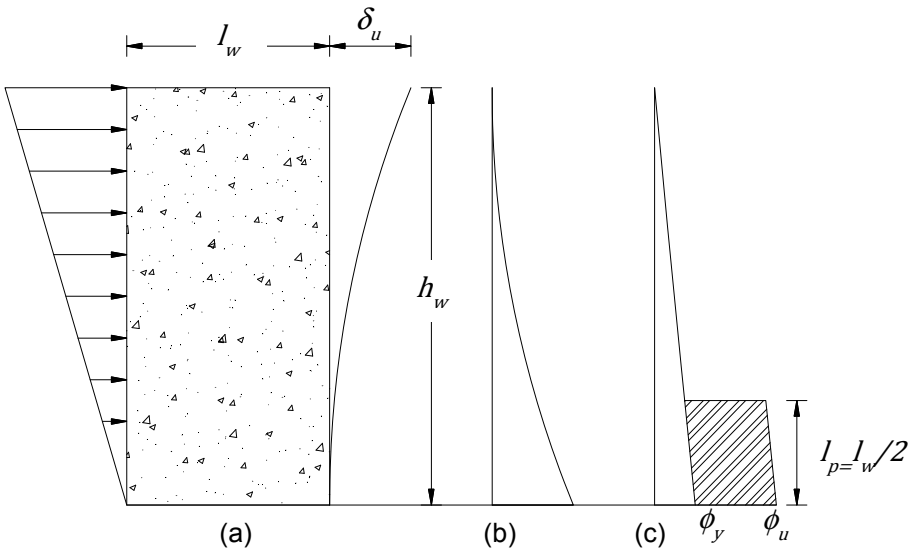

Figure 5.2 Wall flexural deformations: (a) elevation, loading and drift; (b) moments; (c) curvatures.

Given the model of Figure 5.2, the displacement at the top of the wall is approximated by Equation (5.3) (modified from Wallace and Moehle, 1993).

$$\delta_u = \frac{11}{40}\phi_y h_w^2 + (\phi_u - \phi_y) l_p \left(h_w - \frac{l_p}{2}\right) \tag{5.3}$$

Equation (5.4) shows the relation between the top displacement δ_u and the maximum curvature at the wall base ϕ_u for the plastic hinge approach, when the lateral load is applied only at the wall top, which is the case of tested walls presented in Chapter 5.

$$\delta_u = \frac{1}{3}\phi_y h_w^2 + (\phi_u - \phi_y) l_p \left(h_w - \frac{l_p}{2}\right) \tag{5.4}$$

Where ϕ_y is the yielding curvature and l_p is the plastic hinge length, usually considered one half of the wall length l_w. Rearranging terms of Equation (5.4).

$$\phi_u = \frac{1}{l_p \left(h_w - \frac{l_p}{2}\right)} \left(\delta_u - \frac{1}{3}\phi_y h_w^2\right) + \phi_y \tag{5.5}$$

If $\delta_u = DR\ h_w$, where DR is the roof drift ratio, then Equation (5.5) can be expressed as:

$$\phi_u = \frac{h_w}{l_p \left(h_w - \frac{l_p}{2}\right)} \left(DR - \frac{1}{3}\phi_y\ h_w\right) + \phi_y \tag{5.6}$$

Equation (5.6) expresses the curvature at the wall base as a function of the roof drift ratio. A simpler equation considers the top displacement to be due solely to rotation in the assumed plastic hinge zone, according to Figure 5.3 and Equation (5.7). This approach provides a suitable approximation for cases in which most of the curvature is at the base. Suitable examples include prismatic walls in which large inelastic curvatures occur at the base and nonprismatic walls with reduced sections at the plastic hinge region. This last case (called “flag walls”) is very typical in

residential buildings in Chile. According to the approach, the curvature distribution of Figure 5.2 is replaced by a simplified distribution shown in Figure 5.3, where all the elastic curvatures are ignored except those within the plastic hinge. To compensate the low estimate of the wall displacement capacity for a given maximum curvature, the plastic hinge is located centered at the wall base. For this model, the curvature ϕ_u is expressed by Equation (5.7).

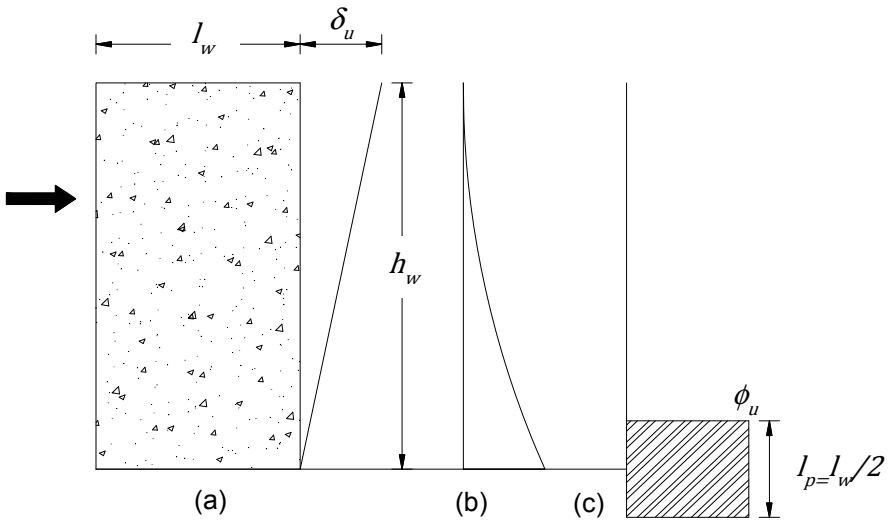

Figure 5.3 Wall flexural deformations: (a) elevation, loading and drift, (b) moments, (c) curvatures.

$$\phi_u = \frac{DR}{l_p} \tag{5.7}$$

5.3 THOMSEN AND WALLACE WALL TESTS

5.3.1 Experimental Program

Thomsen and Wallace (2004) conducted a combined experimental and analytical investigation to evaluate a displacement-based approach (Wallace and Moehle 1992; Wallace 1994) used to assess wall-detailing requirements. The laboratory test program included six wall specimens, approximately quarter-scale, including three with rectangular cross section (one with an opening), two with T-shaped cross section, and one with barbell-shaped cross section with an opening. Figure 5.4 shows the overall geometry of the test specimens. The walls were 12 ft (3.66 m) tall and 4 in. (102 mm) thick, with web and flange lengths of 4 ft (1.22 m). Floor slabs were provided at 3 ft (0.91 m) intervals over the height of the T-shaped walls.

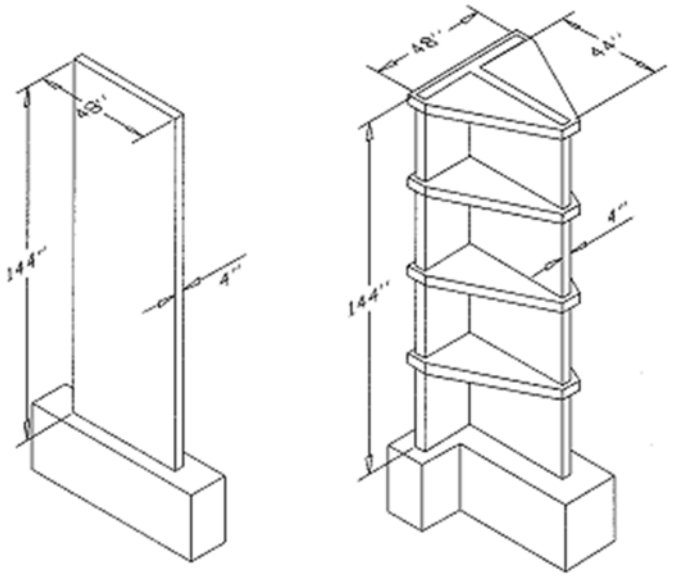

(a) (b)

Figure 5.4 Overall geometry of specimens (a) RW1/RW2; (b) TW1/TW2 (1 in. = 25.4 mm).

A prototype building, representing a multistory office building in an area of high seismicity was used to assist in determining the wall geometry and reinforcing details for the testing program. The prototype rectangular wall is 16 in. (406 mm) thick and 16 ft (4.88 m) long with ten No. 11 (A_b = 1.56in.^{2}; 1000 mm^2) boundary vertical bars and No. 5 (A_b = 0.31in.^{2}; 200 mm^2) vertical and horizontal web reinforcement spaced at 12 in. (305 mm). Similar reinforcing quantities are used at the boundaries and within the webs for the T-shaped walls. The wall specimens tested were approximately one-quarter scale representations of the prototype walls. Boundary vertical steel consisted of eight No. 3 (A_b = 0.11in.^{2}; 71 mm^2) bars, whereas web bars were deformed No. 2 (A_b = 0.049 in.^{2}; 32 mm^2). Areas of boundary and web steel were selected to be roughly equivalent to 1/16 (square of the scale factor) of those for the prototype walls so as to produce a similar neutral axis depth relative to the wall length in comparison with the prototype walls. The depth of the neutral axis for an axial load of $0.10A_g f'_c$ and an extreme fiber compression strain of 0.003 is 9.7 in. or $0.20l_w$ (246 mm) for the rectangular wall specimens. Neutral axis depths for an extreme fiber strain of 0.003 are 2 in. or $0.042l_w$ (51 mm) and 24.5 in. or $0.51l_w$ (670 mm) for the flange in compression and tension, respectively, for the T-shaped wall specimens loaded parallel to the stem of the T.

Detailing requirements at the boundaries of the wall specimens were evaluated using the displacement-based design approach presented by Wallace (1994, 1995). In this approach, the design displacement is related to the curvature and strain demands at the critical section, and special transverse reinforcement is provided over the length of the wall cross section where the compression strain exceeds a critical value, typically taken as 0.003. A design roof drift equal to 1.5% of the wall height, or 2.16 in. (55 mm) was selected to determine the required transverse reinforcement at the wall boundaries for the test specimens. This drift was selected because it represents a reasonable upper bound drift level for structural wall buildings (Wallace and Moehle 1992), and more importantly for the test program, because transverse reinforcement was required

at the wall boundaries (that is the extreme fiber compression strain exceeded the critical strain of 0.003). For a lower design drift, the lateral drift capacity of all the specimens would be limited by buckling of longitudinal reinforcement due to the relatively large spacing of the transverse reinforcement. The next figures show the cross sections of the test walls.

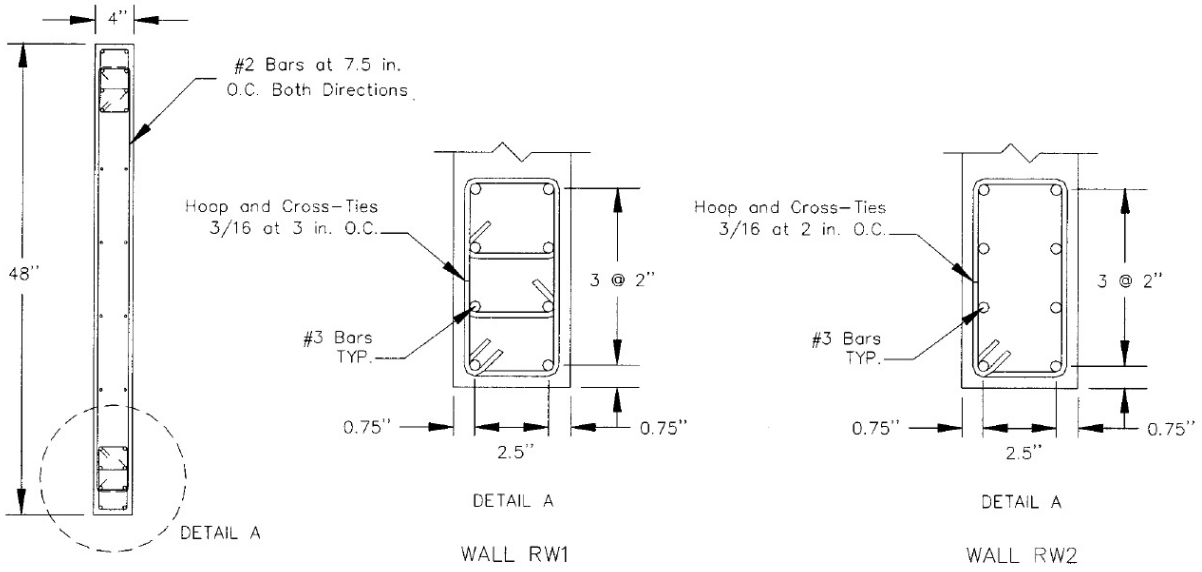

Figure 5.5 Walls RW1 and RW2 reinforcing details (1 in. = 25.4 mm).

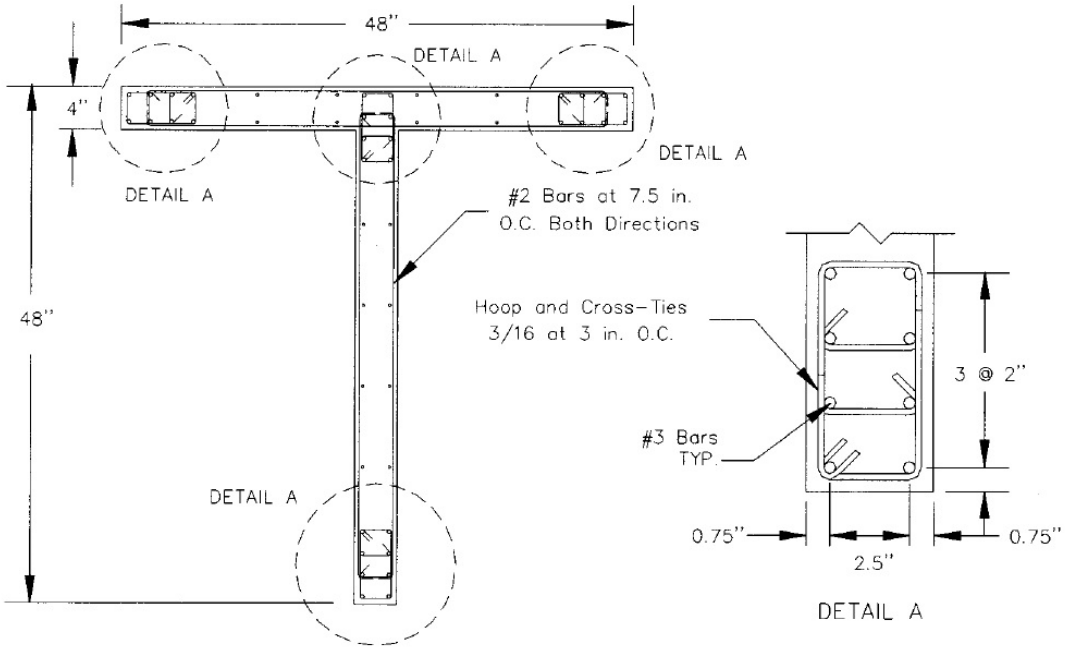

Figure 5.6 Wall TW1 reinforcing details (1 in. = 25.4 mm).

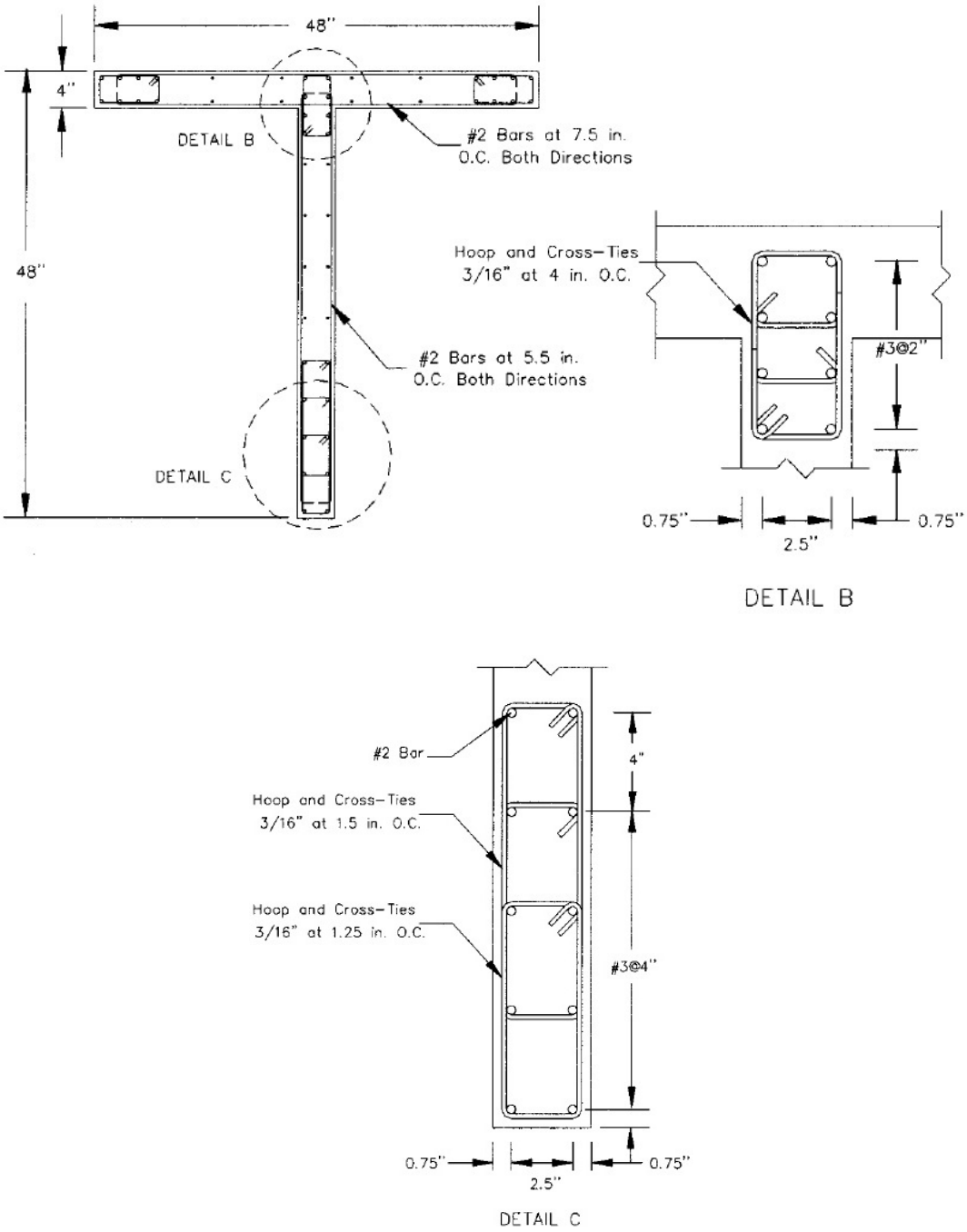

Figure 5.7 Wall TW2 reinforcing details (1 in. = 25.4 mm).

Design compressive strengths were 4,000 psi (27.6 MPa); however, strengths at the time of testing ranged from 4,150 to 8,460 psi (28.7 to 58.4 MPa) with mean compressive strengths at the base of the wall specimens (0 to 3 ft; 0 to 914 mm) of 4,580, 4,925, 6,330, and 6,050 psi (31.6, 34.0, 43.6, and 41.7 MPa) for specimens RW1, RW2, TW1, and TW2, respectively. Three types of reinforcing steel were used in this study: (1) typical Grade 60 (414 MPa) deformed No. 3 (9.5 mm) bars for longitudinal reinforcement, (2) deformed No. 2 (6.4 mm) bars for uniformly

distributed horizontal and vertical web reinforcement, and (3) 3/16 in. (4.75 mm) diameter smooth wire for boundary transverse reinforcement. The boundary transverse reinforcement was heat treated to produce material properties similar to those of Grade 60 (414 MPa) reinforcing steel. For comparison between analytical and experimental strain profiles, analytical models consider measured material properties of each specimen.

The wall specimens were tested in an upright position, as shown in Figure 5.8. A specially fabricated steel load transfer assembly was used to transfer both axial and lateral loads to the wall specimen. An axial load of approximately $0.10A_g f'_c$ was applied at the top of the wall by hydraulic jacks mounted on top of the load transfer assembly. The axial stress was maintained constant throughout the duration of each test. Cyclic lateral displacements were applied to the walls by a 125 kip (556 kN) hydraulic actuator mounted horizontally to a reaction wall 12 ft (3.66 m) above the base of the wall. Out-of-plane support was provided to prevent twisting of the wall during testing.

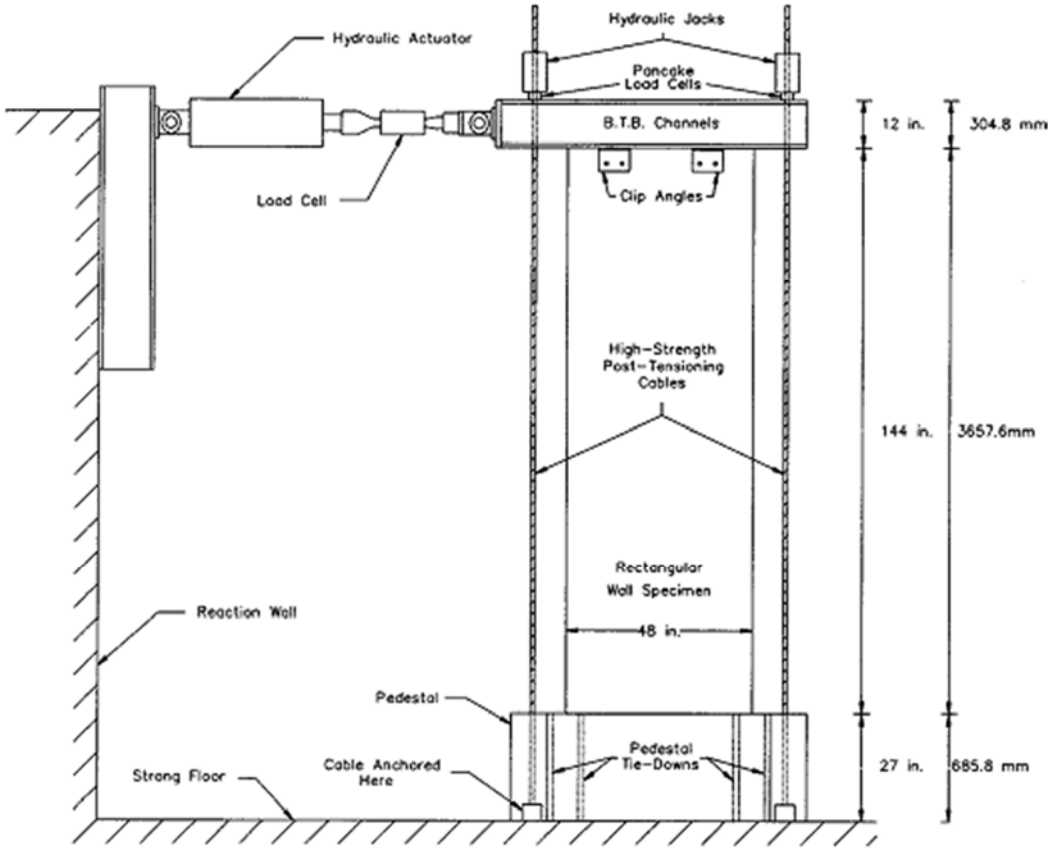

Figure 5.8 Specimen test setup – RW1 and RW2.

Figure 5.9 shows the displacement history applied to RW2. The displacement history for RW1 was similar to RW2, except that the four additional cycles at 1% and 1.5% drift were not applied after applying the first two cycles at 1.5% drift. Displacement histories for TW1 and TW2 are identical to RW2.

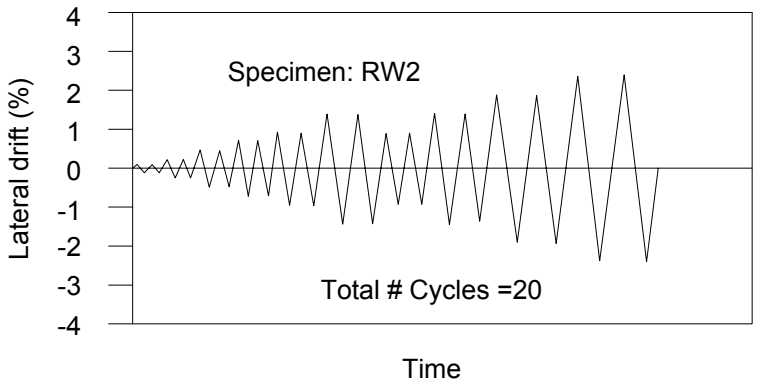

Figure 5.9 Applied displacement history.

5.3.2 Experimental and Analytical Response

Strain profiles at the base of specimens were not available for ultimate drift ratios (only available for wall TW1). In order to study the onset of out-of-plane instability, it is required to estimate this profile and three analytical approaches are followed for this purpose: nonlinear finite element model in TNO DIANA, a plastic hinge approach and direct extrapolation of strains using the experimental values at lower drifts. Figure 5.10 shows the TNO DIANA models used for this study. These models consist of curved shell elements with embedded reinforcement (full bonding), total strain crack model for concrete and Giuffré-Menegotto-Pinto (Menegotto et al. 1973, Filippou et al. 1983) material for steel. Modeling details were provided in section 2.4.

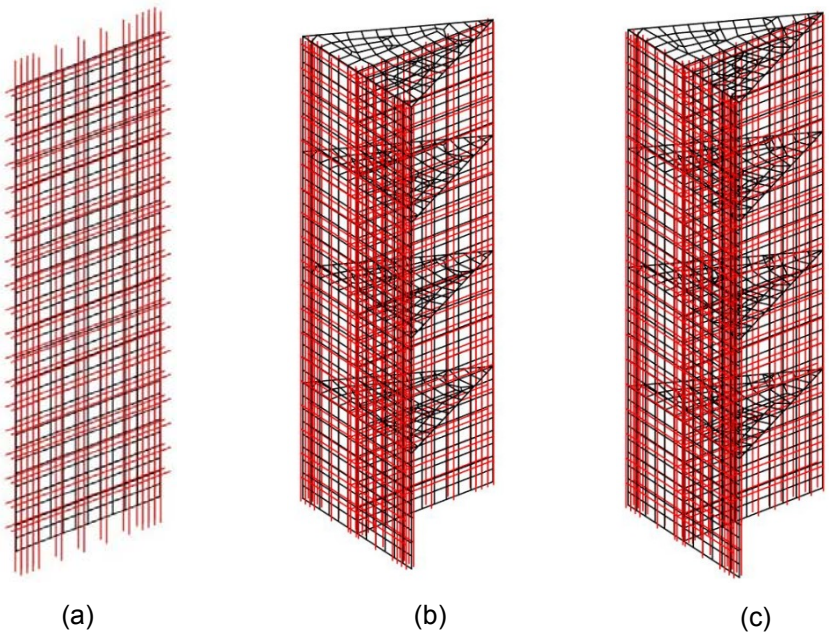

Figure 5.10 TNO DIANA finite element models, a) RW1 and RW2, b) TW1 and c) TW2.

The plastic hinge approach requires estimation of the moment-curvature relations at the wall base. These curves are obtained using the software XTRACT based on material properties indicated in section 5.3.1. Figure 5.11 presents the relation for each wall specimen.

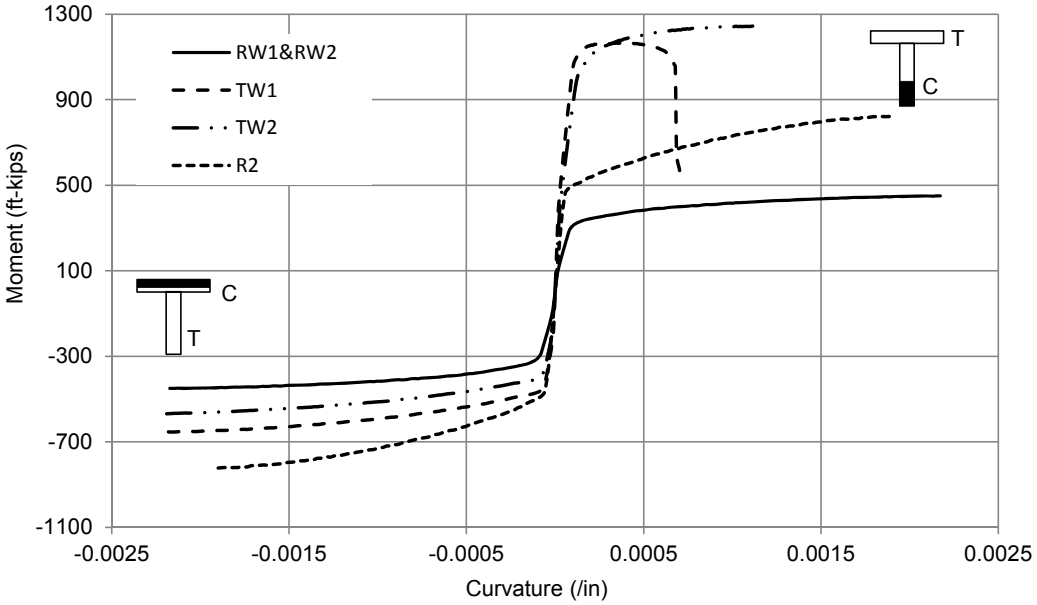

Figure 5.11 Moment-curvature diagrams for specimens obtained from XTRACT (1 in. = 25.4 mm; 1 ft-kips = 1.36 kN-m).

5.3.2.1 Rectangular Specimen RW1

Figure 5.12 shows the experimental lateral load versus lateral displacement curve. For comparison, the analytical curve obtained from the TNO DIANA model is also shown. There is a good agreement between the experimental curve and the curve obtained from finite elements analysis.

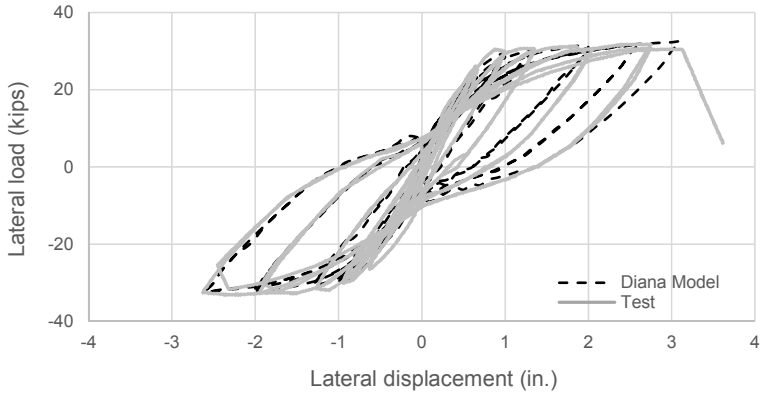

Figure 5.12 Experimental and analytical response for wall RW1 (1 kip = 4.45 kN, 1 in. = 25.4 mm).

Figure 5.13 presents a comparison between experimental and TNO DIANA analytical strain profiles for three drift ratios: 1.0%, 1.5% and 2.0%. As indicated before, the experimental strain profile at the ultimate drift ratio of 2.5% is not available and an analytical estimation will be

considered. One advantage of finite element models is that plane sections do not need to remain plane. From Figure 5.13, the finite element model underestimates the maximum tensile strain at the wall boundary for all drift ratios. This is somewhat unexpected given that slip of reinforcement from the foundation is not accounted for in the analytical model.

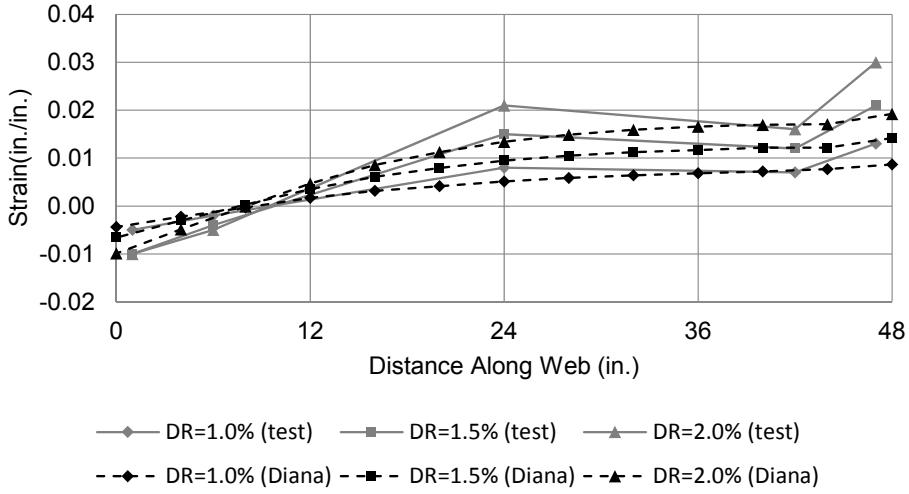

Figure 5.13 Measured strain versus analysis strain distribution from TNO DIANA nonlinear finite element model (1 in. = 25.4 mm).

Figure 5.14 compares measured and calculated strain profiles using the plastic hinge approach according to Equation (5.4), considering a plastic hinge length of $l_w/2$, where l_w is the wall length. The approach considers that plane sections remains plane. However, the analysis strain distribution shows good accuracy with respect to the experimental values, and for this case there is no underestimation of the maximum tensile strain at the wall boundary. Figure 5.14 also includes an analytical estimation of the strain profile at the ultimate drift ratio of 2.5%. For this case the maximum tensile strain at the wall boundary is close to 0.04.

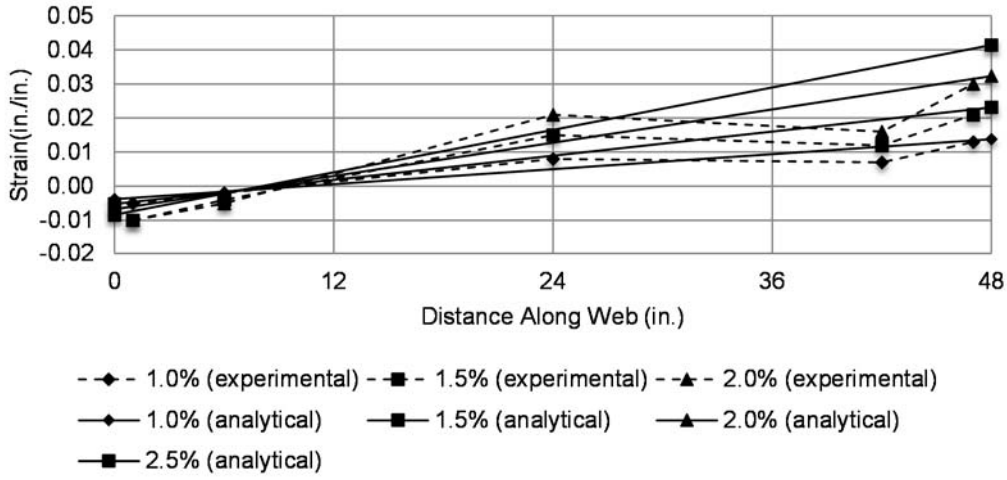

Figure 5.14 Measured strain versus analysis strain distribution plastic hinge approach l_p=0.5l_w (1 in. = 25.4 mm).

A third approach to estimate the maximum tensile strain at the wall boundary is extrapolation from experimental values obtained at lower drift ratios. Figure 5.15 shows the maximum tensile strain at the wall boundary versus drift ratio, analytical values up to 2% drift ratio and a second order polynomial fit, which allows to extrapolate the strain at a higher drift ratio. From Figure 5.15, the estimated maximum tensile strain at the ultimate drift ratio of 2.5% is slightly higher than 0.04, which approximately matches the value previously obtained from the plastic hinge approach (Figure 5.14).

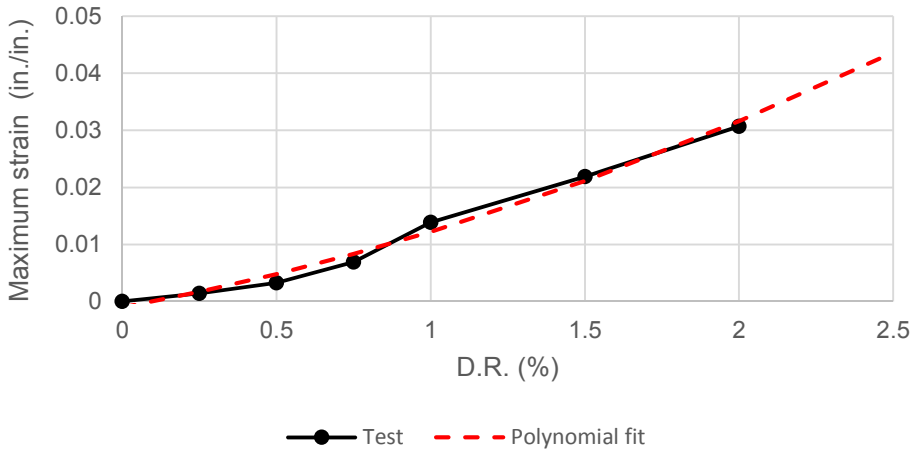

Figure 5.15 Maximum tensile strain at wall boundary versus drift ratio, test values and polynomial fit.

5.3.2.2 Rectangular Specimen RW2

Figure 5.16 shows the experimental lateral load versus lateral displacement curve and the curve obtained from finite element analysis. The analytical curve is an excellent representation of the response measured during the test.

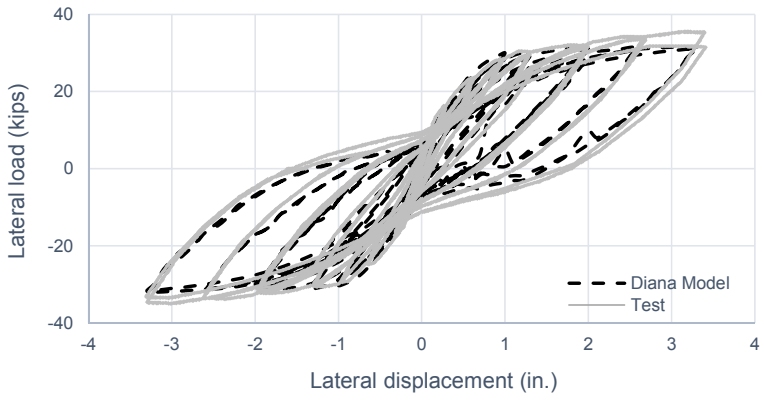

Figure 5.16 Experimental and analytical response for wall RW2 (1 kip = 4.45 kN, 1 in. = 25.4 mm).

The vertical strain profile at the wall base is first estimated from the finite element model. Figure 5.17 shows a comparison between experimental an analytical strain profiles (obtained from the TNO DIANA model) at three drift ratios: 1%, 1.5% and 2%. Strains at the ultimate drift ratio were not available and an analytical estimation will be used to evaluate the onset of out-of-plane instability.

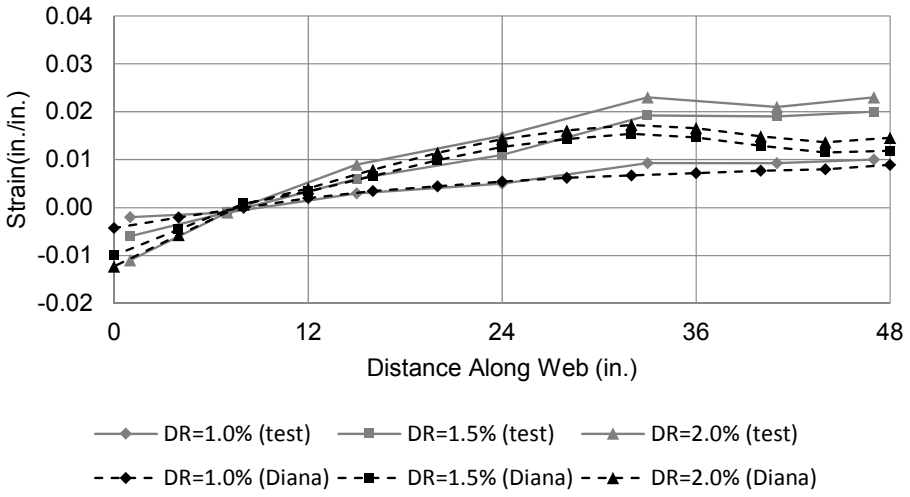

Figure 5.17 Measured strain versus analysis strain distribution from TNO DIANA nonlinear finite element model (1 in. = 25.4 mm).

From Figure 5.17 it is observed that the finite element model underestimates the maximum tensile strain at the wall boundary for all drift ratios. Finite element analysis of specimen RW1 also showed similar behavior. The second approach used to estimate the strain demand at the wall base is the plastic hinge approach. Figure 5.18 compares measured and calculated strain profiles using the plastic hinge approach with a plastic hinge length equal to $l_w/2$, where l_w is the wall length. The approach overestimates the maximum tensile strain at the wall boundary for all drift ratios. Figure 5.18 also shows an analytical estimation of the strain profile at the ultimate drift ratio of 2.5%. For this case, the maximum tensile strain is 0.04 at the wall boundary.

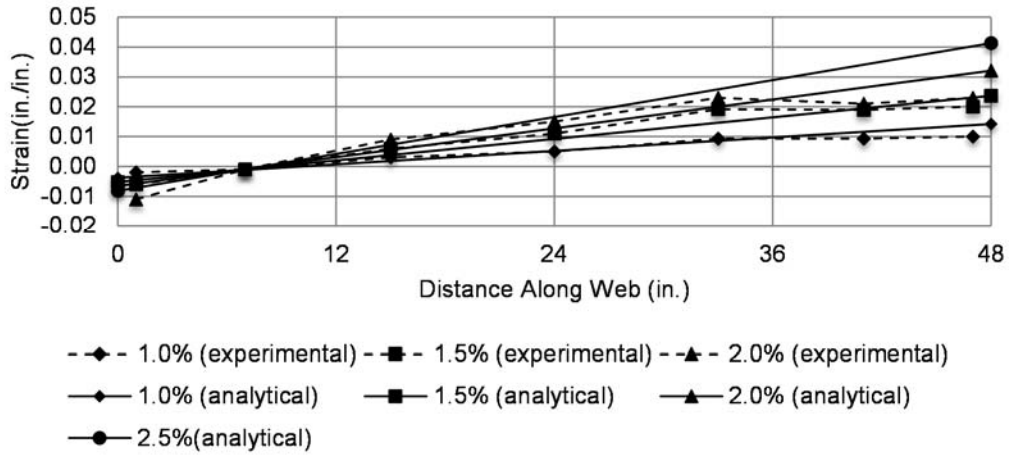

Figure 5.18 Measured strain versus analysis strain distribution plastic hinge approach $l_p = 0.5\ l_w$ (1 in. = 25.4 mm).

Finally, according to Figure 5.19, the estimated value for the maximum tensile strain at the wall boundary obtained from extrapolation of data at lower drift ratios is 0.035.

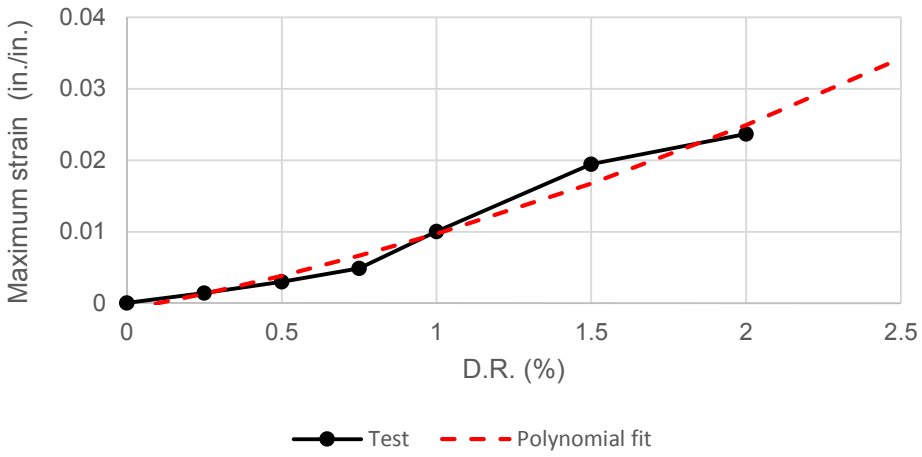

Figure 5.19 Maximum tensile strain at wall boundary versus drift ratio, test values and polynomial fit.

5.3.2.3 T-shaped Specimen TW1

Even though measured strains at the ultimate drift ratio of 1.5% were available for this specimen, analytical estimations of strain profiles are obtained in order to evaluate the accuracy of the models used for these studies. Figure 5.20 shows the experimental cyclic response, where positive load/displacement corresponds to the case of wall flange in compression. The analytical response obtained from the finite element model is also shown. For this case, the large spacing of hoops and crossties at the wall stem (Figure 5.6) allowed buckling of all boundary bars (and some web bars) to occur, which caused brittle failure. The finite element model considers full bonding between reinforcement bars and concrete and does not model bar buckling. This can explain why the analytical response does not fit well the experimental response for this particular wall.

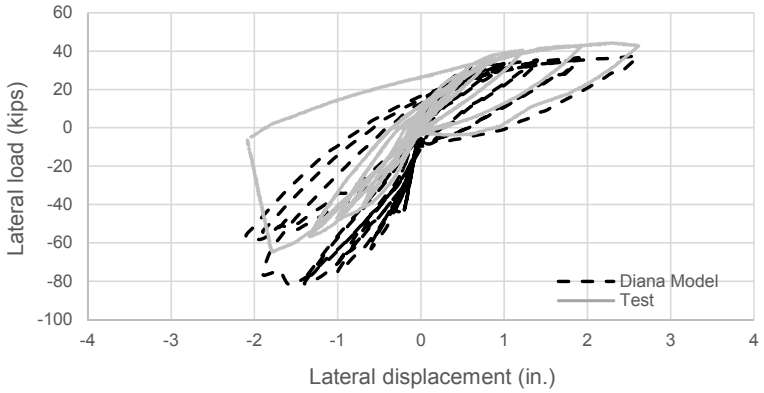

Figure 5.20 Experimental and analytical response for wall TW1 (1 kip = 4.45 kN, 1 in. = 25.4 mm).

Figure 5.21 shows a comparison between measured strain profiles and analysis estimations obtained from the nonlinear finite element model. There is a good estimation of the strain profile at the wall base for all drift ratio.

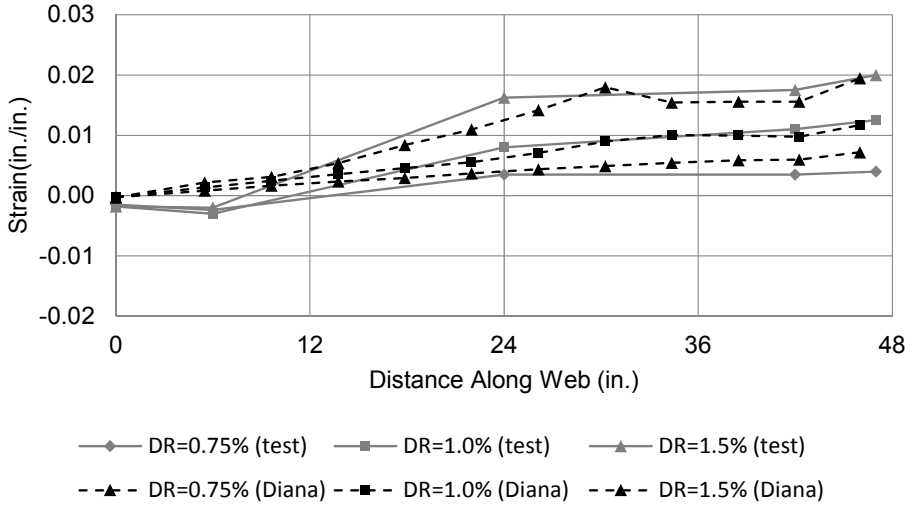

(a)

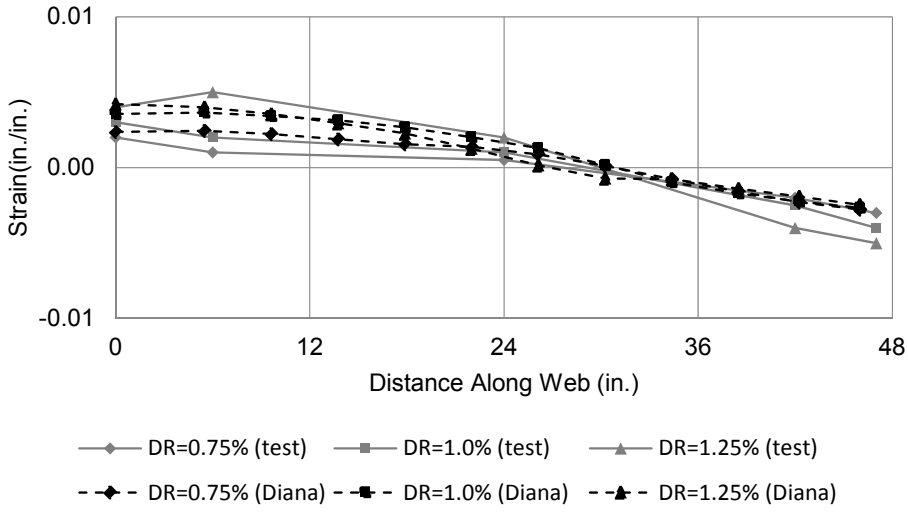

(b)

Figure 5.21 Measured strain versus analysis strain distribution from TNO DIANA nonlinear finite element model, a) flange in compression, b) flange in tension (1 in. = 25.4 mm).

Figure 5.22 compares measured and calculated strain profiles using the plastic hinge approach (l_p=0.5l_w), according to section 5.2. Even though the accuracy of the analytical strain distribution is not as good as for the case of rectangular walls and it seems to overestimate the maximum tensile strain at the wall stem for all drift levels, the approximation is acceptable considering the simplicity of the model. This over-prediction of the strain profile may be partially attributable to the assumption in the analytical model that the entire flange is effective in both compression and tension.

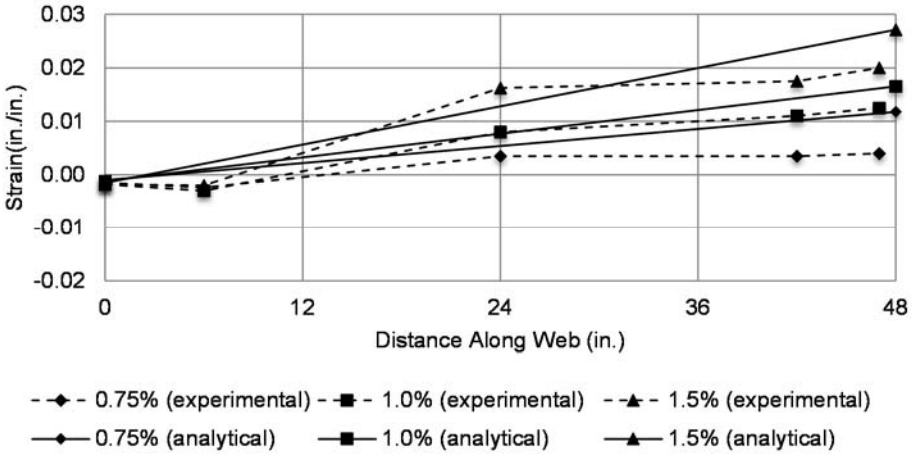

(a)

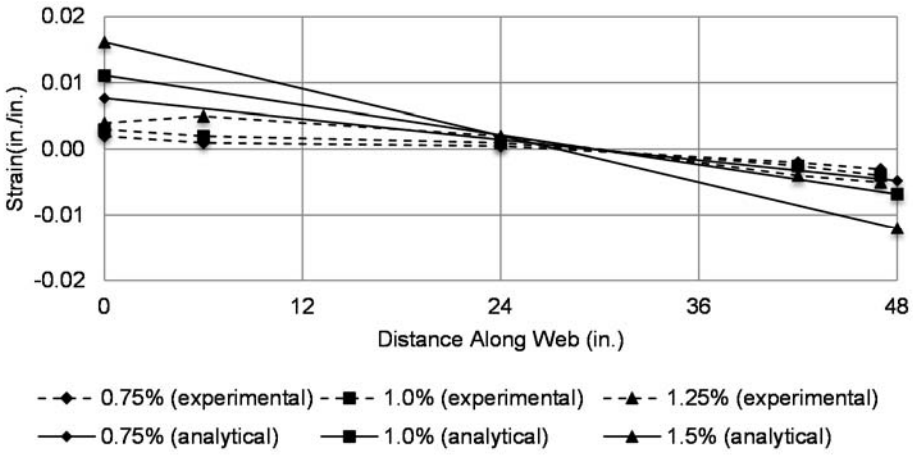

(b)

Figure 5.22 Experimental and plastic hinge (l_p = 0.5 l_w) strain profiles for wall TW1 (a) flange in compression; (b) flange in tension (1 in. = 25.4 mm).

5.3.2.4 T-shaped Specimen TW2

Figure 5.23 shows the experimental and analytical (finite element model) lateral load versus lateral displacement response for wall TW2.

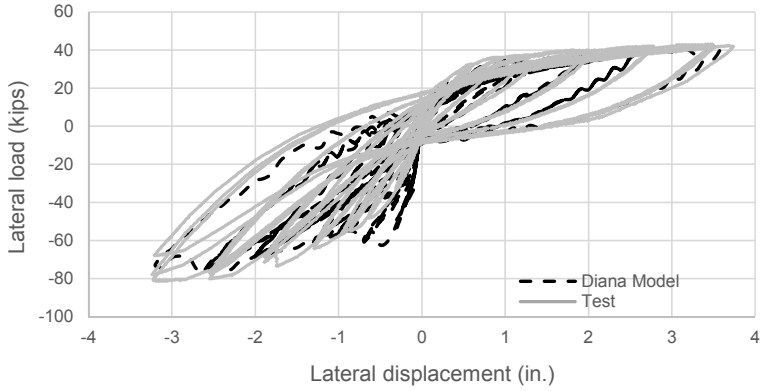

Figure 5.23 Experimental and analytical response for wall TW1 (1 kip = 4.45 kN, 1 in. = 25.4 mm).

Figure 5.24 compares the measured strain profiles and analysis estimations obtained from the nonlinear finite element model. There is a small underestimation of the maximum tensile strain at the wall stem when the flange is in compression for all drift ratios.

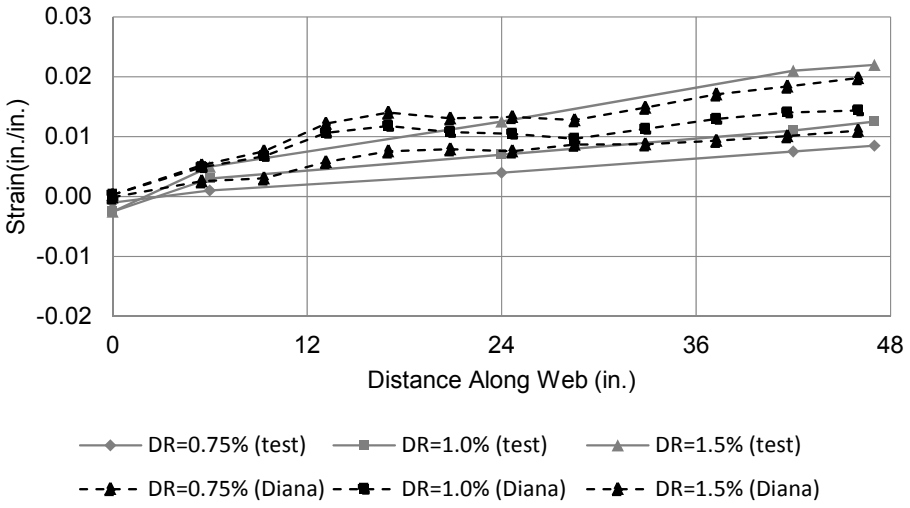

(a)

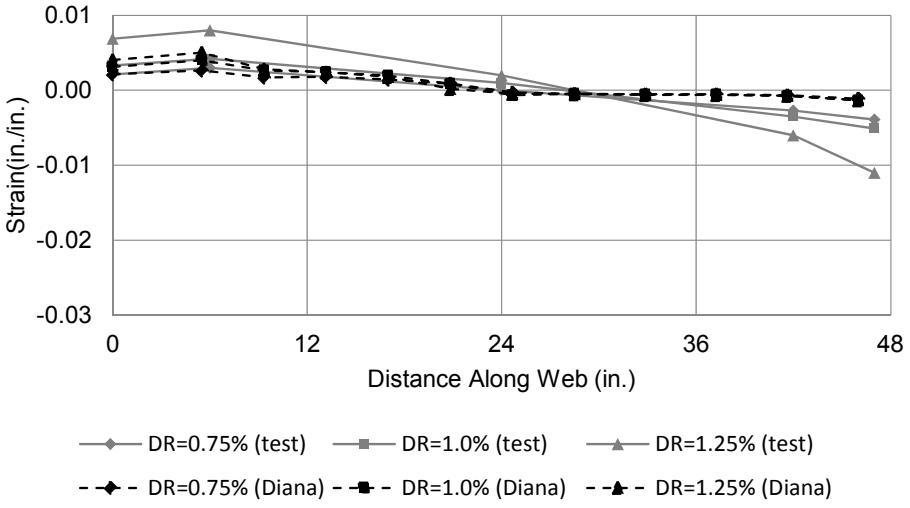

(b)

Figure 5.24 Measured strain versus analysis strain distribution from TNO DIANA nonlinear finite element model, a) flange in compression, b) flange in tension (1 in. = 25.4 mm).

Figure 5.25 compares measured and calculated strain profiles using the plastic hinge approach (l_p=0.5l_w). The analysis strain distribution shows good accuracy with respect to the experimental values when the flange is in compression. For the case of flange in tension, there is a slight overestimation of the maximum tensile strain for all drift levels. The plastic hinge approach gives remarkable predictions of strain profiles considering the simplicity of its formulation.

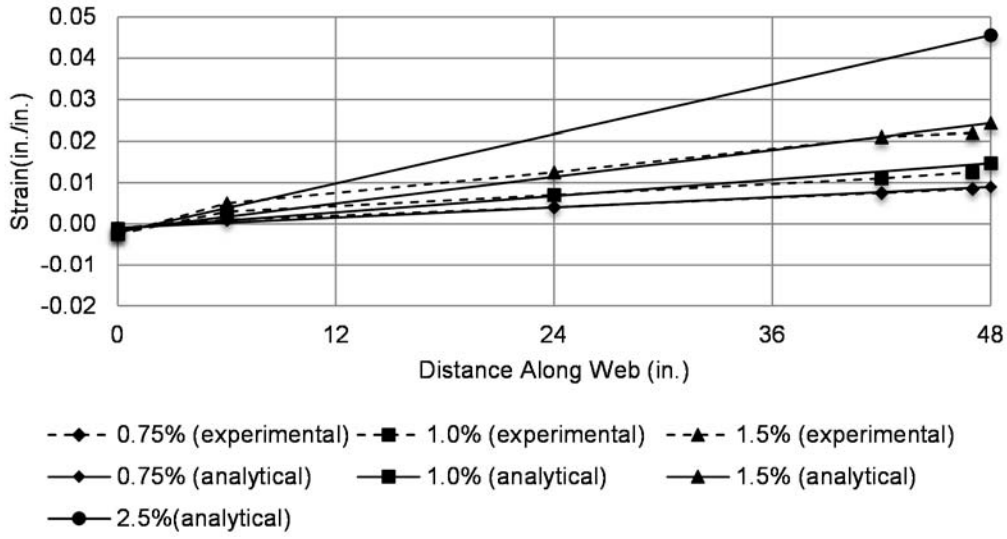

(a)

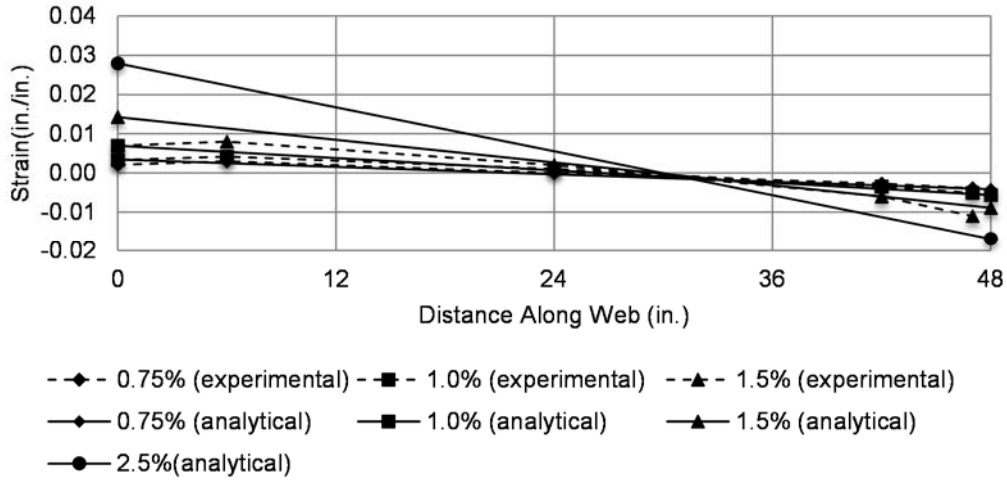

(b)

Figure 5.25 Experimental and plastic hinge (l_p = 0.5 l_w) strain profiles for wall TW2 (a) flange in compression; (b) flange in tension (1 in. = 25.4 mm).

Figure 5.25 also includes an estimation of the strain profile at 2.5% drift ratio, using the plastic hinge approach. The estimated maximum tensile strain at the wall stem is close to 0.05.

Figure 5.26 shows the extrapolation of the maximum tensile strain at the wall stem from the data obtained at lower drift ratios. At 2.5% drift ratio, the strain is slightly over 0.05. Thomsen and Wallace reported drift ratios up to 3% for this specimen, for which the estimated value of the tensile strain is close to 0.07.

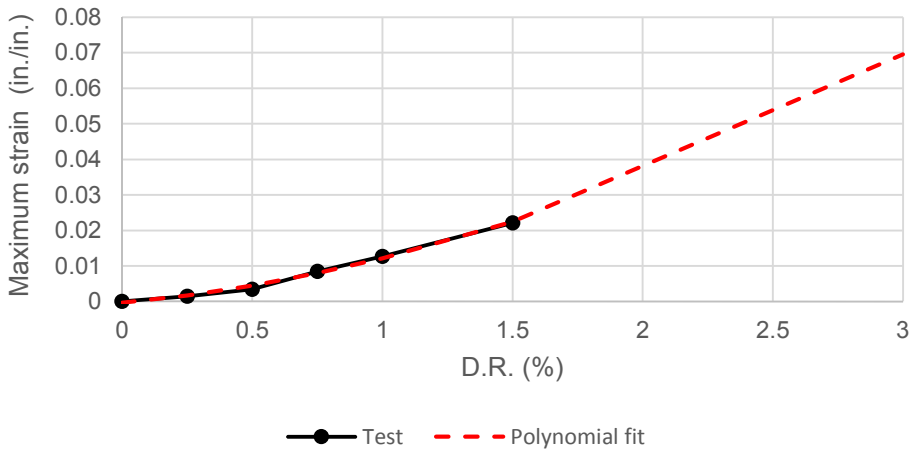

Figure 5.26 Maximum tensile strain at wall boundary versus drift ratio, test values and polynomial fit.

5.3.3 Evaluation of the Onset of Out-of-Plane Instability

Figure 5.27 shows some pictures of the damaged boundary regions for all four specimens.

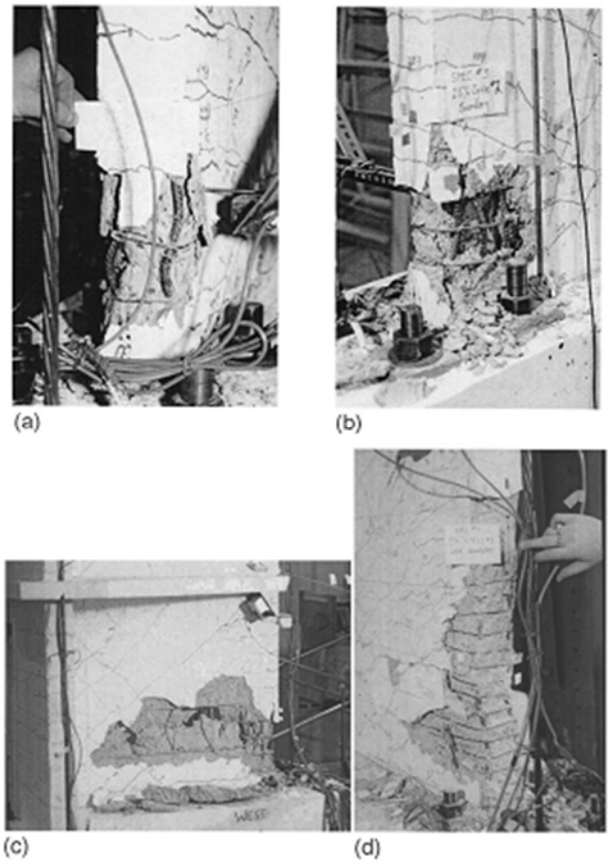

Figure 5.27 Specimens failure, after Thomsen and Wallace (1995) (a) RW1 (b) RW2 (c) TW1 (d) TW2.

Some highlights of the response observed during the tests for these four specimens are now presented (Thomsen and Wallace, 2004). For specimen RW1, two cycles at 2.0% lateral drift were completed prior to significant loss in lateral load capacity at approximately 2.5% drift due to buckling of longitudinal reinforcement. This failure mode was anticipated given the relatively large spacing ($8d_b$) of the hoops and crossties at the wall boundary. Behavior of specimen RW2 was very similar to RW1, except lateral load capacity was maintained even after two complete cycles at 2.5% lateral drift. The improved behavior is attributed to the closer spacing of the hoops ($5.33d_b$) at the wall boundaries, which delayed the onset of buckling of the longitudinal reinforcement. ACI 318-99 uses a maximum hoop/crosstie spacing of $6d_b$ to suppress buckling of vertical bars. Spacing of special boundary element transverse reinforcement exceeded this limit for RW1 and TW1 ($8d_b$), was slightly less than this for RW2 ($5.33d_b$), and considerably less than this for TW2 ($4d_b$). For TW1, as a result of the poor detailing provided at the boundary of the web opposite the flange, the lateral load capacity dropped suddenly at an applied lateral drift of approximately 1.25%. The loss in lateral load capacity is attributed to the large spacing of transverse reinforcement used at the wall boundary, which was inadequate to suppress buckling of the longitudinal reinforcement. Transverse reinforcement at the boundary opposite the flange was placed at a closer spacing and over an increased depth of the cross section for Specimen TW2 compared with specimen TW1 and it did not experience a loss of lateral load capacity until the second and third cycles at a lateral drift level of approximately 2.5%. The test was stopped midway through the first cycle at a lateral drift level of 3.0%. Under displacements that cause compression in the wall web, the entire web boundary element began to experience an out-of-plane stability failure at approximately 0.75% lateral drift.

The most important parameter for the evaluation of the onset of out-of-plane instability is the maximum tensile strain at the base of the wall boundary required to buckle it during load reversal. The simplified mechanics of global instability presented in section 2.2 was derived for a prismatic column, fixed at the top and bottom, subjected to uniform tension/compression cycles. As a first step in this buckling evaluation, OpenSees models of isolated boundary elements are used to estimate the tensile strain prior buckling. Each boundary element is modeled using ten (RW1 and RW2) or twelve (TW1 and TW2) nonlinear beam-column elements with fibers, force-based formulation and corotational transformation for nonlinear geometry. Nonlinear material models are those described in sections 2.3.4, 2.3.5 and 2.3.6. Material regularization is considered according to section 2.3.5. Axial forces are applied as point forces at the nodes. Rectangular specimens RW1 and RW2 are supported at the base and top only. A fixed support at the base and a roller support at the top are reasonable analysis assumptions. The case of T-shaped walls is different. The slabs provide intermediate lateral support and this is considered for analysis. Figure 5.28 depicts the OpenSees models, where the axial force profile along the height is also shown.

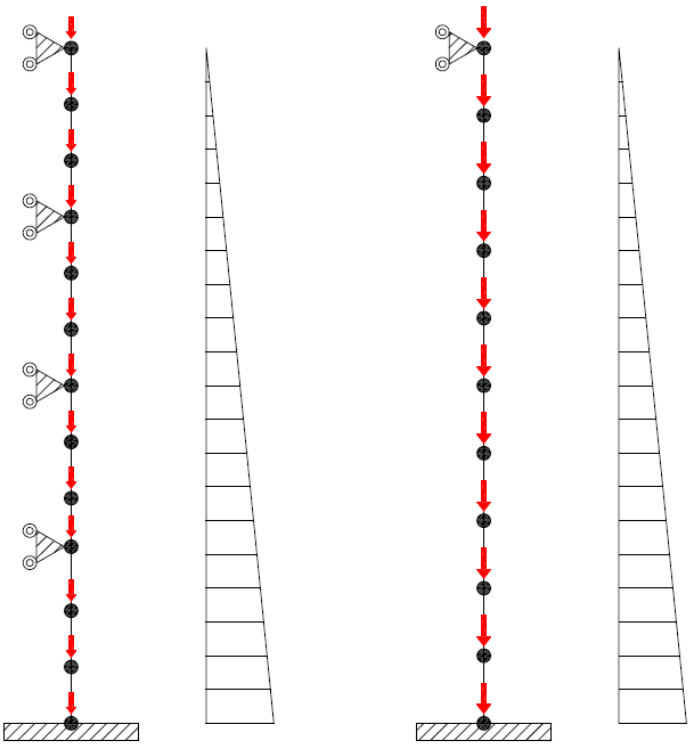

(a) (b)

Figure 5.28 OpenSees models for slender wall boundaries: a) TW1 and TW2, b) RW1 and RW2.

The boundary elements are analyzed considering incremental tension cycles similar to those shown in Figure 4.3. The peak vertical displacement is increased in 0.1 in. increments until reaching buckling failure during load reversal. Strain profiles at ultimate drift ratios, analytically estimated in sections 5.3.2.1 and 5.3.2.2, showed that compressive strain at wall boundaries is higher than the concrete spalling strain. Therefore, this buckling analysis is performed with the core section only (2.5 x 6 in. for specimens RW1, RW2 and TW1, 2.5 x 16 in. for specimen TW2). Figure 5.29 shows the instability analysis results for wall RW1. Figure 5.29a shows the average strain versus axial force at the base, Figure 5.29b is the tensile strain normalized by the yielding strain over the height at the peak prior buckling, Figure 5.29c is the axial load normalized by its maximum value over the height and Figure 5.29d is the OpenSees buckled shape. The red line represents the theoretical buckled shape from the simplified mechanics (fixed-fixed support and uniform strain profile), shown for comparison. Figure 5.30 to Figure 5.32 present the same information for the other specimens.

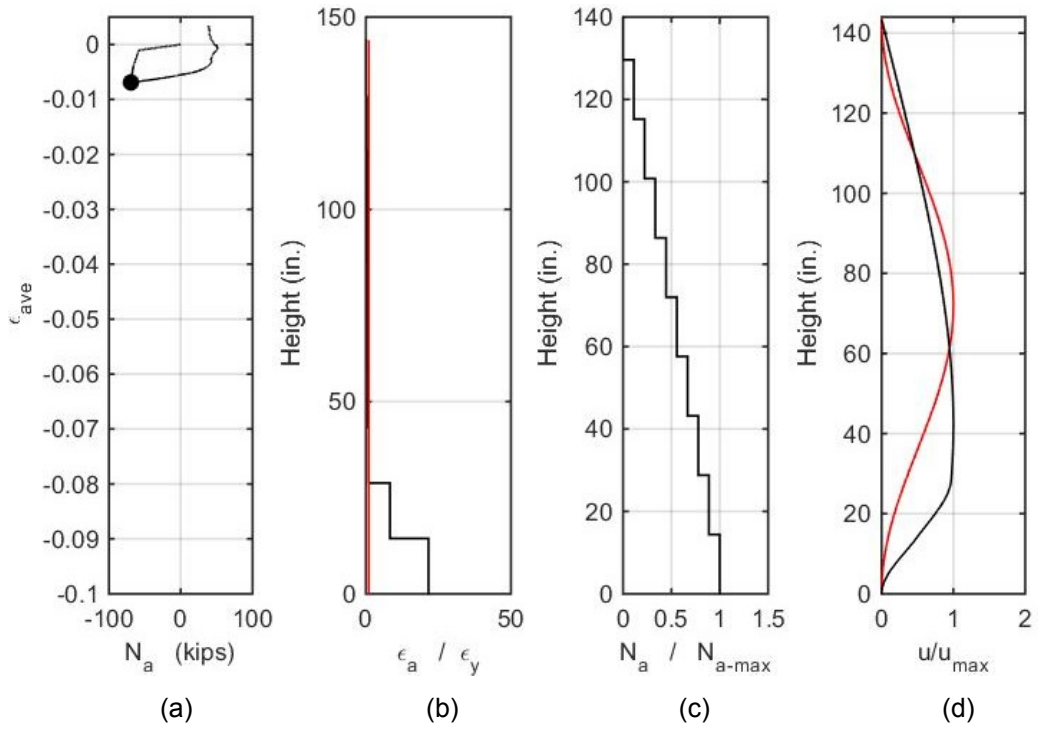

Figure 5.29 **Boundary element of wall RW1: a) average axial strain versus axial force at the base, b) normalized axial strain, c) normalized axial force, d) normalized buckled shape.**

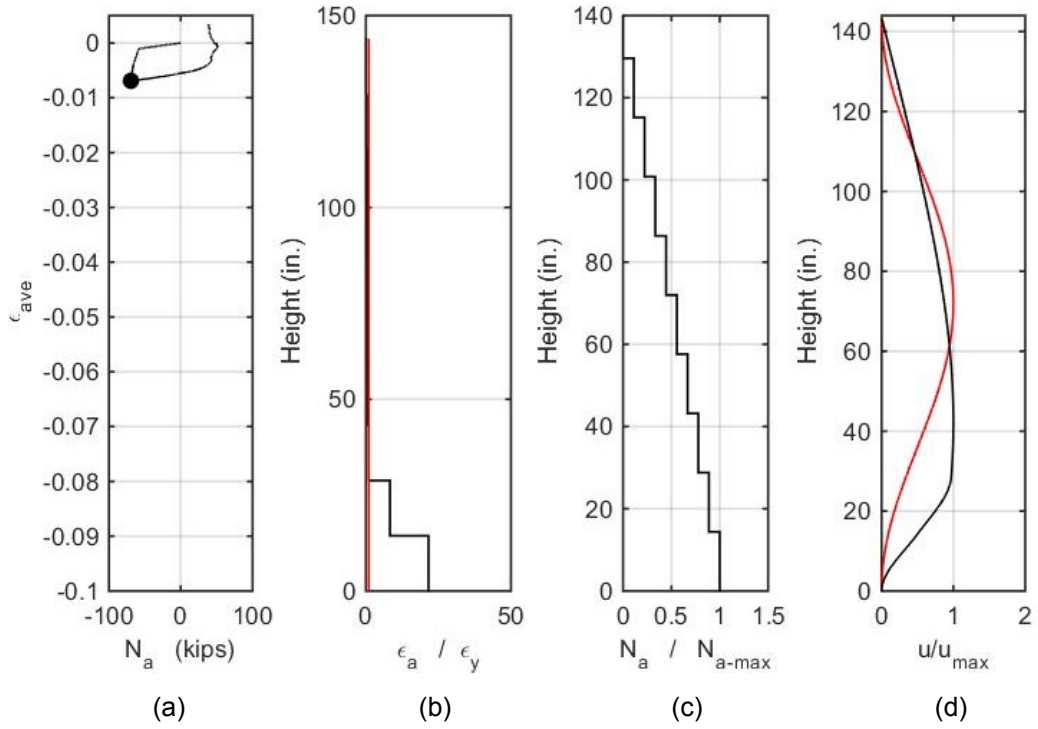

Figure 5.30 **Boundary element of wall RW2: a) average axial strain versus axial force at the base, b) normalized axial strain, c) normalized axial force, d) normalized buckled shape.**

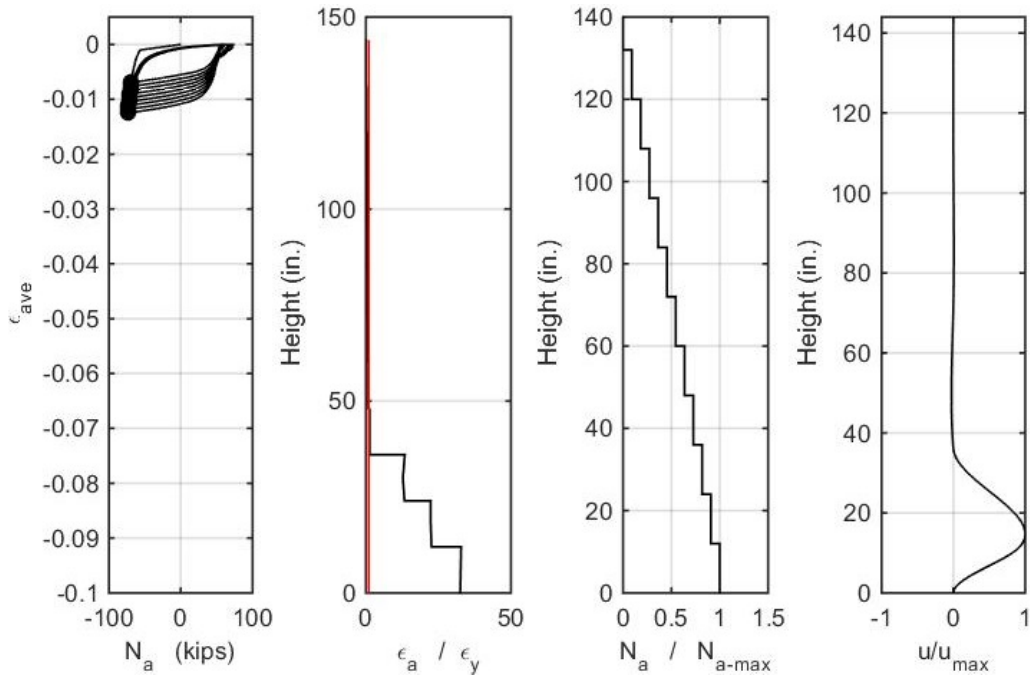

(a) (b) (c) (d)

Figure 5.31 Boundary element of wall TW1: a) average axial strain versus axial force at the base, b) normalized axial strain, c) normalized axial force, d) normalized buckled shape.

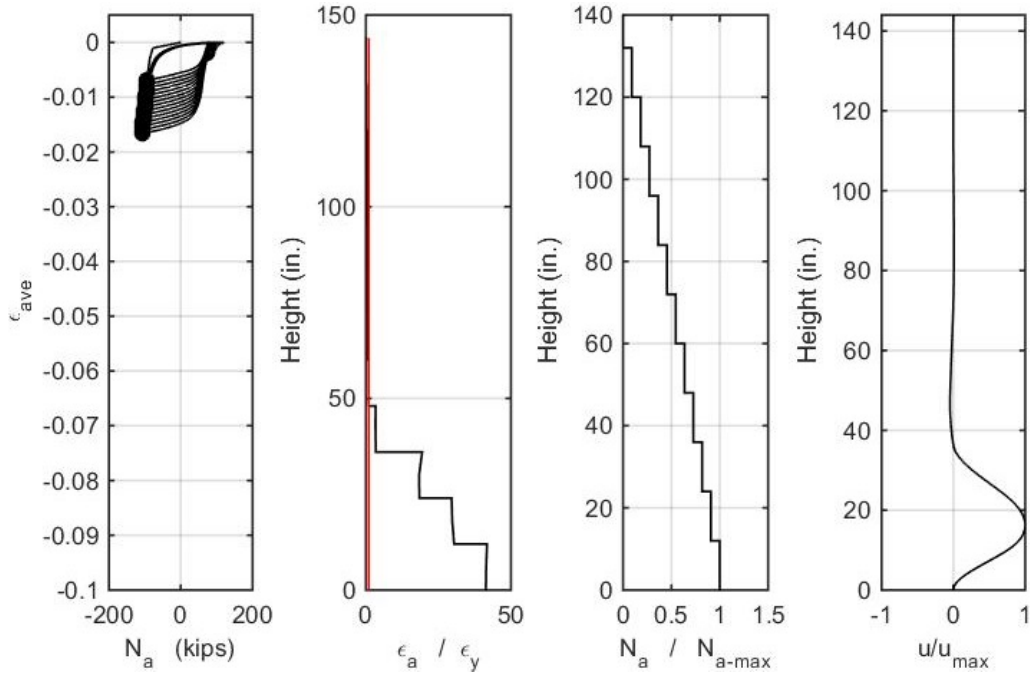

(a) (b) (c) (d)

Figure 5.32 Boundary element of wall TW2: a) average axial strain versus axial force at the base, b) normalized axial strain, c) normalized axial force, d) normalized buckled shape.

For the evaluation of the onset of out-of-plane instability, it is required to compare first the maximum tensile strain at the base of the wall boundary measured (or estimated) from tests and the value needed to buckle the element according to the OpenSees modeling (ϵ_{sm}). For walls RW1 and RW2, $\epsilon_{sm} \approx 22\epsilon_y$, which is close to 0.046. Estimated strains are 0.04 for these walls, lower but very close to the required value to buckle the wall. However, buckling was not observed for these two cases, and buckling of longitudinal reinforcement triggered the failure, probably due to the spacing of the hoops and crossties at the wall boundaries. For wall TW1, $\epsilon_{sm} \approx 30\epsilon_y$ or 0.06. The maximum measured strain was 0.02, not close to the required value to buckle the wall. For this case, early failure was triggered by poor detailing of confinement steel at the wall stem. For wall TW2, $\epsilon_{sm} \approx 40\epsilon_y$ or 0.08. The estimated value at the ultimate drift ratio close to 3% is 0.07. This value is very close to the required strain to buckle the wall boundary and this was the failure mode observed during the test (Figure 5.27d).

For the T-shaped walls, where slabs were provided at intermediate points along the height, the analytical buckled shape (Figure 5.31d and Figure 5.32d) indicates that buckling occurs at the first story and the shape is similar to the theoretical solution obtained from analysis of the first story only under fixed-fixed support conditions. This is also observed in the damage region of TW2 shown in Figure 5.27d. The strain demand along the first story height is not constant, as shown in Figure 5.32b, but neglecting the strain variability it is possible to estimate ϵ_{sm} directly from the simplified buckling mechanics considering that the cover has been spalled off. Table 5.1 presents the material and section properties for buckling evaluation according to the simplified mechanics. Table 5.2 presents the results of this analysis for T-shaped walls.

Table 5.1 Properties for buckling calculation (1 in. = 25.4 mm; 1 psi = 0.007 MPa).

Wall	Material Properties, psi		Dimensions, in.						BE Area of Longitudinal Steel A_s, in.^{2}
	f'_c	f_y	Width, b	Length, l_w	Height, H	h_u	BE Length, l_b	Stirrup Clear Cover, c	
RW1	4,580	61,250	4.0	48	144	144	8	0.4	0.88
RW2	4,925	61,250	4.0	48	144	144	8	0.4	0.88
TW1	6,330	61,250	4.0	48	144	32	8	0.4	0.88
TW2	6,050	61,250	4.0	48	144	32	18	0.4	0.98

Table 5.2 Analysis of T-shaped walls from simplified mechanics, cover spalled off.

Wall	Wall Slenderness b_c/kh_u	ρ	m	ξ	κ	ϵ_{sm}
TW1	0.18	4%	0.40	0.14	1	**0.05**
TW2	0.18	2%	0.20	0.20	1	**0.07**

Values of ϵ_{sm} estimated from the simplified mechanics are 0.05 for TW1 and 0.07 for wall TW2. These values are similar to those obtained from OpenSees modeling (0.06 and 0.08). Therefore, the simplified mechanics estimates ϵ_{sm} with a reasonable accuracy (in comparison with more sophisticated models) when the support conditions can be assumed as fixed and the strain profile along the height is constant or close to constant. Now, the question is if the buckling theory can be used in a case where the supports are not fixed-fixed and the strain profiles deviate

appreciably from constrant strain. This is the case of the rectangular walls RW1 and RW2. If the theory is applied directly assuming constant strain along the full height (144 in.), the estimated values of ϵ_{sm} are quite low, as shown in Table 5.3.

Table 5.3 Analysis of rectangular walls from simplified mechanics, cover spalled off.

Wall	Wall Slenderness bc/khu	ρ	m	ξ	κ	εsm
RW1	0.03	4%	0.55	0.11	1	**0.006**
RW2	0.03	4%	0.51	0.12	1	**0.006**

Values of ϵ_{sm} estimated in Table 5.3 are not realistic because the strain profile is not even close to constant along the wall full height. The influence of the axial force profile along the height in the onset of out-of-plane instability was studied in section 4.2, and Figure 4.9 proposed a linear relation to increase the value of ϵ_{sm} obtained from the simplified mechanics is such cases. However, the analyzed cases were several axial force profiles in columns with fixed supports at the top and bottom. Neglecting the change in ϵ_{sm} caused by the top support, it is possible to apply Figure 4.9 directly in Table 5.3, and the estimated value for ϵ_{sm} is $5 \cdot 0.006 = 0.03$. This value is a conservative estimation of $\epsilon_{sm} = 0.045$, obtained from the OpenSees modeling with the proper boundary conditions. This analysis suggests that Figure 4.9 can be used to obtain a conservative estimation of ϵ_{sm} even for cases where rotation at the top is not restrained.

5.4 PORTLAND CEMENT ASSOCIATION WALL TESTS

5.4.1 Experimental Program

Oesterle et al. (1976) conducted a combined experimental and analytical investigation to develop design criteria for reinforced concrete structural walls in earthquake resistant buildings. The primary purpose of the investigation was to determine the ductility, energy dissipation and strength of the walls. As a part of the experimental program, reversing loads were applied to isolated walls. The results of nine tests were presented. One of the rectangular specimens (R2) experienced out of plane buckling (after thirty-five loading cycles) at an average drift ratio of 2.8%. Only this case will be presented and analyzed in this section. Test specimens were approximately 1/3-scale representations of full-size walls, although no specific prototype walls were modeled. Controlled variables included in the tests were the shape of the wall cross section, the amount of main flexural reinforcement and the amount of hoop reinforcement around the main flexural reinforcement. In addition, one wall was subjected to monotonic loading and one wall was repaired and retested. Table 5.4 provides a summary of test specimen details.

Table 5.4 Summary of test specimens.

Specimen	Shape	Reinforcement (%)			
		ρ_f	ρ_h	ρ_n	ρ_s
R1	Rectangular	1.47	0.31	0.25	-
R2	Rectangular	4.00	0.31	0.25	2.07
B1	Barbell	1.11	0.31	0.29	-
B3	Barbell	1.11	0.31	0.29	1.28
B4 (monotonic loading)	Barbell	1.11	0.31	0.29	1.28
B2	Barbell	3.67	0.63	0.29	-
B5	Barbell	3.67	0.63	0.29	1.35
B5R (repaired specimen)	Barbell	3.67	0.63	0.29	1.35
F1	Flanged	3.89	0.71	0.3	-

Where:

- ρ_f Ratio of main flexural reinforcement area to gross concrete area of boundary element
- ρ_h Ratio of horizontal shear reinforcement area to gross concrete area of a vertical section of wall web
- ρ_n Ratio of vertical web reinforcement area to gross concrete area of a horizontal section of wall web
- ρ_s Ratio of effective volume of confinement reinforcement to the volume of core in accordance with Equation A.4 of ACI 318-71

Figure 5.33 shows the dimensions of test specimens.

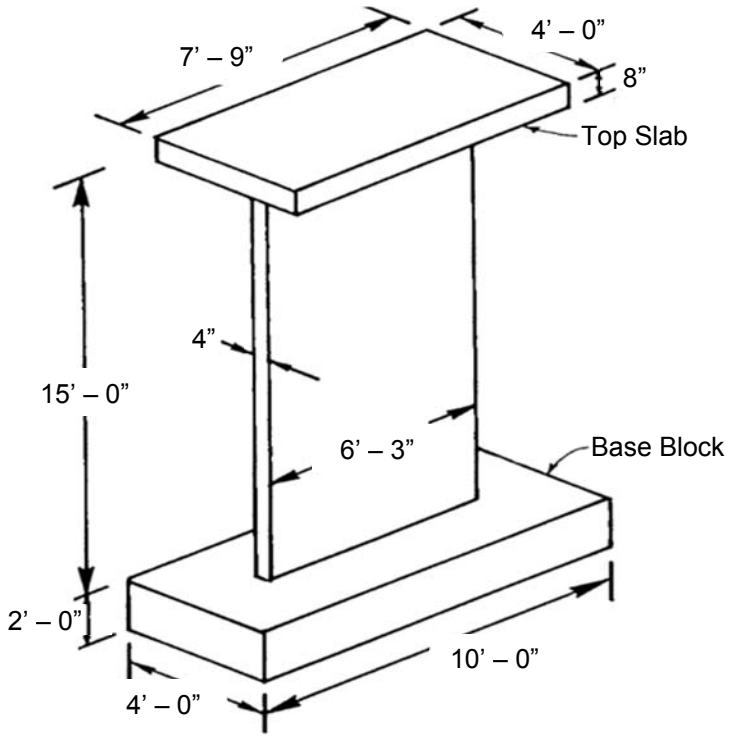

Figure 5.33 Nominal dimensions of test specimens with rectangular cross section (1 ft = 0.30 m).

In proportioning the walls, the design moment was calculated following procedures in the ACI Building Code. Strain hardening of the steel was neglected. Horizontal shear reinforcement was provided so that the calculated design moment would be developed. Shear reinforcement was provided to satisfy the ACI Building Code. Design yield stress of the steel was 60 ksi (414 MPa) and design concrete strength was 6,000 psi (41.4 MPa). The test specimens were constructed in six vertical lifts. Each specimen was loaded as a vertical cantilever with forces applied through the top slab. The test specimens were loaded in a series of increments. Each increment consisted of three complete reversed cycles. About three increments of force were applied prior to initial yielding. Subsequent to initial yielding, loading was controlled by deflections in 1 in. increments. Free vibration tests were conducted at selected stages as the number and magnitude of loading increments applied to the specimen increased. These tests were carried out to determine the frequency and damping characteristics of the walls. Figure 5.33 shows the overall dimensions of specimen R2. The boundary element was taken to extend 7.5 in. (191 mm) from each end of the wall. The percentage of flexural reinforcement shown in Table 5.4 was chosen to give a section moment capacity corresponding to high nominal shear stress. Nominal vertical web reinforcement provided in the wall was 0.25% of the gross concrete area of the horizontal wall section. This is the minimum amount permitted by the 1971 ACI Building Code. Once the nominal vertical reinforcement percentage were selected, bar sizes and locations were determined based on modeling and construction requirements. The moment capacity of the section was calculated according to Section 10.2 of the 1971 ACI Building Code. Design yield stress of the steel was taken as 60 ksi, and design concrete strength was taken as 6,000 psi. Strain hardening of the steel was neglected for section design. The vertical reinforcement was continuous from the base block

to the bottom of the top slab. The vertical bars were lap spliced with the top slab bars in the top 32 in. (0.81 m) of the wall. Horizontal shear reinforcement was designed to develop the calculated ACI nominal moment capacity. The shear design was made according to Section 11.16 of the 1971 ACI Building Code. The horizontal reinforcement was placed at a constant spacing over the height of the wall. Horizontal steel in the boundary elements (rectangular hoop and supplementary crosstie reinforcement) were provided in accordance with Section A.6.4 of the 1971 ACI Building Code. This confinement was placed at a spacing of 1.33 in. (34 mm) over the first 6 ft (1.83 m) of the wall. Ordinary column ties were used over the remaining height of the wall. Anchorage for the horizontal steel was provided by embedment in the boundary elements plus a standard 90° hook around the outer main flexural steel.

Figure 5.34 shows the reinforcing details. Confinement reinforcement was detailed according to Section A.6.4.3 of the 1971 ACI Building Code. A ten bar diameter extension was used on all confinement steel hooks. Each end of the supplementary crossties had a 180-degree hook.

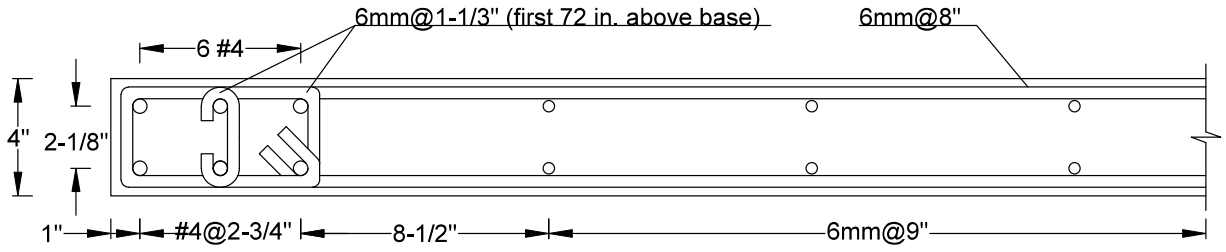

Figure 5.34 Wall R2 reinforcing details (1 in. = 25.4 mm).

The concrete compressive strength was determined from compressive tests on 6x12-in. (152x305 mm) cylinders. No. 4 bars conforming to ASTM A615 Grade 60 designation were used as reinforcement. Deformed 6 mm hot rolled bars with properties similar to Grade 60 were also used. Measured properties of the materials are:

- Concrete
  - f'_c = 6,700 psi (46 MPa)
- Steel (No. 4 bars)
  - f_u = 102.7 ksi (708 MPa)
  - f_y = 65.3 ksi (450 MPa)
- Steel (6mm bars)
  - f_u = 100.2 ksi (691 MPa)
  - f_y = 77.6 ksi (535 MPa)

Figure 5.35 shows the apparatus used for walls testing.

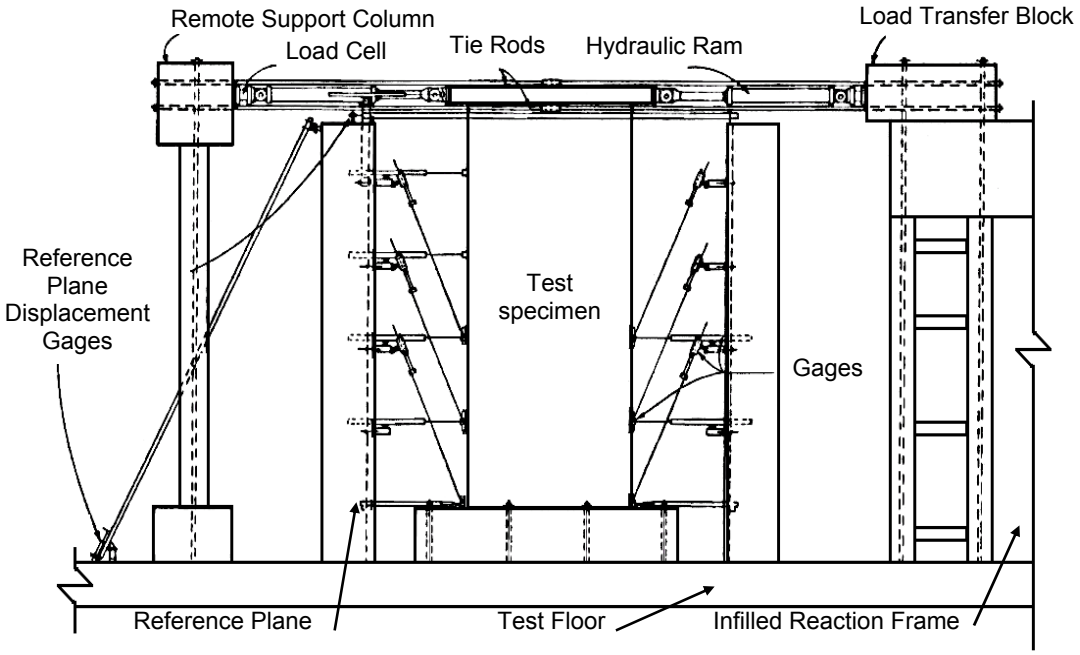

Figure 5.35 Wall testing apparatus.

Each test specimen was post-tensioned to the floor using eight 1-3/8 in. (34.9 mm) diameter stress steel bars. Loads were applied to the specimen as a vertical cantilever with concentrated forces at the top. Hydraulic rams on each side of the specimen alternately applied force to first one side and then the other side of the top slab. Reactions from the applied loads were transferred to the test floor through a large infilled reaction frame. For specimen R2, the test consisted of 39 loading cycles. Figure 5.36 shows the applied displacement history.

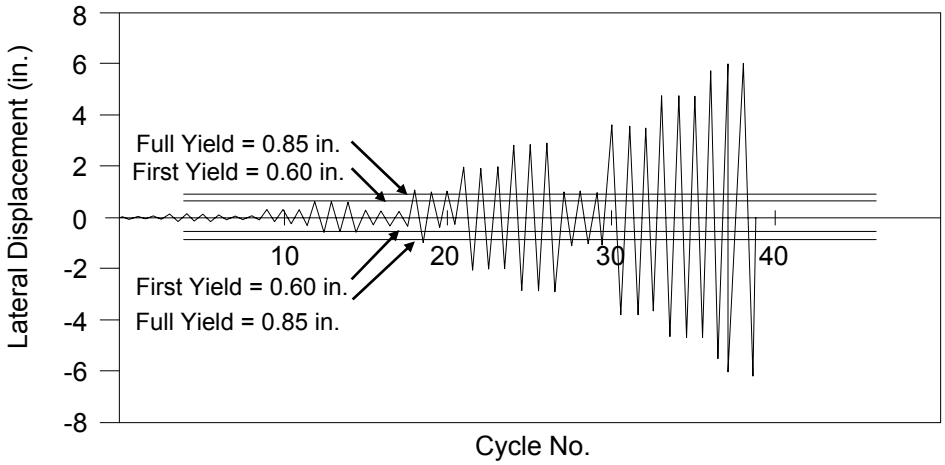

Figure 5.36 Applied displacement history (1 in. = 25.4 mm).

5.4.2 Experimental and Analytical Response

Complete measured strain profiles at the base of the specimen were not available for drift ratios higher than 0.6%. Two models are used to estimate those demands: TNO DIANA finite elements model (details provided in section 2.4) and a plastic hinge model (according to Figure 5.2). Figure 5.37 presents the TNO DIANA model. This model consists of curved shell elements with embedded reinforcement (full bonding), total strain crack model for concrete and Giuffré-Menegotto-Pinto (Menegotto et al. 1973, Filippou et al. 1983) material for steel. Modeling details were provided in section 2.4.

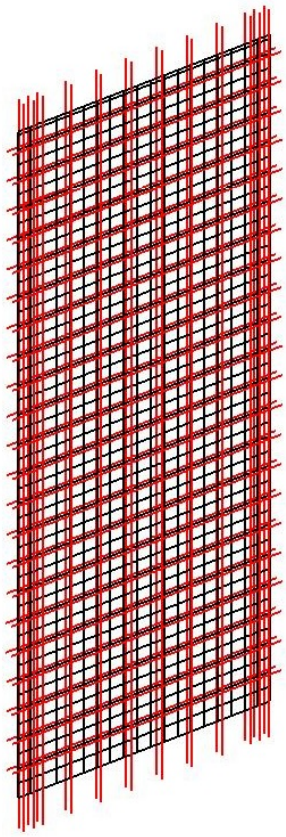

Figure 5.37 TNO DIANA finite element model for wall R2.

Figure 5.38 shows the experimental lateral load versus lateral displacement response and the analytical response obtained from the finite elements model. Analysis was conducted until Cycle 32, a 4 in. (101.6 mm) deflection cycle, at which point lateral bracing was added to the test set-up at 3 ft-6 in. above the wall base, in order to restrain the out-of-plane displacement observed at the wall boundary. Up to this point, there is a good agreement between the measured and the analytical estimation of the response.

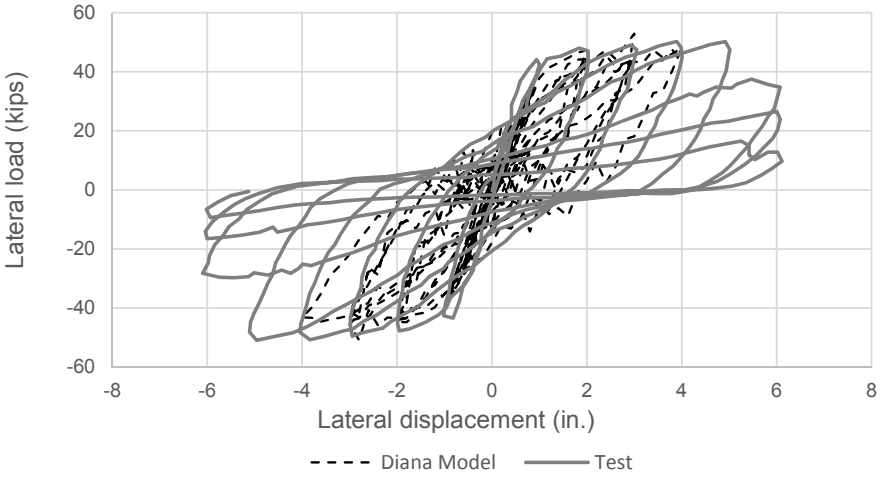

Figure 5.38 Experimental and analytical response for wall R2 (1 kip = 4.45 kN, 1 in. = 25.4 mm).

Figure 5.39 shows the moment-curvature relation considered for the plastic hinge model. This relation was obtained from XTRACT, considering measured material properties according to section 5.4.1.

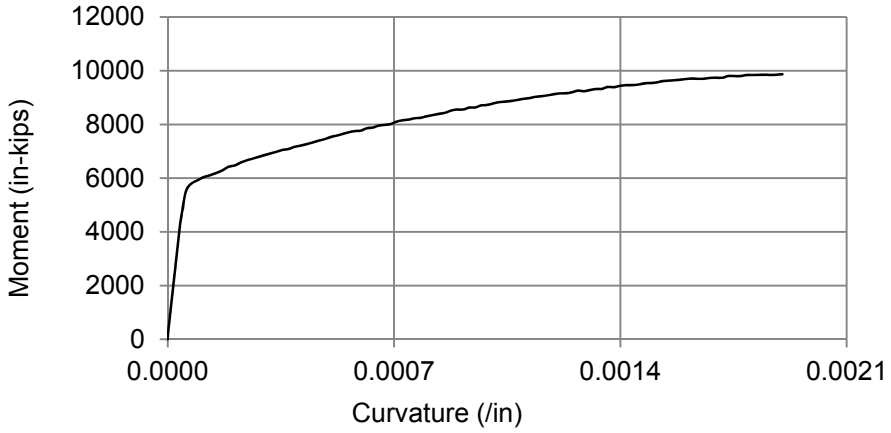

Figure 5.39 Moment-curvature relation for wall R2 (1 in. = 25.4 mm; 1 in-kips = 0.11 kN-m).

Figure 5.40 shows the measured strain profile at the base of wall R2 for 0.60% drift ratio. Strain values at higher drift ratios were not available and they are analytically estimated from finite element modeling and the plastic hinge approach, where the plastic hinge length is taken as $l_w/2$. The figure shows estimations at 0.8%, 1.5% and 2.0% drift ratio from both models. Finite element analysis was conducted until Cycle 32, 2.2% drift ratio cycle, when lateral support was added to restrain out-of-plane displacement at the wall edge. Figure 5.40 also shows an estimation of the strain profile at the maximum measured drift ratio of 2.8% drift ratio. This estimation is obtained only from the plastic hinge model. Both analytical estimations of strains are accurate in comparison with the measured strains at 0.6% drift ratio. At higher drifts, estimations of strains are consistently lower for the finite elements model.

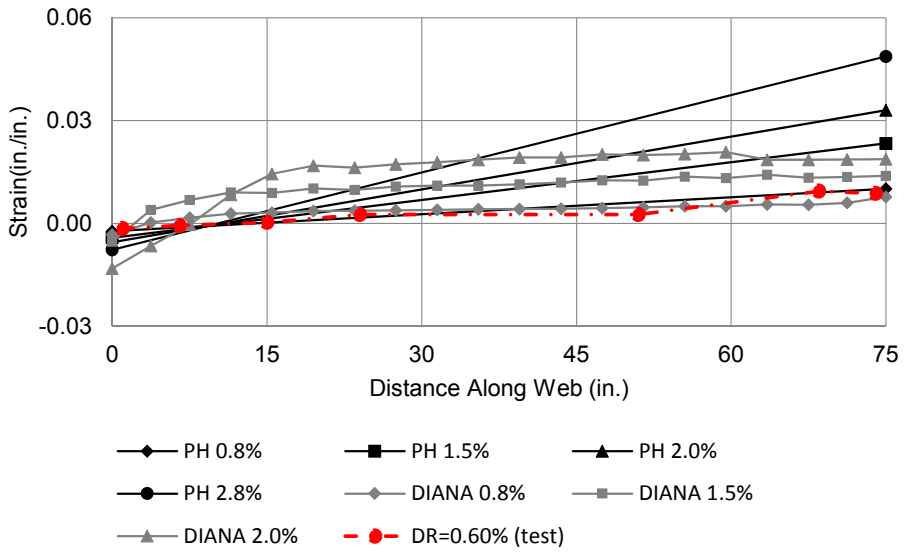

Figure 5.40 Measured and analytical strain distribution at the base of wall R2.

Figure 5.41a shows the deformed shape of wall R2, obtained from DIANA analysis, at the point where lateral bracing was added at 42 in. over the wall base (after Cycle 32, a 4 in. deflection cycle). Figure 5.41b shows the out-of-plane displacement at the wall edge for this point and for the first peak of Cycle 28 (a 1 in. deflection cycle).

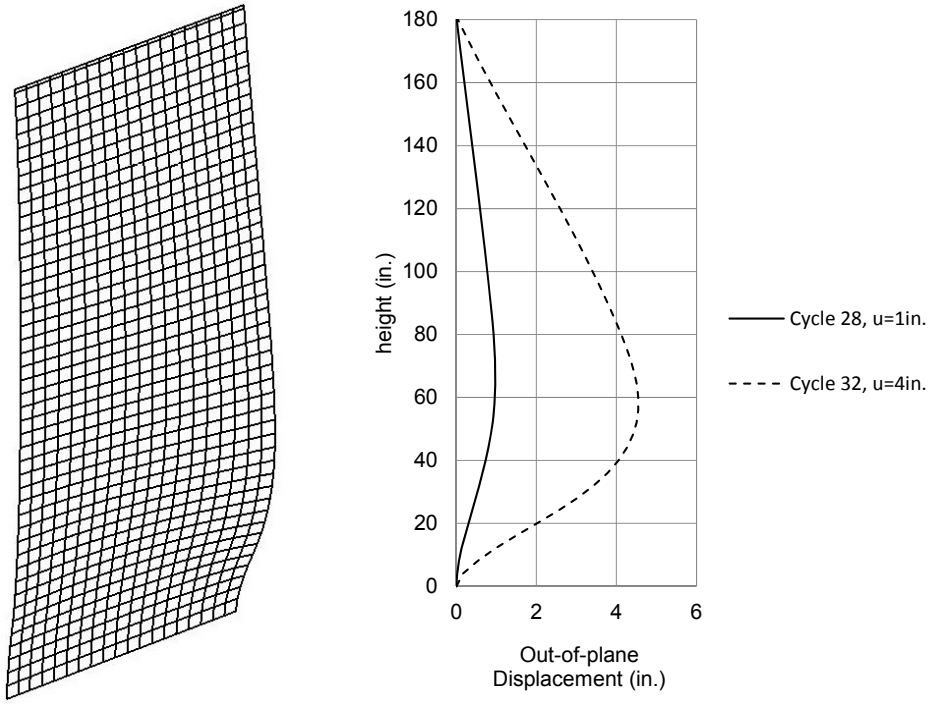

Figure 5.41 a) Analytical estimation of the deformed shape of wall R2 at the point where lateral bracing was added to the test set-up, b) out-of-plane-displacement along the height at the wall edge.

5.4.3 Evaluation of the Onset of Out-of-Plane Instability

Some highlights of the response observed during the test are now presented (Oesterle et al., 1976). First indication of crushing of the outer shell at the base of the wall had been noted in Cycle 22. A notable increase in spalling and flaking along the horizontal cracks was observed during the 3 in. deflection cycles. During Cycle 28, a 1 in. (25.4 mm) deflection cycle, bowing of the compression end was observed. The compression boundary element was 0.25 in. (6.4 mm) out of plane at a point 3 ft-6 in. (1.1 m) above the base. Although this bowing progressed further with each cycle the load carrying capacity of the wall remained stable. After Cycle 32, the compression end of the wall was 3 in. (76.2 mm) out of plane at point 3 ft-6 in. (1.1 m) above the base. Figure 5.42 shows the specimen after Cycle 32. The test was stopped after Cycle 32 and lateral bracing was added to the test step-up. From Figure 5.41, analytical estimations for the out-of-plane displacement at the wall edge at 42 in. over the base are 0.6 in. for Cycle 28 and 4 in. for Cycle 32. Both values are reasonably close to the reported values.

An omni-direction ball caster was placed against the face of the each boundary element at a level 3 ft-6 in. (1.1 m) above the base. This simulated lateral support at approximately the first story height. The test was continued with the third 4 in. (101.6 mm) deflection Cycle 33. Considerable grinding and spalling along web cracks occurred during the 4 in. deflection cycles. Also, the end hooks of several horizontal bars started to open during the 4 in. cycles. In Cycle 35, a large out of plane displacement of the compression zone within the lower 3 ft-6 in. (1.1 m) height was observed and the load carrying capacity of the wall decreased. The maximum negative load in the third cycle of the 5 in. (127.0 mm) deflection increment was 79% of the maximum in the first cycle. Several bars fractures in Cycle 37 and out of plane displacement of the compression zones progressed further. Considerable crushing and loss of concrete occurred in subsequent cycles and the load carrying capacity continued to decrease. The specimen sustained at least 80% of the maximum measured load through 14 complete inelastic cycles. The last inelastic loading increment in which the load was sustained at or above 80% of the maximum for all 3 cycles was at ±4 in. (±101.6 mm).

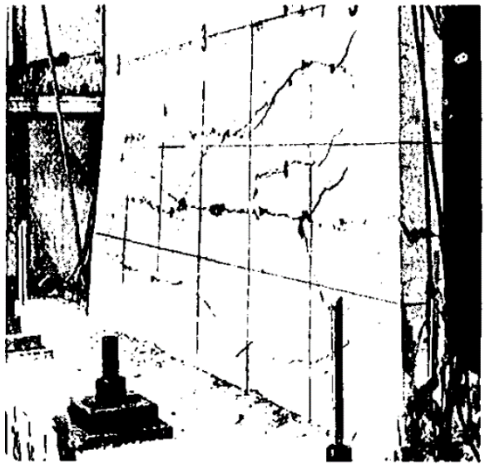

Figure 5.42 Lateral displacement of compression zone after 4 in. deflection in wall R2.

The lateral support at the first story level was not present during the major portion of the test. Therefore, the onset of out-of-plane instability is analyzed without considering this intermediate support. The maximum tensile strain required to buckle the wall boundary during

load reversal (ϵ_{sm}) is first estimated from an OpenSees model (see Figure 5.28b). Figure 5.43 shows the analysis results.

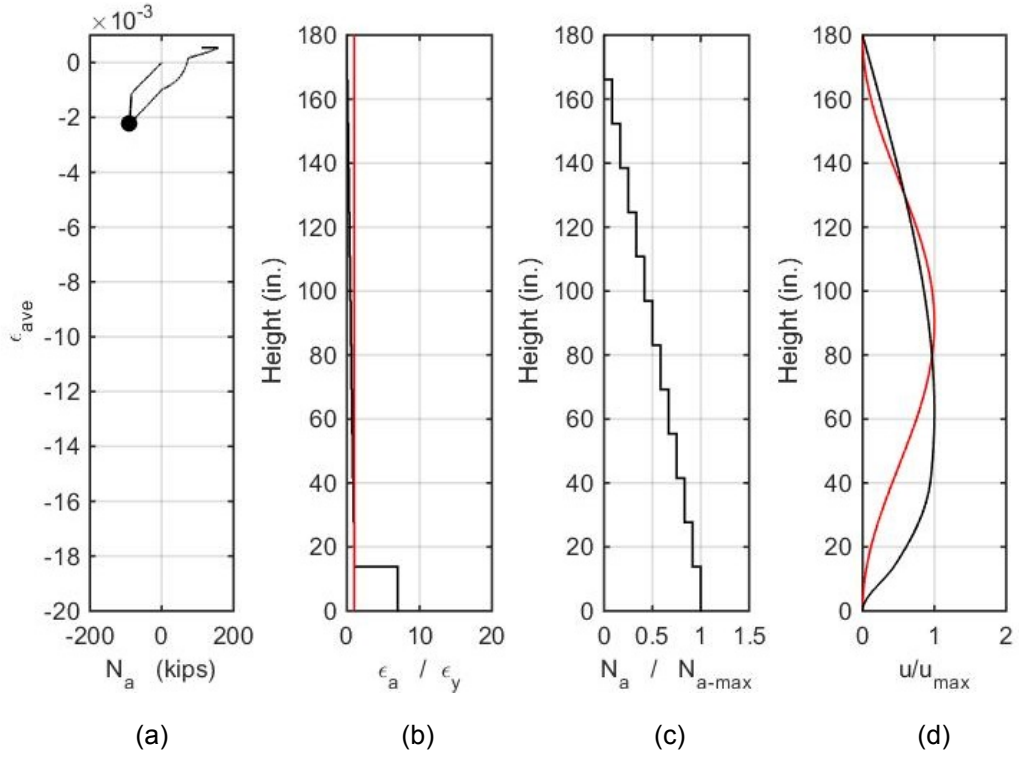

Figure 5.43 Boundary element of wall R2: a) average axial strain versus axial force at the base, b) normalized axial strain, c) normalized axial force, d) normalized buckled shape.

The analysis considers spalling in the region close to the wall base prior to buckling, which is consistent with reported observations. According to Figure 5.43b, it is required to have a vertical strain at the base of the wall boundary close to $\epsilon_{sm} \approx 8\epsilon_y$, or 0.02 to buckle the boundary during load reversal. The estimated value for the maximum tensile strain at the wall boundary (Figure 5.40) before Cycle 33 is higher than $8\epsilon_y$, and therefore the onset of buckling is an expected response, as observed during the test and in the finite elements model. If the simplified mechanics is applied directly assuming constant strain along the full height (180 in.), the estimated value of ϵ_{sm} is low, as shown in Table 5.6.

If we apply Figure 4.9 directly in Table 5.6, the estimated value for ϵ_{sm} is 5·0.005=0.025, close to 0.02 obtained from the more accurate OpenSees model. The analysis suggests that Figure 4.9 can be used to improve the estimation of ϵ_{sm}.

Table 5.5 Properties for buckling calculation (1in. = 25.4 mm; 1 psi = 0.007 MPa).

Wall	Material Properties, psi		Dimensions, in.						BE Area of Longitudinal Steel A_s, in.^{2}
	f'_c	f_y	Width, b	Length, l_w	Story Height, H	h_u	BE Length, l_b	Stirrup Clear Cover, c	
R2	6,700	65,300	4.0	75	180	180	8	0.5	1.18

Table 5.6 Analysis of R2 from simplified mechanics, cover spalled off.

Wall	Wall Slenderness b_c/kh_u	ρ	m	ξ	κ	ϵ_{sm}
R2	0.02	7%	0.72	0.10	1	**0.005**

6 Global Instability in Slender Walls of Chilean Buildings

6.1 INTRODUCTION

Prior 2010, lateral buckling in slender walls and columns had been observed only in a few laboratory tests. Following the 2010 Chile earthquake, buckling in slender walls was reported in two residential buildings. Both experienced severe post-earthquake damage. Relative to other types of damage in walls, cases of documented overall wall buckling behavior in Chile were relatively few and often associated with significant residual drift in the building (ATC-94, 2014). This chapter presents detailed studies carried on three Chilean buildings (Buildings #1, #2 and #3). Buckling was reported in some walls of Buildings #1 and #2. Building #3 collapsed during the 2010 Chile earthquake, and for this case an evaluation of the onset of lateral buckling is performed to determine if buckling was one of the multiple causes that triggered collapse. Modal response spectrum analysis is used to estimate the roof drift ratio of Buildings #1 and #2, using linear fixed-base models developed in ETABS. Results of linear analyses reported by others (Tanyeri, 2014; Hilson, 2014) are used to estimate the roof drift ratio of Building #3. Several models of isolated walls are considered for estimation of strain demands at the first story to perform an evaluation of the onset of lateral buckling, using the simplified mechanics theory presented in section 2.2. These studies are fundamental to determine the failure mechanism in slender walls that experienced out-of-plane instability in actual buildings. Later, recommendations for the improvement for current design standards are made based on these studies.

6.2 BUILDING #1[2]

6.2.1 Building Description

Building #1 is located in San Pedro de la Paz, Chile. The structure was severely damaged following the 2010 Maule earthquake. The building was designed during 2007-2008 and constructed in 2009. It has fifteen stories and two subterranean levels. The seismic force-resisting system is composed of reinforced concrete walls of 7.87 in. (200 mm) typical thickness. The gravity force-resisting system comprises the reinforced concrete walls plus some interior reinforced concrete columns. The typical story height is 8.37 ft (2.55 m). There are some discontinuities in the vertical members

[2] Data for Building #1 obtained from DICTUC reports (2010).

in the first story with respect to the upper stories. For example, walls K and Ñ (and other walls) step back from the building perimeter by approximately 6.5 ft (2 m), resulting in reduced wall length in the first story compared with typical stories above (walls of this configuration are is commonly known as “flag walls”). The building sustained a variety of apparent damage during the 2010 earthquake, with main damage characterized by wall crushing in the first story or in subterranean levels. Some walls, and in particular the first story wall along line Ñ, showed apparent out-of-plane buckling (Figure 1.1). Figure 6.1 shows the typical plan view and Figure 6.2 shows the first-story plan view.

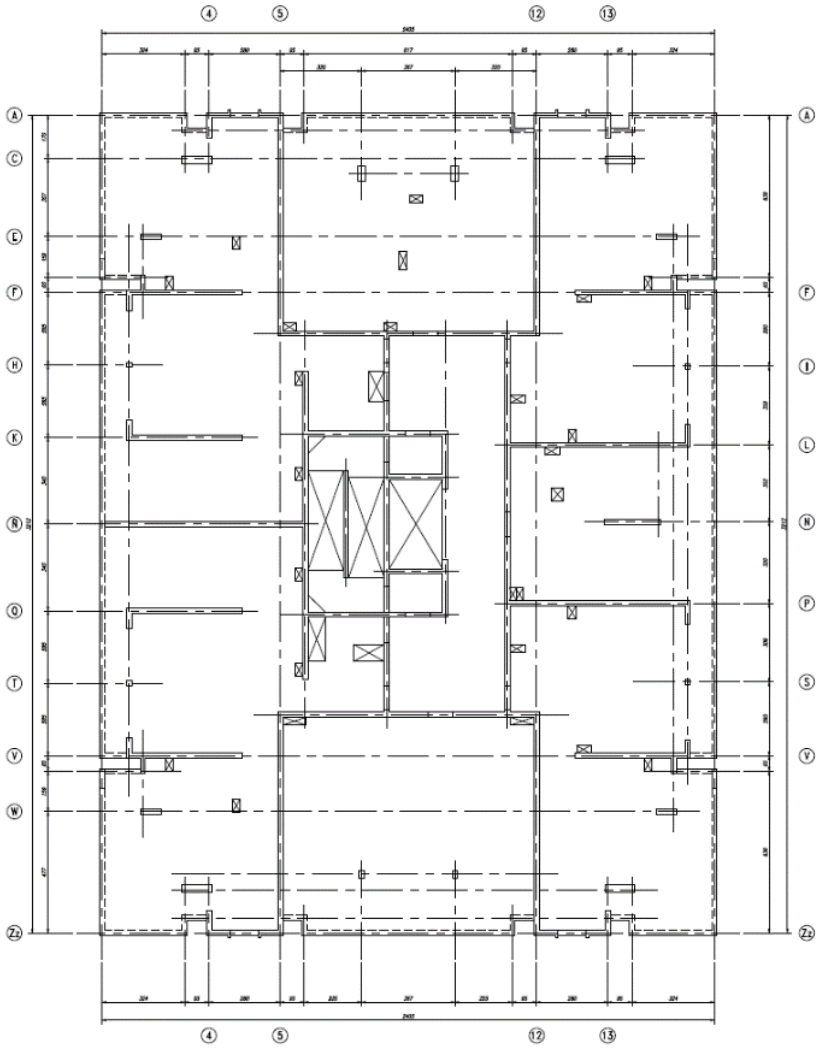

Figure 6.1 Building #1 – Typical plan view.

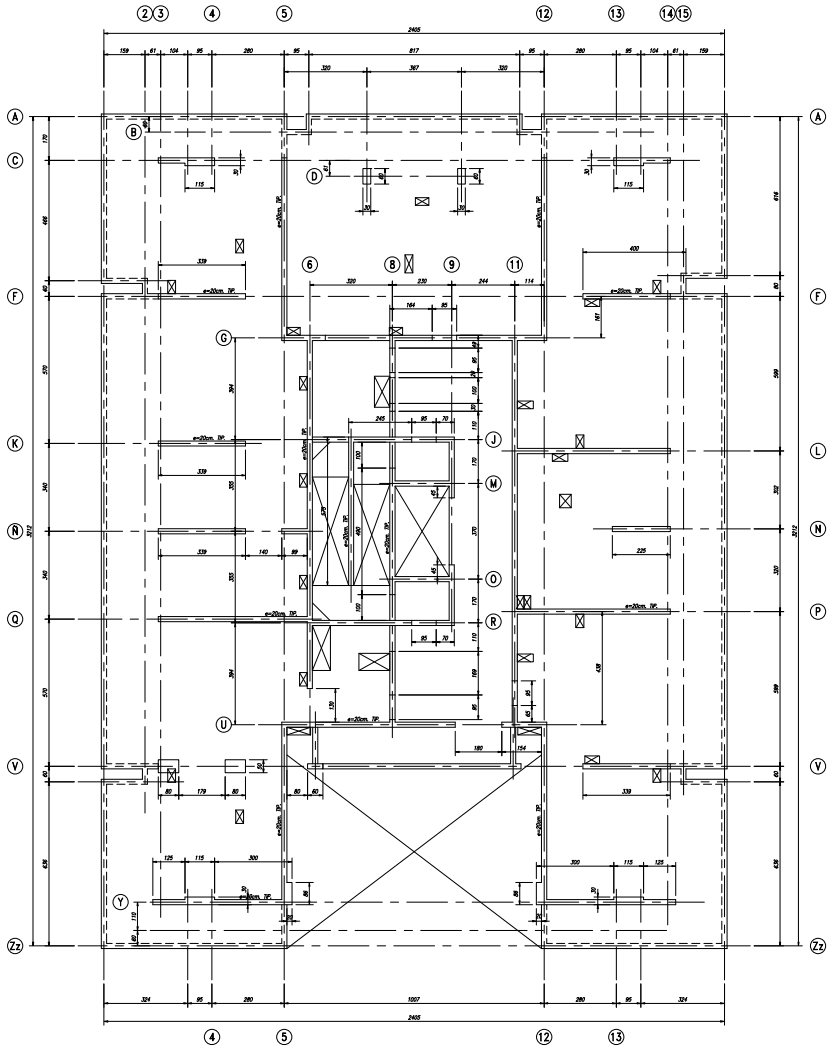

Figure 6.2 Building #1 – First story plan view.

6.2.2 Loads and Design Standards

Gravity and seismic loads were calculated following the Chilean standards NCh 1537 Of. 1986 and NCh 433 Of. 1996. Table 6.1 shows the calculated gravity loads. For the seismic mass 50% of live load is considered.

Table 6.1 Gravity loads for Building #1.

Floor	Slab thickness, in. (mm)	Dead Load, psf (kPa)	Live Load, psf (kPa)
-2	7.87 (200)	112.99 (5.41)	10.03 (0.48)
-1	7.87 (200)	112.99 (5.41)	10.03 (0.48)
1	5.91 (150)	87.09 (4.17)	10.03 (0.48)
2 to 14	5.91 (150)	87.09 (4.17)	10.03 (0.48)
Roof	5.91 (150)	87.09 (4.17)	10.03 (0.48)

Reinforced concrete members were designed according to ACI 318 (2005). Parameters considered in seismic design according to NCh 433. Of. 1996 are: building category C, seismic zone 3, soil type 3 and 5% damping ratio. Standard NCh 433. Of. 1996 defines the response spectrum for design according to Equations (6.1) to (6.3).

$$S_\alpha = \frac{I A_0 \alpha}{R^*} \tag{6.1}$$

$$\alpha = \frac{1 + 4.5\left(\frac{T_n}{T_0}\right)^p}{1 + \left(\frac{T_n}{T_0}\right)^3} \tag{6.2}$$

$$R^* = 1 + \frac{T^*}{0.1T_0 + \frac{T^*}{R_0}} \tag{6.3}$$

Where:

- S_α Pseudo acceleration
- I Importance factor, equal to 1 for building category C
- A_0 Peak ground acceleration, equal to 0.4 g for seismic zone 3
- g Acceleration of gravity 386 in./s^2 (9.81 m/s^2)
- T_n Mode nth vibration period (s)
- T_0 Soil dependent parameter, equal to 0.75 (s) for soil type III
- p Soil dependent parameter, equal to 1 for soil type III
- T^* Vibration period of the mode with highest equivalent mass in the analysis direction (s)
- R_0 Response modification factor = 11

Figure 6.3 presents the design response spectrum without response modification factor ($R^* = 1$).

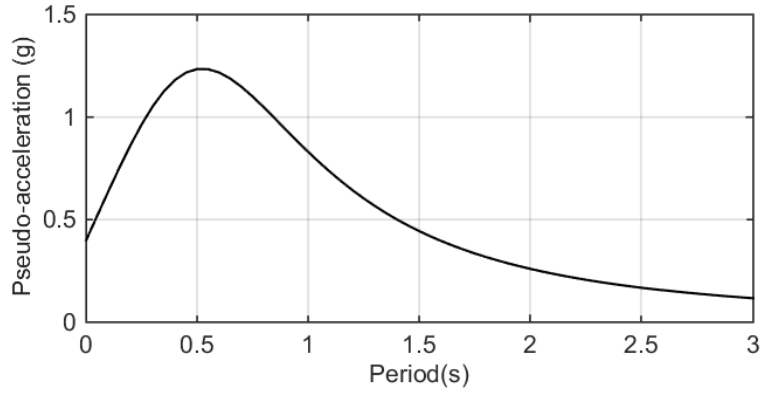

Figure 6.3 NCh 433 Of. 1996 elastic response spectrum (for *R=1).**

6.2.3 Nominal and Measured Material Properties

The nominal material properties specified by design are: concrete H30 confidence interval 90%, maximum compressive strength in cubic specimen 4,350 psi (30 MPa) and reinforcement steel A63-42H, tensile strength f_u = 91 ksi (630 MPa), yield strength f_y = 60 ksi (420 MPa). Table 6.2 shows the f'_c required for each concrete grade according to the Chilean standard NCh 430 Of. 2008.

Table 6.2 NCh 430 Of. 2008 conversion table.

Concrete grade (NCh170 confidence interval 90%)	f'_c, psi (Mpa)
H20	2,320 (16)
H25	2,900 (20)
H30	3,630 (25)
H35	4,350 (30)
H40	5,080 (35)
H45	5,800 (40)

Therefore, for this case f'_c = 3,630 psi (25 MPa). Concrete real strength was determined from tests following the Chilean standards NCh 1171/1 Of.2001 and NCh 1171/2 Of.2001. Table 6.3 quantifies those tests. Table 6.4 and Table 6.5 indicate the dimensions of cores and the location where they were obtained. Table 6.6 shows the results of the compressive strength tests.

Table 6.3 Building #1 tests (DICTUC, 2010).

Test	Quantity
Compressive strength	12
Thickness determination	12
Density determination	12
Detailed visual inspection	12

Table 6.4 Dimensions of cores (DICTUC, 2010).

Core	Height, in (mm)*	Diameter, in (mm)	Slenderness	Unit weight, pcf (kg/m3)
TH01	6.9 (174)	4 (101)	1,72	148 (2375)
TH02	6.8 (173)	4 (101)	1,71	147 (2353)
TH03	5.2 (132)	4 (101)	1,31	148 (2376)
TH04	6.8 (173)	4 (101)	1,71	145 (2326)
TH05	4.1 (104)	4 (101)	1,03	149 (2386)
TH06	7 (179)	4 (101)	1,77	146 (2344)
TH07	6.3 (161)	4 (101)	1,59	148 (2370)
TH08	4.6 (118)	4 (101)	1,17	146 (2340)
TH09	7 (179)	4 (101)	1,77	147 (2357)
TH10	6.9 (174)	4 (101)	1,72	145 (2315)
TH11	4.3 (110)	4 (101)	1,09	145 (2327)
TH12	6.5 (166)	4 (101)	1,64	141 (2266)

(*) Height includes surface preparation of top and bottom of the cylinder prior testing.

Table 6.5 Locations where cores were obtained (DICTUC, 2010).

Core	Position
TH01	Wall level -2, axis K between 3-5, 4.43 ft (1.35 m) from 3 and 3.61 ft (1.10 m) from floor level.
TH02	Wall level -1, axis 5 between C-G, 4.87 ft (1.48 m) from C and 2.20 ft (0.67 m) from floor level.
TH03	Wall level -1, axis L between 11-14, 3.94 ft (1.20 m) from 14 and 1.97 ft (0.60 m) from floor level.
TH04	Wall level 1, axis U between 5-9, 4.27 ft (1.30 m) from 9 and 3.12 ft (0.95 m) from floor level.
TH05	Wall level 1, axis 11 between G-U, 21.65 ft (6.60 m) from U and 3.84 ft (1.17 m) from floor level.
TH06	Column level 1, axis F between 12-14, 3.77 ft (1.15 m) from 14 and 4.27 ft (1.30 m) from floor level.
TH07	Wall level 2, axis 12 between ZZ-U, 12.14 ft (3.70 m) from ZZ and 3.44 ft (1.05 m) from floor level.
TH08'	Slab level 1, axis U-V between 8-9, 0.98 ft (0.30 m) from U and 2.62 ft (0.80 m) from 9.
TH09	Wall level 4, axis Q between 5-1, 9.84 ft (3.00 m) from 1 and 3.94 ft (1.20 m) from floor level.
TH10	Wall level 6, axis 5 between A-G, 10.33 ft (3.15 m) from A and 3.02 ft (0.92 m) from floor level.
TH11'	Slab level 9, axes E-G between 9-12, 9.02 ft (2.75 m) from G and 4.53 ft (1.38 m) from 12.
TH12'	Wall level 13, axis 5 between U-ZZ, 11.32 ft (3.45 m) from ZZ and 4.43 ft (1.35 m) from floor level.

Table 6.6 Measured concrete compressive strength (DICTUC, 2010).

Core	Maximum Load, lb (kN)	Core compressive strength, psi (MPa)	Cylinder compressive strength, psi (MPa)	Cubic compressive strength, psi (MPa)
TH01	116,451 (518)	9,384 (64.7)	9,384 (64.7)	10,109 (69.7)
TH02	100,265 (446)	8,079 (55.7)	8,079 (55.7)	8,804 (60.7)
TH03	99,141 (441)	7,977 (55.0)	7,977 (55.0)	8,702 (60.0)
TH04	97,117 (432)	7,818 (53.9)	7,818 (53.9)	8,543 (58.9)
TH05	108,133 (481)	8,702 (60.0)	8,702 (60.0)	9,427 (65.0)
TH06	90,598 (403)	7,295 (50.3)	7,295 (50.3)	8,021 (55.3)
TH07	115,552 (514)	9,311 (64.2)	9,311 (64.2)	10,037 (69.2)
TH08	76,435 (340)	6,150 (42.4)	5,598 (38.6)	6,324 (43.6)
TH09	109,482 (487)	8,818 (60.8)	8,818 (60.8)	9,543 (65.8)
TH10	71,040 (316)	5,714 (39.4)	5,598 (38.6)	6,324 (43.6)
TH11	70,365 (313)	5,671 (39.1)	5,047 (34.8)	5,773 (39.8)
TH12	67,443 (300)	5,424 (37.4)	5,279 (36.4)	6,005 (41.4)

Chilean standard NCh 1171/1 Of. 2001 specifies the use of a slenderness modification factor to obtain the cylinder compressive strengths from the core compressive strengths ($f_c' = K_1 f_{core}$), according to Table 6.7. These factors have been considered in Table 6.6.

Table 6.7 Modification factor according to Chilean standard NCh 1171/1 Of. 2001.

Slenderness (h/d)	Factor K_1
2.00	1.00
1.75	0.98
1.50	0.96
1.25	0.93
1.00	0.87

Following the 2010 Chile earthquake, one wall apparently buckled in the first story of Building #1 (Figure 1.1). As response in the first story was the primary interest, linear and nonlinear models were assembled based on the compressive strength obtained from a first-story core. Periods would not be much affected by using an alternative value for compressive strength. Therefore, the cubic compressive strength is considered as 8,000 psi (55 MPa), cylinder strength f'_c = 7,300 psi (50 MPa), and the elasticity modulus is E_c = 4,800 ksi (33,000 MPa). For linear analysis, the effective flexural and axial rigidity (including cracking) is used, according to ASCE 41 (2006), section 6.3.1.2: walls-cracked $0.5E_c I_g$ (flexural) and $0.4E_c A_w$ (shear), columns $0.3E_c I_g$ (flexural) and $0.4E_c A_w$ (shear), slabs $1/3E_c I_g$ (flexural). Kent and Park (1971) unconfined concrete model is used for nonlinear analysis. Measured reinforcement properties from coupons from the building are tensile strength f_u = 110 ksi (759 MPa) and yield strength f_y = 73.4 ksi (506 MPa).

6.2.4 Soil Properties

Layers of the foundation soil reported by the project geotechnical engineer (EMPRO, 2007) are:

- H-1 From 0.0 ft to 18.0 ft (0.00m-5.50m)
- H-2 From 18.0 ft to 34.4 ft (5.50m-10.50m)
- H-3 From 34.4 ft to 38.1 ft (10.50m-11.60m)
- H-4 From 38.1 ft to 50.7 ft (11.60m-15.45m)
- H-5 From 50.7 ft to 52.2 ft (15.45m-15.90m)
- H-6 From 52.2 ft to 65.8 ft (15.90m-20.06m)

Table 6.8 indicates the soil parameters for each layer. According to the Chilean standard NCh 433 Of. 1996, the soil classifies as type III for seismic zone 3.

Table 6.8 Soil properties per layer (EMPRO, 2007).

	H-1	H-2	H-3	H-4	H-5	H-6
USCS classification	SP,SM	SP	ML	SP	ML	SP
Fines (%)	<12%	3	84	1	57	3
Plasticity index	NP	NP	NP	NP	NP	NP
Solids specific weight (Gs)	2.7	2.77	2.53	2.7	2.61	2.76
Nspt, blows/ft	>40	29 to 73	9	57 to 62	13	>60
Internal friction angle	38	38	-	40	-	42
Effective cohesion, psi (MPa)	0	0	-	0	0	0

6.2.5 Recorded Ground Motion

Instruments recorded the ground acceleration during the 2010 Chile earthquake at a nearby station (Colegio Concepción, San Pedro de la Paz) owned by the Seismological Service at the Department of Geophysics at the University of Chile (GUC). The station is located at 0.8 miles (1.3 km) from the building site and this is the available record closest to the building site. Ramirez and Vivallos (2009) described the type of soil of the area where the building is located as alluvial deposits of the Bio-Bio River, fine to medium sands with little silt, with some layers of coastal sand deposits and anthropogenic filling on top. The soil classifies as type 3 according to the Chilean standard NCh433 Of. 1996 (section 6.2.2). Figure 6.4 to Figure 6.6 show the acceleration records for the three measured directions.

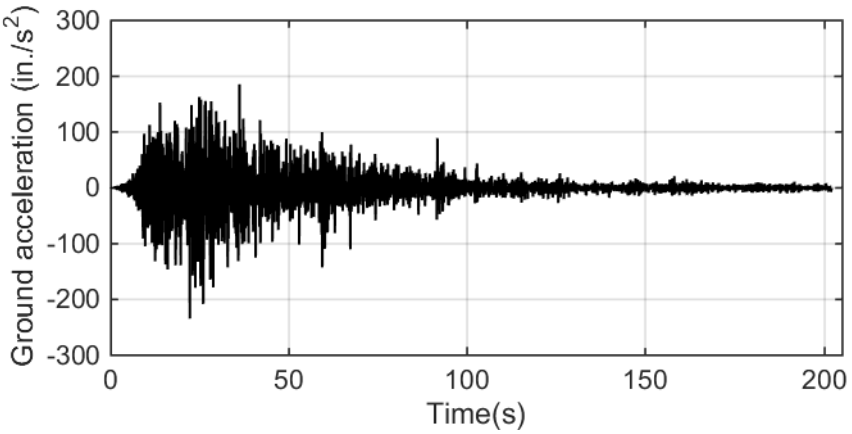

Figure 6.4 Corrected ground motion east-west direction (1 in. = 25.4 mm).

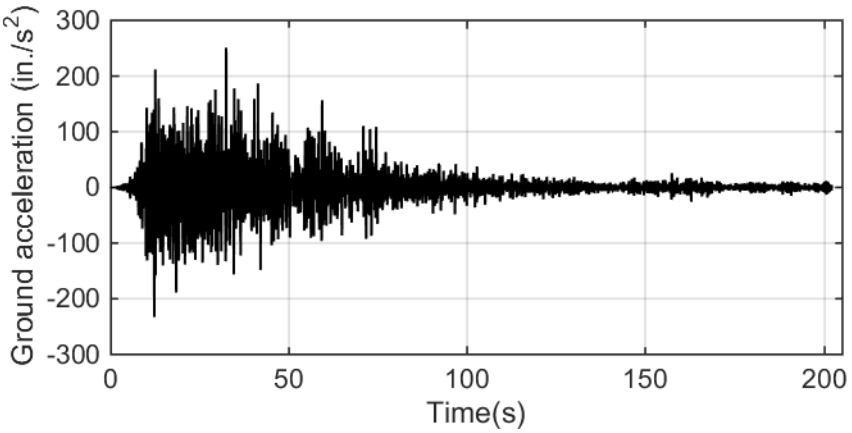

Figure 6.5 Corrected ground motion north-south direction (1 in. = 25.4 mm).

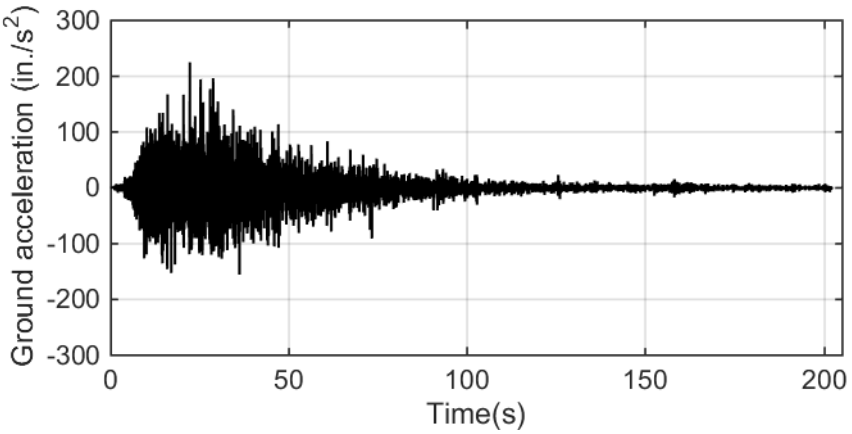

Figure 6.6 Corrected ground motion up-down direction (1 in. = 25.4 mm).

Figure 6.7 to Figure 6.9 show the pseudo acceleration, pseudo velocity, and the displacement response spectrum (2% damping ratio).

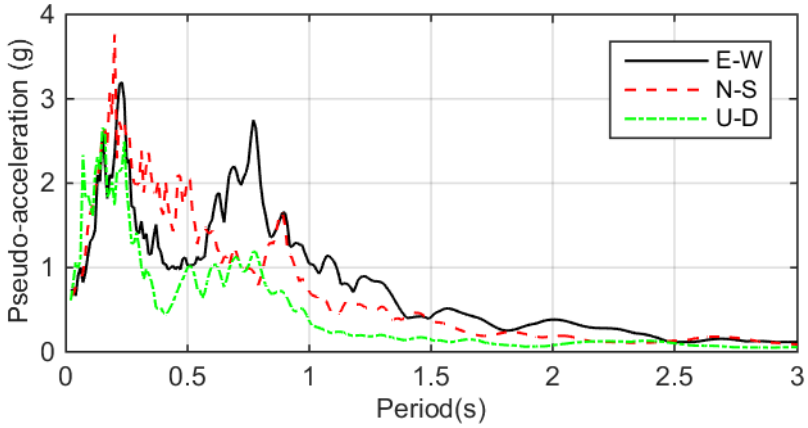

Figure 6.7 Pseudo acceleration spectrum.

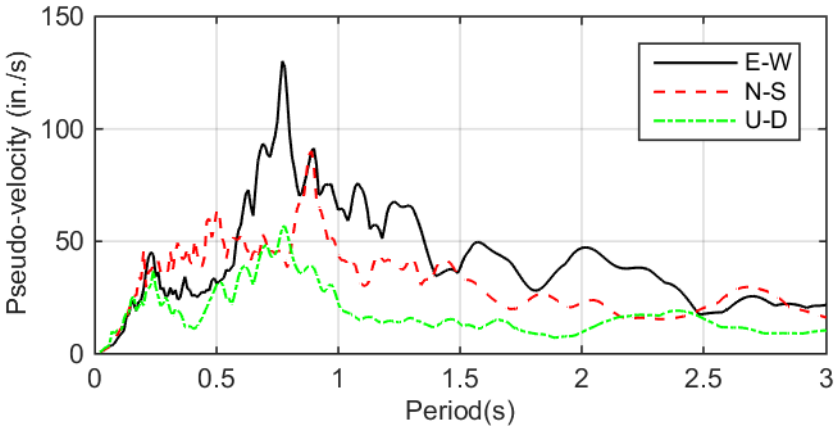

Figure 6.8 Pseudo velocity spectrum (1 in. = 25.4 mm).

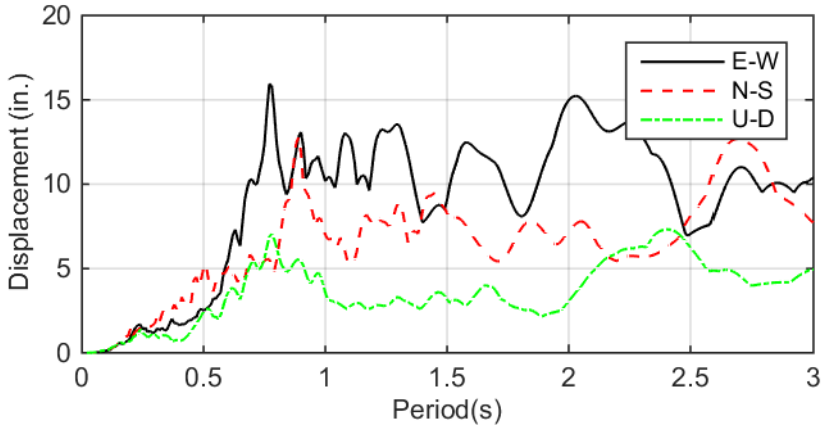

Figure 6.9 Displacement spectrum (1 in. = 25.4 mm).

The first mode period in the east-west direction, estimated from an ETABS linear model in section 6.2.7, is $T = 0.57\ s$. This period is based in several assumptions regarding material properties and loads. In Figure 6.7 it can be observed that the calculated period falls in the valley of the east-west spectrum, and a large peak is observed at $T \sim 0.76\ s$. Therefore, a sensitivity analysis should be done regarding the first-mode period and its influence on the calculated structure response. According to Figure 6.9, in the east-west direction the peak spectral displacement is between 9.8-15.8 in. (250-400 mm) for the reasonable building period range. Therefore, the maximum roof drift ratio is close to $DR = 1.43\%$. This assumes that peak displacement response of the nonlinearly responding building is the same as that of the building with linear-elastic properties.

Figure 6.10 compares the calculated pseudo-acceleration spectrum (2% damping ratio) and the NCh 433 Of. 1996 design spectrum (R*=1). It is observed that the design pseudo-accelerations are largely exceeded in the east-west direction within the plausible period range.

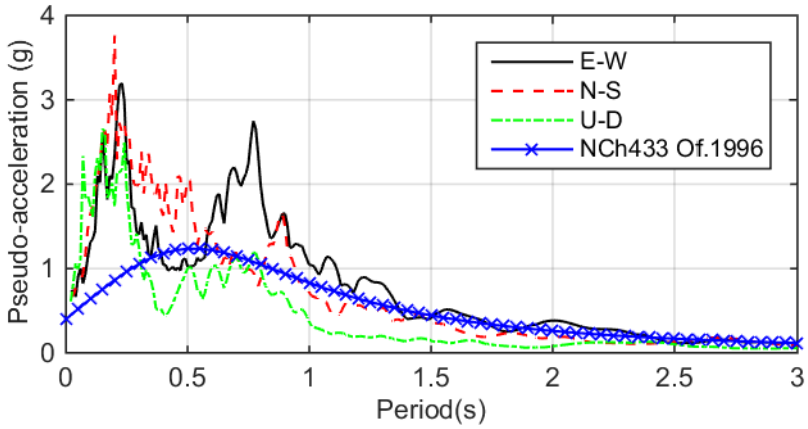

Figure 6.10 Pseudo acceleration spectrum comparison.

Figure 6.11 presents a tripartite plot for the three recorded directions.

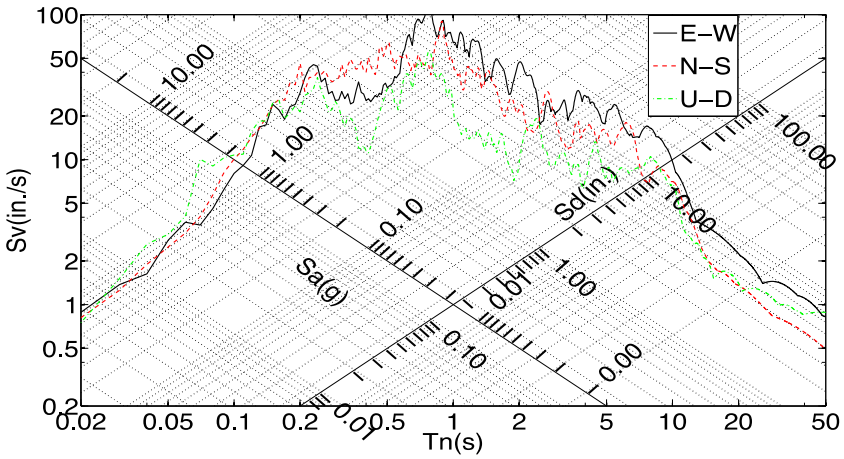

Figure 6.11 Tripartite plot for east-west, north-south and up-down motion (1 in. = 25.4 mm).

From Figure 6.11 for the period range $0.57\,s \leq T \leq 0.76\,s$ the structure is in the displacement preserved zone, and therefore the maximum roof drift ratio obtained from linear analysis is expected to be close to the nonlinear maximum drift ratio.

6.2.6 Damage Reported Following the 2010 Chile Earthquake

The main building post-earthquake damage is described in this section (DICTUC, 2010). Even though no major exterior damage is apparent, the floors cantilevering from the walls to form balconies showed obvious sagging.

Figure 6.12 Exterior views: (a) east view; (b) axis A; (c) west view; (d) axis Zz (after DICTUC, 2010).

Severe damage, which affects the structure stability, was observed from the second subterranean level to the first story, in walls oriented east-west between axes 12 and 14. In general terms, this entire line of walls failed in one of those stories. Repetitive damages were observed from the second to the fourteenth story, but these did not appear in the judgment of the author to affect the structure stability. Finally, in the fifteenth story and in the mechanical room, damage increases due to the changes on the lateral force-resisting system.

The main damage in the second subterranean level is concentrated in two walls. Damaged concrete has been removed and supplementary reinforcement cages have been added adjacent to the original wall sections.

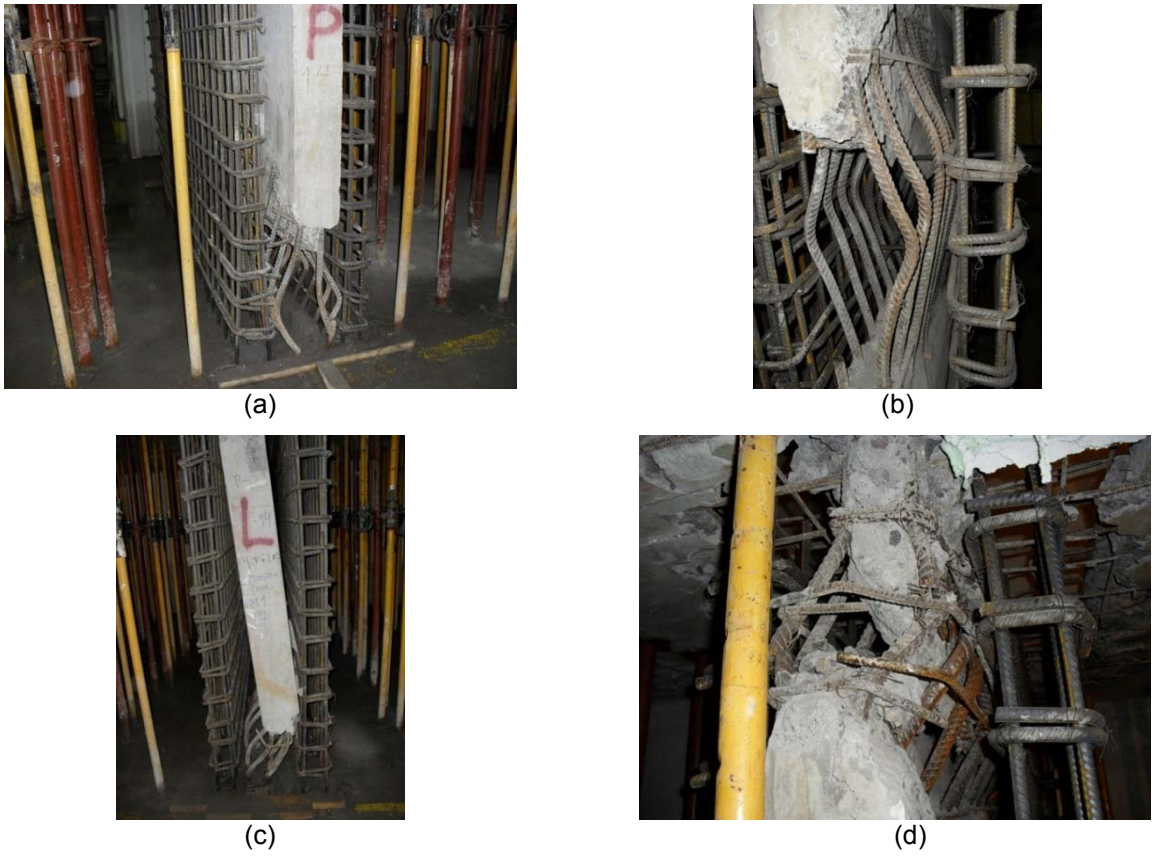

Figure 6.13 Damage in second subterranean level: (a) axis P, between axes 12 and 14; (b) detail of axis P; (c) axis L, between axes 11 and 14; (d) axis G, between axes 7 and 10 (after DICTUC, 2010).

Similar damage was observed in the first subterranean level. There were two failures in walls located in axis V and F, between 14 and 12.

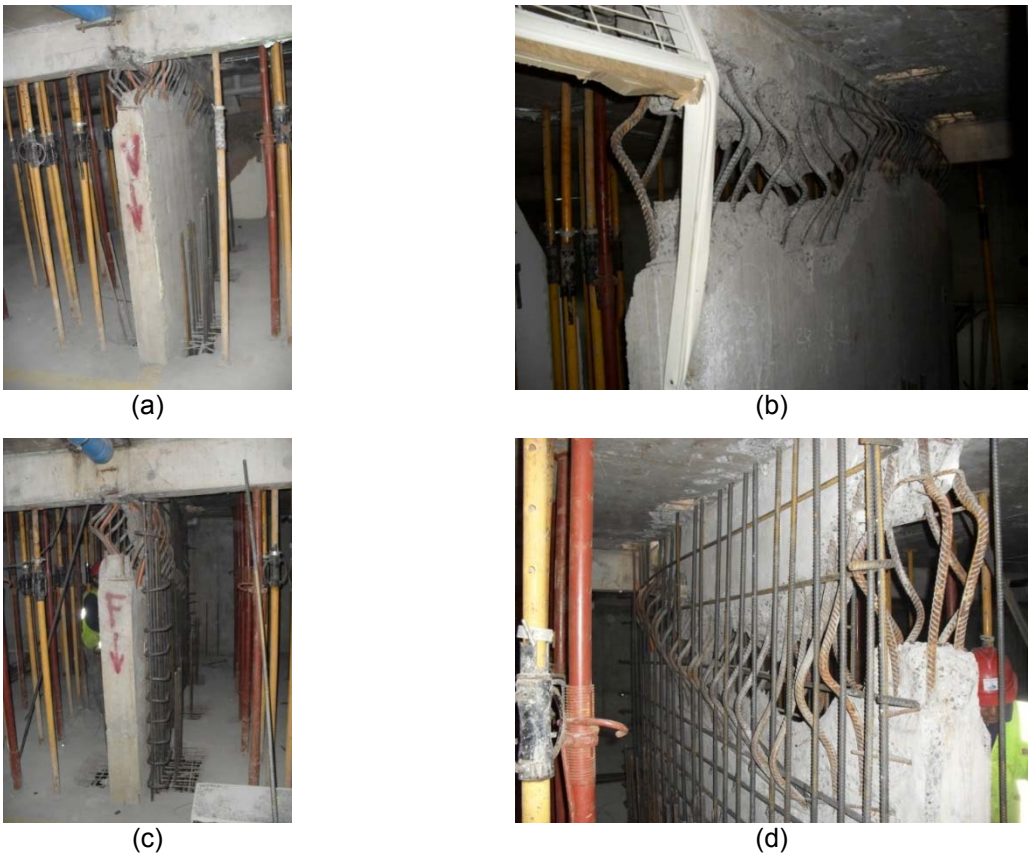

(a) (b)

(c) (d)

Figure 6.14 Damage in first subterranean level: (a) axis V, between axes 12 and 14; (b) detail of axis V; (c) axis F, between axes 12 and 14; (d) detail of axis F (after DICTUC, 2010).

In the first story, two specific failures types were observed. The wall in axis Ñ, between axes 3 and 4, had apparent compressive failure. Note that axis Ñ wall had an irregularity (indicated in Figure 6.22) in this story that could have been a contributing factor. The axis J wall, between axes 6 and 9, also had a compressive failure.

Figure 6.15 First story damage: (a) axis Ñ, between axes 3 and 5; (b) detail of axis Ñ; (c) axis J, between axes 6 and 8; (d) detail of axis J (after DICTUC, 2010).

Another important damage was located in axis U, between axes 5 and 9. This wall had a compressive failure. This failure was consistent with the predominant east-west direction of the earthquake. It should be noticed that this is an L-shaped wall (flange in axis 5), so the flange may have had an influence in the failure mode.

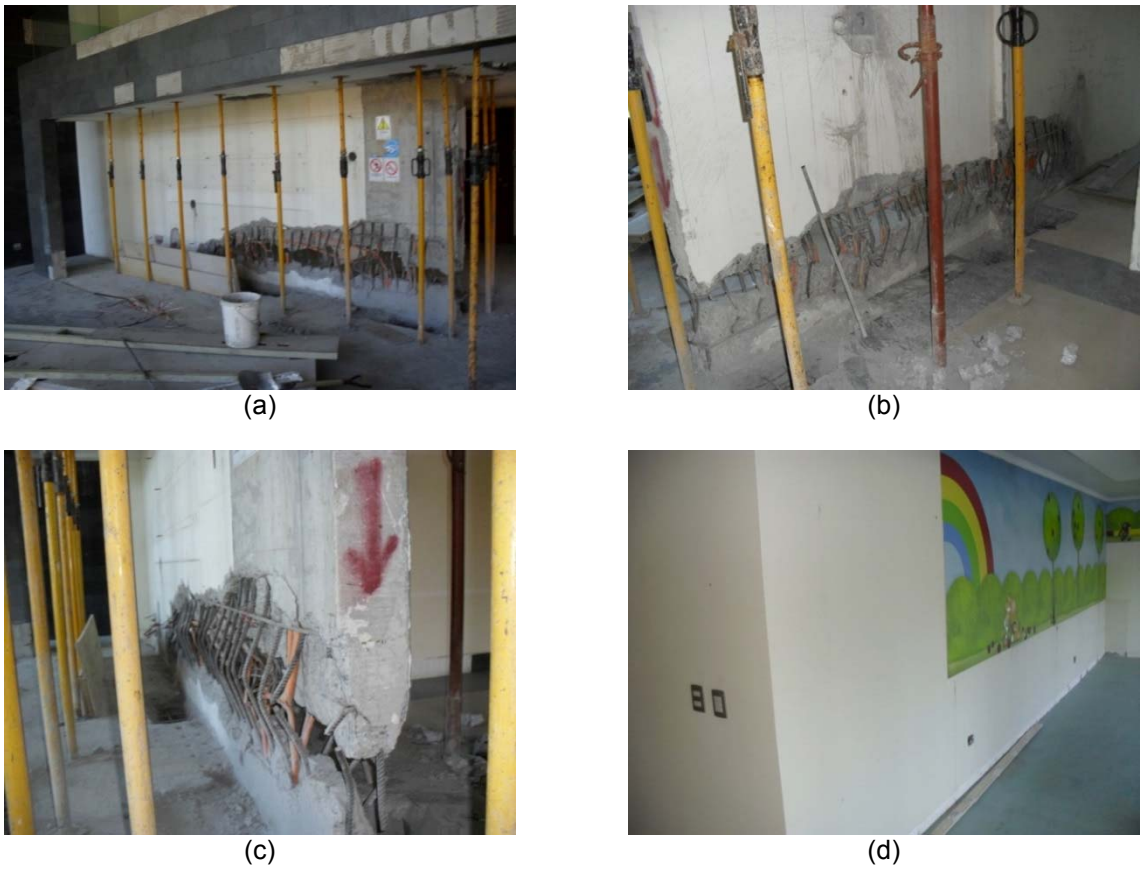

(a) (b) (c) (d)

Figure 6.16 First story damage: (a) axis U, between axes 5 and 9; (b) detail of axis U; (c) axis U, between axes 5 and 9; (d) axis 5, between axes U and Y (after DICTUC, 2010).

At the four corners of the building, in the first story, there are walls of non-uniform thickness (200/300 mm). Failures can be observed in the section of thickness change.

(a) (b) (c) (d) (e) (f)

Figure 6.17 First story damage: (a) axis C, between axes 13 and 14; (b) axis C, between axes 13 and 14; (c) axis C, slab damage; (d) axis C, between axes 3 and 4; (e) axis Y, between axes 3 and 4; (f) axis Y, between axes 13 and 14 (after DICTUC, 2010).

Connections between walls and slabs sustained damage as shown next.

(a) (b)

Figure 6.18 Second story damage in axis C, between 13 and 14: (a) view 1; (b) view 2 (after DICTUC, 2010).

6.2.7 ETABS Model for Building #1

The onset of out-of-plane instability in slender walls of Building #1 is analyzed using nonlinear models of isolated walls. For the analysis of isolated walls, it is required first to estimate the displacement demand at the roof. This demand is estimated from a response spectrum analysis of the full building using the software ETABS. Figure 6.19 shows the linear fixed-base model for Building #1.

Figure 6.19 ETABS model for Building #1.

Table 6.9 presents the periods and modal participating mass ratios for the first ten modes of the building.

Table 6.9 Modal analysis output for Building #1.

Mode	Period (s)	Modal mass ratio east-west direction	Modal mass ratio north-south direction
1	0.78	0.18	0.00
2	0.57	60.19	0.02
3	0.47	0.02	60.16
4	0.19	0.00	0.18
5	0.18	0.05	0.01
6	0.15	0.14	0.05
7	0.14	11.92	0.07
8	0.13	2.26	0.42
9	0.12	0.60	1.43
10	0.11	0.20	10.04

From Table 6.9, the second mode (period $T = 0.57\ s$) has the highest effective modal mass in east-west direction, and the third mode (period $T = 0.47\ s$) has the highest effective modal mass in north-south direction. As noted in section 6.2.5, according to the elastic response spectrum of the nearby recorded ground motion, lateral displacement is sensitive to the vibration period, with peak displacement occurring for fundamental period $T = 0.76\ s$. In order to evaluate the worst case scenario, the seismic mass was increased in the model to achieve this target period of $T = 0.76\ s$. Modifying the stiffness properties could have done this as an alternative approach. The building modal analysis output is then modified as shown in Table 6.10.

Table 6.10 Modal analysis output for Building #1 with increased seismic mass.

Mode	Period (s)	Modal mass ratio east-west direction	Modal mass ratio north-south direction
1	1.05	0.18	0.00
2	0.76	60.19	0.02
3	0.63	0.02	60.16
4	0.26	0.00	0.19
5	0.18	14.02	0.00
6	0.17	0.12	1.02
7	0.16	0.00	11.24
8	0.10	0.02	0.88
9	0.09	13.43	1.55
10	0.08	1.59	13.13

Section 6.2.8 presents the analysis results of nonlinear models of isolated walls, all of them oriented in the east-west direction. To proceed with those analyses, it was necessary to estimate first the maximum displacement that the building experienced during the earthquake. Figure 6.20 shows the maximum lateral displacement over the height in the east-west direction for the building

with increased seismic mass, which is the worst case scenario regarding the demand of lateral displacement.

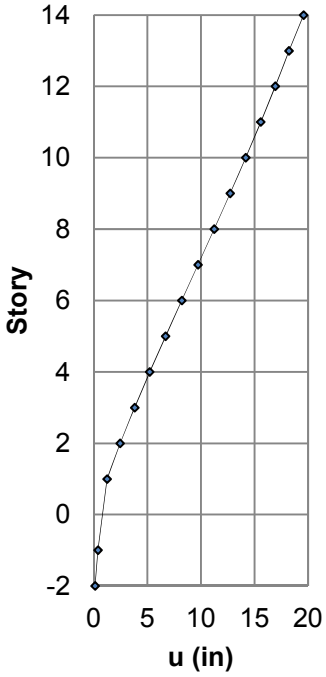

Figure 6.20 Maximum lateral displacement, east-west direction (1 in. = 25.4 mm).

From Figure 6.20 the maximum roof drift ratio is 1.4%, which is consistent with the first estimation presented in section 6.2.5.

6.2.8 Nonlinear Models of Isolated Walls

An evaluation of the onset of out-of-plane instability requires an estimation of the maximum strain demand at the wall base. Two walls of Building #1, both oriented in the east-west direction, are analyzed using nonlinear models of isolated walls. Figure 6.21 shows the selected walls in a plan view. Wall Ñ is the only one that showed apparent buckling following the 2010 Chile earthquake (Figure 1.1). The other wall was selected because of its proximity to wall Ñ (within 12 ft) and because it did not show appreciable post-earthquake damage at the first story. This observation can be used bound the analysis results.

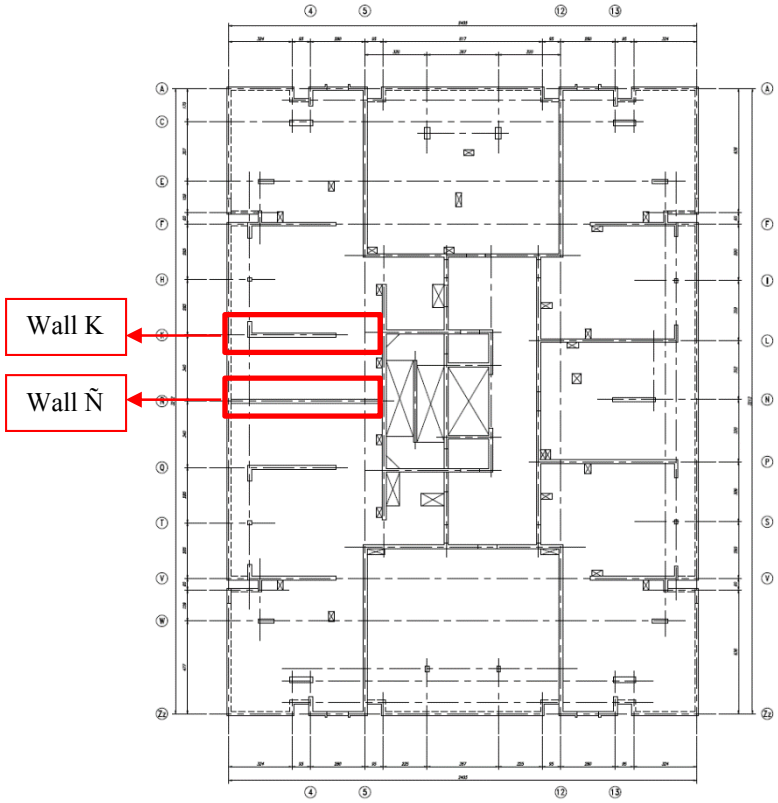

Figure 6.21 Analyzed walls for Building #1.

Nonlinear analysis of isolated walls includes integration of curvatures along the height and a plastic hinge approach according to Figure 5.3. Only for wall Ñ the analysis also includes a PERFORM 3D nonlinear model. These isolated models are used to estimate strain profiles at the base for buckling evaluation.

6.2.8.1 Analysis of Wall in Axis Ñ

Several analyses were performed for the wall with the most obvious buckling as pictured in Figure 1.1. Figure 6.22 shows an elevation view of wall Ñ.

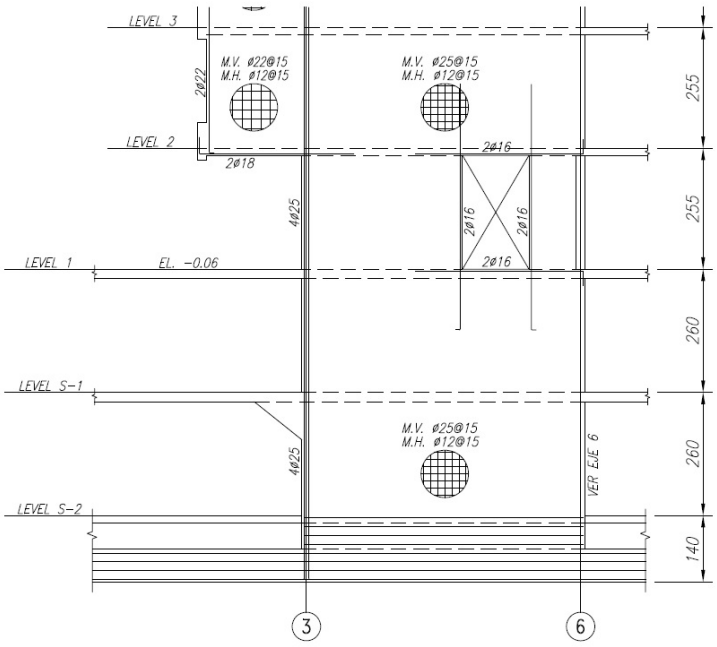

Figure 6.22 Elevation view of wall Ñ, dimensions in cm (1 cm = 0.39 in.).

Figure 6.23 shows the tributary area (typical floor) considered for the model of the isolated wall.

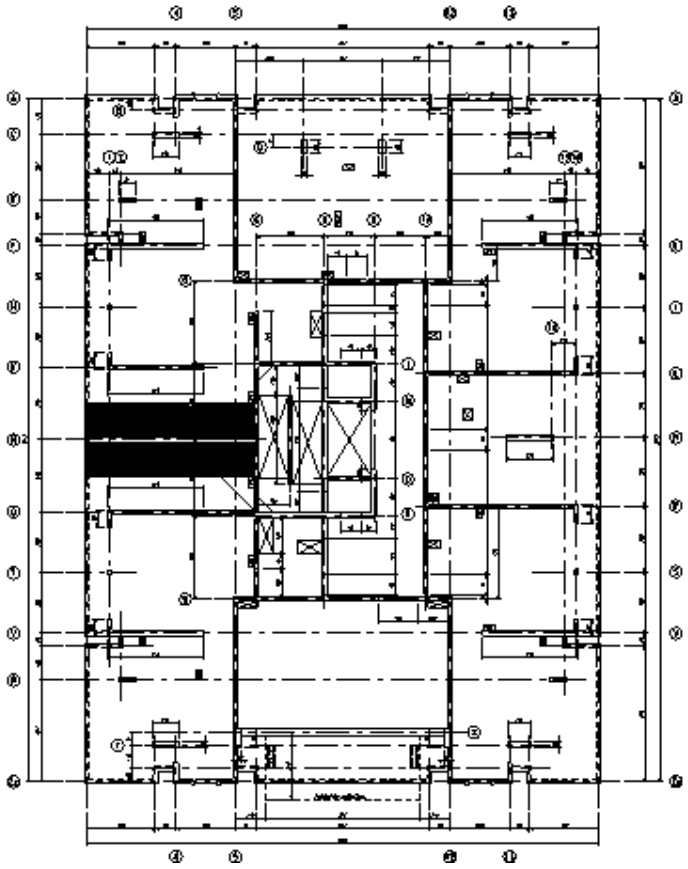

Figure 6.23 Tributary area at level 2-14 (typical floor).

Table 6.11 indicates total load at each floor.

Table 6.11 Gravity load per floor wall Ñ.

Floor	Area, ft^2 (m^2)	Dead Load, kips (kN)	Live Load, kips (kN)
-2	400.80 (37.24)	45.15 (200.84)	4.10 (18.24)
-1	400.80 (37.24)	45.15 (200.84)	4.10 (18.24)
1	248.10 (23.05)	21.60 (96.08)	2.54 (11.30)
2 to 14	284.70 (26.45)	24.78 (110.23)	2.92 (12.98)
Roof	339.60 (31.55)	29.56 (131.49)	3.48 (15.48)

The axial load at the first story bottom level is P= 863 kips (3839 kN). Therefore $P/A_g f'_c$=0.05.

6.2.8.1.1.1 Curvature Integration Approach

The procedure indicated in section 5.2 is followed. The simplified model has concentrated nonlinearity in the first story, and linear elastic behavior is assumed in the other stories. This is reasonable considering the wall has a relatively weak first story due to a setback. For the first story, the moment curvature relation is calculated with XTRACT. For the upper stories, the cracked properties indicated in ASCE 41 (2006) are used. Figure 6.24 shows the section properties considered in the XTRACT model.

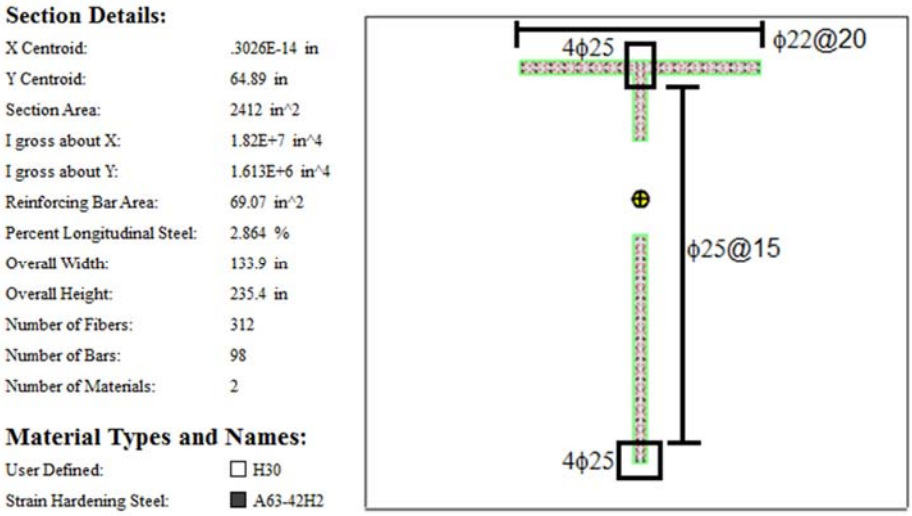

Figure 6.24 XTRACT model section properties for wall Ñ (1 in. = 25.4 mm, bars diameter in mm).

Figure 6.25 shows the moment-curvature relations for the flange in compression and in tension.

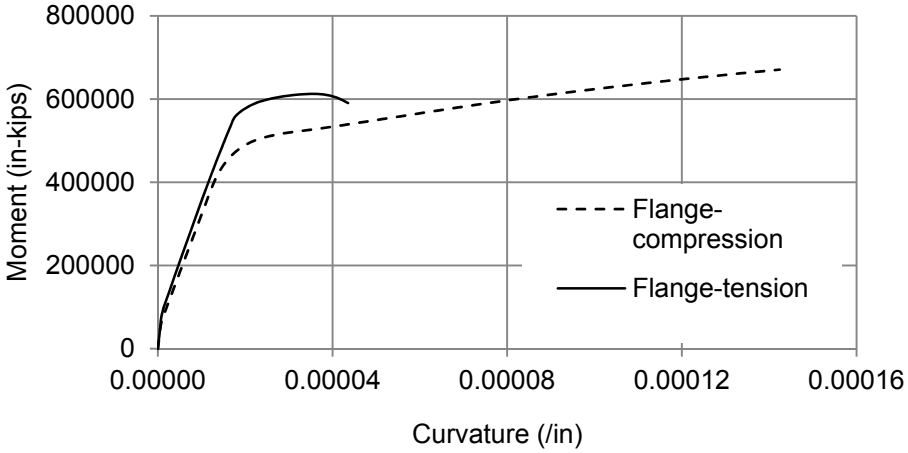

Figure 6.25 Moment-curvature relations axial load *N*=863 kips (1 in. = 25.4 mm; 1 in. - kips = 0.11 kN-m).

The lateral force pattern used for this analysis is inverted triangular. The total force was increased until reaching the target drift of 1.43%, the value obtained from linear analysis of the entire building. For the case of the flange in compression, the target displacement is reached without crushing in concrete or fracture in steel. Figure 6.26 shows the normalized moment and curvature over the height for this case.

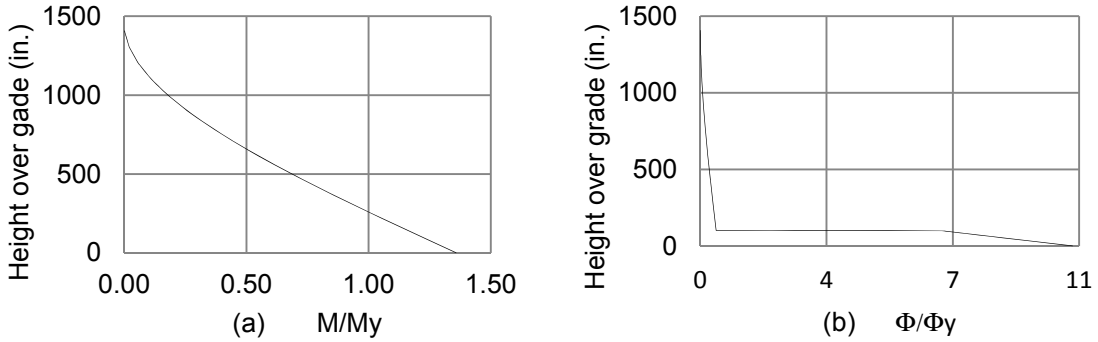

Figure 6.26 (a) Normalized moment; (b) curvature for flange in compression.

As expected, the curvature demand is concentrated in the first story. (Note that the calculated curvature distribution shows a sharp spike toward the base level, indicating that the calculated strain and curvature may be sensitive to minor variations in the deformation or moment demands. A plastic hinge model is used later in this chapter to reduce the sensitivity of the result. For the case of flange in tension, Figure 6.27 shows the normalized moment and curvature over the height. For this case, concrete at the wall stem crushes at a drift ratio of 0.49%.

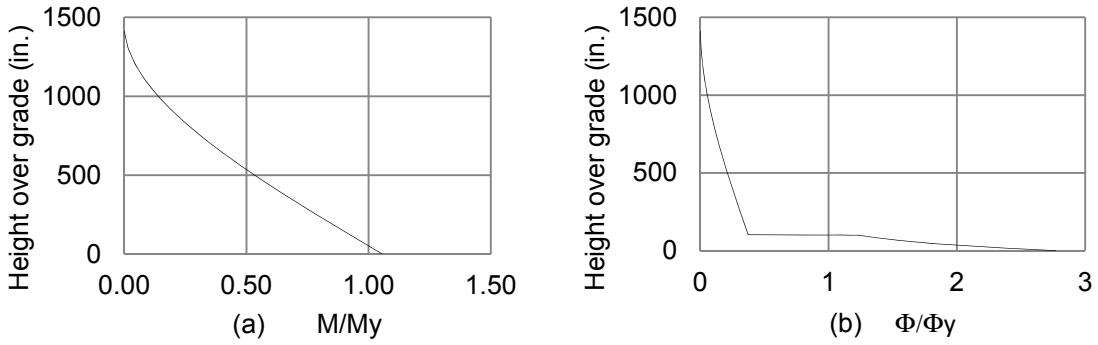

Figure 6.27 (a) Normalized moment; (b) curvature for flange in tension.

Figure 6.28 shows the calculated section strain profiles, under the assumption that plane sections remain plane.

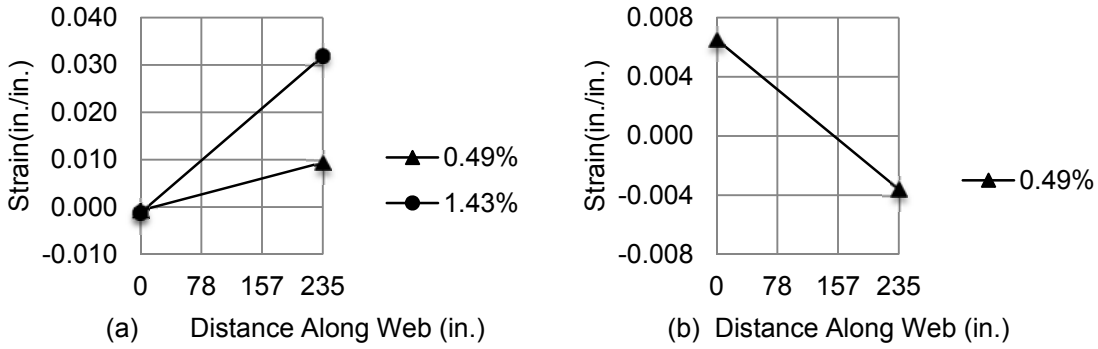

Figure 6.28 Strain profiles for wall Ñ from curvature integration: (a) flange in compression; (b) flange in tension.

Figure 6.28a shows that for the case of the flange in compression, the target drift ratio of 1.43% is reached without concrete crushing at the wall flange or bar fracture at the wall stem, and the maximum tensile strain at the wall boundary is 0.03. Figure 6.28b shows that for the flange in tension, the ultimate state is triggered by concrete crushing at the wall stem, when the maximum compressive strain reaches 0.004. The roof drift ratio at this point is 0.49%. At this drift ratio, Figure 6.28a shows a maximum tensile strain at the wall stem of 0.01 when the flange is in compression. These estimations of strain profiles at the wall base will be used later in section 6.2.9 for the evaluation of the onset of out-of-plane instability.

6.2.8.1.2 Plastic Hinge Approach

As was indicated in section 6.2.8.1.1.1, the wall has a relatively weak first story due to a setback. The nonlinear behavior will be concentrated here, and the contribution to the top displacement of the elastic deformation in the upper stories is expected to be small in comparison to the contribution given by the first story nonlinearity. A simplified plastic hinge approach according to Figure 5.3 is appropriate to model this behavior. For the case of the flange in compression, the curvature at 1.43% drift ratio is given by $\phi_u = 1.43\%/(0.5 \cdot 235) = 1.22 \cdot 10^{-4}$ in.$^{-1}$. For the flange in tension, the ultimate state is triggered by concrete crushing at the wall stem, at a curvature $\phi_u =$

$4.36 \cdot 10^{-5}$ in.$^{-1}$ and the estimated drift ratio is DR $= \phi_u \, l_p = 4.36 \cdot 10^{-5} \cdot 0.5 \cdot 235 = 0.51\%$. Figure 6.29 shows the calculated section strain profiles.

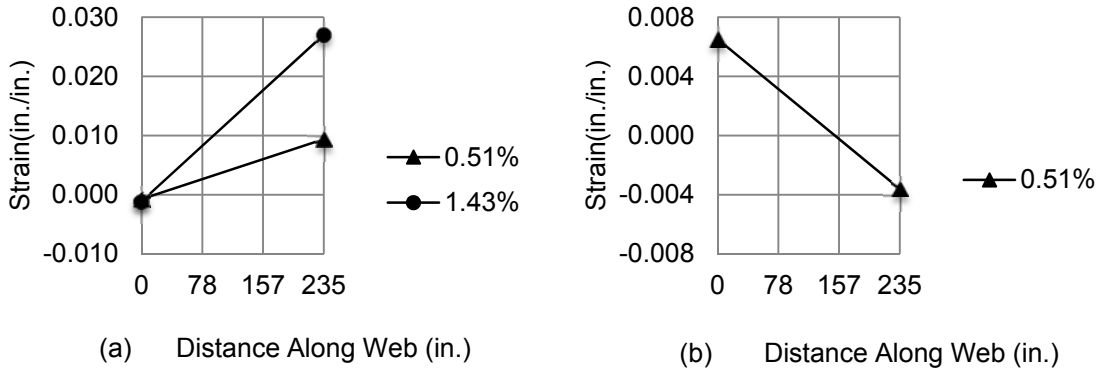

Figure 6.29 Strain profiles for wall Ñ from plastic hinge approach: (a) flange in compression; (b) flange in tension.

The strain profiles obtained from both approaches (curvature integration and plastic hinge) are very similar. There is only a minor difference in the value of drift ratio at which concrete crushing is triggered at the wall stem.

6.2.8.1.3 PERFORM 3D Model

Only for this wall, a non-linear fixed-base model was developed using PERFORM 3D. Two different analyses are performed:

a) Non-linear response history analysis. The seismic mass is calculated by tributary areas considering 50% of the live load. A factor is applied over the seismic load to get 1.43% roof drift ratio (maximum value estimated from ETABS model of the building). The ground motion is defined in section 6.2.5.

b) Pushover analysis. An inverted triangular lateral force pattern is applied. A pushover analysis is performed until reaching a roof drift ratio of 1.43%.

From these two analyses it is possible to estimate strain profiles at the wall base. Figure 6.30 shows the base-overturning moment versus roof drift ratio for the nonlinear response history analysis.

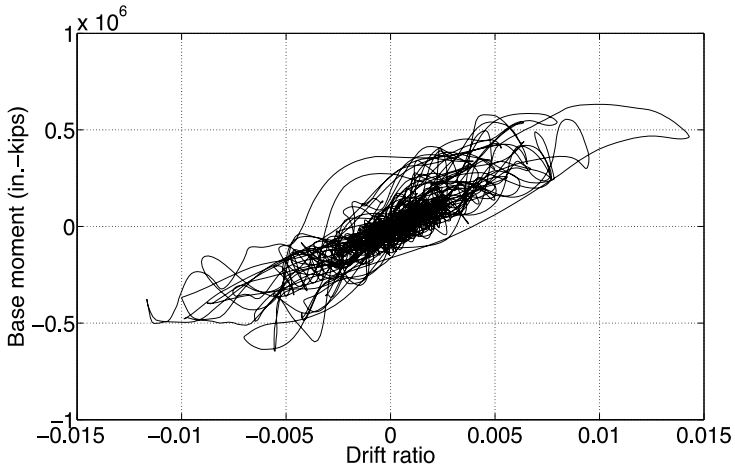

Figure 6.30 Nonlinear response history analysis – base overturning moment v/s roof drift ratio (1 in.-kips = 0.11 kN-m).

Figure 6.31 and Figure 6.32 show calculated section strain profiles from nonlinear response history and pushover analyses. Strain profiles are shown for the drift ratio that crushes the wall stem in compression and for the target drift ratio of 1.43% when the wall stem is in tension.

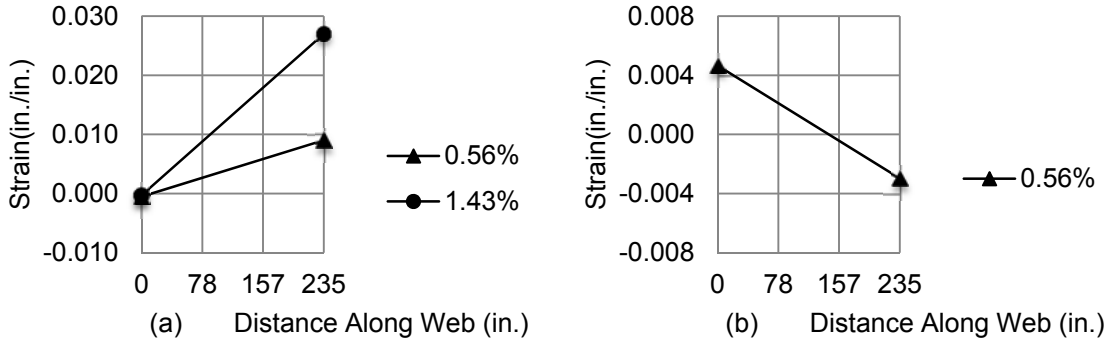

Figure 6.31 Strain profiles for wall Ñ from nonlinear response history analysis: (a) flange in compression; (b) flange in tension.

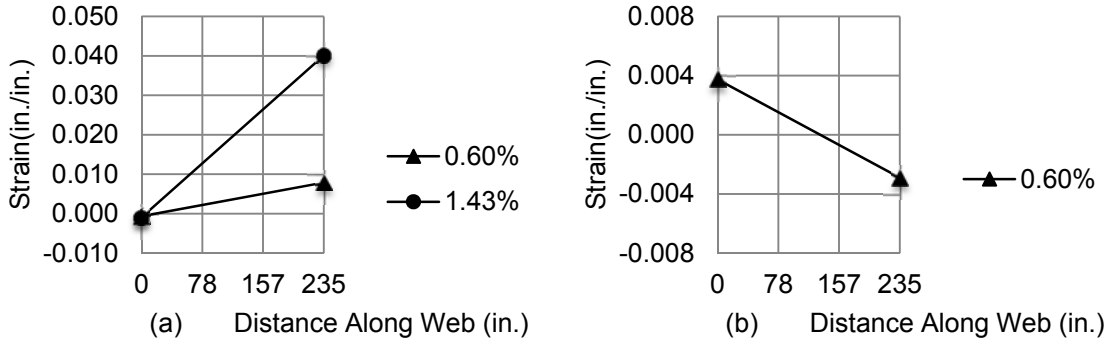

Figure 6.32 Strain profiles for wall Ñ from pushover analysis: (a) flange in compression; (b) flange in tension.

Both figures show the strain profile at 1.43% drift ratio when the flange is in compression. For this case, the maximum tensile strain at the wall stem is close 0.03 for the dynamic analysis and 0.04 for the pushover analysis. Both analyses showed crushing at the wall stem for lower drifts (close to 0.60%). At this drift ratio, when the flange is in compression, the tensile strain at the wall stem is 0.01.

6.2.8.2 Analysis of Wall in Axis K

Figure 6.33 shows the elevation of wall K. For this wall, curvature integration and the plastic hinge approach are used to estimate strain profiles at the base.

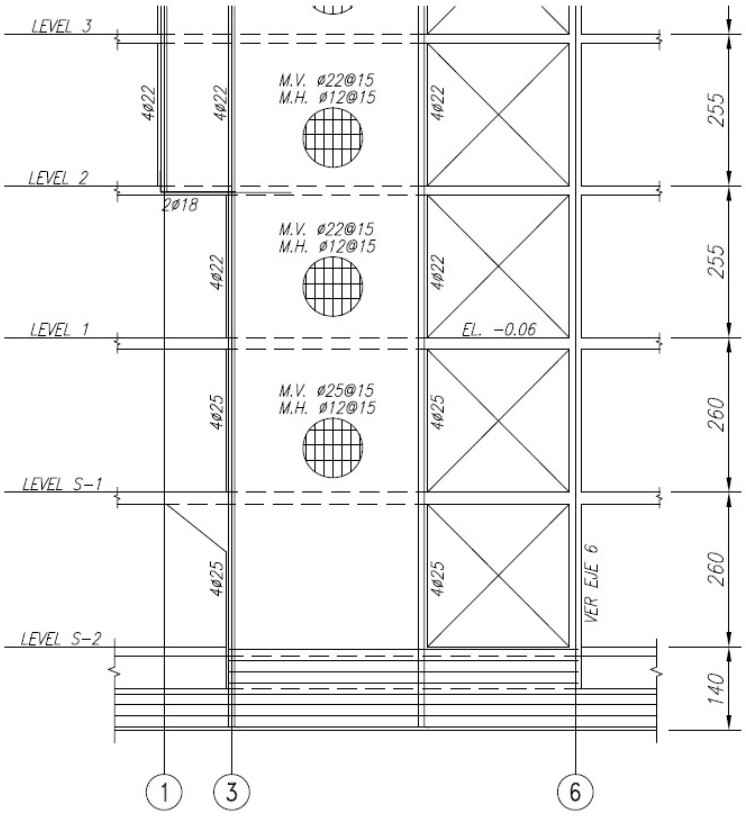

Figure 6.33 Elevation view of wall K, dimensions in cm (1 cm = 0.39 in.).

Figure 6.34 shows the tributary area for gravity loads (typical floor).

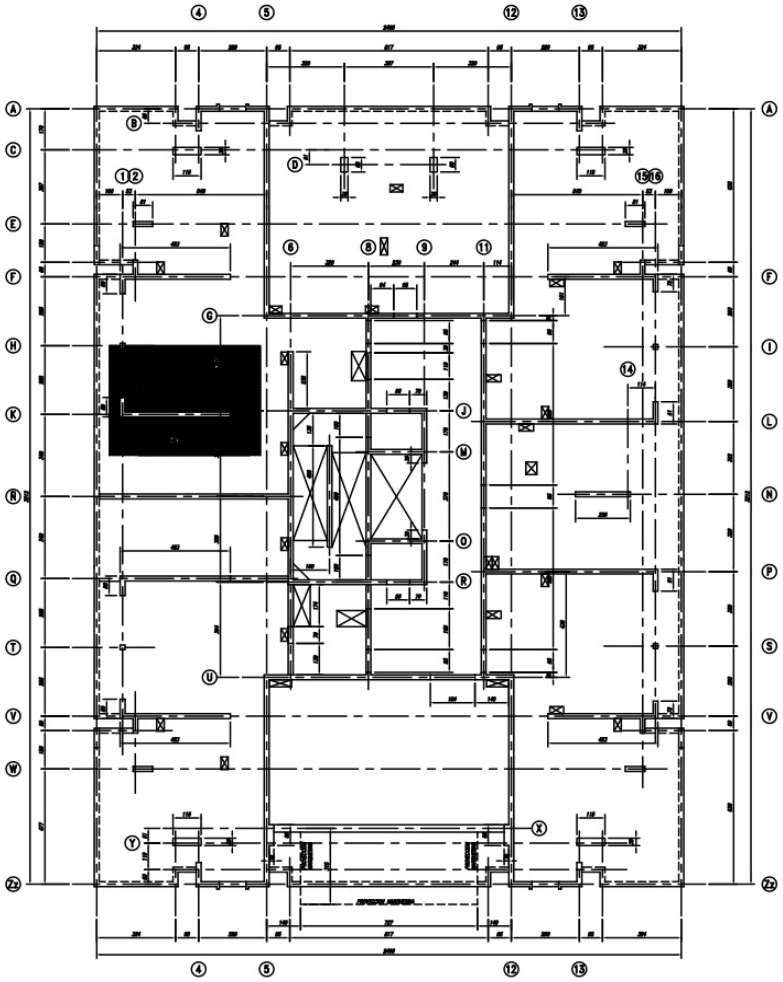

Figure 6.34 Tributary area at level 2-14 (typical floor).

Table 6.12 gives the total gravity load per floor for wall K.

Table 6.12 Gravity load per floor wall K.

Floor	Area, ft^2 (m^2)	Dead Load, kips (kN)	Live Load, kips (kN)
-2	368.34 (34.22)	41.49 (184.56)	3.77 (16.77)
-1	368.34 (34.22)	41.49 (184.56)	3.77 (16.77)
1	275.98 (25.64)	24.02 (106.85)	2.83 (12.59)
2 to 14	303.90 (28.23)	26.45 (117.66)	3.11 (13.83)
Roof	249.29 (23.16)	21.70 (96.53)	2.55 (11.34)

The axial load at the first story bottom level is P= 633 kips (2816 kN). Therefore, $P/A_g f'_c$ = 8.5%.

6.2.8.2.1 Curvature Integration Approach

This analysis follows the procedure introduced in section 6.2.8.1.1.1. Figure 6.35 shows the section properties used in the XTRACT model.

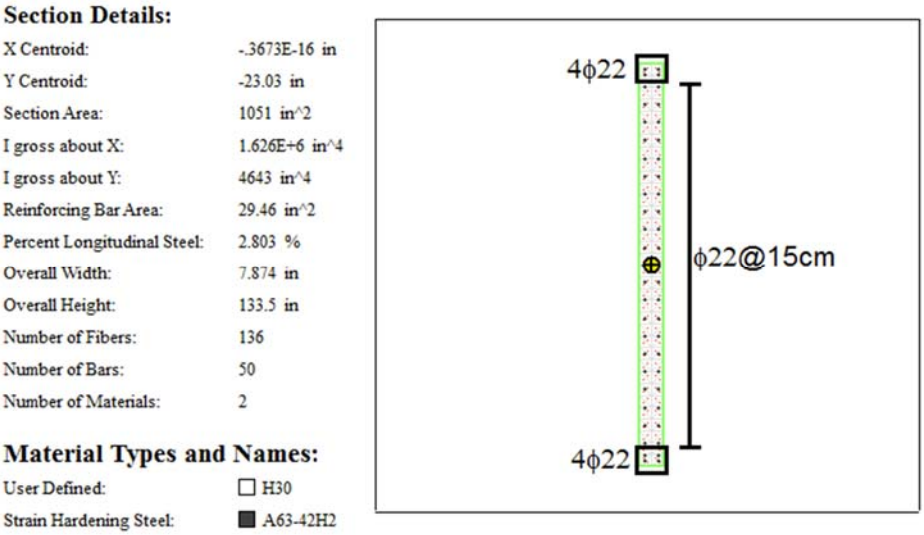

Figure 6.35 XTRACT model section properties for wall K (1 in. = 25.4 mm, bars diameter in mm).

Figure 6.36 shows the moment-curvature relation.

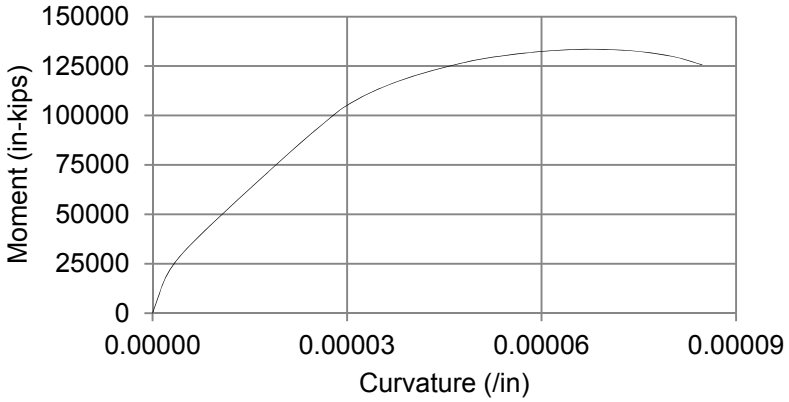

Figure 6.36 Moment-curvature relation axial load *N*=633 kips (1 in. = 25.4 mm; 1 in. - kips = 0.11 kN-m).

The lateral load pattern is also inverted triangular and was increased until reaching 1.43% drift ratio, target value obtained from ETABS. Figure 6.37 plots the normalized moment and curvature over the building height.

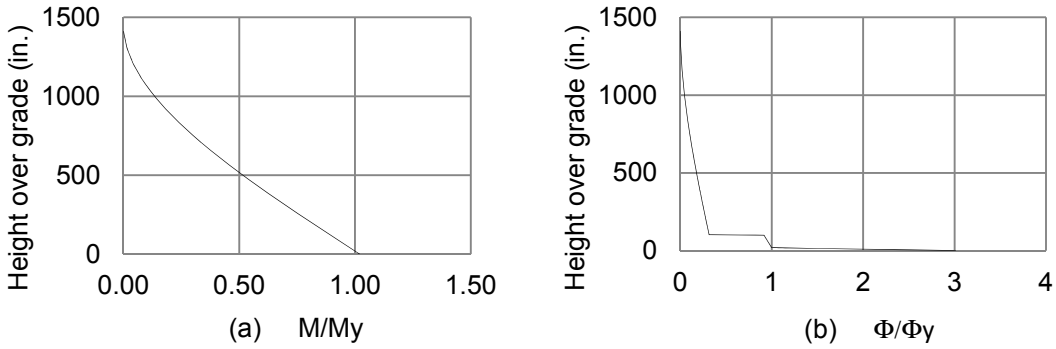

Figure 6.37 (a) Normalized moment; (b) curvature.

As expected, all the curvature demand is concentrated in the first story. Again the calculated curvature distribution shows a sharp spike toward the base level, indicating that the calculated strain and curvature may be sensitive to minor variations in the deformation or moment demands. Analysis showed that crushing at the wall boundary occurs at a drift ratio of 0.63% and a compressive strain of 0.004. For this drift, Figure 6.38 shows the calculated section strain profile. The maximum tensile strain at the opposite wall boundary is 0.008.

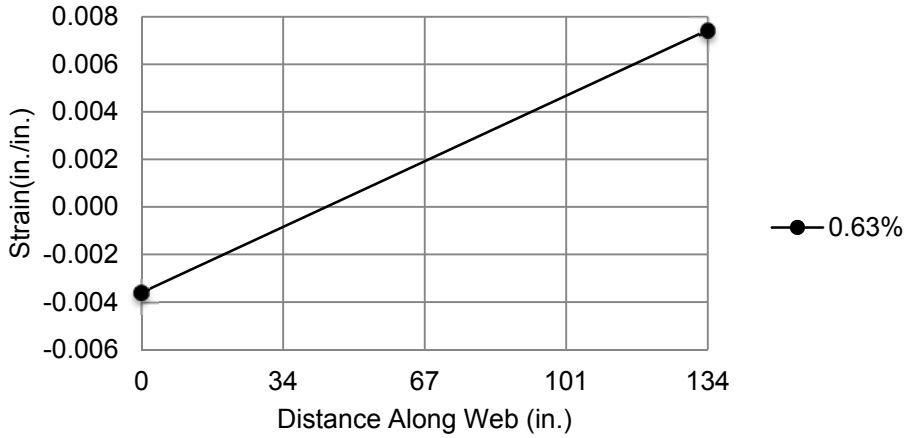

Figure 6.38 Strain profile for wall K from curvature integration.

6.2.8.2.2 Plastic Hinge Approach

A simplified plastic hinge approach according to Figure 5.3 is now used. The ultimate state is triggered by concrete crushing at the wall boundary, at a curvature $\phi_u = 8.47 \cdot 10^{-5}$ in.$^{-1}$. Therefore, the estimated drift ratio is DR $= \phi_u \, l_p = 8.47 \cdot 10^{-5} \cdot 0.5 \cdot 134 = 0.57\%$.

Figure 6.39 shows the calculated section strain profiles at the drift ratio that crushes the wall boundary in compression. The estimated value for the maximum tensile strain in the opposite boundary is 0.008.

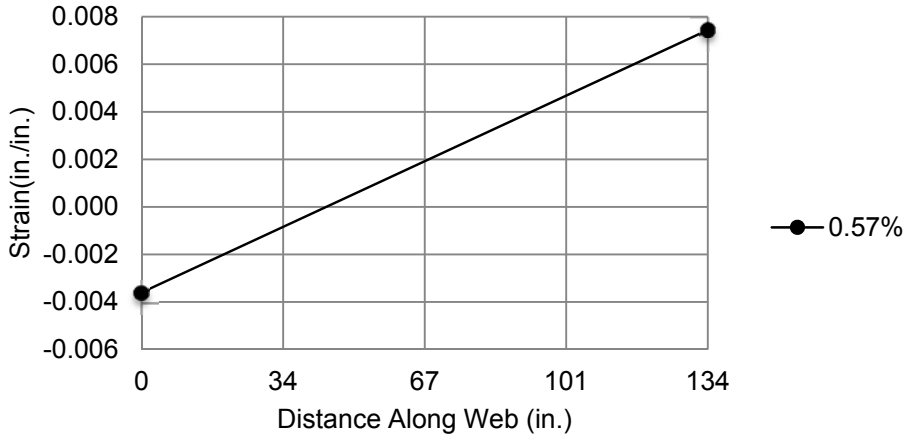

Figure 6.39 Strain profile for wall K from plastic hinge approach.

6.2.9 Evaluation of the Onset of Out-Of-Plane Instability

The simplified mechanics of section 2.2 represents a prismatic column under uniform tension/compression cycles and fixed supports at the top and bottom. The most important parameter for the evaluation of instability is the maximum tensile strain required to buckle the element during load reversal. Analysis of sections 4 and 5.3.3 showed that the simplified mechanics model can be used for cases where the strain profile is nearly uniform strain over the height, and the effect of the strain distribution along the length of the wall is not relevant when the wall length is more than $10t_w$. The analyzed walls typically have a setback at the first story by architectural requirements. For these cases, it is reasonable to assume that the plastic hinge extends over the first story height and therefore the strain demand is constant or close to constant along the first story height. Moreover, similar cases (see TW2 in section 5.3.3) show that the boundary element buckles like a fixed-fixed element at the first story. For this reason, the simplified mechanics is used here to evaluate the onset of out-of-plane instability. Table 6.13 shows the properties used in buckling calculation for these two walls.

Table 6.13 Properties for buckling calculation (1in. = 25.4 mm; 1 psi = 0.007 MPa).

Wall	Material Properties, psi		Dimensions, in.						BE Area of Longitudinal Steel A_s, in.^{2}
	f'_c	f_y	Width, b	Length, l_w	Story Height, H	h_u	BE Length, l_b	Stirrup Clear Cover, c	
Ñ	7,300	73,400	7.9	235	94	94	9	0.8	3.04
K	7,300	73,400	7.9	133	94	94	9	0.8	2.36

Table 6.14 shows the buckling calculation for these walls, considering that spalling does not occur before buckling. Therefore, the total wall width (b_w) is considered.

Table 6.14 Buckling calculation when spalling does not occur.

Wall	Wall Slenderness b/kh_u	ρ	m	ξ	κ	ϵ_{sm}
Ñ	0.17	4%	0.41	0.14	0.78	**0.034**
K	0.17	3%	0.32	0.16	0.79	**0.039**

Table 6.15 shows the buckling calculation for these walls, when spalling precedes buckling. Therefore, the core width (b_c) is considered.

Table 6.15 Buckling calculation when spalling precedes buckling.

Wall	Core Width, bc	Wall Slenderness bc/khu	ρ	m	ξ	κ	ϵ_{sm}
Ñ	4.4	0.09	7%	0.74	0.09	1	**0.013**
K	4.5	0.10	6%	0.56	0.11	1	**0.015**

For wall Ñ, different values of ϵ_{sm} were obtained from different analyses, according to Table 6.16.

Table 6.16 Boundary bar tensile strain for different analyses in wall Ñ.

Analysis	ϵ_{sm}
PERFORM 3D nonlinear response history analysis	0.03
PERFORM 3D pushover analysis DR=1.43%	0.04
Numerical integration of curvatures DR=1.43%	0.03
Simplified plastic hinge DR=1.43%	0.03

For the buckled wall Ñ, all the models produce similar conclusions, presented in Figure 6.40. For lateral loading that puts the flange in tension, the stem crushes for roof drift ratio of approximately 0.5%. According to Table 6.14, a prior peak tensile strain of $\epsilon_{sm} \approx 0.03$ is required to soften the wall sufficiently to cause out-of-plane buckling in the previously intact wall stem. To reach this peak of $\epsilon_{sm} \approx 0.03$, however, requires roof drift ratio around 1.4%. Although this drift ratio is plausible given the response spectrum for the site, it is approximately three times the drift ratio required to crush the wall stem. Therefore, it seems much more likely that the wall crushed first for loading that put the stem in compression, and the damaged section then buckled out of plane. If it is assumed that spalling of cover concrete leaves an intact core, Table 6.15 indicates that the reduced section would be prone to out-of-plane buckling at the roof drift ratio close to 0.5%.

Rectangular wall K is located immediately adjacent to wall Ñ (Figure 6.21). Therefore, it is reasonable to conclude that the walls were subjected to nearly identical displacement histories. This wall experienced minor failure in the boundary, apparently due to compression. As with wall Ñ, the wall has a setback at the first story (Figure 6.33). Simplified models integrating curvature over height, including a plastic-hinge model, were used to study likely strain demands in the first story, using the same approach as was used for wall Ñ. According to these models, crushing of the wall boundary is expected for roof drift ratio of approximately 0.6% as shown in Figure 6.40

(slightly larger than the value required for wall Ñ). Maximum tensile strain is approximately 0.008 at this drift ratio. According to Table 6.14, a prior peak tensile strain of $\epsilon_{sm} \approx 0.04$ is required to soften the wall sufficiently to cause out-of-plane buckling after spalling. These combined results indicate that crushing of the wall boundary would be expected to precede wall buckling. As noted, the wall sustained minor concrete crushing, with no evidence of out-of-plane buckling. The damage state for wall K suggests that the wall did not undergo drifts significantly exceeding 0.6% (onset of crushing). Thus, it seems even less likely that wall Ñ could have reached lateral drifts required for buckling to control the behavior.

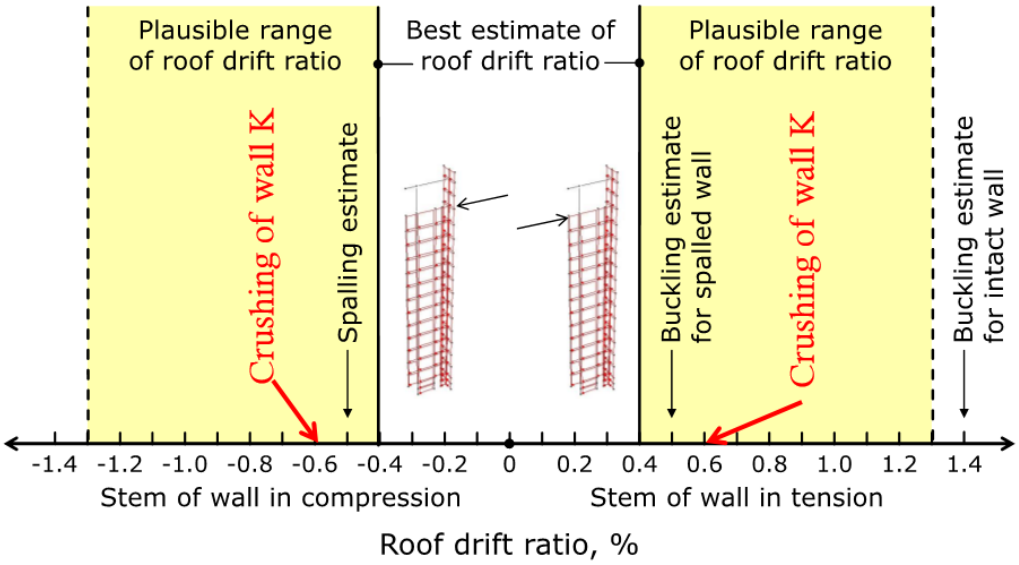

Figure 6.40 Interpretation of wall Ñ analysis.

6.3 BUILDING #2[3]

6.3.1 Building Description

Building #2 is located in Santiago, Chile. The structure was severely damaged following the 2010 Maule earthquake. The building was designed in 2006 and constructed in 2009. It has twenty stories and four subterranean levels. Its total plan area is approximately 220,660 ft^2 (20,500 m^2). The gravity and seismic force-resisting system are composed of reinforced concrete walls of 6.69 in. (170 mm) typical thickness. The typical story height is 8.27 ft (2.52 m). Figure 6.41 shows the typical plan view.

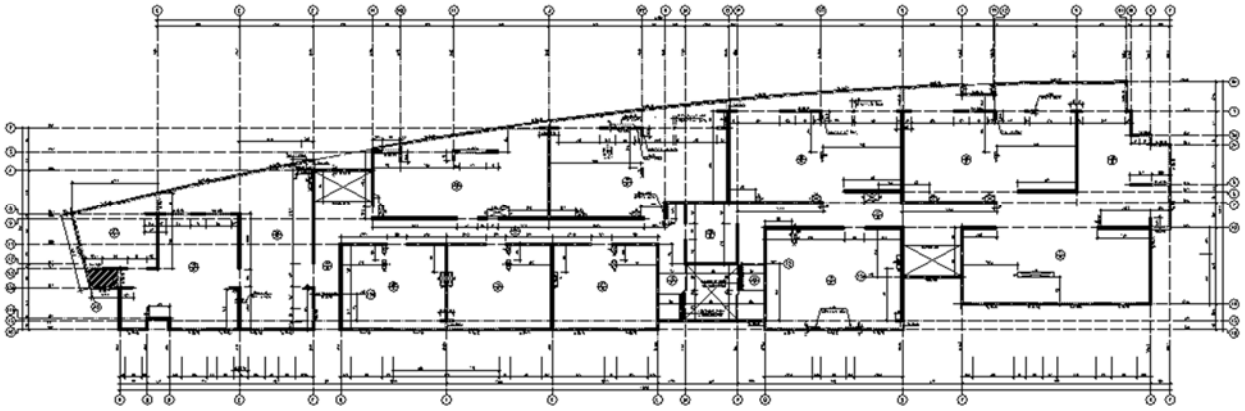

Figure 6.41 Building #2 – Typical plan view.

The damage is mainly concentrated in the first subterranean level, in walls indicated in Figure 6.42.

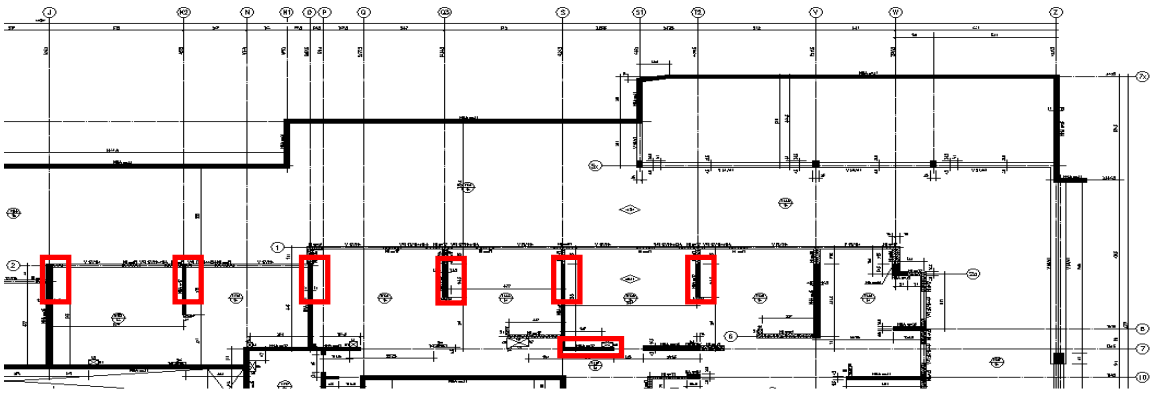

Figure 6.42 Building #2 – Damaged walls in the first subterranean level.

[3] Data for Building #2 obtained from DICTUC reports (2010 and 2012).

6.3.2 Loads and Design Standards

Gravity and seismic loads were calculated following the Chilean standards NCh 1537 Of. 1986 and NCh 433 Of. 1996. Reinforced concrete members were designed according to ACI 318 (2005). Table 6.17 shows the calculated gravity loads. For the seismic mass, 50% of live load is considered.

Table 6.17 Gravity loads per floor.

Floor	Slab thickness, in. (mm)	Dead Load, psf (kPa)	Live Load, psf (kPa)
-4 to -1	7.09 (180)	102.00 (4.88)	10.03 (0.48)
1 to 20	5.51 (140)	82.00 (3.93)	10.03 (0.48)

The parameters used in the building seismic design according to NCh 433. Of. 1996 are: building category C (importance factor I =1), seismic zone 2 ($A_0 = 0.3g$), soil type II ($T_0 = 0.30s$, $p = 1.5$) and 5% damping ratio. Equations were previously defined in section 6.2.2. Figure 6.43 presents the elastic response spectrum without response modification factor ($R^* = 1$).

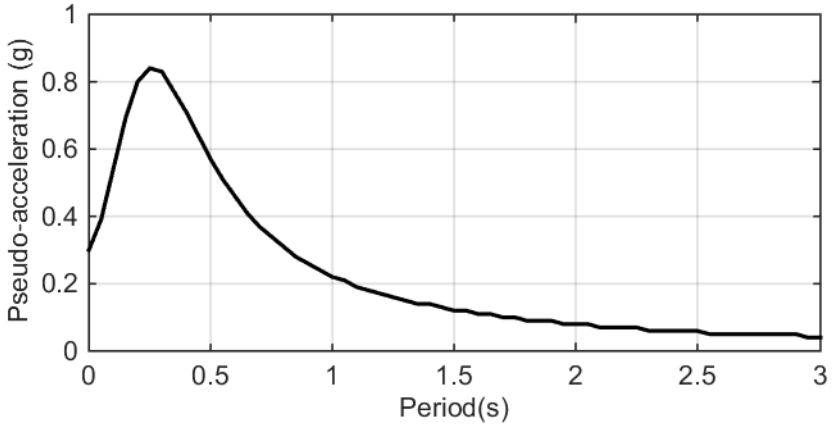

Figure 6.43 NCh 433 Of. 1996 elastic response spectrum (for *R=1).**

6.3.3 Nominal and Measured Material Properties

According to the building design documents, the nominal material properties are: concrete H25 confidence interval 90%, maximum compressive strength in cubic test specimen 3,600 psi (25 MPa) and reinforcement steel A63-42H, tensile strength f_u= 91 ksi (630 MPa), yield strength f_y = 60 ksi (420 MPa). From Table 6.2, the cylinder compressive strength is f'_c= 2,900 psi (20 MPa). For this analysis, real material properties (DICTUC, 2012) are used instead of nominal properties. Concrete compressive strength is determined from cores testing.

Two buckled walls are analyzed in this section: Walls O and K2. Compressive strengths for both walls at the first subterranean level, where out-of-plane instability occurred, are f'_c= 3,800 psi (25.9 MPa) for wall O and f'_c= 4,100 psi (28.5 MPa) for wall K2. For linear analysis, the effective flexural and axial rigidity (including cracking) is used, according to ASCE 41 (2006). Values of effective stiffness were indicated in section 6.2.3. Kent and Park (1971) unconfined concrete model is used for nonlinear analysis. Measured reinforcement properties from coupons from the building are tensile strength f_u= 110 ksi (759 MPa) and yield strength f_y = 73.3 ksi (506 MPa).

6.3.4 Recorded Ground Motion

Instruments recorded the ground acceleration during the 2010 Chile earthquake in several locations in Santiago. Three stations close to the building site, operated by University of Chile, are located in Santiago-Centro, La Florida and Peñalolén (records available in terremotos.ing.uchile.cl). The highest displacement demands are obtained for the Santiago-Centro record. This station is the closest to the building site and it is located at 3.1 miles (5 km). The soil type is expected to be similar in both sites, type II according to the Chilean standard NCh 433 Of. 1996. Therefore, the Santiago-Centro record is selected for analysis. Figure 6.44 to Figure 6.46 show the acceleration records for the three measured directions.

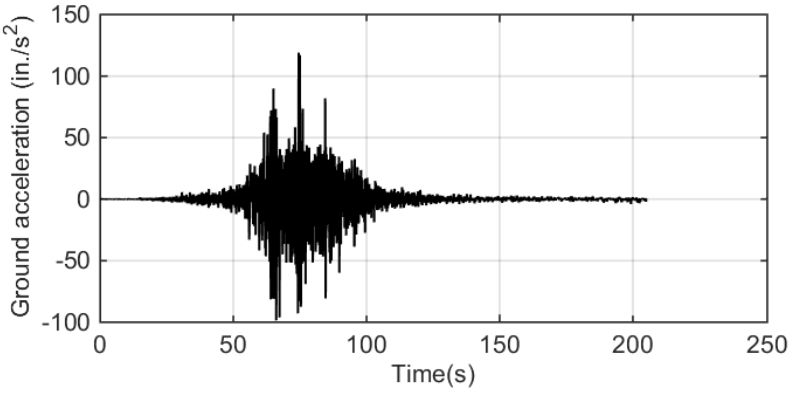

Figure 6.44 Corrected ground motion east-west direction (1 in. = 25.4 mm).

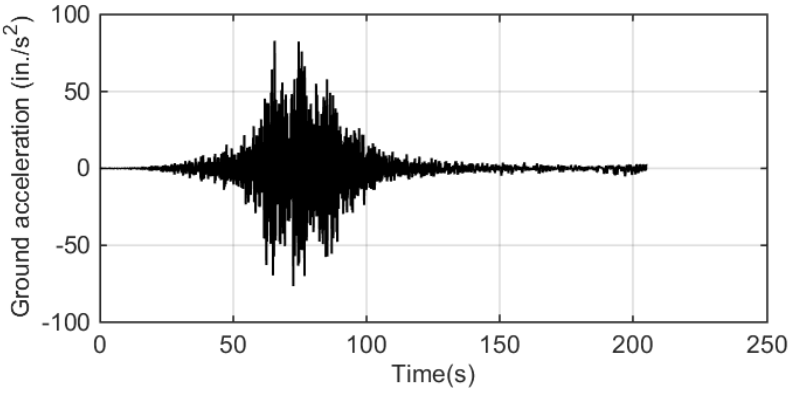

Figure 6.45 Corrected ground motion north-south direction (1 in. = 25.4 mm).

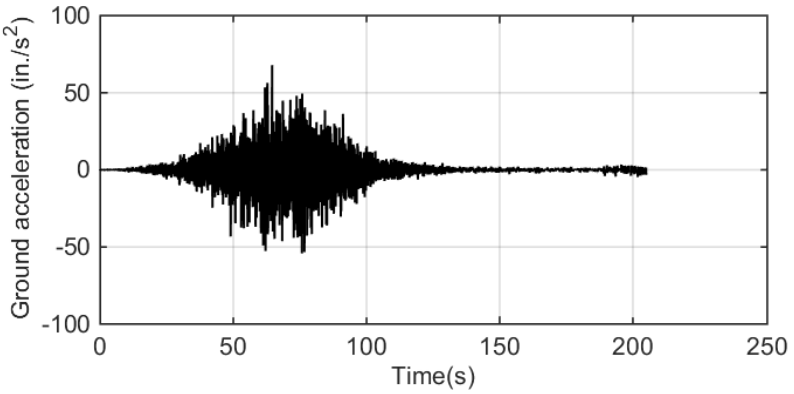

Figure 6.46 Corrected ground motion up-down direction (1 in. = 25.4 mm).

Figure 6.47 to Figure 6.49 show the pseudo acceleration, pseudo velocity, and the displacement response spectrum (2% damping ratio).

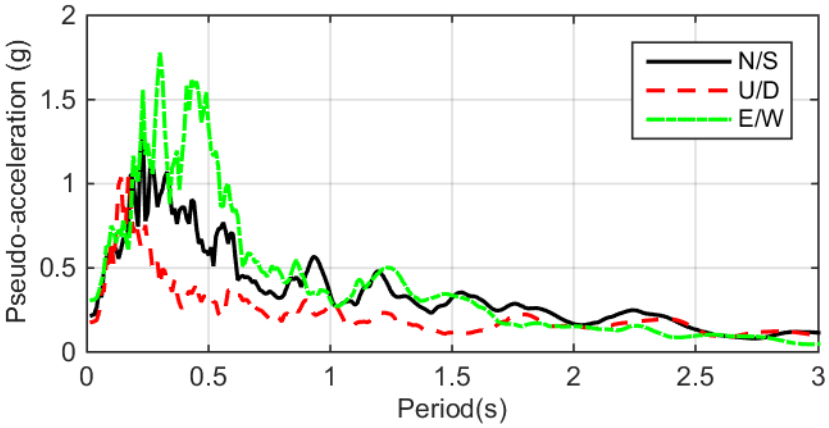

Figure 6.47 Pseudo acceleration spectrum.

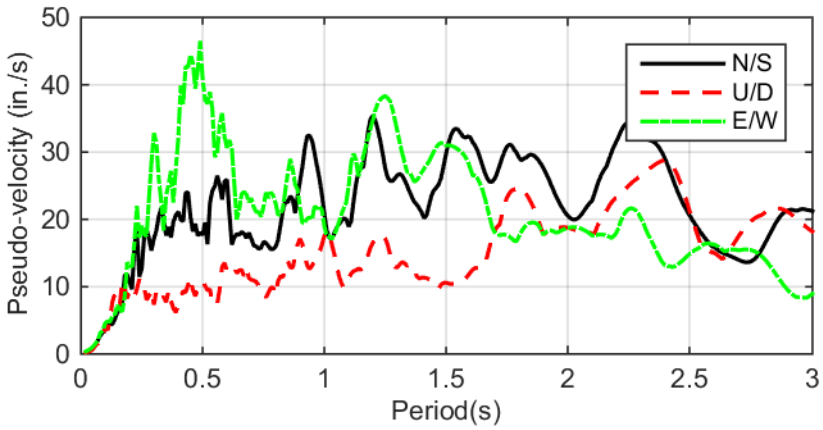

Figure 6.48 Pseudo velocity spectrum (1 in. = 25.4 mm).

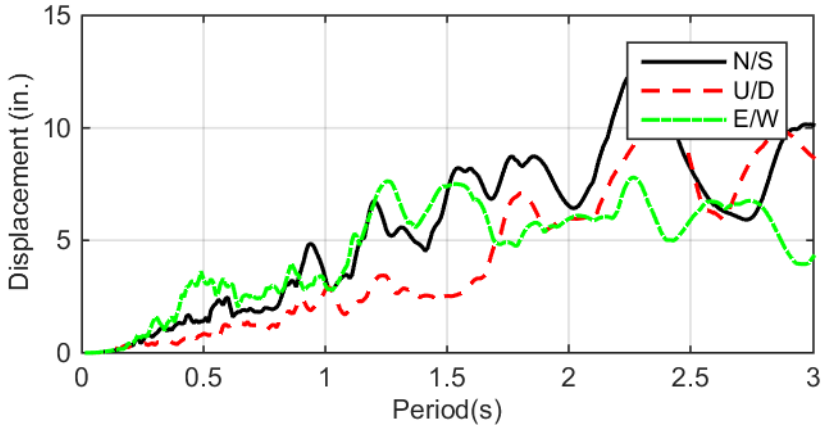

Figure 6.49 Displacement spectrum (1 in. = 25.4 mm).

From a ETABS linear analysis model of the building (section 6.3.6), the first-mode period in the east-west direction is $T = 1.56\ s$. This period is based on several assumptions regarding material properties and loads. According to Figure 6.49, in the east-west direction the peak spectral displacement is close to 7.5 in. (190 mm) for the reasonable building period range. Therefore, an estimated value for the maximum roof drift ratio is 0.60%. Figure 6.50 shows a comparison between the computed PSA spectrum (2% damping ratio) and the NCh 433 Of. 1996 design spectrum (R^*=1). The computed PSA spectrum exceeds the design spectrum at all periods.

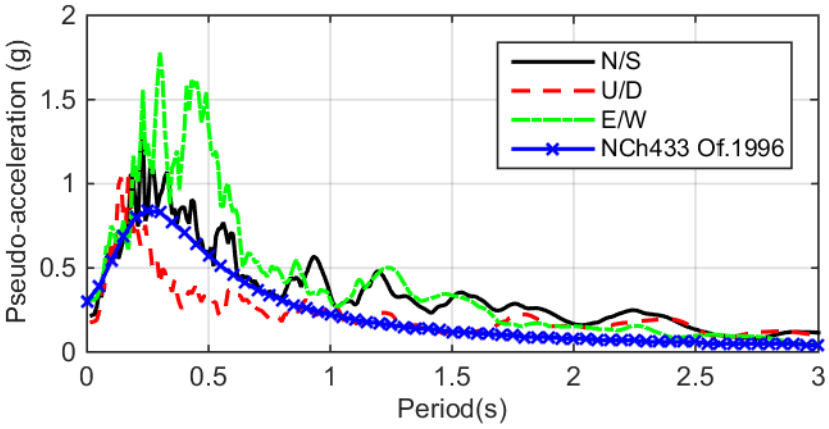

Figure 6.50 Pseudo acceleration spectrum comparison.

Figure 6.51 shows a tripartite plot for the three recorded directions.

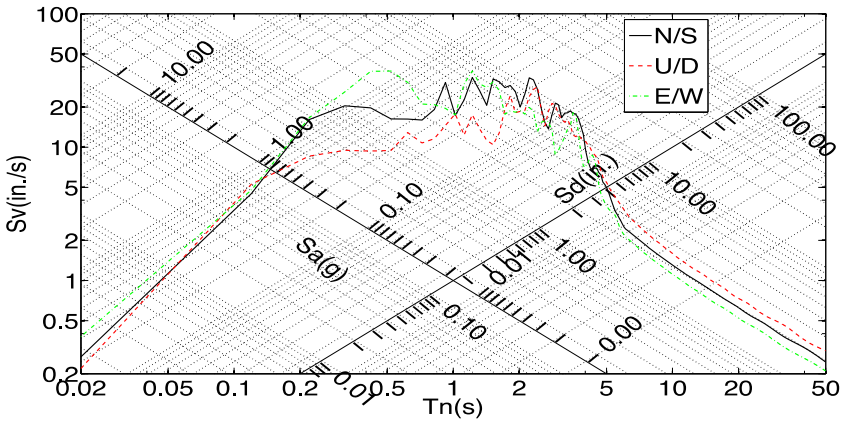

Figure 6.51 Tripartite plot for east-west, north-south and up-down motion (1 in. = 25.4 mm).

From Figure 6.51, for $T = 1.56\,s$ (first-mode period in the east-west direction) the structure is in the displacement preserved zone, and therefore the maximum roof drift ratio obtained from linear analysis is expected to be close to the nonlinear maximum drift ratio.

6.3.5 Damage Reported Following the 2010 Chile Earthquake

The main post-earthquake damage of Building #2 (DICTUC, 2010) is described in this section. Figure 6.52 shows exterior views of the building.

(a) (b)

Figure 6.52 Exterior views of Building #2: (a) west face; (b) north face (after DICTUC, 2010).

The main damage is concentrated in the first subterranean level, in six walls in the east/west direction, as pictured in Figure 6.53.

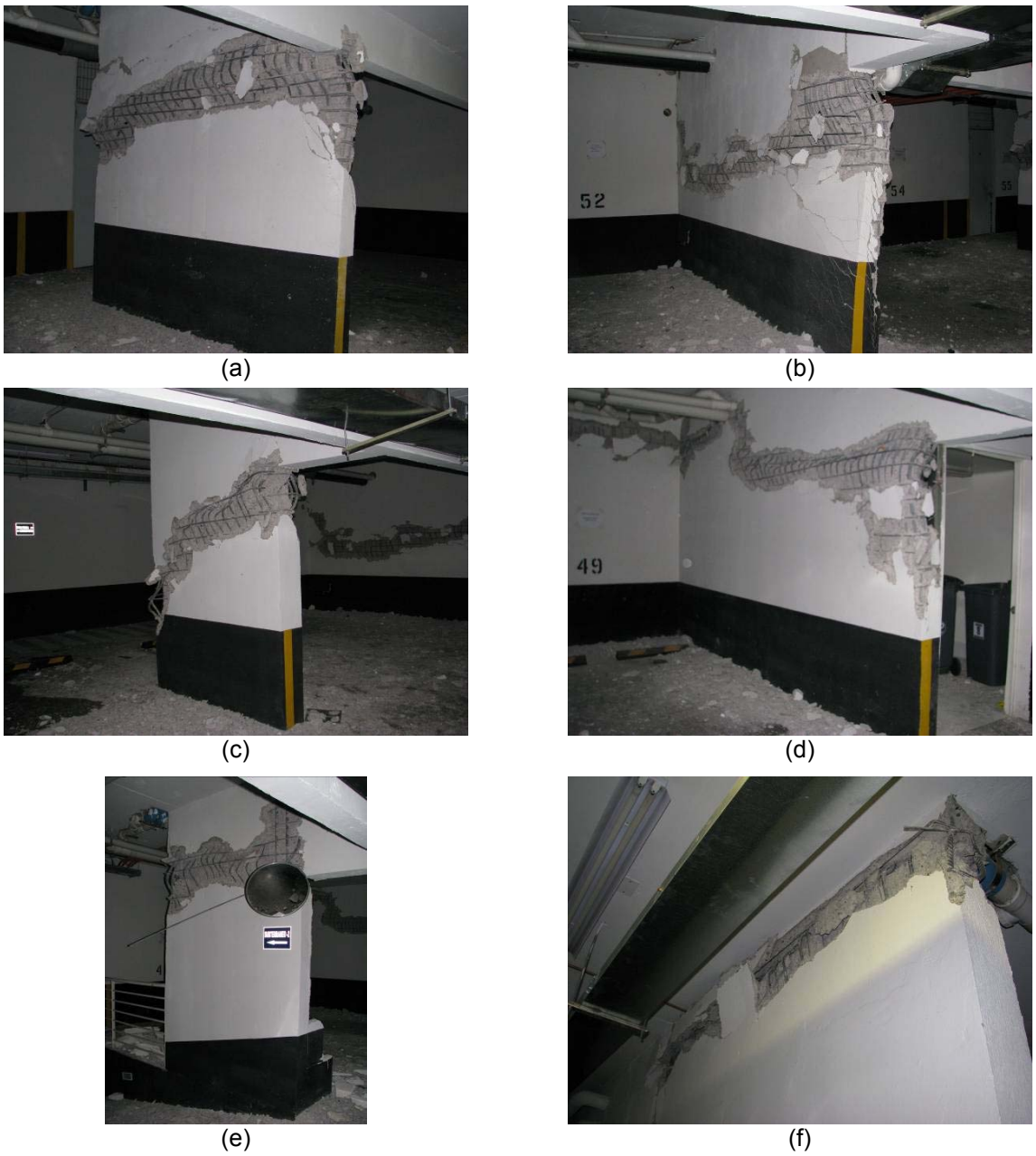

(a) (b) (c) (d) (e) (f)

Figure 6.53 Damaged walls in first subterranean level: (a) axis K2; (b) axis O; (c) axis Q3; (d) axis S; (e) axis T2; (f) axis 7 (after DICTUC, 2010).

Second to fourth subterranean levels do not show damage. In the first story, only minor damage is observed. In the second story, there is one damaged wall, as shown in Figure 6.54.

(a) (b)

Figure 6.54 Damaged walls in second story, axis J: (a) view 1; (b) view 2 (after DICTUC, 2010).

6.3.6 ETABS Model for Building #2

The onset of out-of-plane instability in slender walls of Building #2 is analyzed using nonlinear models of isolated walls. For the analysis of isolated walls, it is required first to estimate the displacement demand at the roof. This is achieved through a model of the building in ETABS and response spectrum analysis. Figure 6.55 shows the linear fixed-base model for Building #2.

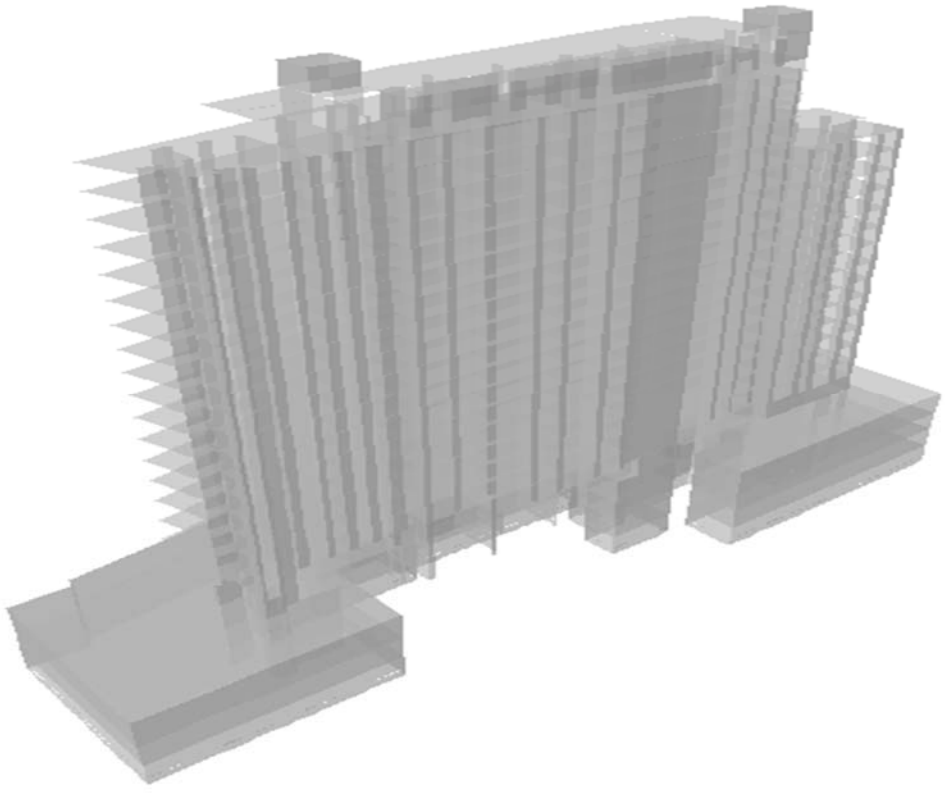

Figure 6.55 ETABS model for Building #2.

Table 6.18 shows the building modes periods and modal participating mass ratios.

Table 6.18 Modal analysis output for Building #2.

Mode	Period (s)	Modal mass ratio east-west direction	Modal mass ratio north-south direction
1	1.56	0.01	52.76
2	1.25	1.06	1.70
3	0.75	51.94	0.10
4	0.31	0.04	19.08
5	0.28	0.25	0.02
6	0.21	12.27	0.09
7	0.16	0.33	8.76
8	0.13	0.12	3.24
9	0.11	10.58	0.04
10	0.09	0.45	5.85
11	0.06	18.22	0.74
12	0.05	0.17	5.93

From Table 6.18, the third-mode has the highest effective modal mass in building longitudinal direction (north-south, $T = 0.75\ s$), and the first-mode has the highest effective modal mass in transverse direction (east-west, $T = 1.56\ s$). The two analyzed walls are both oriented in the east-west direction. Figure 6.56 shows the maximum lateral displacement over the height for the east-west direction.

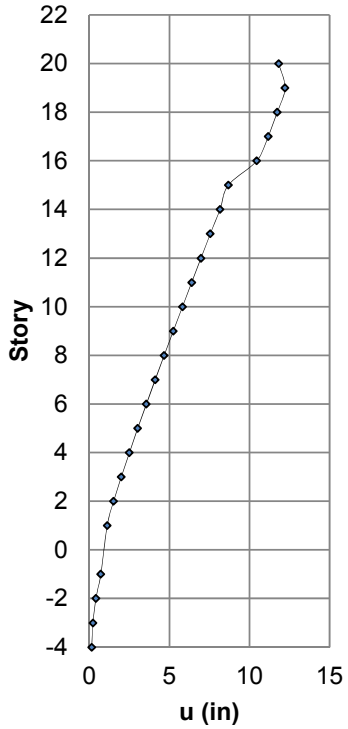

Figure 6.56 Maximum lateral displacement, east-west direction (1 in. = 25.4 mm).

Therefore, the estimated value for the maximum roof drift ratio is 0.64%, close to the estimation presented in section 6.3.4.

6.3.7 Nonlinear Models of Isolated Walls

An evaluation of the onset of out-of-plane instability requires an estimate of the maximum strain demand at the wall base. Two walls of Building #2 oriented in the east-west direction, are analyzed using nonlinear models of isolated walls. Figure 6.57 shows the selected walls in a plan view. Both walls (O and K2) showed apparent buckling following the 2010 Chile earthquake, as shown in Figure 6.53a and b.

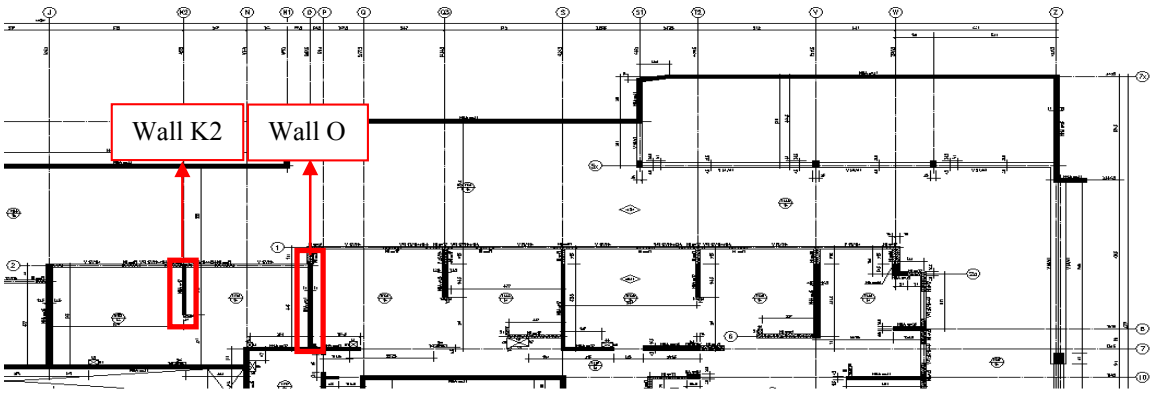

Figure 6.57 Analyzed walls for Building #2.

For this analysis, only the plastic hinge approach, according to Figure 5.3, is used to estimate strain profiles at the base for buckling evaluation.

6.3.7.1 Analysis of Wall in Axis O

Figure 6.58 shows an elevation view of wall O.

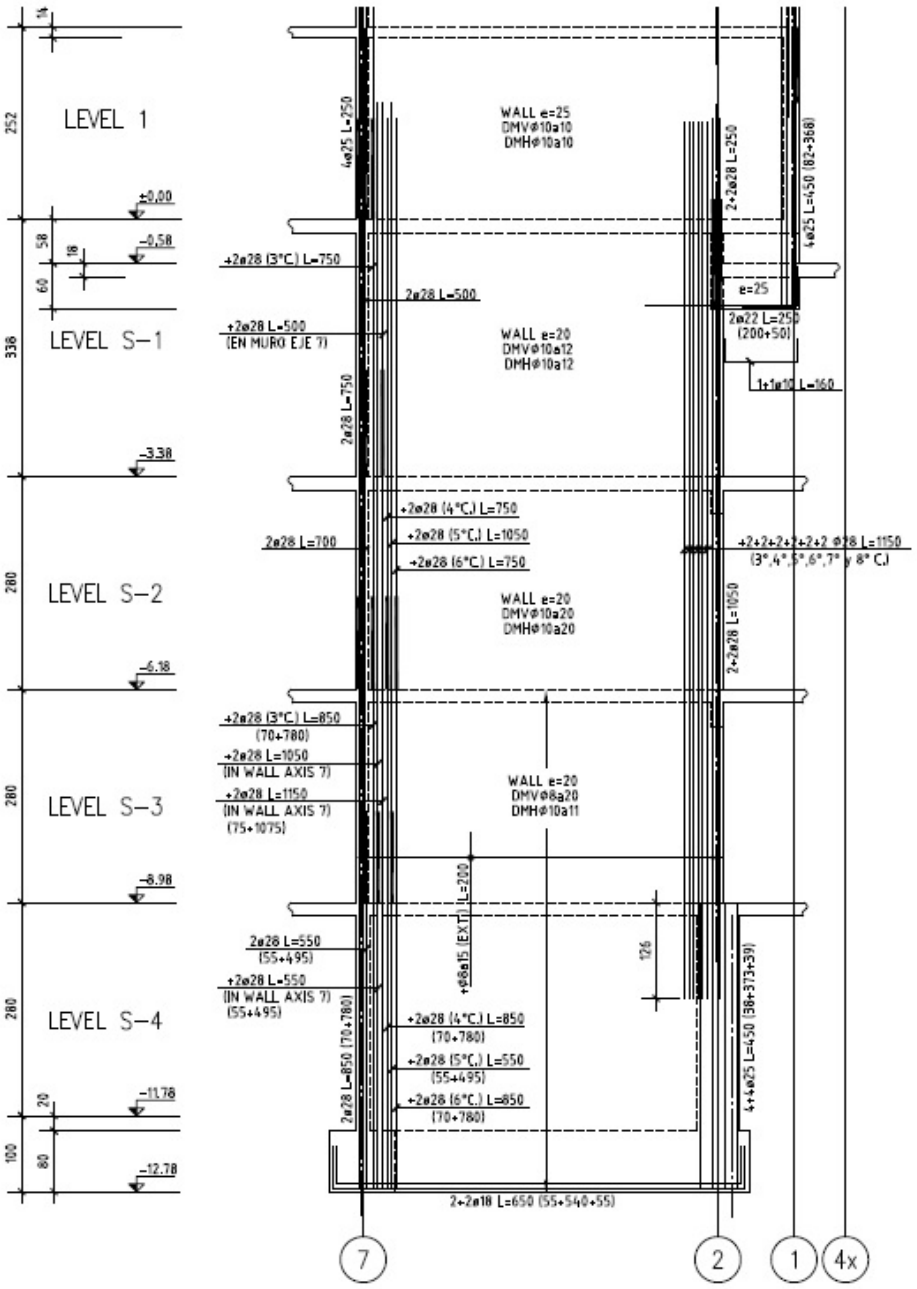

Figure 6.58 Elevation view of wall O, dimensions in cm (1 cm = 0.39 in.).

In this case, the setback is located at the first subterranean level, buckling was reported at this level (section 6.3.5), and therefore the hinge location for the plastic hinge model is considered at the first subterranean level. This simplified model considers the wall as a cantilever column with fixed base at the bottom of the first subterranean level. Therefore, a small lateral displacement is allowed at the grade level.

Figure 6.59 shows the section properties for XTRACT model.

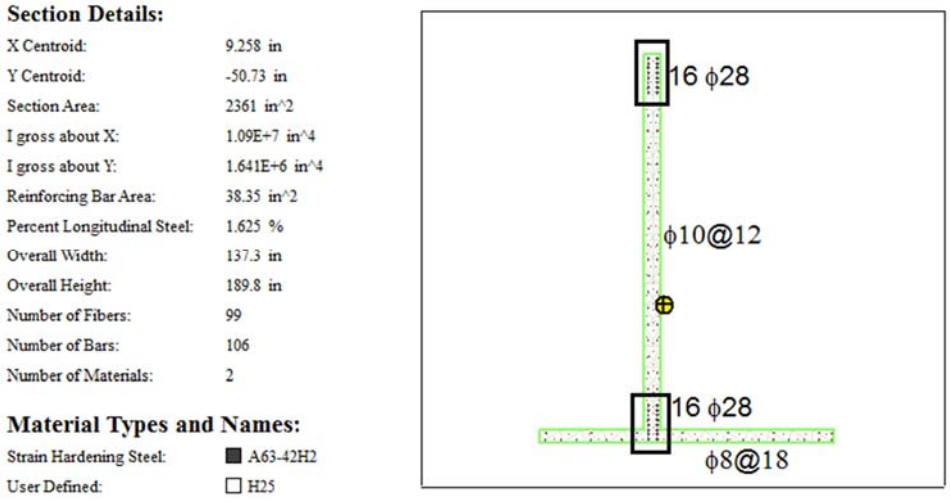

Figure 6.59 XTRACT model section properties for wall O (1 in. = 25.4 mm, bars diameter in mm).

Figure 6.60 shows the moment-curvature relations for the flange in compression and in tension.

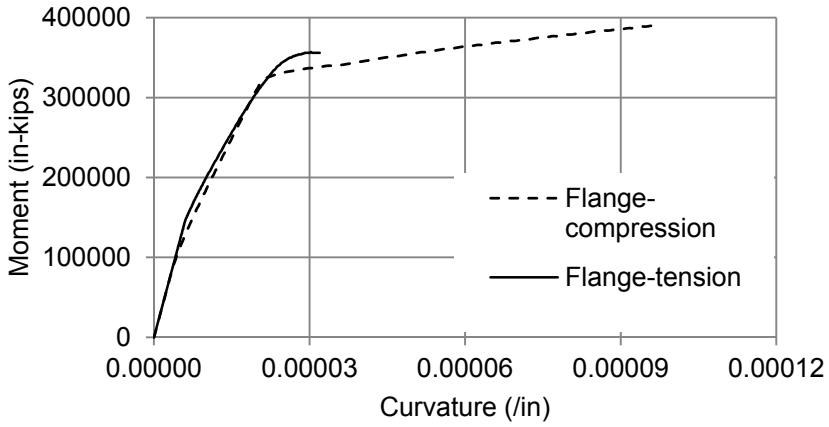

Figure 6.60 Moment-curvature relations axial load *N*= 2048 kips (1 in. = 25.4 mm; 1 in. – kips = 0.11 kN-m).

The curvature demand at the wall base for the estimated maximum roof drift ratio of 0.6% is $\phi_u = 0.6\%/(0.5 \cdot 189.8) = 6.32 \cdot 10^{-5}$ in.$^{-1}$. Figure 6.61 shows the calculated strain profiles.

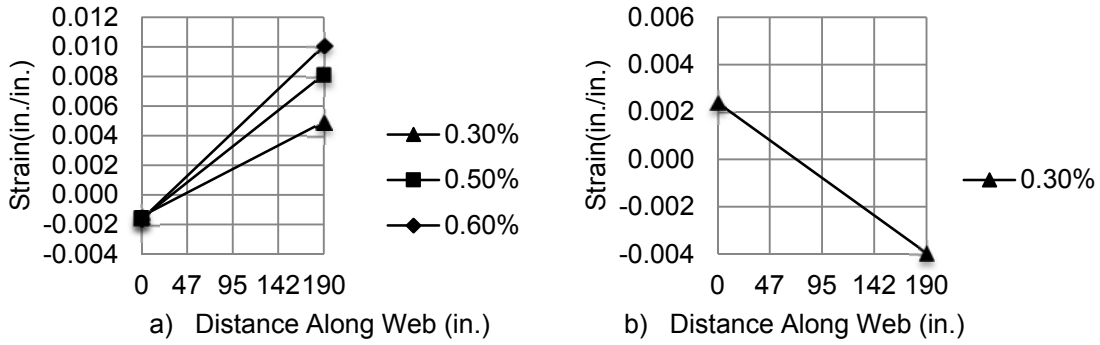

Figure 6.61 Strain profiles for wall O from plastic hinge approach: (a) flange in compression; (b) flange in tension.

Figure 6.61b shows the strain profile at the wall base for the case of the wall stem in compression at 0.3% roof drift ratio, the limit at which concrete crushing occurs at the stem. This indicates that estimated maximum roof drift ratio of 0.6% cannot be reached without crushing the wall stem first. Figure 6.61a shows the strain profile at the wall base at 0.3%, 0.5% and 0.6% roof drift ratio, for the lateral load that compresses the wall flange. For this case, the maximum tensile strain at the wall stem is close to 0.01 when the maximum roof drift ratio is reached and 0.004 for the drift that causes failure at the wall stem when the load acts in the opposite direction.

6.3.7.2 Analysis of Wall in Axis K2

Figure 6.62 shows an elevation of wall K2. As in wall O, the simplified model considers the wall as a cantilever column with fixed base at the bottom of the first subterranean level and the plastic hinge located at this level.

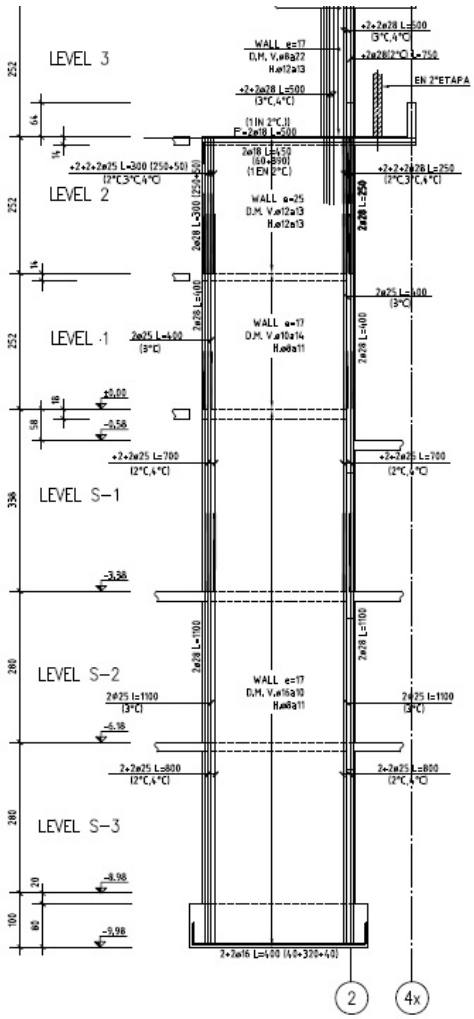

Figure 6.62 Elevation view of wall K2, dimensions in cm (1 cm = 0.39 in.).

Figure 6.63 shows the section properties for XTRACT model.

Section Details:

X Centroid:	-.4460E-16 in
Y Centroid:	86.27E-3 in
Section Area:	747.3 in^2
I gross about X:	818.8E+3 in^4
I gross about Y:	2386 in^4
Reinforcing Bar Area:	27.29 in^2
Percent Longitudinal Steel:	3.651 %
Overall Width:	6.693 in
Overall Height:	111.7 in
Number of Fibers:	120
Number of Bars:	62
Number of Materials:	2

Material Types and Names:

Strain Hardening Steel:	A63-42H2
User Defined:	H25

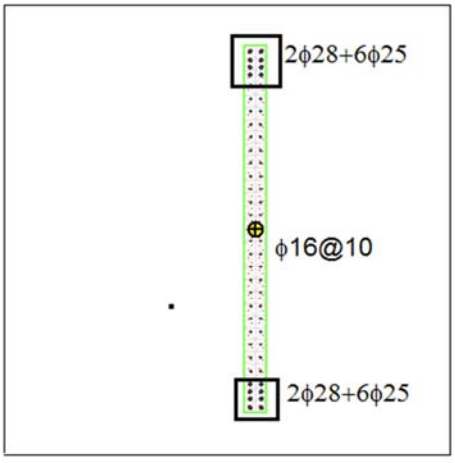

Figure 6.63 XTRACT model section properties for wall K2 (1 in. = 25.4 mm, bars diameter in mm).

Figure 6.64 shows the XTRACT moment-curvature relation.

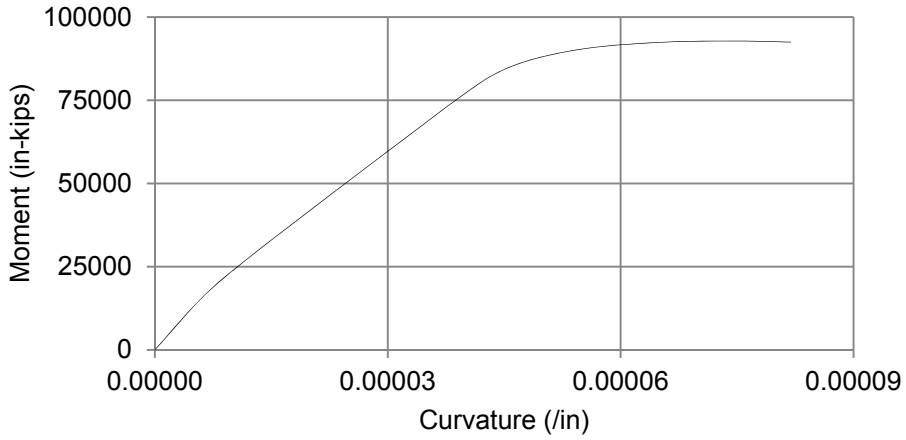

Figure 6.64 Moment-curvature relation axial load *N*= 562 kips (1 in. = 25.4 mm; 1 in. – kips = 0.11 kN-m).

The curvature demand at the wall base for the estimated maximum roof drift ratio of 0.6% is $\phi_u = 0.6\%/(0.5 \cdot 111.7) = 1.07 \cdot 10^{-4}$ in.$^{-1}$. Section analysis shows that the ultimate state is triggered by concrete crushing at the wall boundary for a curvature of $\phi_u = 8.19 \cdot 10^{-5}$ in.$^{-1}$ and a drift ratio of DR $= \phi_u \, l_p = 8.19 \cdot 10^{-5} \cdot 0.5 \cdot 112 = 0.5\%$. Figure 6.65 shows the strain profile at 0.5% drift ratio. The maximum tensile strain at the wall boundary when the opposite boundary crushes in compression is 0.005.

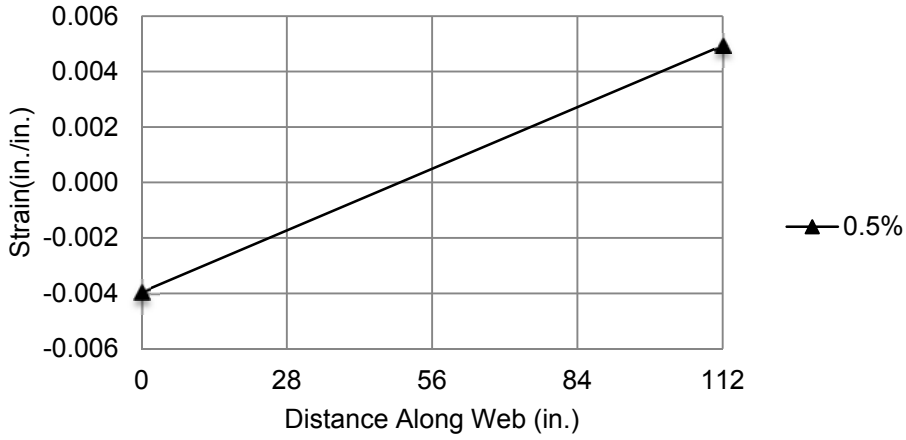

Figure 6.65 Strain profile for wall K2 from plastic hinge approach.

6.3.8 Evaluation of the Onset of Out-of-Plane Instability

Table 6.19 shows the material and section properties used in the analysis of the onset of out-of-plane instability. Table 6.20 and Table 6.21 present the buckling calculations from the simplified mechanics of section 2.2, for intact cover and spalled off cover prior to buckling.

The simplified mechanics is used here for buckling evaluation under the assumption that the strain demand over the height of the first subterranean level is close to constant, which seems to be reasonable given the geometry of the walls. According to Table 6.20, to buckle the previously intact walls O and K2 requires a maximum tensile strain close to 0.01 prior load reversal. This value can be reached at the stem of wall O at a drift ratio of 0.6% (Figure 6.61a).

In wall K2, analysis shows that reaching this strain is not possible without crushing the boundary first (Figure 6.65). Wall K2 analysis suggests that buckling was a secondary failure mode after the cover is spalled off, which occurs at a drift ratio close to 0.5%. When the onset of buckling is evaluated after the cover is spalled off, Table 6.21 indicated that reaching a tensile strain of 0.007 at the wall boundary is enough to buckle it during load reversal, and the estimated strain demand is 0.005 (Figure 6.65), which is close to the required strain. For wall O, at 0.5% drift ratio, the estimated value for the maximum tensile strain at the stem is 0.008, more than the required value to buckle the stem after the cover is spalled off according to Table 6.21. Figure 6.61b indicates that spalling at the stem of wall O occurs at a drift ratio of 0.3%.

Therefore, similar conclusions are obtained from the analysis of Buildings #1 and #2. Analyses suggest buckling of slender walls in Chilean buildings was a secondary failure model that followed crushing of the wall boundary. For Building #2, this likely occurred at a drift ratio close to 0.5% or 0.6%.

Table 6.19 Properties for buckling calculation (1in. = 25.4 mm; 1 psi = 0.007 MPa).

Wall	Material Properties, psi		Dimensions, in.						BE Area of Longitudinal Steel A_s, in.^{2}
	f'_c	f_y	Width, b	Length, l_w	Story Height, H	h_u	BE Length, l_b	Stirrup Clear Cover, c	
K2	4,100	73,300	7.9	190	126	126	10	0.8	6.47
O	3,800	73,300	7.9	112	126	126	22	0.8	15.27

Table 6.20 Buckling calculation when spalling does not occur.

Wall	ρ	m	ξ	κ	ϵ_{sm}
K2	8%	1.43	0.06	0.78	**0.012**
O	9%	1.72	0.05	0.79	**0.011**

Table 6.21 Buckling calculation when spalling precedes buckling.

Wall	Wall Slenderness b_c/kh_u	ρ	m	ξ	κ	ϵ_{sm}
K2	0.07	14%	2.56	0.04	1	**0.007**
O	0.07	15%	2.97	0.03	1	**0.007**

6.4 BUILDING #3[4]

6.4.1 Building Description

Alto Rio building was located in the city of Concepción, Chile. The structure collapsed following the 2010 Maule earthquake, as pictured in Figure 6.66. The building was designed between 2006 and 2007 and its construction was completed in 2009. It had rectangular plan with fifteen stories in the south end and twelve stories in the north end (stepped elevation at the roof level), and two subterranean levels. The maximum building height was 125 ft (38 m), the typical story height of 8.2 ft (2.5 m) with first story height of 9.8 ft (3 m). Each subterranean plan area was 11,140 ft^2 (1,035 m^2). Plan area of a typical story was 5,170 ft^2 (480 m^2). The structure comprised reinforced concrete slabs of 5.9 in. (150 mm) thickness with structural walls of 7.9 in. (200 mm) typical thickness. The building foundation was a reinforced concrete slab of 32 in. (800 mm) thickness.

Figure 6.66 Collapse of Alto Rio building following 2010 Maule earthquake, after IDIEM (2010).

[4] Data for Building #3 obtained from IDIEM reports (2010).

Figure 6.67 shows the plan view of a typical story. Figure 6.68 shows the plan view of the first story, where failure apparently triggering the collapse occurred in the short direction of the building.

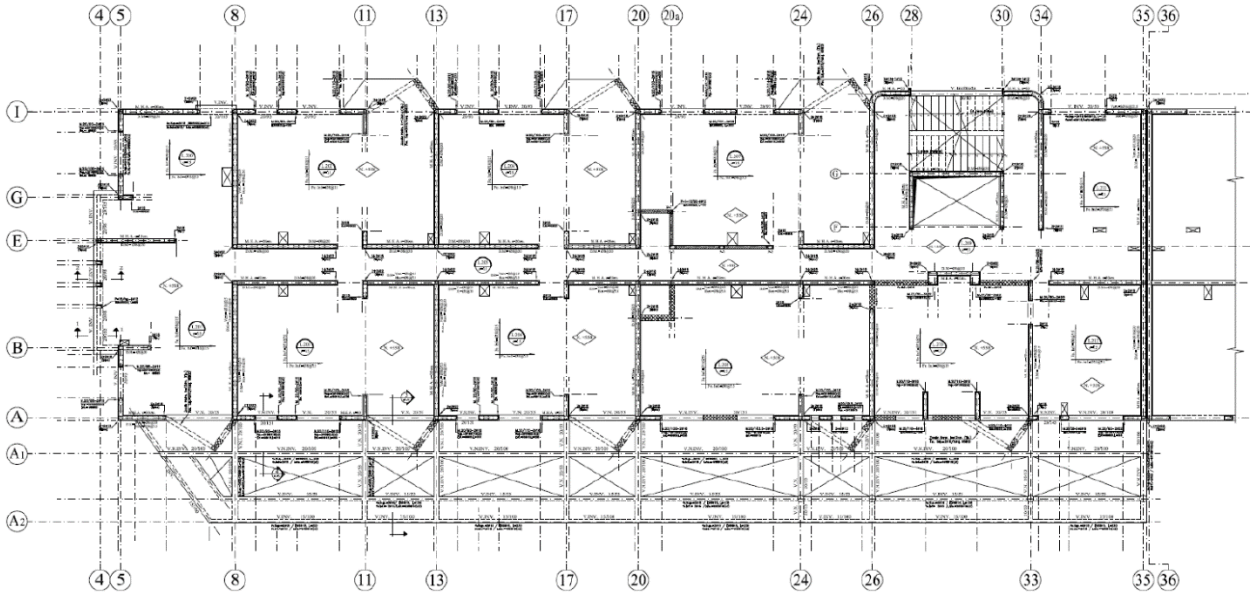

Figure 6.67 Alto Rio building – Plan view of typical story.

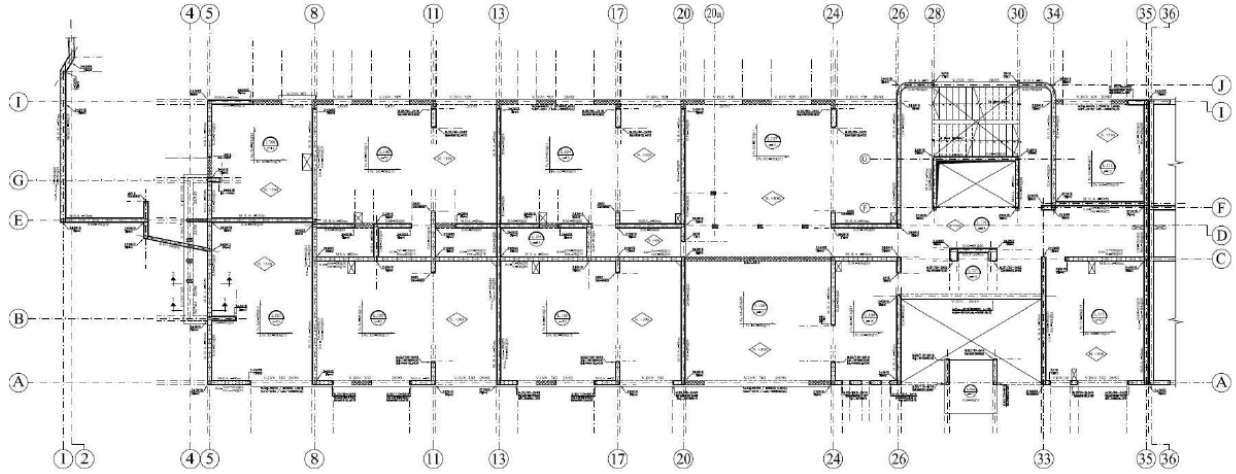

Figure 6.68 Alto Rio building – Plan view of first story.

6.4.2 Loads and Design Standards

Gravity and seismic loads were calculated following the Chilean standards NCh 1537 Of. 1986 and NCh 433 Of. 1996. Reinforced concrete members were designed according to ACI 318 (2005). The parameters used in the building seismic design according to NCh 433. Of. 1996 are: building category C (importance factor I=1), seismic zone 3 ($A_0 = 0.4g$), soil type II ($T_0 = 0.30s$, $p = 1.5$) and 5% damping ratio. Equations were previously defined in section 6.2.2. Figure 6.69 shows the elastic response spectrum without response modification factor ($R^* = 1$).

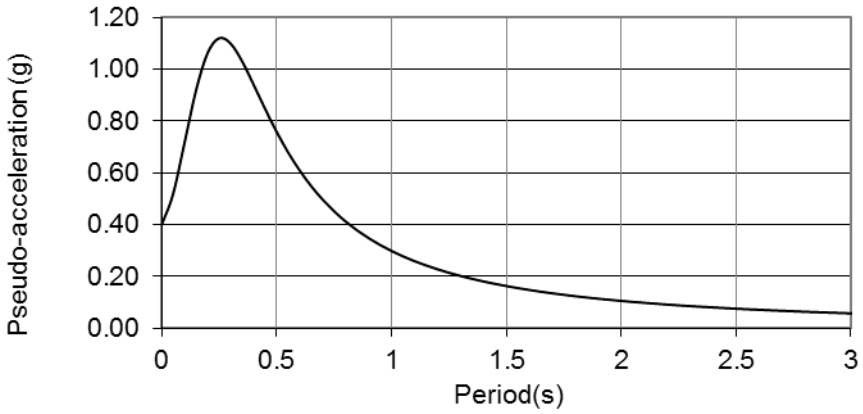

Figure 6.69 NCh 433 Of. 1996 elastic response spectrum (for R^*=1).

6.4.3 Nominal and Measured Material Properties

Specified concrete grades, according to the building design documents, are: H30 in foundations, H30 from the second subterranean level up to the second level above grade and H25 for the rest of the building. Chilean standard NCH420 Of. 2008 defines the cylinder strength f_c' for each case, and those values were indicated in Table 6.2. For this case, f_c'=2,900 psi (20 MPa) for H25 concrete, and 3,630 psi (25 MPa) for H30 concrete. The reinforcement steel grade is A63-42H, nominal tensile strength f_u= 91 ksi (630 MPa) and nominal yield strength fy = 60 ksi (420 MPa). For the evaluation of the onset of out-of-plane instability from the simplified mechanics, real material properties (IDIEM, 2010) are used instead of nominal properties. Reinforcement steel properties were measured from coupons (Table 6.22) and concrete compressive strengths were determined from cores testing (Table 6.23).

Table 6.22 Measured reinforcement steel strength at first story (IDIEM, 2010).

Bar	Location	Diameter, in. (mm)	Yielding, psi (Mpa)	Fracture, psi (Mpa)	Elongation (%)
1	Story 1, axis 8-A	1(25)	61,496(424)	105,442(727)	17.5
2	Story 1, axis 8-A	1(25)	67,007(462)	106,023(731)	19
3	Story 1, axis 13-A	0.9(22)	69,038(476)	112,114(773)	17.5
4	Story 1, axis 13-A	0.9(22)	70,633(487)	109,213(753)	17
5	Story 1, axis 13-A	0.9(22)	69,908(482)	109,939(758)	19
6	Story 1, axis 13-A	0.7(18)	69,038(476)	108,488(748)	18
7	Story 1, axis 13-A	0.6(16)	98,481(679)	111,099(766)	9.5
8	Story 1, axis 20a-B-C	0.6(16)	70,778(488)	111,824(771)	19.5
9	Story 1, axis 20a-B-C	0.5(12)	70,198(484)	102,107(704)	14
10	Story 1, axis 11-C	0.9(22)	70,633(487)	109,939(758)	17.5
11	Story 1, axis 5-A	0.7(18)	66,862(461)	97,610(673)	14
14	Story 1, axis 8-A	0.3(8)	72,954(503)	106,748(736)	12
16	Story 1, axis 11-C-B	0.9(22)	69,908(482)	109,939(758)	16
18	Story 1, axis 17-A	0.6(16)	75,710(522)	114,000(786)	14.5
20	Story 1, axis 20-A	0.6(16)	68,603(473)	100,366(692)	16.5
21	Story 1, axis 20-A	0.6(16)	72,229(498)	102,397(706)	16
22	Story 1, axis 24-C	1(25)	70,633(487)	101,381(699)	18
23	Story 1, axis 24-C	1(25)	68,893(475)	100,801(695)	20.5
24	Story 1, axis 24-A	1(25)	66,427(458)	106,603(735)	17.5
25	Story 1, axis 24-A	1(25)	63,236(436)	106,023(731)	16
26	Story 1, axis 24-A	1.1(28)	58,305(402)	97,030(669)	17.5
27	Story 1, axis 24-A	0.6(16)	72,229(498)	102,397(706)	16.5
28	Story 1, axis 26-A	0.7(18)	67,443(465)	106,748(736)	18
29	Story 1, axis 33-A	1(25)	65,847(454)	105,442(727)	20
30	Story 1, axis 33-A	1(25)	68,168(470)	99,496(686)	19
31	Story 1, axis 33-A	1(25)	66,427(458)	98,336(678)	18
34	Story 1, axis 33-C-B	0.7(18)	69,618(480)	107,328(740)	17.5
35	Story 1, axis 33-C-B	0.7(18)	68,023(469)	105,587(728)	20
36	Story 1, axis C-33-26	1(25)	68,168(470)	101,381(699)	19.5
37	Story 1, axis 35-C	0.4(10)	85,717(591)	107,473(741)	10.5

Table 6.23 Measured concrete compressive strength at first story (IDIEM, 2010).

Core	Location	Core compressive strength, psi (Mpa)	Cylinder compressive strength, psi (Mpa)	Cubic compressive strength, psi (Mpa)
T1	Story 1, axis 8 B-C	6,301(43.4)	(*)	(*)
T2	Story 1, axis E 5-8	4395(30.3)	4153(28.6)	4,864(33.5)
T3	Story 1, axis C 8-11	6,585(45.4)	(*)	(*)
T4	Story 1, axis 20a A-C	6,059(41.8)	(*)	(*)
T5	Story 1, axis 24 A-B	6,514(44.9)	(*)	(*)
T10	Story 1, axis 5 I-G	5,874(40.5)	(*)	(*)
T11	Story 1, axis E 2-5	7,325(50.5)	(*)	(*)
T25	Story 1, axis A 17-20	6,329(43.6)	(*)	(*)

(*) Not reported.

The evaluation of the onset of out-of-plane instability is performed for three walls, all oriented in the building short direction, in axes 8, 13 and 20, between axes D and I. Instability is expected to occur at the first story. Therefore, for analysis, measured material properties at the first story are considered. Reinforced bars used in wall stems had diameters 0.9 in. (22 mm) and 0.7 in. (18 mm). The average measured yielding stress these bars was 69 ksi (476 MPa). Analysis of the wall in axis 8 considers the concrete compressive strength measured in core T1 of 6.3 ksi (43 MPa). For walls in axes 8 and 20, analysis is performed considering the concrete compressive strength measured in core T4 of 6.0 ksi (41 MPa). For all cases, strength reduction factors due to core slenderness are negligible.

6.4.4 Recorded Ground Motion

Instruments recorded the ground acceleration during the 2010 Chile earthquake in Colegio Inmaculada Concepción, located in downtown Concepción at 0.7 miles (1.2 km) from the building site. This station, operated by University of Chile, is the closest to the building site (record available in terremotos.ing.uchile.cl). The site where the record was obtained and the building site are located in the same type of soil, alluvial deposits of the Bio-Bio river (Ramirez and Vivallos, 2009), and ground motions are expected to be similar. The ground motion measured in downtown Concepción is considered for analysis. Figure 6.70 to Figure 6.72 show the acceleration records for the three measured directions, where the east-west direction corresponds to the transverse (short) direction of the building.

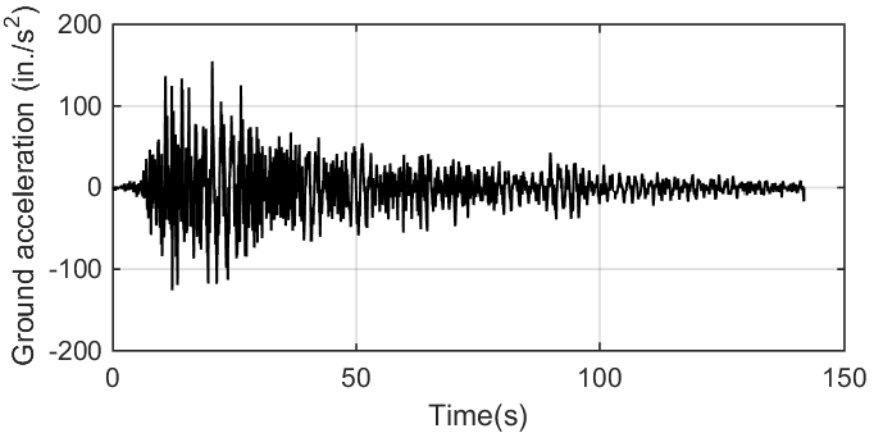

Figure 6.70 Corrected ground motion east-west direction (1 in. = 25.4 mm).

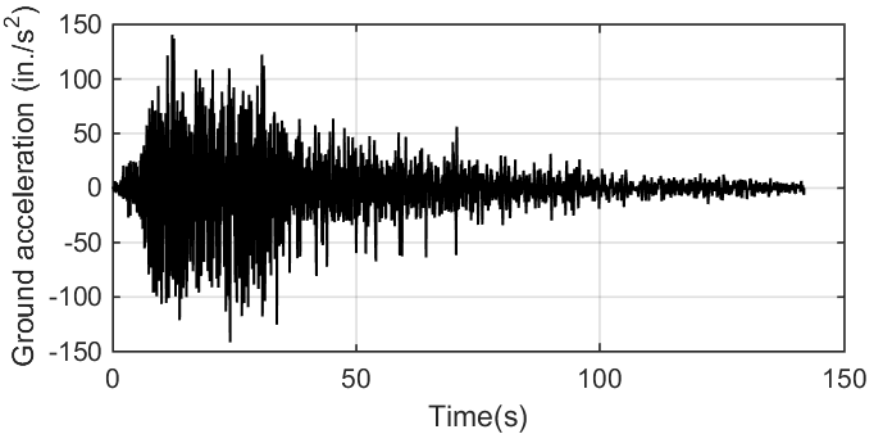

Figure 6.71 Corrected ground motion north-south direction (1 in. = 25.4 mm).

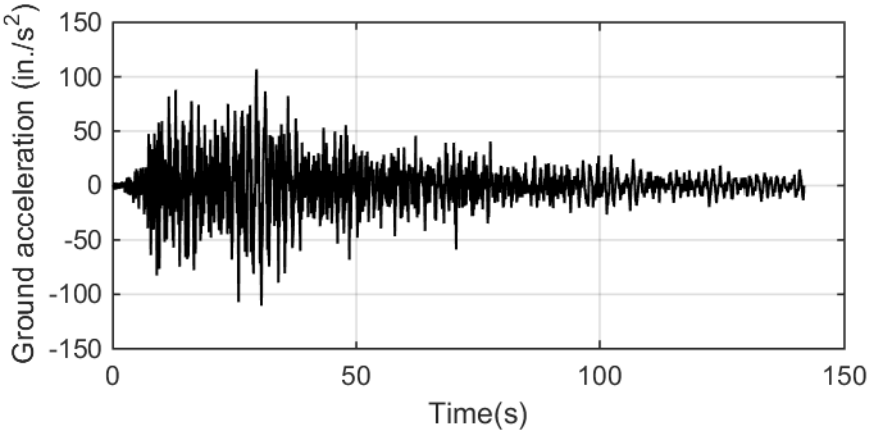

Figure 6.72 Corrected ground motion up-down direction (1 in. = 25.4 mm).

Figure 6.73 to Figure 6.75 show the pseudo acceleration, pseudo velocity, and the displacement response spectrum, calculated for 2% damping ratio.

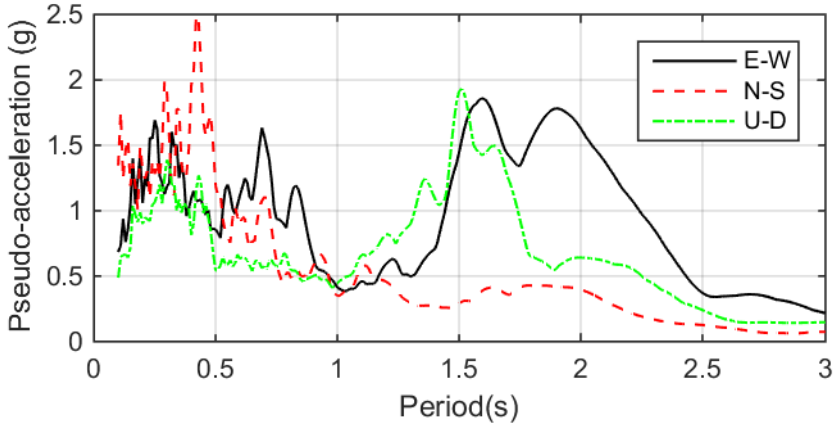

Figure 6.73 Pseudo acceleration spectrum.

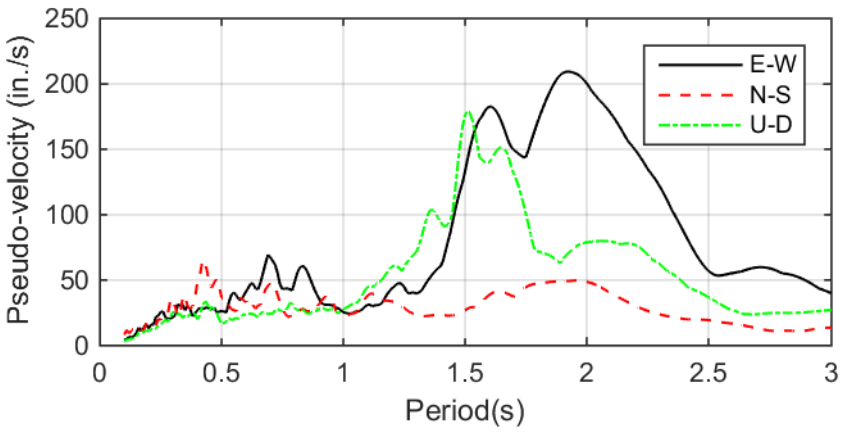

Figure 6.74 Pseudo velocity spectrum (1 in. = 25.4 mm).

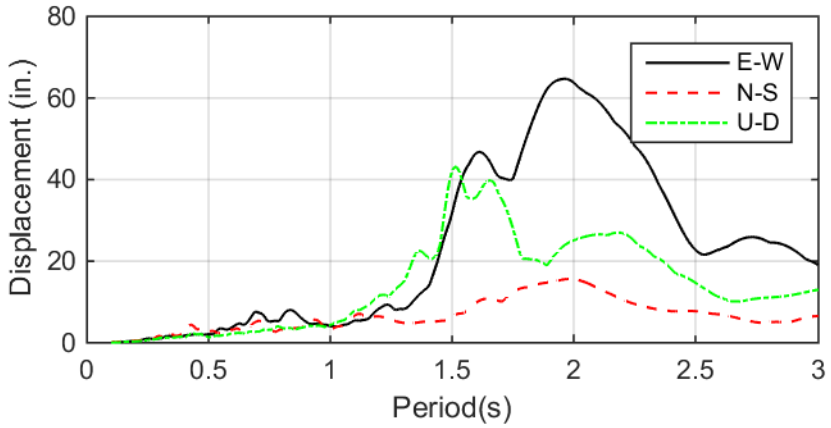

Figure 6.75 Displacement spectrum (1 in. = 25.4 mm).

Table 6.24 shows the building vibration periods reported by Tanyeri (2014). Values were obtained from a linear elastic model of the complete structure using the software ETABS. The model considered effective flexural stiffness of $0.5E_cI_g$ according to ASCE 41-06, where E_c is the concrete Young's modulus of 4,470 psi (31 MPa) and I_g is the second moment of inertia of the gross section. The Young's modulus E_c was calculated from ACI318 considering measured strength obtained from core tests (IDIEM, 2010). The seismic mass considered 25% of the live load. The model included flexibility of walls and columns extending below the grade level, but lateral translational degrees of freedom were fixed at the lowest subterranean level.

Table 6.24 Calculated vibration periods, after Tanyeri (2014).

Mode	Period (s)	Direction
1	0.81	Tranverse
2	0.71	Longitudinal
3	0.58	Torsional
4	0.19	Longitudinal
5	0.17	Transverse
6	0.14	Torsional

Tanyeri (2014) reported roof drift ratios of 0.7% in the building transverse direction and 0.46% in the longitudinal direction, both obtained from response spectrum analysis with 2.5% damping ratio, considering the ground motion recorded in downtown Concepción. Analyses of Chilean buildings in this research consider 2% damping ratio for response spectrum analysis. From Figure 6.75, for the reasonable period range in the transverse direction (where the three selected walls are oriented), the estimated displacement of a SDOF system is 8 in. This gives an estimation of the roof drift ratio of 0.85%, the value considered for this study. This is consistent with the roof drift ratio reported by Hilson (2014).

Figure 6.76 shows a comparison between the computed PSA spectrum (2% damping ratio) and the NCh 433 Of. 1996 design spectrum (R^*=1). The computed PSA spectrum exceeds the design spectrum at many periods.

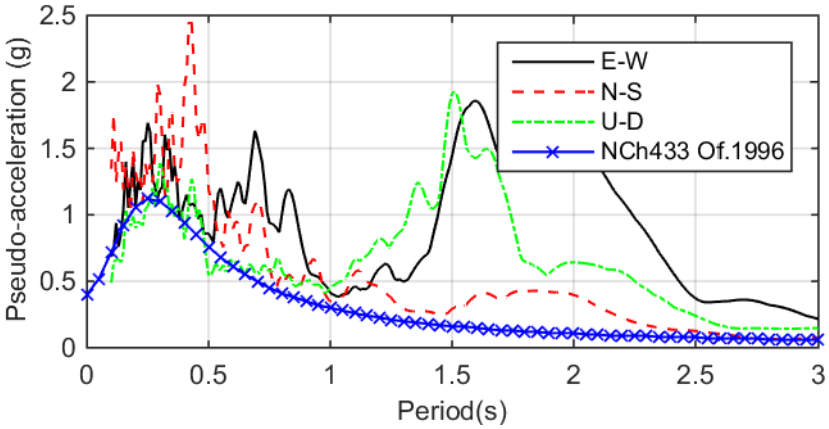

Figure 6.76 Pseudo acceleration spectrum comparison.

Figure 6.77 shows a tripartite plot for the three recorded directions.

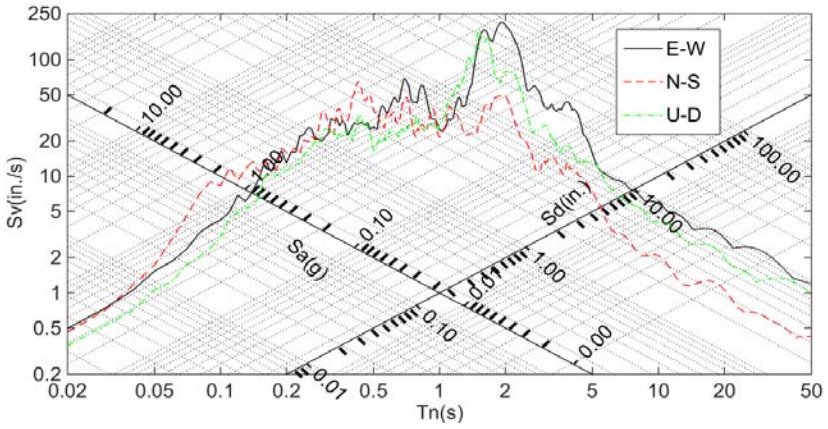

Figure 6.77 Tripartite plot for east-west, north-south and up-down motion (1 in. = 25.4 mm).

From Figure 6.77, for $T = 0.81\,s$ (first-mode period in the east-west direction) the structure is in the displacement preserved zone, and therefore the maximum roof drift ratio estimated from linear analysis (0.85%) is expected to be close to the nonlinear maximum drift ratio.

6.4.5 Damage Reported Following the 2010 Chile Earthquake

The building collapsed completely during the 2010 Chile earthquake. This section presents highlights of the damage observed during post-earthquake inspection (IDIEM, 2010), with special focus on walls in axes 8, 13 and 20, all oriented in the building short direction (east-west). These are the walls selected to perform an evaluation of out-of-plane instability. Figure 6.78a and b show two post-earthquake views of building, both taken from the north side. Inspection showed that the podium level was the critical level of the structure and the building upper portion rigidly overturned in the east direction and collapsed, with the west side of the building subjected to high tensile forces and the east to high compressive forces (Tanyeri, 2014). When the building collapsed, its east side impacted the wall located at the perimeter of the subterranean level, which seems to have caused the fracture at the ninth level of the building, as pictured in Figure 6.78. Inspection of the foundation did not show significant damage.

(a) (b)

Figure 6.78 Collapse of Alto Rio building, a) view from the north side towards east, b) view from the north side towards west (after IDIEM, 2010).

In axis 8, the failure was observed at the base of the first story, near the intersection with axis A. Then the failure surface climbed to a height of 16 in. (0.4 m) over the base and progressed horizontally until axis B, where it climbed diagonally again until axis C and then declined gradually towards the base (Figure 6.79a). Figure 6.79b shows lap splice failure at the intersection of axes 8 and A. Figure 6.79c shows compressive failure in axis 8 between axes A and B. Figure 6.79d shows lap splice failure and bar fracture at the intersection of axes 8 and C.

(a) (b)

(c) (d)

Figure 6.79 Damage in axis 8 (after IDIEM, 2010).

In axis 13, the failure was observed at 71 in. (1.8 m) above the base at the first story, near the intersection with axis A. Then the failure surface declined gradually towards the base until a height of 32 in. (0.8 m) and progressed further to the base until reaching axis C (Figure 6.80). Figure 6.80e shows that the concrete at the intersection of axes 13 and A was completely crushed due to large compressive force and poor lateral confinement.

(a) (b)

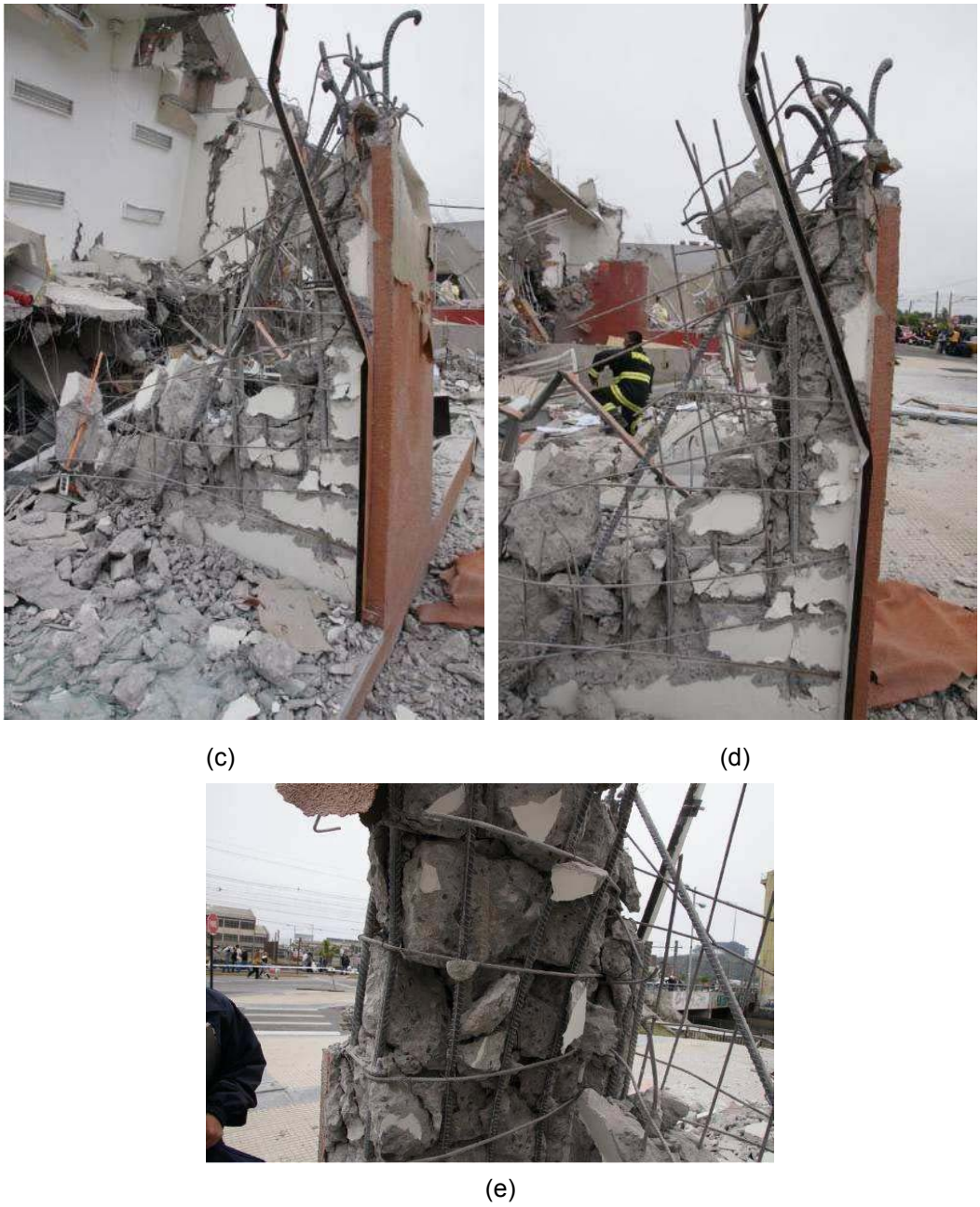

(c) (d)

(e)

Figure 6.80 Damage in axis 13 (after IDIEM, 2010).

Failure in the wall located in axis 20 occurred at a height of 55 in. (1.4 m) above the base at the first story, near axis A (Figure 6.81). The top portion of this wall showed heavy damage consistent to out-of-plane loading (IDIEM, 2010).

(a)

(b)

(c)

Figure 6.81 Damage in axis 20 (after IDIEM, 2010).

Based on post-earthquake inspection, IDIEM (2010) sketched the observed damage in axes 8, 13, and 20 (Figure 6.82).

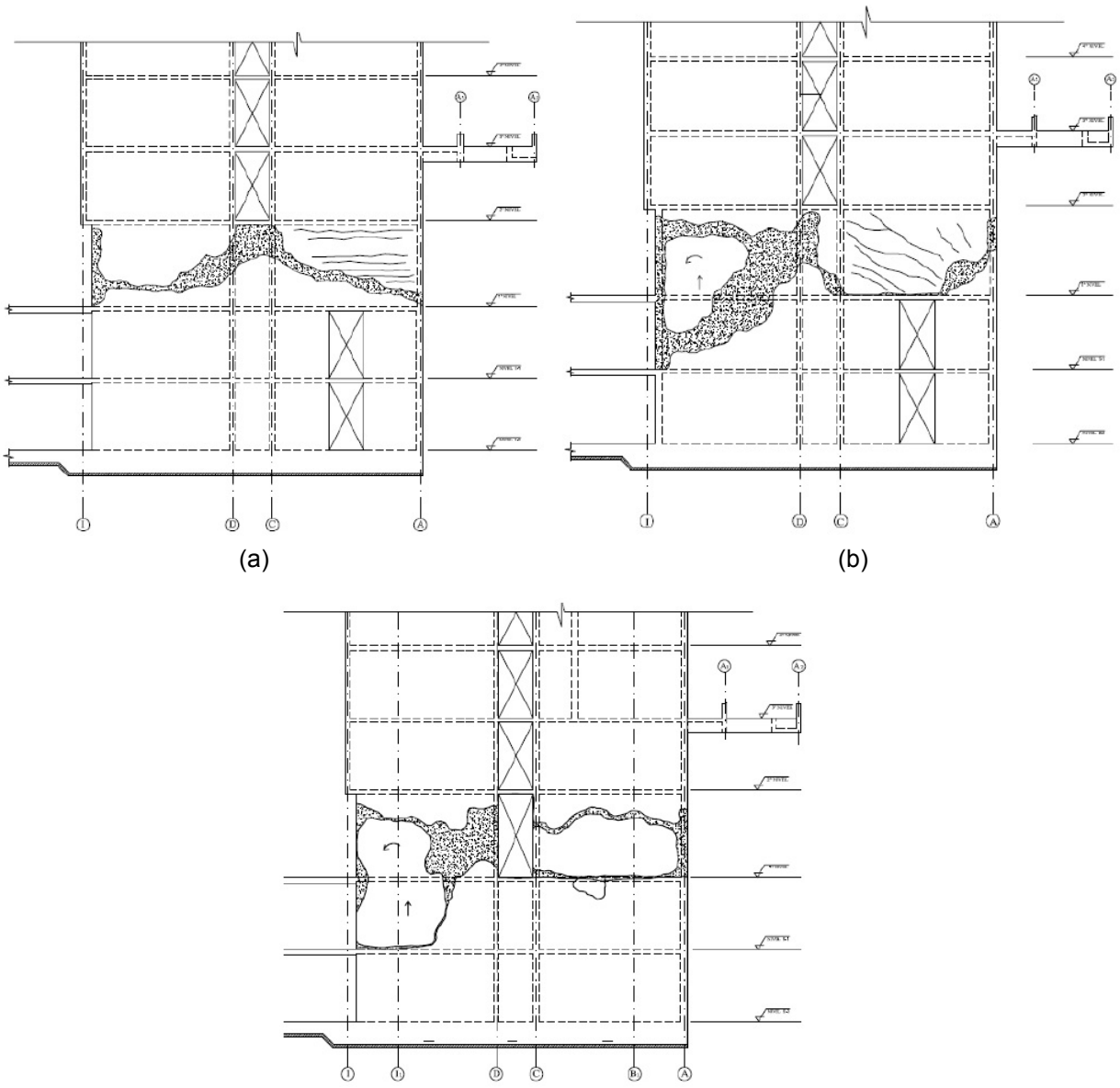

Figure 6.82 Sketch of damage: a) axis 8, b) axis 13, c) axis 20 (after IDIEM, 2010).

6.4.6 Nonlinear Models of Isolated Walls

Three walls of Alto Rio building at the first story, all of them oriented in the east-west direction, are analyzed using nonlinear models of isolated walls. Figure 6.83 shows the selected walls in a plan view.

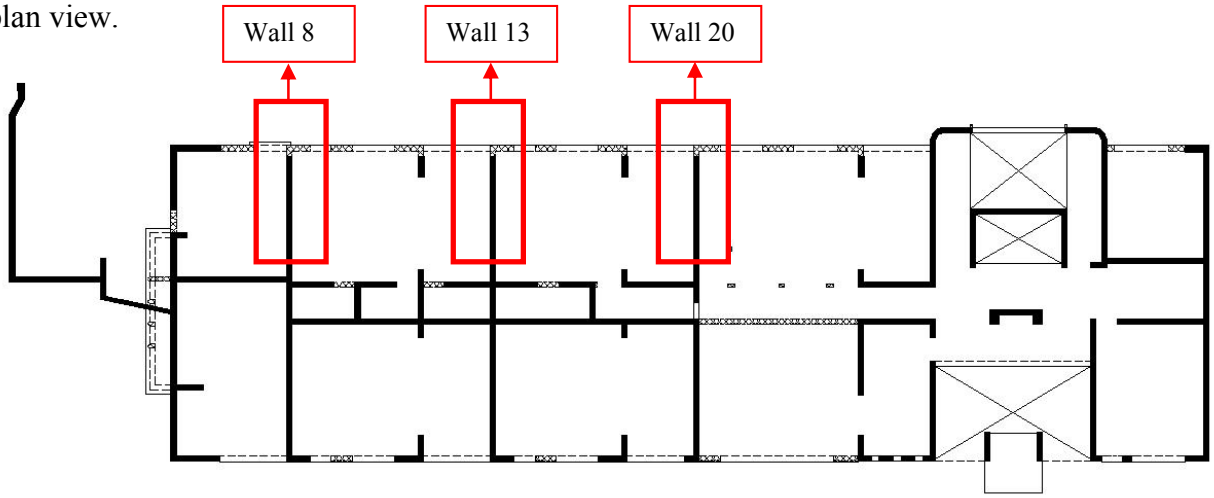

Figure 6.83 Analyzed walls for Alto Rio building.

This analysis is conducted considering the plastic hinge model introduced in Figure 5.3.

6.4.6.1 Analysis of Wall in Axis 8, between Axis D and I

Figure 6.84 shows an elevation view of axis 8. At the first story, this wall was continuous along the entire building width. Above the first story, a stack of corridor openings of 4 ft (1.2 m) width divided it into two separate walls connected only by floor slabs, without coupling beams. Structural drawings show that the wall had a small flange of 3 ft (0.9 m) width at the intersection with axes A and I, starting at the first story (axis A) or the second story (axis I) and extending up to the building top. This flange prevented out-of-plane instability of the wall at the axis A edge. At axis I, the wall stepped back from the building perimeter by 1.3 ft (0.4 m) at the first story, and the flange was discontinued. Figure 6.82a presented a sketch with the post-earthquake damage in axis 8, where damage was concentrated in the first story. It is noteworthy that the first story considered as a solid wall has strength and stiffness higher than upper stories. However, a failure surface can deviate from a horizontal plane, such that the first story wall can become the weak element supporting the set-back (or flag) wall above it. This plausibly explains the critical damage concentrated in that story. Consequently, the wall edge close to axis I could be especially prone to buckle, given that was subjected to large vertical strains.

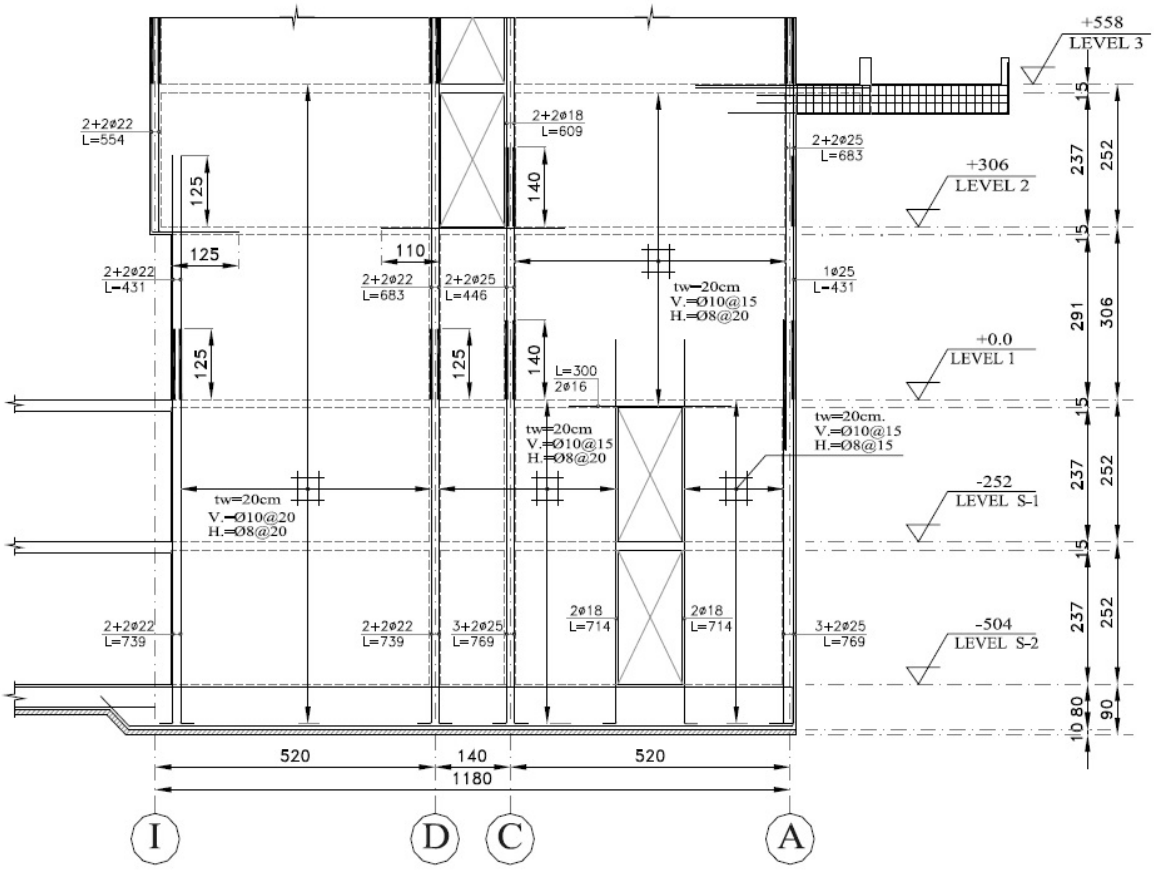

Figure 6.84 Elevation view of axis 8, dimensions in cm (1 cm = 0.39 in.).

The plastic model model shown in Figure 5.3 is used to determine the strain demands at the base of the first story of the wall in axis 8, between axes D and I. This model considers only the top lateral displacement caused by the nonlinear behavior in the plastic hinge region, defined for this case at the first story. The moment-curvature relation used in the plastic hinge region is obtained from Hilson (2014), who defined a critical section at the first story. Figure 6.85 presents the first-story critical section and Figure 6.86 presents the corresponding moment-curvature relation for flange in compression and in tension.

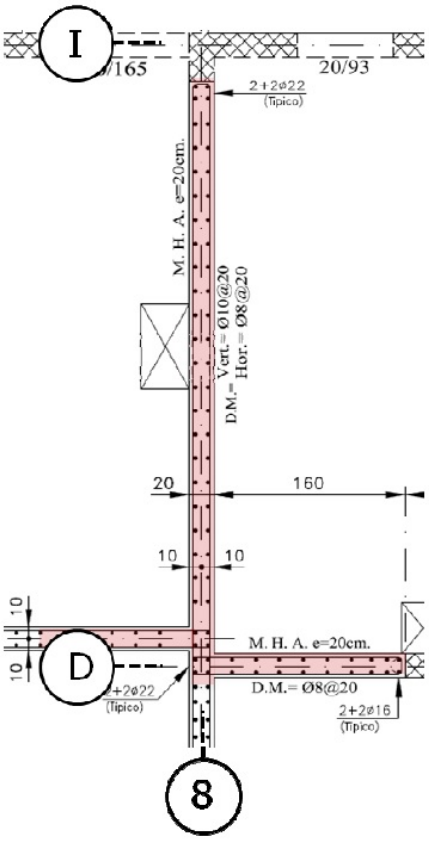

Figure 6.85 Critical section at the first story for wall in axis 8, between axis D and I, dimensions in cm (1 cm = 0.39 in.), after Hilson, 2014.

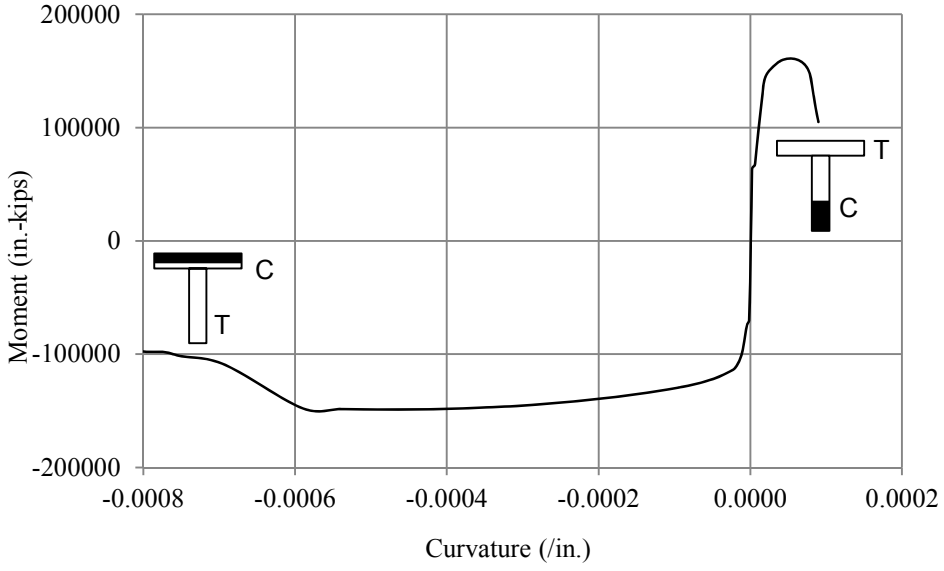

Figure 6.86 Moment-curvature relation for critical section at the first story and expected axial force (1 in. = 25.4 mm; 1 in-kips = 0.11 kN-m), after Hilson, 2014.

For this model, the curvature demand at the base of the first story for the estimated maximum roof drift ratio of 0.85% is $\phi_u = 0.85\%/(0.5 \cdot 197) = 8.63 \cdot 10^{-5}$ in.$^{-1}$. Figure 6.87 shows the calculated strain profiles.

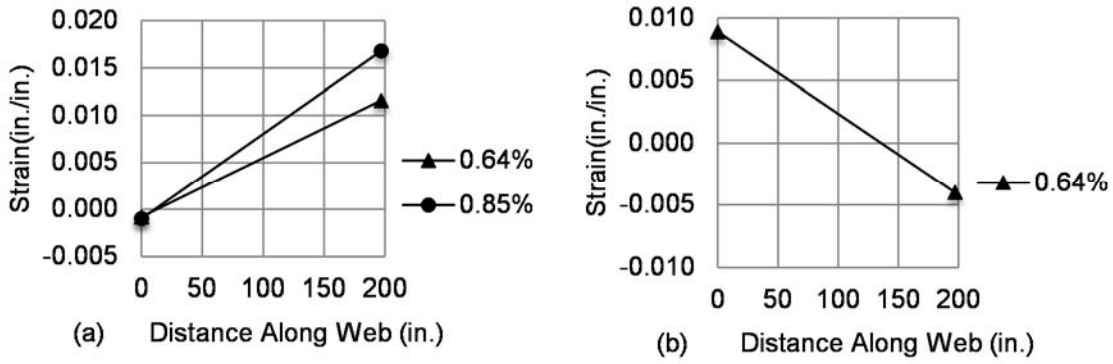

Figure 6.87 Strain profiles for critical section of wall in axis 8, between axes D and I, from plastic hinge approach: (a) flange in compression; (b) flange in tension.

Figure 6.87b shows the strain profile at the plastic hinge region for the case of the wall stem in compression at 0.64% roof drift ratio, the limit at which concrete crushing is calculated to occur in the stem (close to axis I). This seems to indicate that estimated maximum roof drift ratio of 0.85% cannot be reached without crushing the wall stem first. Figure 6.87a shows the strain profile at the wall base at 0.64% and 0.85% roof drift ratio, for the lateral load that compresses the wall flange. For this case, the maximum tensile strain in the wall stem is close to 0.017 when the maximum roof drift ratio is reached and 0.011 for the drift that causes crushing at the wall stem when the load acts in the opposite direction.

6.4.6.2 Analysis of Wall in Axis 13, between Axis D and I

Figure 6.88 shows an elevation of axis 13. This case is similar to axis 8, where only the wall edge close to axis I at the first story was susceptible to buckle, considering that a flange prevented this from occurring in axis I at any upper level starting at the second story. The wall edge located in axis A was not likely to buckle because of a flange that goes from the first story up to the roof. This analysis also considers a critical section between axis D and I at the first story, as shown in Figure 6.89. The moment-curvature relation obtained from Hilson (2014) and shown in Figure 6.90 is used in the plastic hinge region to estimate the strain demands.

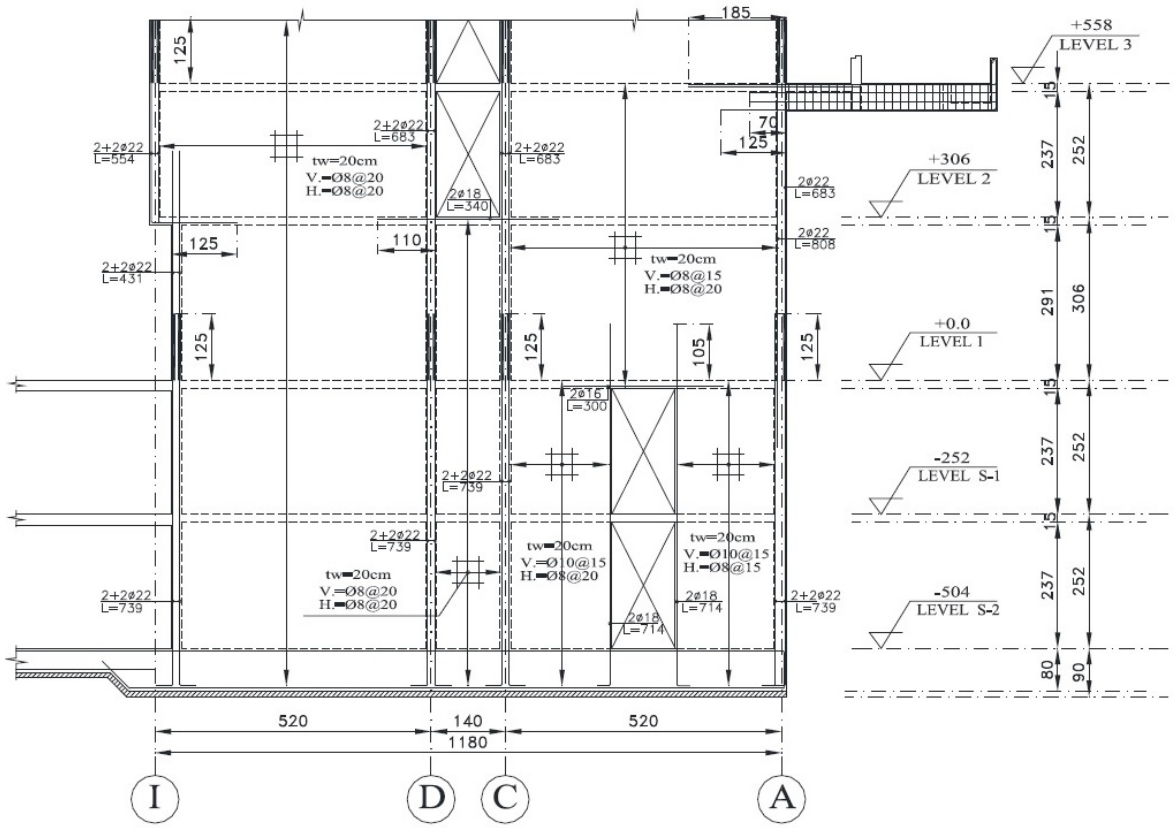

Figure 6.88 Elevation view of axis 13, dimensions in cm (1 cm = 0.39 in.).

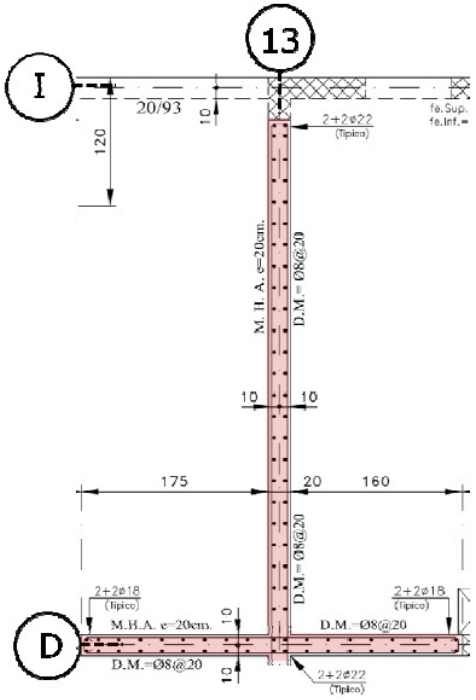

Figure 6.89 Critical section at the first story for wall in axis 13, between axis D and I, dimensions in cm (1 cm = 0.39 in.), after Hilson, 2014.

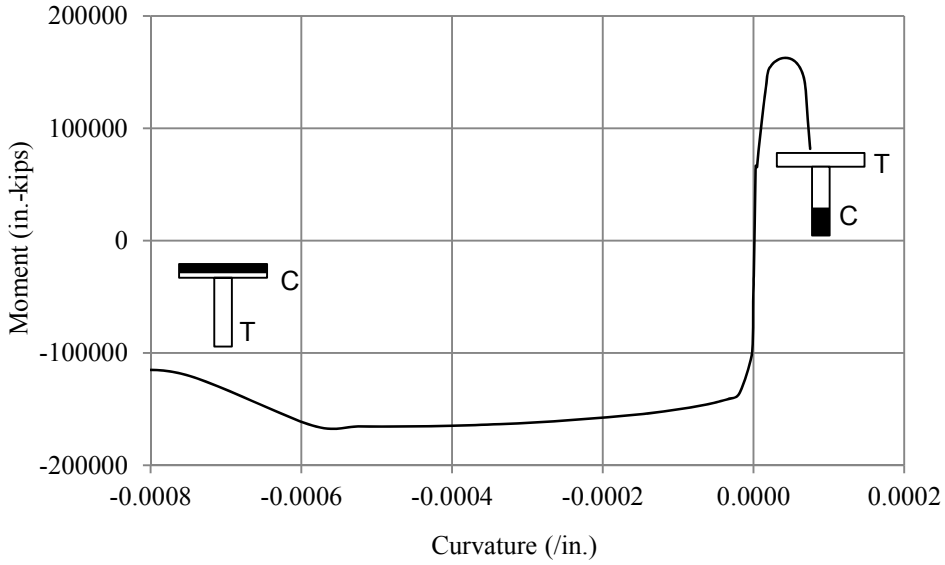

Figure 6.90 Moment-curvature relation for critical section at the first story and expected axial force (1 in. = 25.4 mm; 1 in-kips = 0.11 kN-m), after Hilson, 2014.

The curvature demand at the wall base for the estimated maximum roof drift ratio of 0.85% is also $\phi_u = 8.63 \cdot 10^{-5}$ in.$^{-1}$. Figure 6.91b shows the strain profile at the plastic hinge region for the case of the wall stem in compression at 0.56% roof drift ratio, the limit at which the wall edge close to axis I crushes according to this section analysis. Therefore, the estimated maximum roof drift ratio of 0.85% cannot be reached without crushing the wall stem first. Figure 6.91a shows the strain profile at 0.56% and 0.85% roof drift ratio, for the lateral load that compresses the flange of the critical section. For this case, the maximum tensile strain in the wall stem is 0.016 when the maximum roof drift ratio is reached and 0.011 for the drift that causes crushing at the wall stem when the load acts in the opposite direction.

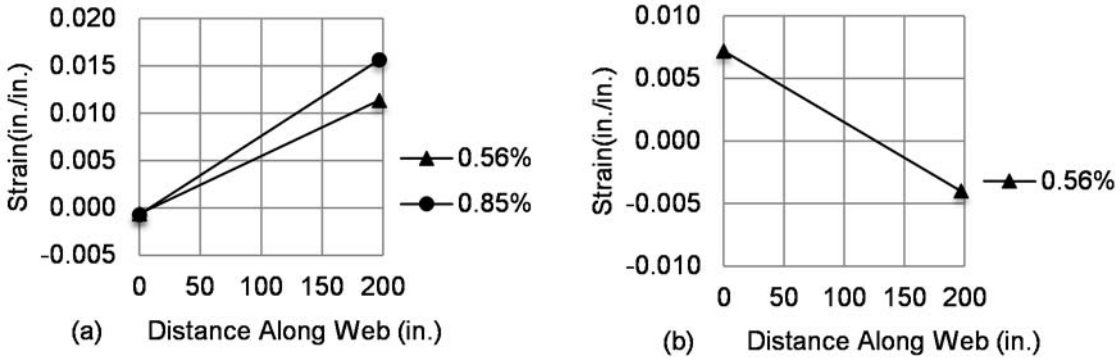

Figure 6.91 Strain profiles for critical section of wall in axis 13, between axes D and I, from plastic hinge approach: (a) flange in compression; (b) flange in tension.

6.4.6.3 Analysis of Wall in Axis 20, between Axis D and I

Figure 6.92 shows an elevation of axis 20. In this case, similar to axes 8 and 13, the damage was concentrated in the first story, as sketched in Figure 6.82c. The wall in axis 20 had a door opening at the first story, between axes C and D. At this story, wall segments between axes D and I and axes A and C were connected by a 23.6in. x 7.9in. (0.6m x 0.2m) coupling beam. In upper stories, a longitudinal corridor separated both segments without coupling beams, and they were connected only by the slab. Figure 6.93 depicts the critical section at the first story. This critical section is considered for moment-curvature analysis, the calculated relation of which is presented in Figure 6.94. Estimations of strain demands are obtained from section analysis and the plastic hinge model shown in Figure 5.3. As in the previous cases, only the wall stem in the first story close to axis I was succeptible to buckle. At any other level, a flange prevented this from occurring.

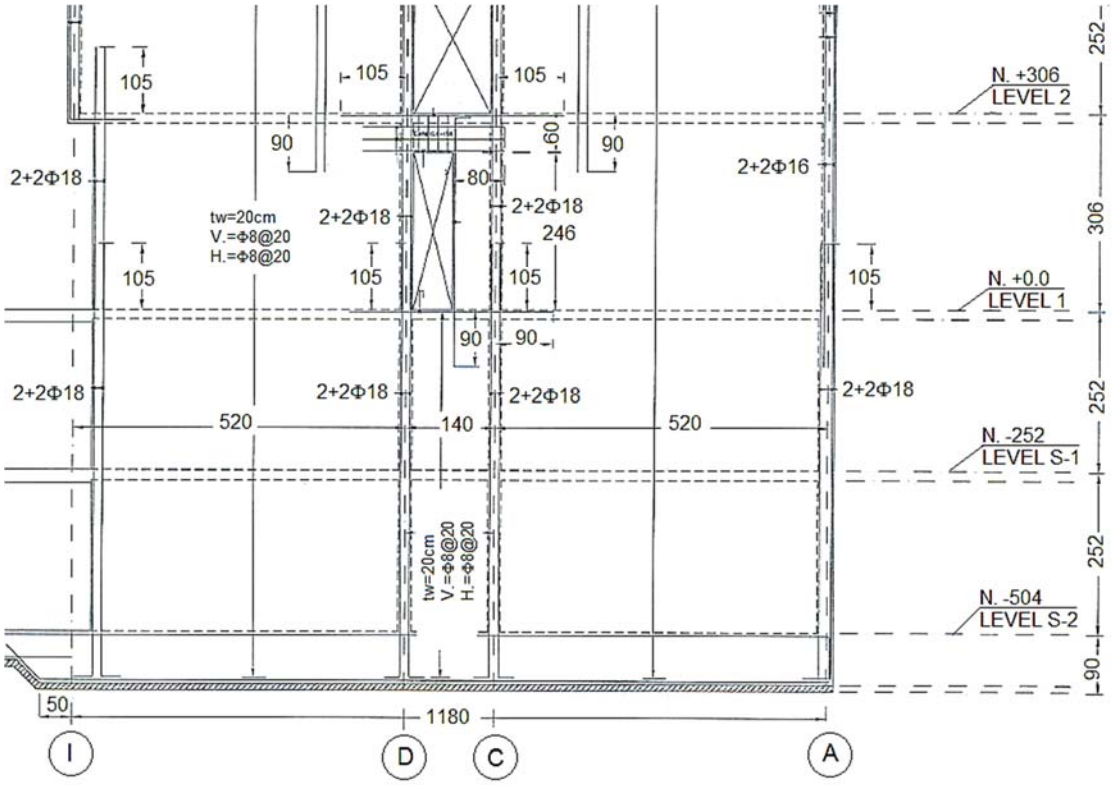

Figure 6.92 Elevation view of axis 20, dimensions in cm (1 cm = 0.39 in.).

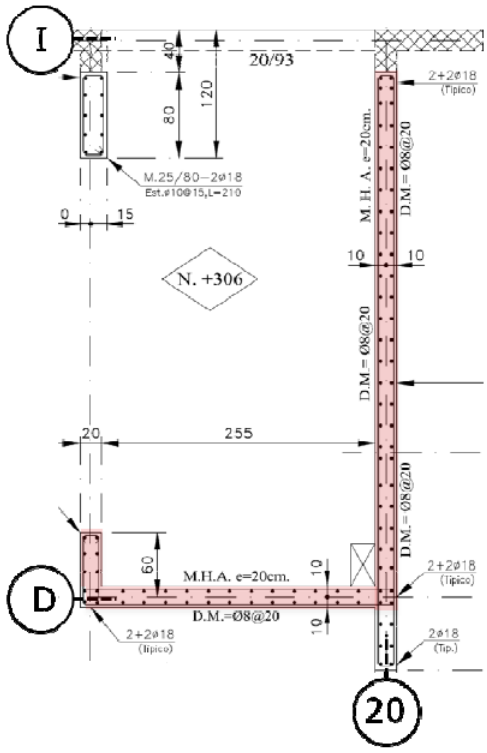

Figure 6.93 Critical section at the first story for wall in axis 20, between axis D and I, dimensions in cm (1 cm = 0.39 in.), after Hilson, 2014.

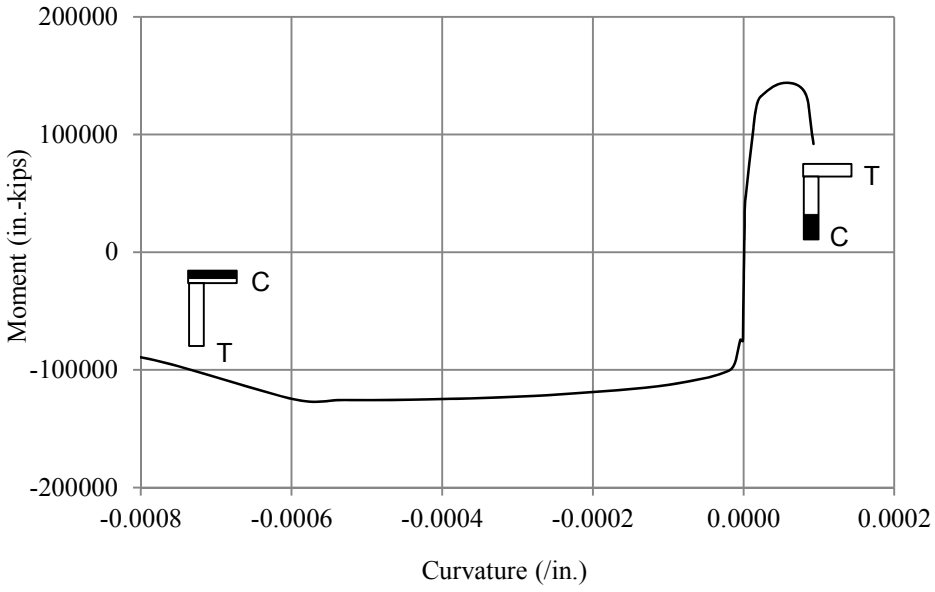

Figure 6.94 Moment-curvature relation for critical section at the first story and expected axial force (1 in. = 25.4 mm; 1 in-kips = 0.11 kN-m), after Hilson, 2014.

The curvature demand at the wall base for the estimated maximum roof drift ratio of 0.85% is $\phi_u = 0.85\%/(0.5 \cdot 197) = 8.63 \cdot 10^{-5}$ in.$^{-1}$. For this curvature, according to Figure 6.95a, the maximum tensile strain at the wall stem is 0.016. Section analysis showed that stem crushing occurs at a roof drift ratio of 0.70%. When the stem is tension, this drift ratio gives a maximum tensile strain of 0.013 (Figure 6.95a).

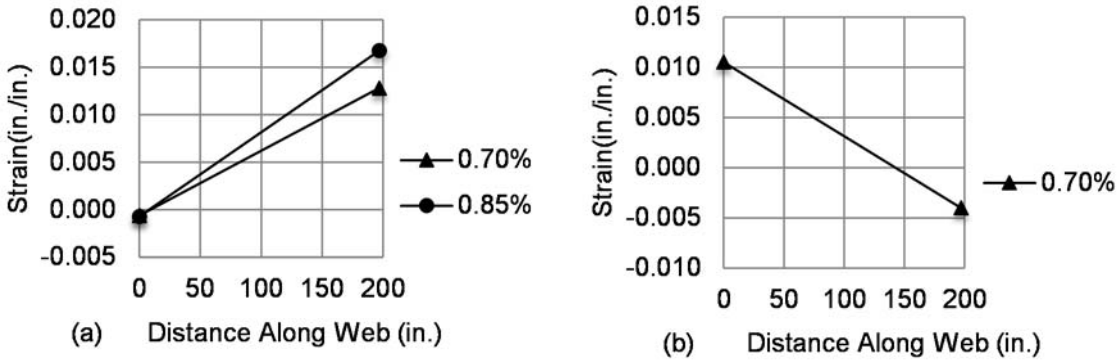

Figure 6.95 Strain profiles for critical section of wall in axis 20, between axes D and I, from plastic hinge approach: (a) flange in compression; (b) flange in tension.

6.4.7 Evaluation of the Onset of Out-of-Plane Instability

Similar to the out-of-plane instability evaluation performed for buildings #1 and #2 (sections 6.1 and 6.3), the simplified mechanics equation introduced in section 2.2 is considered here for the evaluation of the onset of instability in walls 8, 13 and 20 between axes D and I. The assumption behind this analysis is that the nonlinear behavior extended along the entire first story and the vertical strain demand along the edge close to axis I at this level was constant or close to constant, which seems to be a reasonable assumption from the reported post-earthquake damage (section 6.4.5).

Table 6.25 presents the materials properties and dimensions used on this evaluation. According to Table 6.26, to buckle a previously intact stem requires a maximum tensile strain close to 0.03 for the three walls. Moment-curvature analysis of the critical sections at the first story and the plastic hinge model indicated that the maximum tensile strain demand at the stem was close to a half of this value for all walls. Therefore, to buckle an intact wall does not seem to be possible given the estimated demands. However, section analysis of the three walls showed that crushing of the wall stem occurs for all cases at a drift ratios lower than the value estimated from linar analysis, and Table 6.27 shows that buckling of a reduced section, where the cover has been spalled off, requires a maximum tensile strain close to 0.013 for all cases. According to the models used in this section to estimate strain demands, it is possible to reach strains higher than this value right after crushing or during a subsequent cycle prior the maximum estimated drift ratio, and, therefore, instability of the reduced section cannot be ruled out as one of multiple explanations of the reported damage.

Table 6.25 Properties for buckling calculation (1in. = 25.4 mm; 1 psi = 0.007 MPa).

Wall	Material Properties, psi		Dimensions, in.						BE Area of Longitudinal Steel A_s, in.^{2}
	f'_c	f_y	Width, b	Length, l_w	Story Height, H	h_u (in.)	BE Length, l_b	Stirrup Clear Cover, c	
8-D,I	6,300	69,000	7.9	197	115	115	9	0.8	2.36
13-D,I	6,000	69,000	7.9	197	115	115	9	0.8	2.36
20-D,I	6,000	69,000	7.9	197	115	115	9	0.8	1.58

Table 6.26 Buckling calculation when spalling does not occur.

Wall	ρ	m	ξ	κ	ϵ_{sm}
8-D,I	3%	0.35	0.15	0.81	**0.028**
13-D,I	3%	0.36	0.15	0.81	**0.027**
20-D,I	2%	0.24	0.18	0.82	**0.032**

Table 6.27 Buckling calculation when spalling precedes buckling.

Wall	Wall Slenderness b_c/kh_u	ρ	m	ξ	κ	ϵ_{sm}
8-D,I	0.08	5%	0.57	0.11	1	**0.013**
13-D,I	0.08	5%	0.60	0.11	1	**0.013**
20-D,I	0.09	3%	0.39	0.14	1	**0.015**

7 Summary and Conclusions

7.1 SUMMARY

Chapter 1 introduced the problem of out-of-plane instability in slender boundary elements, presented a review of relevant prior studies, code requirements and current design practice. Chapter 1 also defined the research program objectives and scope. Chapter 2 introduced three models for analysis of out-of-plane instability: (a) a simplified mechanics theory for buckling of prismatic columns under uniform tension/compression cycles, based on concepts previously introduced by Paulay and Priestley (1993), (b) nonlinear beam-column elements with force-based formulation, currently implemented in OpenSees and later used for buckling analysis of prismatic columns under uniform and nonuniform tension/compression cycles, (c) nonlinear finite elements (implemented in the software TNO DIANA), shell and solid elements, based on a smeared cracking approach for concrete modeling and full bonding between concrete and reinforcement bars. These finite element models were later used for buckling analysis of columns and walls under cyclic loading. Chapter 3 presented an evaluation of the analytical models for global instability, introduced in Chapter 2, using the results of column tests (Chai and Elayer, 1999). Comparisons between different models and sensitivity studies for the variation of some key parameters were included. In Chapter 4, the effects of force/strain gradients along the wall height and length in the onset of out-of-plane instability were evaluated using OpenSees models for isolated boundary elements and TNO DIANA models for walls. Different cases were considered to provide insight of these effects. Chapter 6 applied the buckling models to the analysis of three buildings that showed some signs of wall instability during the 2010 Chile earthquake. For each building, the material properties and reported damage were summarized. Analytical models were used to estimate the peak roof displacements, and then the plausibility of wall instability being the primary cause of failure was assessed.

7.2 CONCLUSIONS

Based on the results reported herein, and within the limitations of the study parameters, the following conclusions are made:

- Prior to 2010, lateral buckling of slender wall boundaries had been observed only in laboratory tests but not in actual buildings subjected to earthquake shaking. The 2010 Chile earthquake showed that buckling is a potential risk to slender walls that should be considered in the design process.

- The tendency of an intact wall to buckle under cyclic loading depends not only on the aspect ratio h_u/b of the wall boundary but also on the maximum tensile strain experienced by the member prior to axial compression.
- A simplified mechanics model for buckling of prismatic sections under uniform tension/compression cycles has been introduced. Comparison with the results of reinforced prism (column) tests showed that the simplified mechanics model provides a good estimate of the conditions (slenderness and maximum prior tensile strain) required to initiate buckling of uniformly loaded prisms (columns).
- Finite element models were developed to study the reversed cyclic buckling of reinforced prisms (columns). Both (a) force-based nonlinear beam-column elements with fibers and (b) nonlinear finite element models, both using the smeared cracking approach, were developed. It was shown that buckling of reinforced prisms (columns) subjected to cyclic lateral loading can be simulated using these nonlinear finite element models.
- Analytical studies using finite elements were conducted to determine the effects on wall boundary instability of (a) strain gradients along the wall length and (b) strain/moment gradients along the wall height height. These studies showed that the effect of the gradient along the length can be neglected for walls longer than $10t_w$, which is the typical case of walls prone to buckle. The strain gradient along the height can have an important effect of improving the stability of the wall boundary.
- In typical multistory buildings, the assumption of uniform strain along the unsupported height at the first story is often reasonable, and in such cases the onset of out-of-plane instability can be identified using expressions derived from the simplified mechanics model. The theory suggests that walls with one curtain of reinforcement are more vulnerable to lateral instability than walls with two curtains.
- In some special cases, the moment gradient over the unsupported height can influence the buckling tendency of a wall in a building. In such buildings, the assumption of uniform axial demand over the height can lead to an underestimation of the maximum tensile strain required to buckle the boundary element during load reversal. The effects of moment gradient should be considered in such cases.
- A correction factor for the simple mechanics model is proposed to enable estimation of the tendency for wall instability in walls having appreciable moment gradient over height. This factor increases the estimated maximum tensile strain that triggers buckling during load reversal.
- Although it has been demonstrated that lateral buckling may occur in an intact wall without being preceded by crushing, it can also occur as a secondary failure mode after the onset of cover spalling. Complete cover spalling produces a smaller, more slender cross section with greater tendency to buckle, which can happen immediately after spalling or during subsequent cycles.
- Analysis of slender walls in three damaged buildings in Chile suggests that the observed buckling was a secondary failure mode that followed crushing of the boundary element. Stems of T-shaped and L-shaped walls seem to be especially prone to buckle due to the high strain demands that occur during earthquakes, and special considerations should be

made to limit the slenderness ratio for these cases. Analysis of slender walls in one of the buildings indicates that buckling after initial spalling cannot be ruled out as one of the multiple explanations of the observed collapse.

- Building codes should have a slenderness ratio limit for the intended hinge zone of special structural walls. The UBC (1997) limit of $h_u/b \leq 16$ is recommended for walls that maintain their concrete cover. The same limit could be applied to walls for which cover concrete has spalled. However, the limited evidence suggests that the h_u/b limit should apply with b referring to the width of the confined core, which in ACI 318 is defined as b_c.
- Based on consideration of out-of-plane buckling, special structural walls should have two curtains of reinforcement within the intended hinge zone, regardless the shear or the wall thickness, considering that walls with two curtains are less vulnerable to out-of-plane instability.

REFERENCES

Acevedo, C.E., Creagh, A., Moehle, J.P., Hassan, W., Tanyeri, A.C. (2010). Seismic vulnerability of non-special boundary element of shear wall under axial force reversals, *Network for Earthquake Engineering Simulation*, 16 pp.

ACI 318 (2014). *Building code requirements for structural concrete (ACI 318-14) and commentary (ACI 318R-14)*, American Concrete Institute, Farmington Hills, MI.

ACI 363R-92 (1992). *Report on high-strength concrete*, ACI Manual of Concrete Practice (reapproved 1997), American Concrete Institute, Farmington Hills, MI.

Alto Huerto (2010). Building project drawings, *Drawings # 28769-01 to 28769-44*, Concepción, Chile.

ASCE 41 (2006). *Seismic rehabilitation of existing buildings*, American Society of Civil Engineers, Reston VA.

ATC-94 (2014). *Recommendations for seismic design of reinforced concrete wall buildings based on studies of the 2010 Chile earthquake*, Applied Technology Council, Redwood City, California.

Bazant, Z. P., Oh, B. H. (1983). Crack band theory for fracture of concrete. *Mat. and Struct*., 16, 155–177.

Bazant, Z. P., Planas, J. (1998). Fracture and size effect in concrete and other quasibrittle materials. *CRC Press*, Boca Raton, Fla.

Brown, J., Kunnath, S.K. (2000). Low cycle fatigue behavior of longitudinal reinforcement in reinforced concrete bridge columns, *Report No. MCEER-00-0007*, MCEER, SUNY Buffalo, Buffalo, NY.

Chai, Y.H., Elayer, D.T. (1999). Lateral stability of reinforced concrete columns under axial reversed cyclic tension and compression, *ACI Structural Journal*, American Concrete Institute, V. 96, No. 5, pp. 780-789.

Coleman, J., Spacone, E. (2001). Localization issues in force-based frame elements, *Journal of Structural Engineering*, 127(11), 1257-1265.

Comité Européen de Normalization (CEN) (2004). *Eurocode 8: Design of structures for earthquake resistance—Part 1. General rules, seismic actions and rules for buildings (EN 1998–1)*, Brussels.

Creagh, A., Acevedo, C., Moehle, J.P., Hassan, W., Tanyeri, A.C. (2010). Seismic performance of concrete special boundary element, *Network for Earthquake Engineering Simulation*, 18 pp.

Dashti, F., Dhakal, R., Pampanin, S. (2014). Numerical simulation of shear wall failure mechanisms, *2014 NZSEE Conference*, Auckland, New Zealand, New Zealand Society for Earthquake Engineering.

De Borst, R., Feenstra, P. H., Pamin, J., Sluys, L. J. (1994), Some current issues in computational mechanics of concrete structures, *Computer modelling of concrete structures, Proc.*, EURO-C, H. Mang, N. Bićanić, and R. de Borst, eds., Swansea, U.K.

De Borst, R., Nauta, P. (1985). Non-orthogonal cracks in a smeared finite element model, *Eng. Comput. (2)*, pp. 35-46.

DICTUC (2010). Inspección visual y levantamiento de daño edificio Alto Huerto Concepción, *Report # 906575/10-056-EE-01-R0*, Santiago, Chile.

DICTUC (2010). Verificación de correcta ejecución de las obras conforme de diseño edificio Alto Huerto San Pedro de la Paz, *Report # 906575/10-056-EN-01-R0*, Santiago, Chile.

DICTUC (2010). Contrastación de la existencia en terreno de elementos de confinamiento de borde y del plano de algunos muros versus especificaciones de planos estructurales tras sismo del 27 de febrero de 2010. *Report # 878055*, Santiago, Chile.

DICTUC (2012). Resistencia del hormigón y de las barras de refuerzo edificio Emerald, Santiago, Chile.

EMPRO (2007). Informe de mecánica de suelos edificio Alto Huerto, *Report # 71071-07*, Concepción, Chile.

Feenstra, P. H. (1993). Computational aspects of biaxial stress in plain and reinforced concrete. PhD thesis, TU Delft, Delft University of Technology.

Feenstra, P. H., De Borst, R. D., Rots, J. G. (1991). Numerical study on crack dilatancy part I: models and stability analysis, *Journal of engineering mechanics*, 117(4), 733-753.

Feenstra, P.H., De Borst, R., Rots, J.G. (1991). A comparison of different crack models applied to plain and reinforced concrete, *Fracture Processes in Concrete, Rock and Ceramics*, pp. 629–638.

Filippou, F. C., and Fenves, G. L. (2004). *Methods of analysis for earthquake-resistant structures. Earthquake engineering: from engineering seismology to performance-based engineering*, Y. Bozorgnia and V. V. Bertero, eds., Chap. 6, CRC, Boca Raton, Fla.

Filippou, F. C., Popov, E. P., & Bertero, V. V. (1983). Effects of bond deterioration on hysteretic behavior of reinforced concrete joints. *Tech. Rep. EERC 83-19*, Earthquake Engineering Research Center, University of California, Berkeley, 1983.

Goodsir, W.J. (1985). The design of coupled frame-wall structures for seismic actions, *Research report 85-8*, Department of Civil Engineering, University of Canterbury, Christchurch, New Zealand.

Hilson, C.W. (2014). Analytical and experimental studies of seismic performance of reinforced concrete structural wall boundary elements. PhD thesis, University of California, Los Angeles.

IDIEM (2010). Peritaje estructural edificio Alto Río, ciudad de Concepción. Prospección y ensayo de materiales. *Report # 644.424-07 rev. 0*, Santiago, Chile.

IDIEM (2010). Peritaje estructural edificio Alto Río, ciudad de Concepción. Estudio de cálculo estructural – informe n 2. Anexo A: planos de cálculo con observaciones *Report # 644.424-05*, Santiago, Chile.

IDIEM (2010). Peritaje estructural edificio Alto Río, ciudad de Concepción. Descripcion de caída y factores asociados al colapso. *Report # 644.424-00 rev. 1*, Santiago, Chile.

IDIEM (2010). Peritaje estructural edificio Alto Río, ciudad de Concepción. Levantamiento en terreno. *Report # 644.424-06 rev. 0*, Santiago, Chile.

INN (1986). Cargas permanentes y sobrecargas de uso, *Chilean standard # NCh 1537 Of. 1986*, Santiago, Chile.

INN (1996). Diseño sísmico de edificios, *Chilean standard # NCh 433 Of. 1996*, Santiago, Chile.

INN (2001). Hormigón – Testigos de hormigón endurecido – Parte 1: Extracción y ensayo, *Chilean standard # NCh 1171/1 Of.2001*, Santiago, Chile.

INN (2001). Hormigón – Testigos de hormigón endurecido – Parte 2: Evaluación de resultados de resistencia mecánica, *Chilean standard # NCh 1171/2 Of.2001*, Santiago, Chile.

INN (2008). Hormigón armado. Requisitos de diseño y cálculo, *Chilean standard # NCh 430 Of. 2008*, Santiago, Chile.

Hognestard, E. (1951). A study of combined bending and axial load in reinforced concrete members, *Bulletin No. 399*, University of Illinois Engineering Experimental Station.

Karsan, I. D., Jirsa, J. O. (1969). Behavior of concrete under compressive loadings, *Journal of the Structural Division*, 95(12), 2543-2564.

Kent, D.C., Park, R. (1971). Flexural members with confined concrete, *J. Struct. Div. ST7*, 97: 1969-1990.

Kent, D.C. Park, R. (1971). Inelastic behavior of reinforced concrete members with cyclic loading, *Bulleting of the New Zealand Society for Earthquake Engineering*, Vol. 4, no. 1, pp. 108-125.

Manson, S.S. (1953). Behavior of materials under conditions of thermal stress, *Heat Transfer Symposium*, University of Michigan Engineering Research Institute, Ann Arbor, MI.

Mazzoni, S., McKenna, F., Scott, M.H., Fenves, G. (2007). Open system for earthquake engineering simulation: User command-language manual, Pacific Earthquake Engineering Research Center, University of California Berkeley, OpenSees version 1.7.3 user's manual http://opensees.berkeley.edu/OpenSees/manuals/usermanual/index.html.

Menegotto, M., Pinto, P. E. (1973). Method of analysis for cyclically loaded RC frames including changes in geometry and non-elastic behavior of elements under combined normal Force and bending, *IABSE Congress Reports of the Working Commission (Vol. 13)*.

Moehle, J.P. (2014). *Seismic design of reinforced concrete buildings*. Mc Graw Hill Education.

Moehle, J.P., Ghodsi, T., Hooper, J.D., Fields, D.C., Gedhada, R. (2011). Seismic design of cast-in-place concrete special structural walls and coupling beams, *NEHRP Seismic Design Technical Brief No. 6*, NIST, 37 pp.

NZ 3101 (2006). *Concrete structures standard – the design of concrete structures*, Standards, New Zealand, 696 pp.

Coffin, L. F. (1954). A study of the effect of cyclic thermal stresses on a ductile metal, *Transactions of the American Society of Mechanical Engineers*, Vol. 76, pp. 931-950.

Oesterle, R.G., Fiorato, A.E., Johala, L.S., Carpenter, J.E., Russell, H.G., Corley, W.G. (1976). Earthquake resistant of structural walls – tests of isolated walls, Report to National Science Foundation, Portland Cement Association, Construction Technology Laboratories, Skokie.

Parra, P.F., Moehle, J.P. (2014). Lateral buckling in reinforced concrete walls, *Proceedings of the 10th National Conference in Earthquake Engineering*, Earthquake Engineering Research Institute, Anchorage, AK.

Paulay, T., Priestley, M.J.N. (1993). Stability of ductile structural walls, *ACI Structural Journal*, V. 90, No. 4, pp. 385-392.

Ramirez, P., Vivallos, J., (2009). Microzonificación Sismica de la Ciudad de Concepción", *in XII Congreso Geológico Chileno*, Santiago, Chile.

Rashid, Y.R. (1968). Ultimate strength analysis of prestressed concrete pressure vessels, *Nuclear Engineering and Design*, 7(4): 334-344.

Rosso, A., Almeida, J. P., Beyer, K. (2015). Stability of thin reinforced concrete walls under cyclic loads: state-of-the-art and new experimental findings, *Bulletin of Earthquake Engineering*, 1-30.

Rots, J.G. (1988). Computational modeling of concrete fracture, Dissertation, Delft University of Technology, Delft, Netherlands.

Roy, H.E.H., Sozen, M.A. (1964). Ductility of concrete, *Proceedings of the International Symposium on Flexural Mechanics of Reinforced Concrete*, ASCE-ACI, Miami, Fla.

Saatcioglu, M., Razvi, S.R. (1992). Strength and ductility of confined concret, *J. Struct. Eng.*, 118(6), 1590–1607.

Scott, M. H., Hamutçuoğlu, O. M. (2008). Numerically consistent regularization of force-based frame elements, *International journal for numerical methods in engineering*, 76(10), 1612-1631.

Scott, B.D., Park, R., Priestley, M.J.N. (1980). Stress-strain relationships for confined concrete: rectangular sections, Dept. of Civil Engineering, University of Canterbury, 106 pp.

Selby, R.G., Vecchio, F.J. (1993). Three dimensional constitutive relations for reinforced concrete, *Tech. Report 93-02*, Department of Civil Engineering, Univ. of Toronto, Canada.

Spacone, E., Filippou, F. C., Taucer, F. F. (1996). Fiber beam-column model for non-linear analysis of R/C frames: part I, formulation, *Earthquake Engineering and Structural Dynamics*, 25(7), 711-726.

Sritharan, S., Beyer, K., Henry, R. S., Chai, Y. H., Kowalsky, M., & Bull, D. (2014). Understanding poor seismic performance of concrete walls and design implications, *Earthquake Spectra*, 30(1), 307-334.

Tanyeri, A.C. (2014). Seismic performance and modeling of reinforced concrete and post-tensioned precast concrete shear walls. PhD thesis, University of California, Berkeley.

Thomsen, J.H., Wallace, J.W. (2004). Displacement-based design of slender reinforced concrete structural walls-experimental verification, *J. Struct. Eng.*, 130(4), 618-630.

TNO DIANA (2011). Finite element analysis user's manual-release 9.4.4.

UBC (1997). *Uniform building code*, International Conference of Building Officials, Whittier, CA.

Vecchio, F.J., Collins, M.P. (1986). The modified compression field theory for reinforced concrete elements subjected to shear, *ACI Structural Journal*, V. 83, No. 22, pp. 219-231.

Emerald (2006). Building project drawings, *Drawings # 3641-A00 to 3641-A53*, Santiago, Chile.

Wallace, J. W., Massone, L. M., Bonelli, P., Dragovich, J., Lagos, R., Lüders, C., Moehle, J.P. (2012). Damage and implications for seismic design of RC structural wall buildings. *Earthquake Spectra*, 28(S1), S281-S299.

Wallace, J. W. (1995). Seismic design of reinforced concrete shear walls. I: New code format, *J. Struct. Eng*., 121(1), 75–87.

Wallace, J. W. (1994). New methodology for seismic design of reinforced concrete shear walls, *J. Struct. Eng*., 120(3), 863–884.

Wallace, J. W., Moehle, J. P. (1993). An evaluation of ductility and detailing requirements of bearing wall buildings using data from the march 3, 1985, Chile earthquake, *Earthquake Spectra*, 9(1), 137-156.

Wallace, J. W., Moehle, J. P. (1992). Ductility and detailing requirements of bearing wall buildings, *J. Struct. Eng.*, 118(6), 1625–1644.

Appendix A. Buckling in Isolated Boundary Elements with Non-uniform Axial Strain

This appendix is complementary to section 4.2 and presents the results of OpenSees analyses for isolated columns under several axial force profiles.

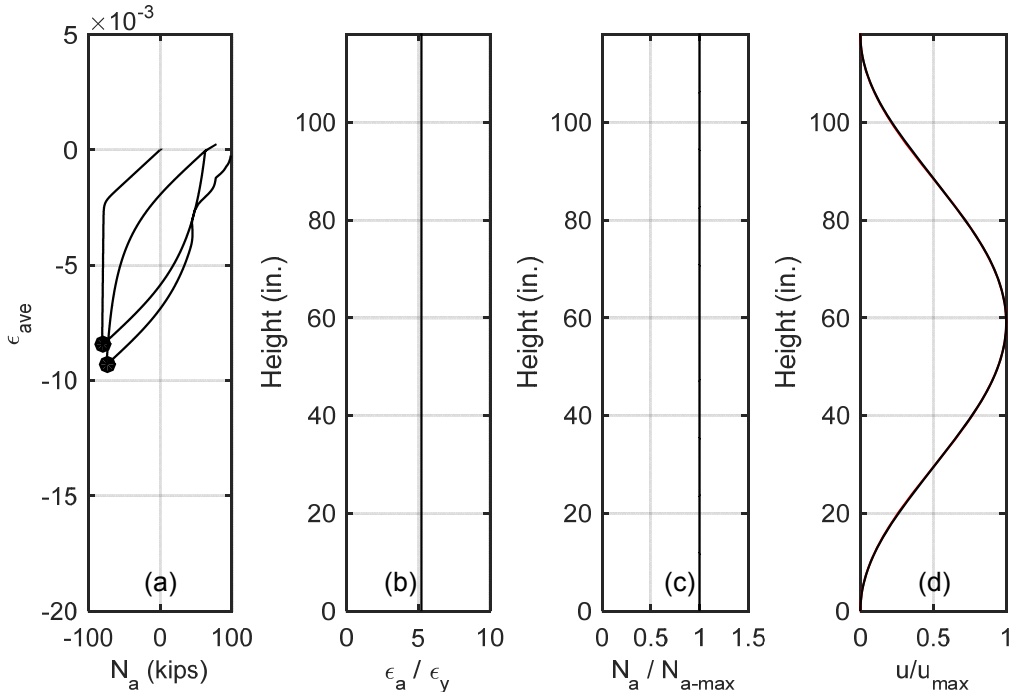

Figure A.1 **Specimen 4WC4_2, α= 1: a) average axial strain versus axial force at the base, b) normalized axial strain, c) normalized axial force, d) normalized buckled shape.**

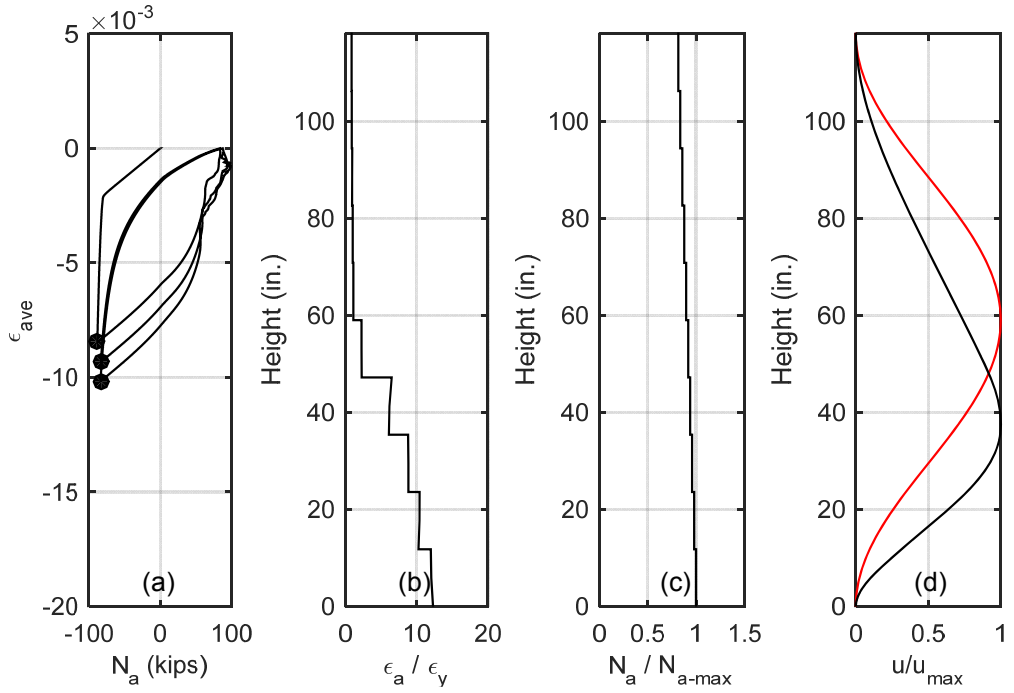

Figure A.2 **Specimen 4WC4_2, α= 0.8: a) average axial strain versus axial force at the base, b) normalized axial strain, c) normalized axial force, d) normalized buckled shape.**

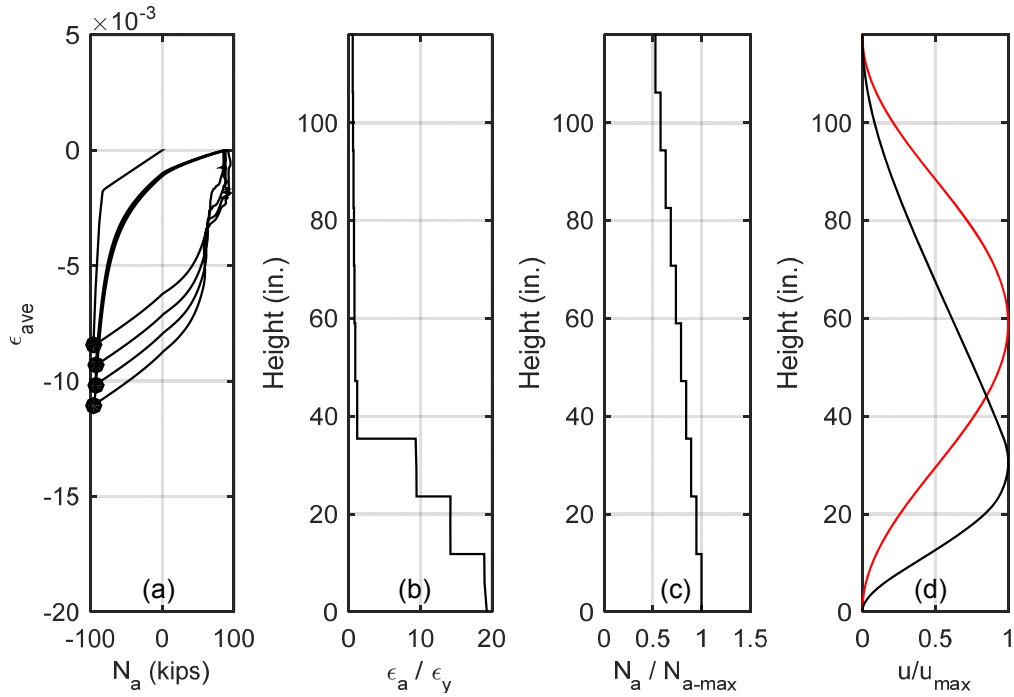

Figure A.3 **Specimen 4WC4_2, α= 0.5: a) average axial strain versus axial force at the base, b) normalized axial strain, c) normalized axial force, d) normalized buckled shape.**

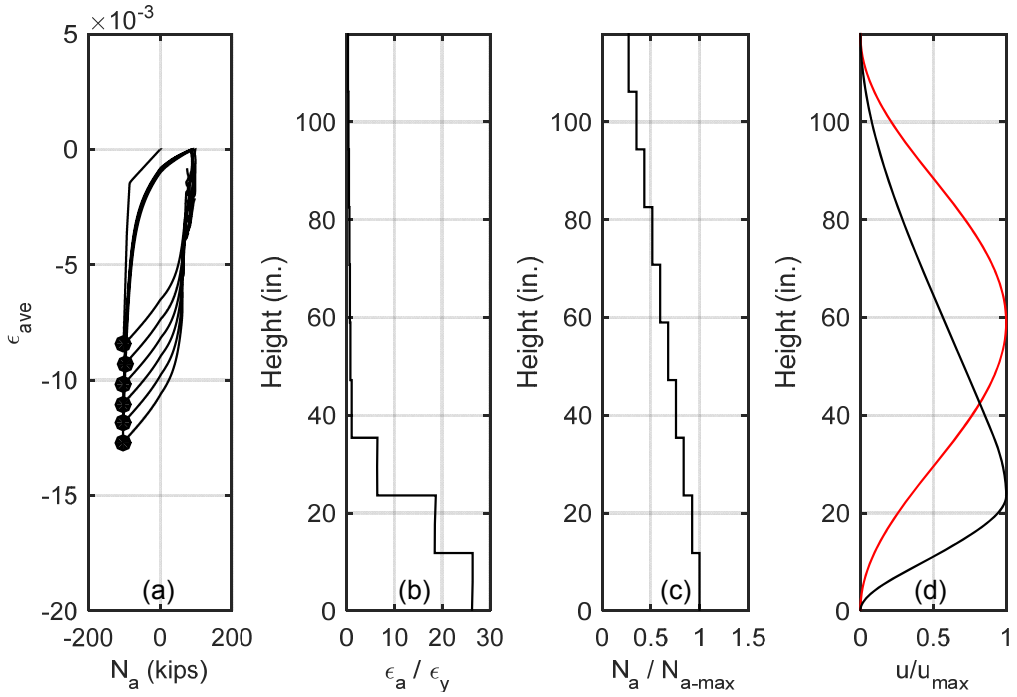

Figure A.4 **Specimen 4WC4_2, α= 0.25: a) average axial strain versus axial force at the base, b) normalized axial strain, c) normalized axial force, d) normalized buckled shape.**

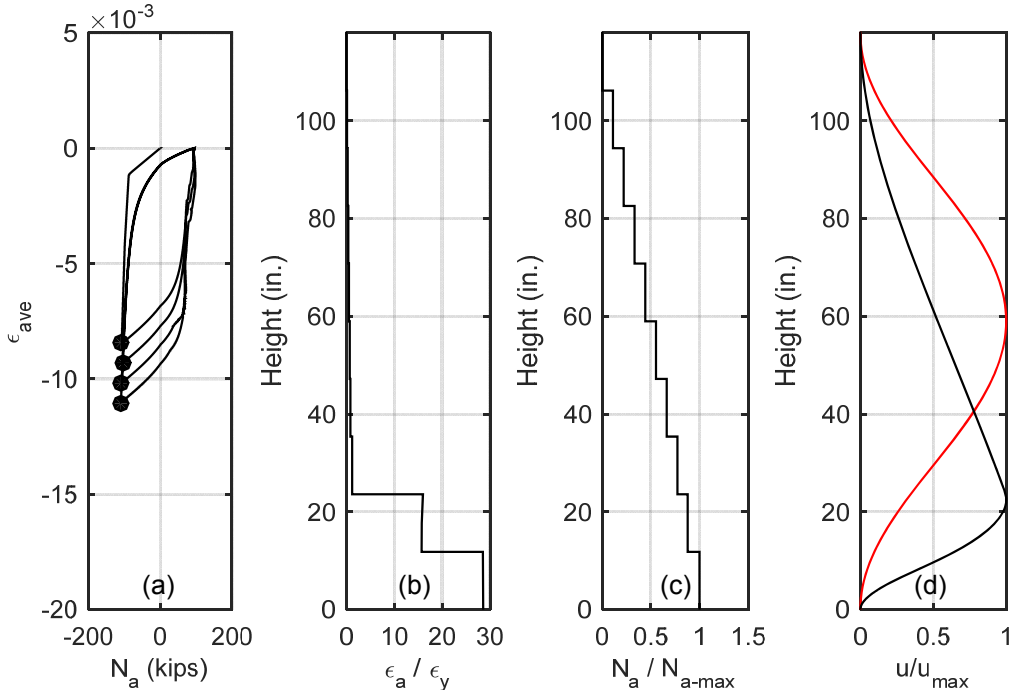

Figure A.5 **Specimen 4WC4_2, α= 0: a) average axial strain versus axial force at the base, b) normalized axial strain, c) normalized axial force, d) normalized buckled shape.**

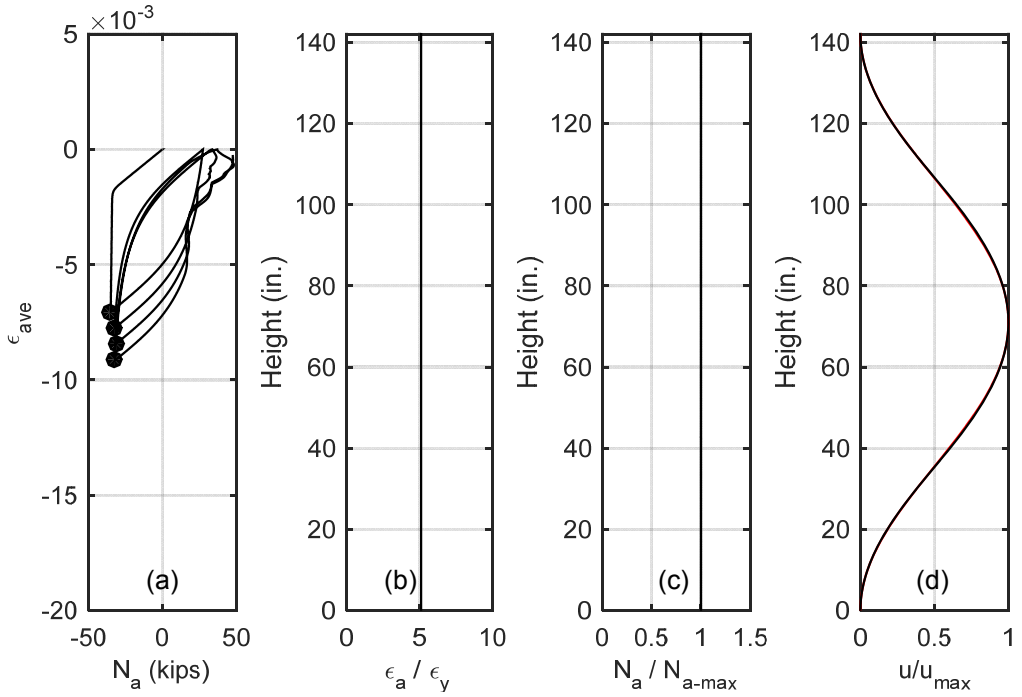

Figure A.6 **Specimen 5WC3_2, α= 1: a) average axial strain versus axial force at the base, b) normalized axial strain, c) normalized axial force, d) normalized buckled shape.**

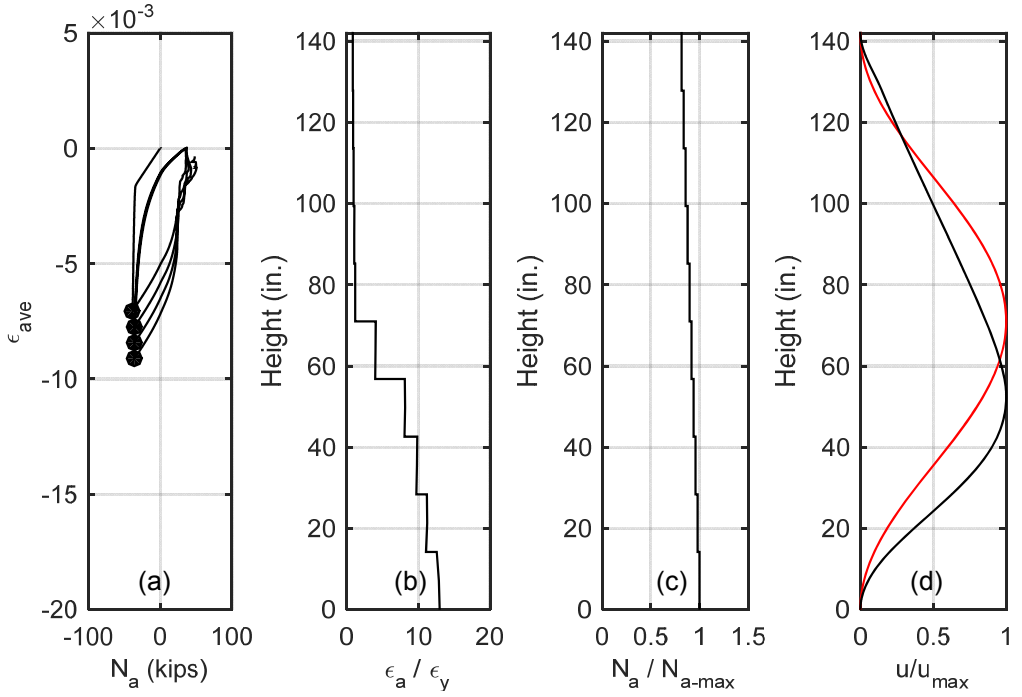

Figure A.7 **Specimen 5WC3_2, α= 0.8: a) average axial strain versus axial force at the base, b) normalized axial strain, c) normalized axial force, d) normalized buckled shape.**

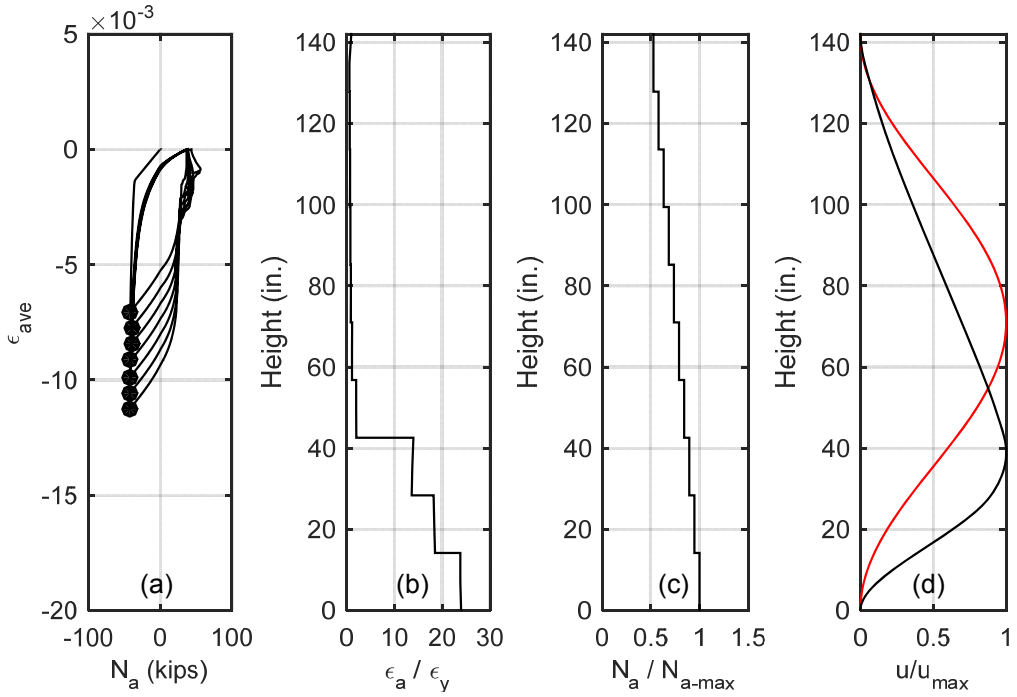

Figure A.8 **Specimen 5WC3_2, α= 0.5: a) average axial strain versus axial force at the base, b) normalized axial strain, c) normalized axial force, d) normalized buckled shape.**

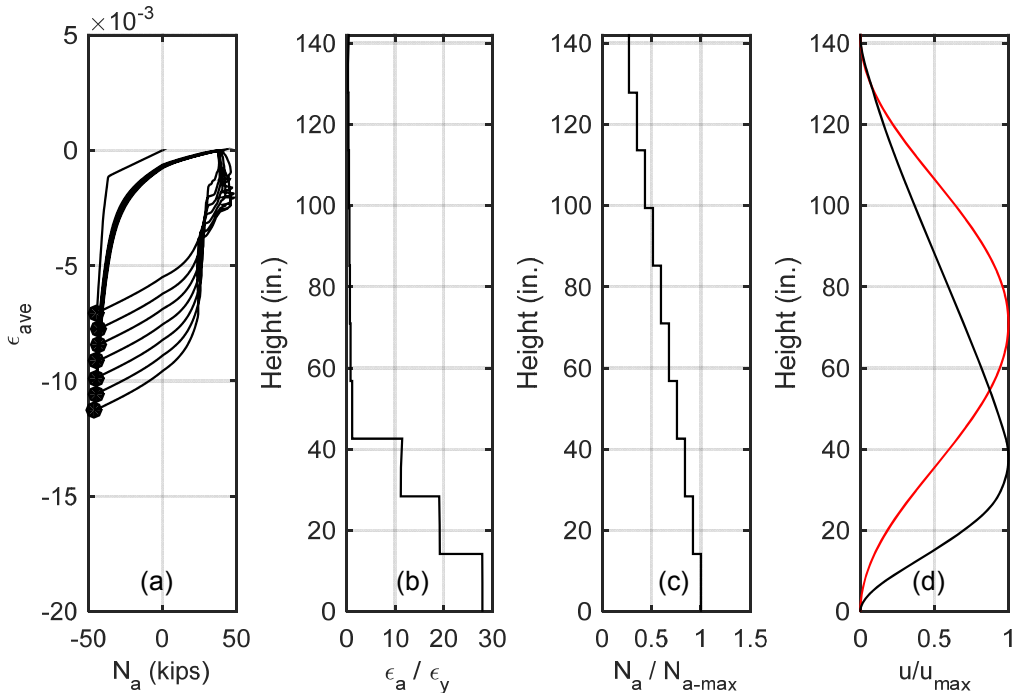

Figure A.9 **Specimen 5WC3_2, α= 0.25: a) average axial strain versus axial force at the base, b) normalized axial strain, c) normalized axial force, d) normalized buckled shape.**

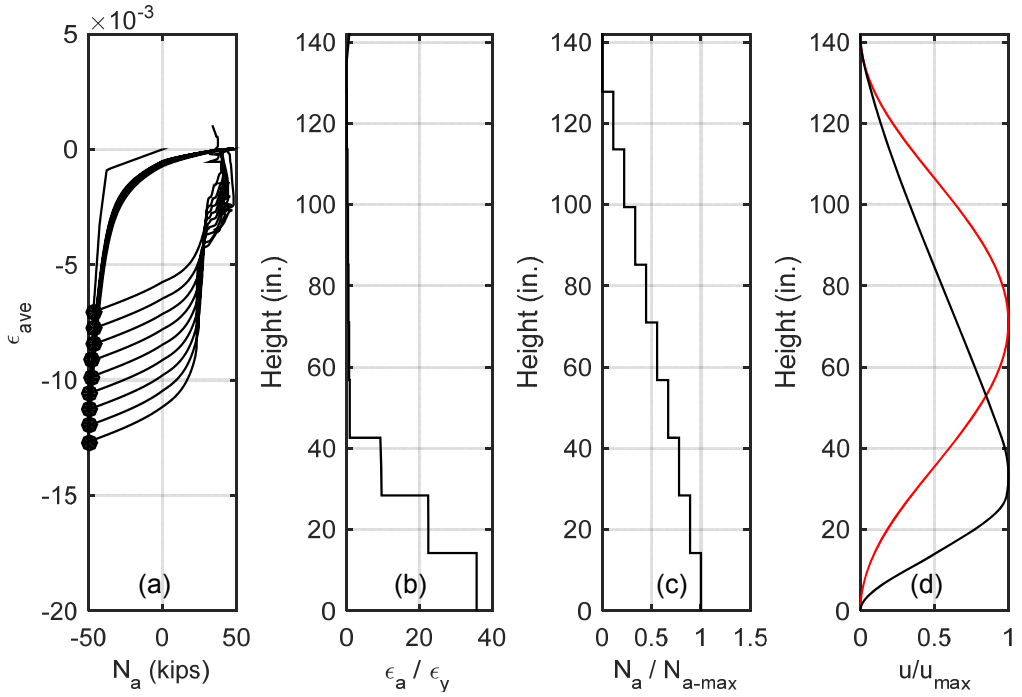

Figure A.10 **Specimen 5WC3_2, α= 0: a) average axial strain versus axial force at the base, b) normalized axial strain, c) normalized axial force, d) normalized buckled shape.**

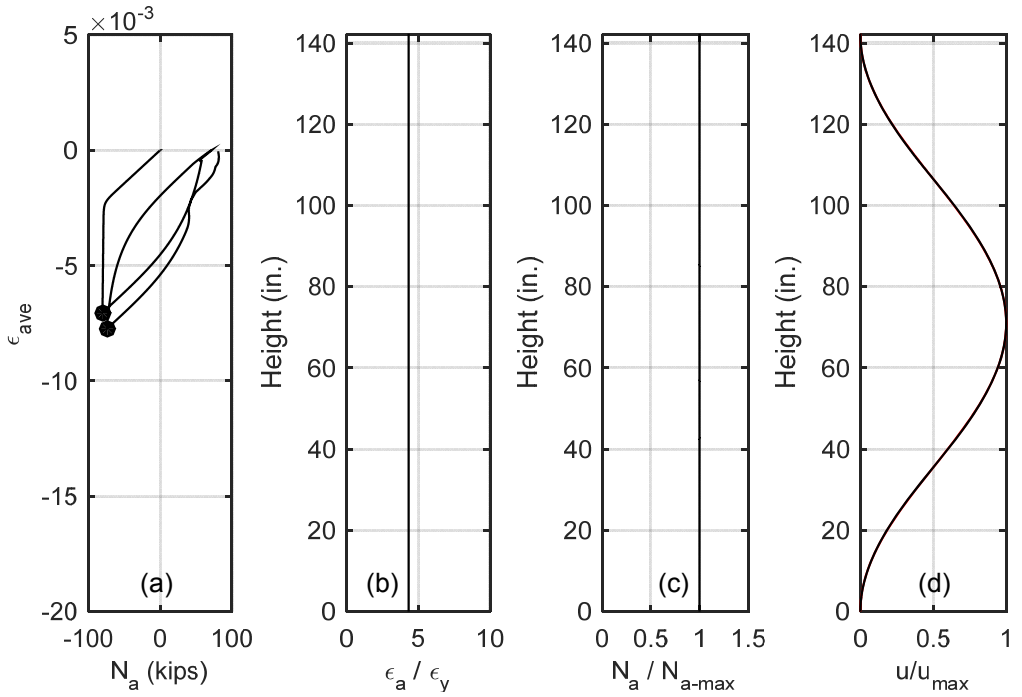

Figure A.11 **Specimen 5WC4_3, α= 1: a) average axial strain versus axial force at the base, b) normalized axial strain, c) normalized axial force, d) normalized buckled shape.**

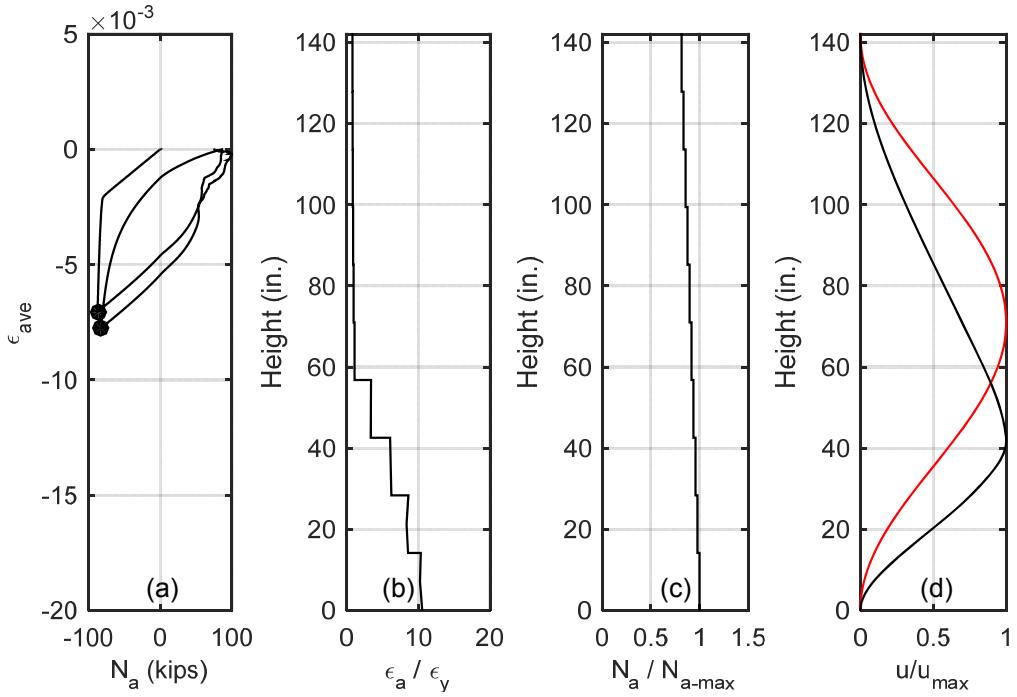

Figure A.12 **Specimen 5WC4_3, α= 0.8: a) average axial strain versus axial force at the base, b) normalized axial strain, c) normalized axial force, d) normalized buckled shape.**

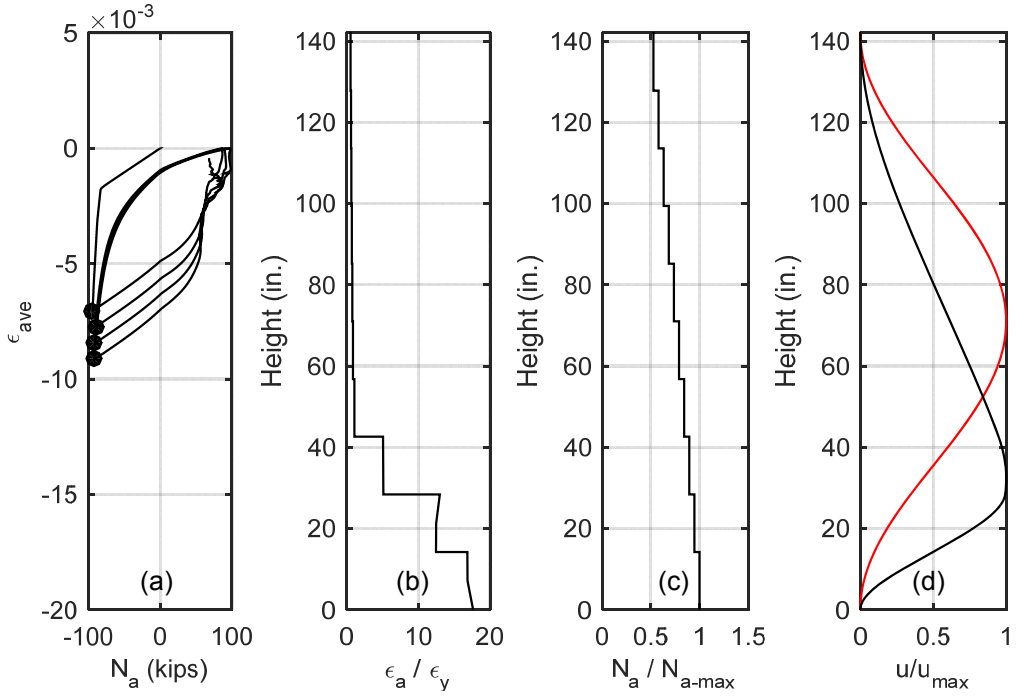

Figure A.13 **Specimen 5WC4_3, α= 0.5: a) average axial strain versus axial force at the base, b) normalized axial strain, c) normalized axial force, d) normalized buckled shape.**

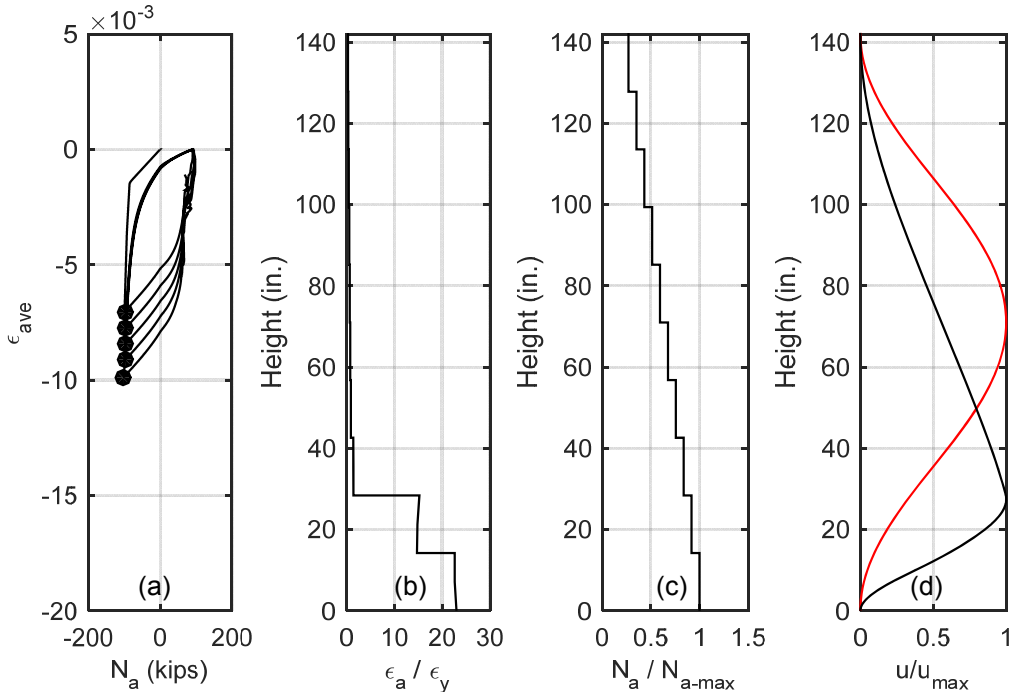

Figure A.14 **Specimen 5WC4_3, α= 0.25: a) average axial strain versus axial force at the base, b) normalized axial strain, c) normalized axial force, d) normalized buckled shape.**

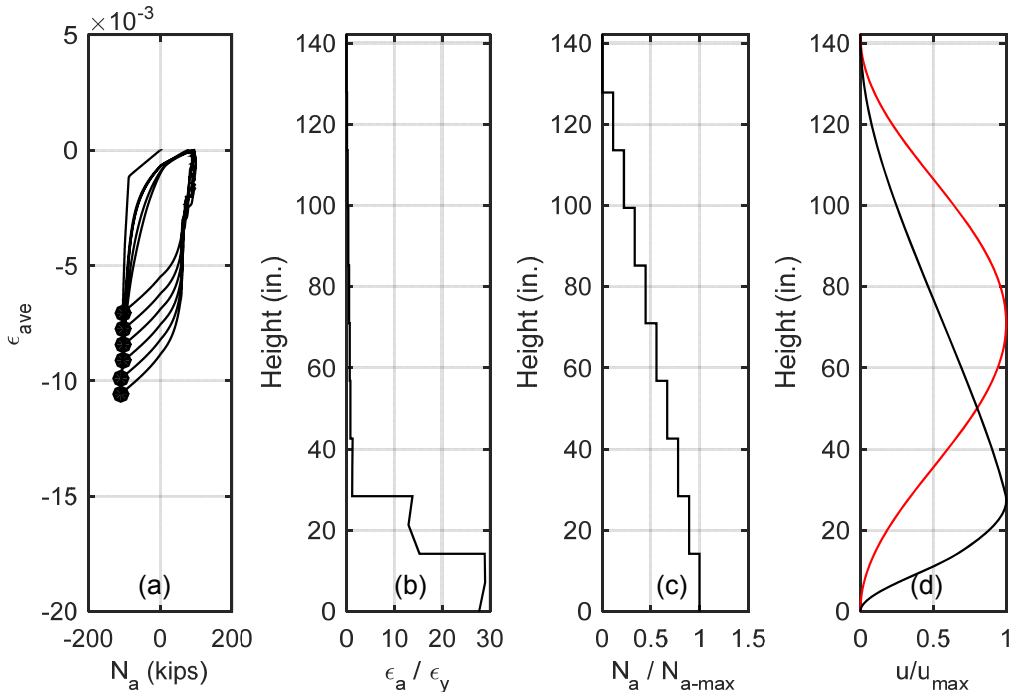

Figure A.15 **Specimen 5WC4_3, α= 0: a) average axial strain versus axial force at the base, b) normalized axial strain, c) normalized axial force, d) normalized buckled shape.**

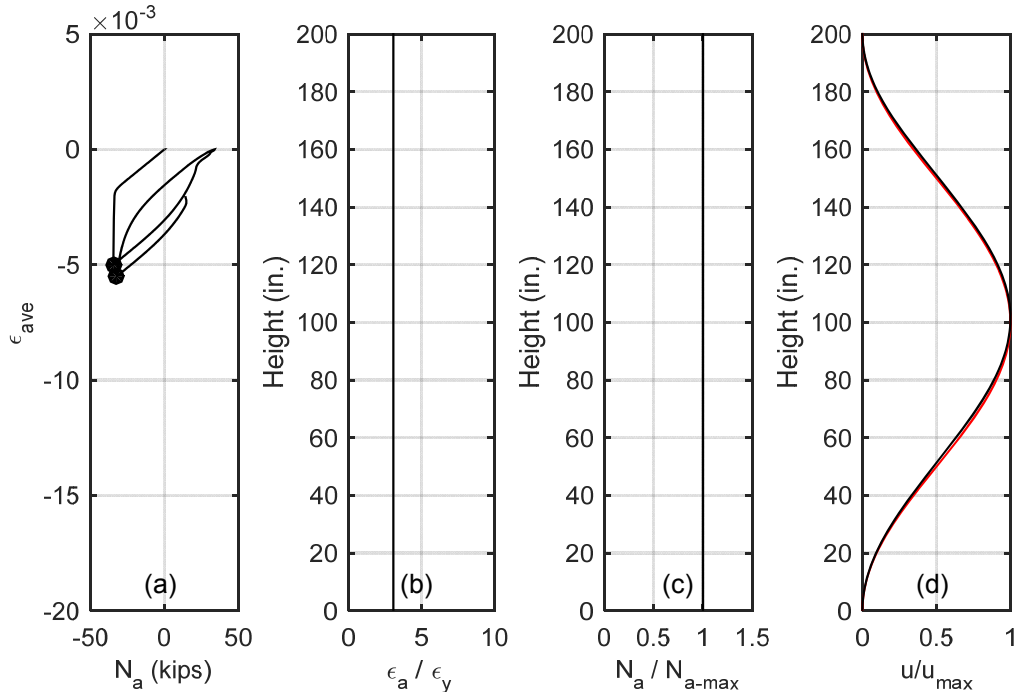

Figure A.16 **Boundary element with h_w/b = 50, α= 1: a) average axial strain versus axial force at the base, b) normalized axial strain, c) normalized axial force, d) normalized buckled shape.**

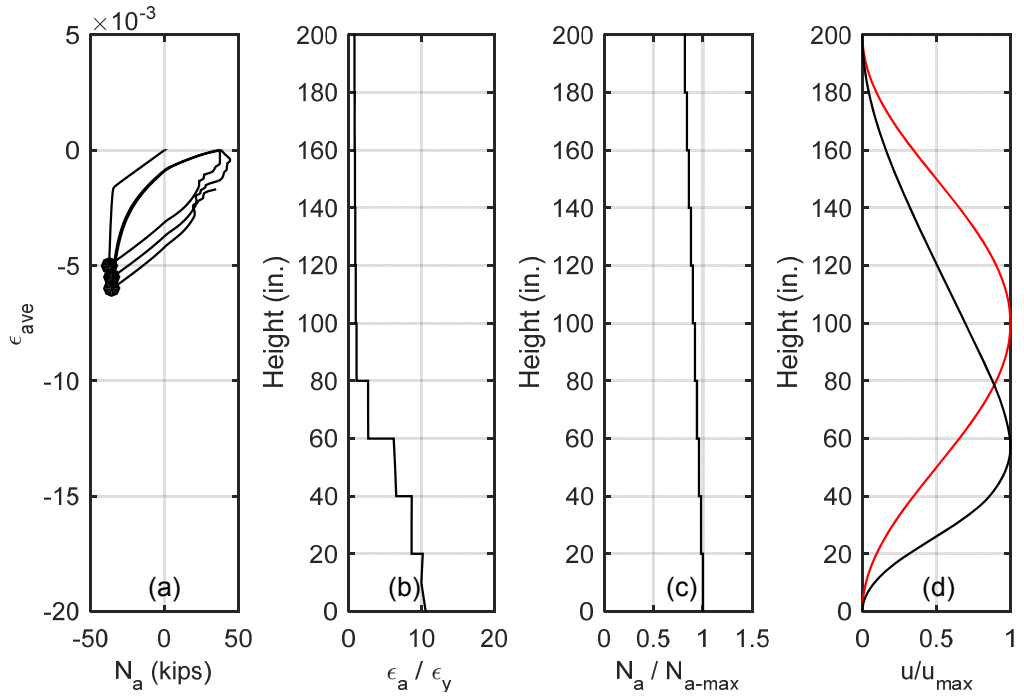

Figure A.17 **Boundary element with h_w/b = 50, α= 0.8: a) average axial strain versus axial force at the base, b) normalized axial strain, c) normalized axial force, d) normalized buckled shape.**

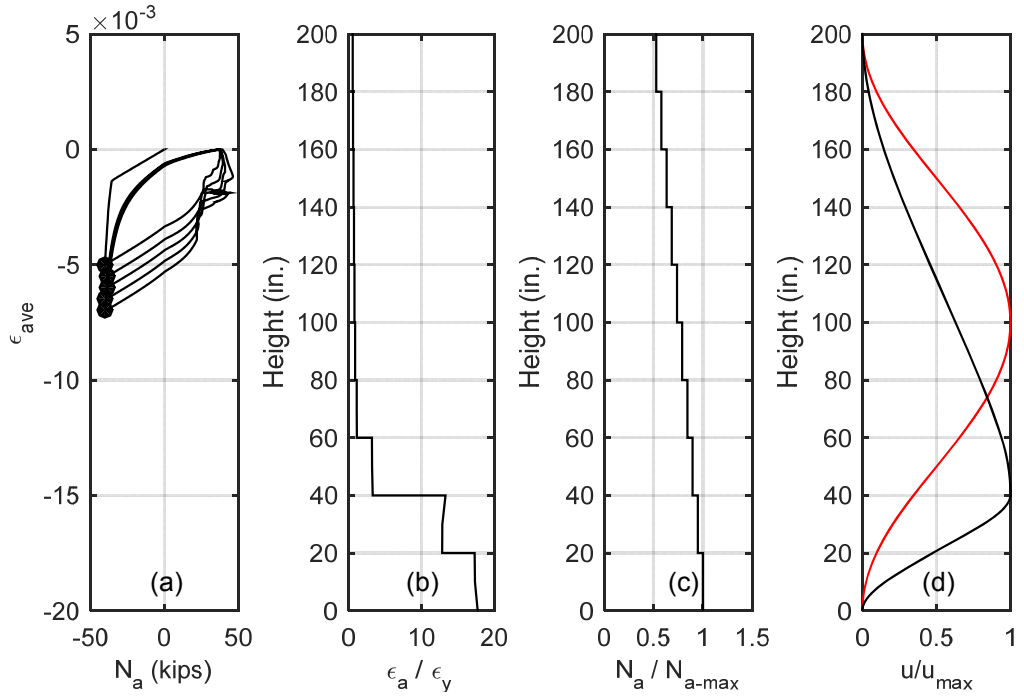

Figure A.18 **Boundary element with h_u/b = 50, α= 0.5: a) average axial strain versus axial force at the base, b) normalized axial strain, c) normalized axial force, d) normalized buckled shape.**

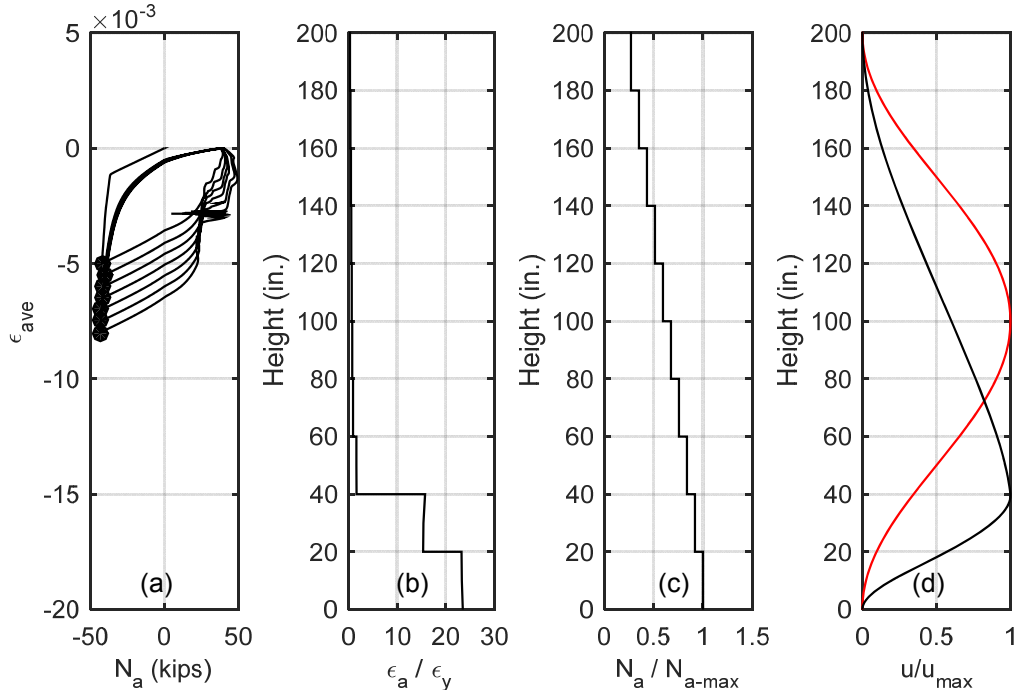

Figure A.19 **Boundary element with h_u/b = 50, α= 0.25: a) average axial strain versus axial force at the base, b) normalized axial strain, c) normalized axial force, d) normalized buckled shape.**

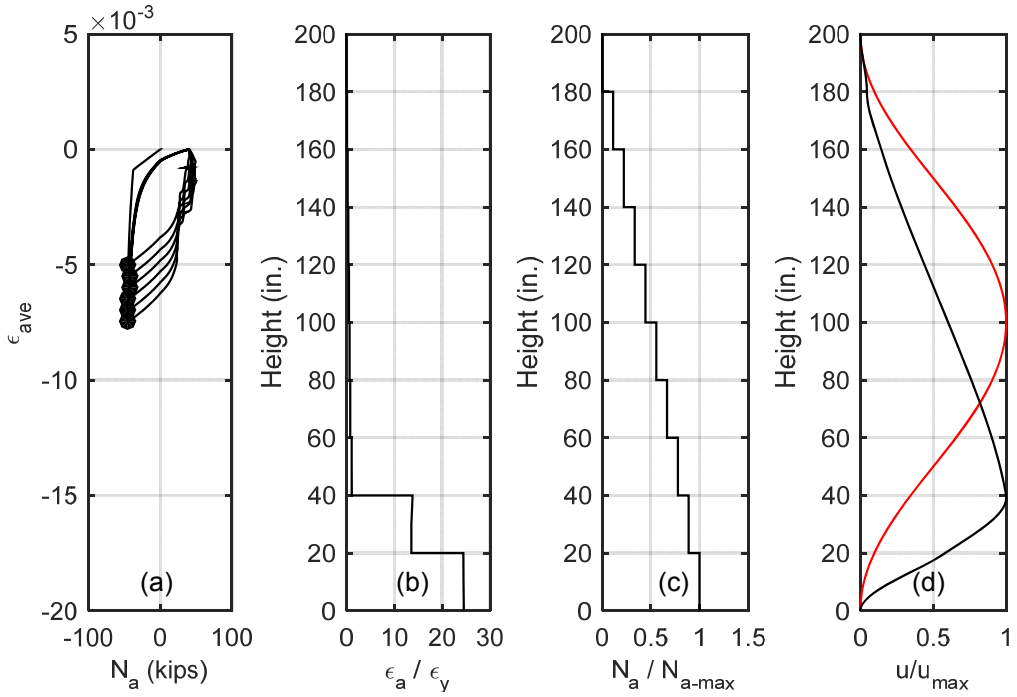

Figure A.20 **Boundary element with h_w/b = 50, α = 0: a) average axial strain versus axial force at the base, b) normalized axial strain, c) normalized axial force, d) normalized buckled shape.**